TECHNISCHE UNIVERSITÄT MÜNCHEN
Lehrstuhl für experimentelle Halbleiterphysik E25
Walter Schottky Institut

Fabrication and Thermoelectric Properties of Sintered Group-IV Nanoparticles

Benedikt Stoib

Vollständiger Abdruck der von der Fakultät für Physik der Technischen Universität München zur Erlangung des akademischen Grades eines

Doktors der Naturwissenschaften

genehmigten Dissertation.

Vorsitzender:	Univ.-Prof. Dr. Martin Zacharias
Prüfer der Dissertation:	1. apl. Prof. Dr. Martin S. Brandt
	2. apl. Prof. Dr. Peter Müller-Buschbaum

Die Dissertation wurde am 02.06.2015 bei der Technischen Universität München eingereicht und durch die Fakultät für Physik am 29.06.2015 angenommen.

Zusammenfassung

Die vorliegende Arbeit untersucht die Herstellung dünner Halbleiterfilme und charakterisiert diese hinsichtlich ihrer Anwendbarkeit für thermoelektrische Energiewandlung. Ausgehend von Nanopartikeln werden Dispersionen angefertigt und zu dünnen Filmen verarbeitet. Zur Erhöhung deren elektrischer Leitfähigkeit ist eine Nachbehandlung nötig, die mit einem intensiven Kurzpulslaser durchgeführt wird. Der Energieeintrag erhitzt und verschmilzt die Nanopartikel, so dass daraus ein Film erheblich verbesserter Konnektivität entsteht. So kann z.B. für undotierte Filme aus Ge-Nanopartikeln die Leitfähigkeit um mehr als fünf Größenordnungen auf durchschnittlich 0,5 S/cm angehoben werden. Für hochdotierte SiGe-Filme werden Leitfähigkeiten von bis zu 100 S/cm gemessen. Die Struktur der lasergesinterten Filme zeigt eine charakteristische mesoporöse Mäanderform, die das Substrat quasi-zweidimensional bedeckt und zu einer durchschnittlichen Reduktion der elektrischen Leitfähigkeit von einer Größenordnung gegenüber der eines vollständig bedeckenden Filmes führt. Im Gegensatz zur elektrischen Leitfähigkeit wird der Seebeckkoeffizient nicht von der Struktur beeinflusst, sondern hängt ausschließlich von der Dotierung des Filmes ab. Im Rahmen dieser Arbeit werden die Halbleiterfilme auf zwei Arten dotiert. Zum einen, indem bereits dotierte Nanopartikel verwendet werden, zum anderen, indem direkt vor dem Lasersintern Dotierstoffe aus einer Flüssigkeit auf die Nanopartikel aufgebracht werden. Das anschließende Lasersintern vereint hierbei die Strukturentwicklung mit der Inkorporation und elektrischen Aktivierung der Dotierstoffe. Diese Methode des Laser-assistierten nasschemischen Dotierens wird in der vorliegenden Arbeit entwickelt und die grundlegenden Einflussgrößen werden bestimmt. Die äußerst vielseitige und reproduzierbare Methode erlaubt es, eine Vielzahl an Gruppe-III- und Gruppe-V-Elementen sowohl zur Dotierung von Si- als auch von Ge-Filme zu verwenden. Ladungsträgerdichten von bis zu $10^{20}\,\mathrm{cm}^{-3}$ können so erreicht werden. Für die vollständige thermoelektrische Charakterisierung muss zudem die Wärmeleitfähigkeit ermittelt werden, was durch die hochkomplexe Struktur der Filme besonders anspruchsvoll ist. Als geeignete Methode wird ein auf Ramanspektroskopie basierendes Verfahren benutzt, für das die Filme so präpariert werden müssen, dass das Substrat keine parasitäre Wärmeleitung beiträgt. Unterstützt durch numerische Simulation können effektive Wärmeleitfähigkeitswerte von 0,5 W/m K für undotierte Ge-Filme und 0,05 W/m K für hochdotierte SiGe-Filme gemessen werden. Eine abschließende Bewertung ergibt, dass die aus Daten unterschiedlicher Proben gewonnenen thermoelektrischen Gütezahlen gleich hoch, wenn nicht sogar etwas höher als in anderen SiGe-basierten Materialien sind.

Abstract

Energy harvesting using solid-state-based thermoelectric generators is one of the topical areas of materials research. High conversion efficiencies require materials with a high Seebeck coefficient, a high electrical and a low thermal conductivity. Structurally complex and heavily doped semiconductors are proposed to fulfill these needs. In this work, the fabrication of laser-sintered Si, Ge and SiGe nanoparticle (NP) thin films and their thermoelectrical performance are investigated . The resulting films are structurally complex on a variety of length scales. Using a high intensity pulsed laser a characteristic structure of the laser-sintered film in the form of well connected meanders evolves, the structural dimensions of this mesoporous network are tunable by the sinter-fluence. Electrical conduction is enhanced by more than 5 orders of magnitude by the laser-sintering process, caused by the increased interconnection of the former NPs. Typical values of 0.5 S/cm are found for undoped Ge, while undoped Si exhibits 10^{-5} S/cm. Doping of the films can further increase the electrical conductivity to up to 100 S/cm. The 2-dimensionality of the meander network effectively reduces the electrical conductivity by one order of magnitude compared to non-porous reference material or non-porous films. The Seebeck coefficient is not influenced by the film morphology but only depends on the samples' doping concentration, which can be as high as 1 %. Both, p- and n-type doping can be realized using two different methods in this work: by already doping the precursor NPs during their synthesis or by application of dopants onto the NP film prior to its laser-sintering. In the latter method the dopant source is a liquid and the sinter laser incorporates and electrically activates the dopants in the host material. The method is called laser-assisted wet-chemical doping and is developed and extensively investigated in this work. Almost all group-III and -V elements can be used to dope Si as well as Ge films using this novel method, leading to charge carrier densities of up to 10^{20} cm^{-3}, as determined by Raman spectroscopy. Beyond the electrical characterization the determination of the in-plane thermal conductivity using optical non-contact methods is a further focus of this work. Prepared in a freely suspended manner, the films are thermally excited by a laser which at the same time evokes Raman scattering. The resulting characteristic wavenumber shift is related to the sample's temperature. Numerical simulations of the temperature distribution allow to deduce the effective thermal conductivity, which is found to be 0.5 W/m K for laser-sintered undoped Ge NPs and 0.05 W/m K for heavily doped laser-sintered SiGe NP films. The thermoelectric figure of merit calculated from these experiments indicates that laser-sintered NP thin films are competitive with other SiGe thermoelectric materials.

Contents

Zusammenfassung i

Abstract iii

1. Introduction 1
1.1. Small Features Make the Difference . . . 1
1.2. Sintered Nanoparticles as a Promising Material and their Treatment in the Present Work . . . 4
1.3. In Brief: The Content of this Work . . . 8

2. Thermoelectric Transport 9
2.1. A Simple Picture of the Origin of a Thermovoltage . . . 10
2.2. Thermoelectric Conversion Efficiency . . . 11
2.3. Theoretical Description of Thermoelectric Transport . . . 17
2.3.1. General Transport Coefficients for Transport of Charge Carriers . 17
2.3.2. Thermal Transport by Phonons . . . 21
2.4. Thermoelectric Parameters in Group-IV Materials . . . 22
2.4.1. Conductivity and Mobility in Poly-Crystalline Materials . . . 22
2.4.2. The Seebeck Coefficient in Group-IV Materials . . . 24
2.4.3. The Thermal Conductivity of Si-Based Materials . . . 27

3. Selected Experimental Techniques 33
3.1. Fourier Transform Infrared Spectroscopy . . . 33
3.2. Measurement of the Electrical Conductivity . . . 34
3.3. Measurement of the Seebeck Coefficient . . . 35
3.4. Raman Spectroscopy . . . 39
3.5. Scanning Electron Microscopy . . . 39

4. Group-IV Nanoparticles and Thin Film Deposition from Nanoparticle Inks 41
4.1. Gas-Phase Growth of Crystalline Nanoparticles . . . 41
4.2. The Nature of the Nanoparticle Surface and its Manipulation . . . 44
4.2.1. As-Deposited and As-Etched Si and Ge Nanoparticles . . . 46
4.2.2. As-Deposited and As-Etched SiGe Alloy Nanoparticles . . . 49

4.2.3. Influence of Etchant Concentration and Etching Duration on the Hydrogen Coverage . . . 52
4.3. Nanoparticle Inks . . . 54
4.4. Thin Film Deposition by Spin-Coating . . . 57

5. Enhancing the Nanoparticle Interconnection 59
5.1. Pulsed Laser-Sintering of Nanoparticle Films to Fabricate Thin Film Materials . . . 60
5.1.1. Experimental Setup and Sintering Procedure . . . 60
5.1.2. Thin Film Morphology and its Dependence on the Laser Fluence 62
5.1.3. Laser-Sintering Nanoparticle Films and its Effect on the Electrical In-Plane Conductivity . . . 70
5.1.4. Current Paths Through the Meander Structure . . . 73
5.1.5. Importance of HF Etching for the Morphology of Laser-Sintered Nanoparticle Films . . . 75
5.2. Current-Activated Pressure-Assisted Densification of Nanoparticles to Fabricate Bulk Materials . . . 76

6. Thermoelectric Properties of Sintered Nanoparticles 79
6.1. Thermoelectricity of Laser-Sintered Undoped Si Nanoparticle Films . . . 79
6.2. Thermoelectricity of Laser-Sintered Undoped Ge Nanoparticle Films . . 80
6.3. Thermoelectricity of Laser-Sintered B-Doped Si Nanoparticle Films . . . 86
6.4. Thermoelectricity of Heavily P-Doped Sintered SiGe Nanoparticles . . . 87

7. Laser-Assisted Wet-Chemical Doping of Sintered Nanoparticle Films 93
7.1. The Principle of Laser-Assisted Wet-Chemical Doping . . . 93
7.2. Doping Liquids for Laser-Assisted Wet-Chemical Doping . . . 95
7.3. Selectivity of Laser-Assisted Wet-Chemical Doping . . . 96
7.4. A Model System for Laser-Assisted Wet-Chemical Doping . . . 97
7.4.1. Experimental Observations for n-Type Doping of Ge Films . . . 97
7.4.2. Simulation of Laser-Assisted Wet-Chemical Doping . . . 99
7.5. Parameters Influencing Laser-Assisted Wet-Chemical Doping . . . 102
7.6. Laser-Assisted Wet-Chemical Doping Transferred to Other Elements . . 105
7.6.1. Group-III and -V Elements for Doping Ge Films . . . 105
7.6.2. Group-III and -V Elements for Doping Si Films . . . 110
7.6.3. Arsenic-Doping of SiGe Alloy Films . . . 112
7.6.4. Solid Solubility and Laser-Assisted Wet-Chemical Doping . . . 113
7.7. Quantitative Dopant Analysis . . . 114
7.7.1. Elemental Abundance of Dopants . . . 114
7.7.2. Raman Scattering by Free Charge Carriers . . . 118

8. Thermal Conductivity Measurements of Sintered Group-IV Nanoparticles 127
8.1. The Challenge to Determine Thermal Conductivities . . . 127

8.2. The Raman Shift Method to Obtain Thermal Conductivities 129
8.2.1. Model System I: 2-Dimensional Conduction of Heat 134
8.2.2. Model System II: 3-Dimensional Conduction of Heat 137
8.2.3. The Raman Shift Method Applied to Thin Films of Laser-Sintered Nanoparticles 138
8.2.4. The Raman Shift Method Applied to Bulk-Nano-Crystalline Si . . 147
8.2.5. The Raman Shift Method Summarized 151
8.3. Lock-In Infrared Thermography to Determine the Thermal Conductivity 152
8.3.1. Fundamentals of Lock-In Infrared Thermography 152
8.3.2. Previous Works on Thermographic Thermal Conductivity Measurements 154
8.3.3. A Proof-of-Principle Measurement 155

9. Conclusion **161**

Acronyms **165**

A. Simulation of Thermoelectric Properties for Laser-Sintered Ge Films **167**

B. Iterative Multigrid Gauss-Seidel Algorithm **173**

C. The Raman Temperature for Heat Spreading into a Semi-Infinite Sample **175**

Bibliography **179**

List of Publications **199**

Acknowledgments **203**

1 Introduction

1.1. Small Features Make the Difference

The increasing importance of advanced materials for applications in electronics, catalysis, energy storage and energy harvesting requires a fundamental understanding of the underlying physical properties of the respective materials. Of particular relevance for a sustainable future are materials for energy harvesting. One approach to this, which was discussed intensely in recent years, is thermoelectric energy conversion. This discipline deals with the motionless solid state-based conversion of temperature differences into electrical energy and vice versa. As it is true for all heat-to-electricity conversions, the efficiency of thermoelectric devices is limited by the Carnot efficiency. However, not all materials are similarly suited to be used in thermoelectric devices. The applicability of certain materials to thermoelectrics can be assessed by their dimensionless figure of merit ZT, which only depends on material-specific parameters and should be maximized when optimum efficiency is aimed at. As will be discussed in detail in the following chapters, ZT can be written as

$$ZT = \frac{S^2\sigma}{\kappa}T, \tag{1.1}$$

where T is the operating temperature, S is the Seebeck coefficient, σ is the electrical conductivity and κ is the thermal conductivity of the material.

For a long time, maximum ZT values found hardly surpassed 1,[Maj04] which limited thermoelectrics to niche applications. Examples are space missions, which use radioisotope thermoelectric batteries for an independent and long lasting energy supply.[Ben06] In the early 1990s, the group of Mildred Dresselhaus at MIT published predictions that ZT can be drastically enhanced in quantum well superlattice structures of the aniso-

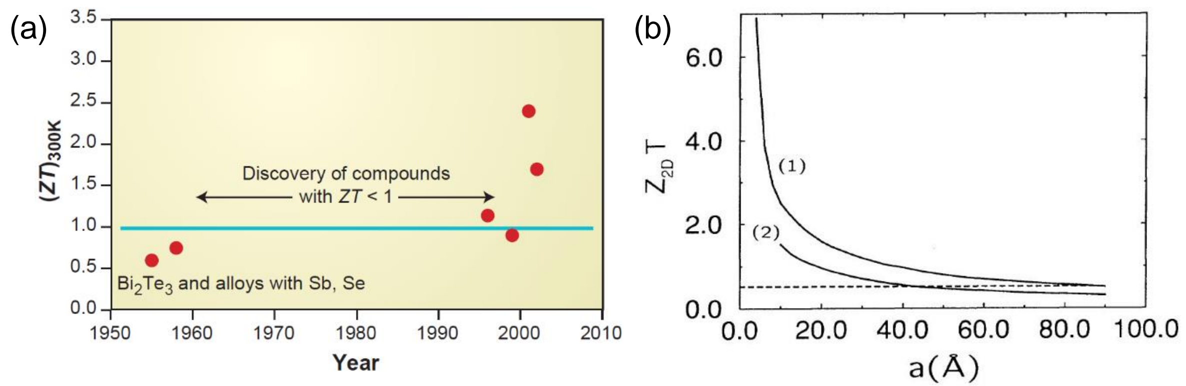

Figure 1.1. Historical development of the thermoelectric figure of merit and its possible improvement in quantum well structures: (a) For a long time, the figure of merit has been smaller than 1.[Maj04]. In the early 1990s predictions on the figure of merit for quantum well structures of Bi_2Te_3 lead to increased research and to an improvement of ZT above 1. (b) These curves from Ref. Hic93a predict a superior ZT of Bi_2Te_3 quantum well structures compared to bulk Bi_2Te_3 (dashed line), when the layer thickness is reduced. (1) and (2) mark two different orientations of the layers with respect to their crystal structure.

tropic material Bi_2Te_3, which is one of the best thermoelectric materials with $ZT = 0.6$ at room temperature.[Hic93a, Hic93b, Hic96] Two effects contribute here: First, the confinement of electrons increases the Seebeck coefficient since the lowest subband is energetically above the conduction band edge of the respective n-type bulk material. The more pronounced the confinement by decreasing the well thickness in the superlattice, the larger this constant. This first effect alters the electronic transport properties and increases the numerator of Eq. 1.1. The second effect alters the transport of heat and uses the fact that phonons scatter off the interfaces between the superlattice layers more effectively as their distance becomes comparable to the phonon mean free path. This reduces the denominator in Eq. 1.1. The theoretically predicted ZT from both effects in such a superlattice structure is shown in Fig. 1.1 (b) for two relative orientations of the layers with different crystal orientations. Compared to the dashed line which indicates the figure of merit of the bulk material, ZT for the superlattice structure may be enhanced by up to one order of magnitude.

Starting with this work by Hicks et al. the field of nanostructured thermoelectrics rapidly grew.[Hic93a] Still today, research focusses on the two mentioned concepts of altering the electronic band structure to increase, both, the Seebeck coefficient and the electrical conductivity, and of reducing the thermal conductivity by introducing scattering centers for phonons. However, it turned out that in most materials it is advisable to first concentrate on the latter. As an example, it is much easier to reduce the crystalline quality (affecting κ) of semiconductors than to perfectly engineer and control the electronic landscape (influencing $S^2\sigma$). Applying techniques such as grinding bulk material, followed by hot pressing, this strategy has already been followed in the early space missions, which used SiGe with micrometer-sized grains to reduce the lattice thermal conductivity.

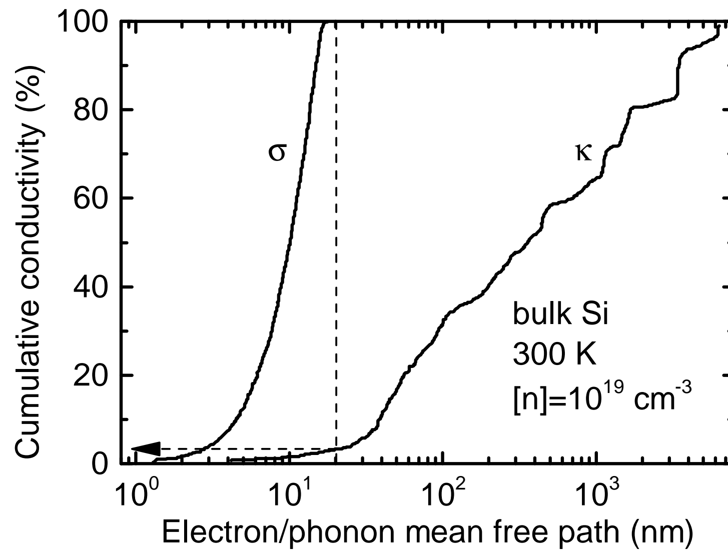

Figure 1.2. Cumulative electrical and thermal conductivities in Si: For room temperature the thermal and electrical conductivities are shown in a cumulative plot as a function of the quasiparticles' mean free path. Limiting the mean free path of phonons to 20 nm by an appropriate scattering center would drastically reduce the thermal conductivity κ, while the electronic transport would be left unaffected. The figure is adapted from Ref. Qiu15.

Today, many concepts are discussed to additionally structure thermoelectric materials. However, attention has to be paid not to adversly affect the transport of charge carriers by this. A concept that considers that fact is called *phonon-glass-electron-crystal*, which assumes that the mean free path of phonons is larger than the mean free path of charge carriers, so that the latter hardly "see" the scattering centers for phonons.[Nol99]

This concept is exemplarily shown in Fig. 1.2 for bulk Si at room temperature.[Qiu15] These theoretical data show the normalized cumulative electrical and thermal conductivities as a function of the mean free path of electrons and phonons, respectively. The electrical current is conducted by electrons with a mean free path of less than 20 nm, whereas thermal conduction requires phonons with a substantially larger mean free path. Introducing additional scattering on a scale of 20 nm (vertical dashed line) electrons would remain unaffected. Heat transport by phonons is hindered and the total thermal conductivity would be reduced, increasing the ratio σ/κ in Eq. 1.1.

To maximize the phonon scattering rate for the whole phonon spectrum, it is desirable to have an *all-scale hierarchical disorder* in the material, so that phonons of all wavelengths are affected.[Bis12] This can be achieved by combining a variety of structural features, ranging from disorder on the atomic scale caused by alloying, small-sized grains, embedded nanoparticles (NPs) or precipitates, and porosity on the nano- and micron-scale.[Maj04, Her05, Kim06, Min07, Wan08, Min09a, Min09c, Lee09, Yu10, Lee10, Tan10, Lan10, Wan11, Joh11, Pet11]

With the increasing number of reports on the synthesis of nanowires also their applicability for thermoelectrics has been investigated. Even for Si, which in bulk form

is no competitive thermoelectric material, nanowires showed reasonable figures of merit.[Li03, Bou08] It has been noticed that the roughness of the nanowire surface distinctively affects the phonon scattering and is, thus, desirable for thermoelectric optimization.[Hoc08, Lim12]

As pointed out, in most materials systems it is much more complex to engineer the electronic band structure to enhance electronic properties. Among the concepts discussed in the context of the nominator in Eq. 1.1 are modulation doping by embedding NPs with different doping and band gap, an alteration of the density of electronic states due to nano-inclusions, the effect of strain and, in general, the optimization of doping.[Fal08, Her08, Zeb11, Yu12, Pei12, Kim13]

As has become obvious from the above discussion, the introduction of small-scale features is believed to be of potential benefit for increasing the thermoelectric figure of merit. Some up-to date reviews on complex, low-dimensional and nanostructured thermoelectrics may help the interested reader to further satisfy their thirst for information.[Rif03, Dre07, Sny08, Sch08b, Soo09, Med09, Min09b, Kan10, Vin10, Sha11, Nie11, Zeb12, Sch14]

1.2. Sintered Nanoparticles as a Promising Material and their Treatment in the Present Work

One widely followed approach to obtain materials for thermoelectrics is bottom-up fabrication starting from NPs. Nanoparticles can be synthesized with high crystalline quality and their electronic properties, such as n- and p-type doping, can be adjusted in a controlled manner. The present thesis persues such a bottom-up fabrication using SiGe NPs which are characterized in their initial state in Chap. 4. The main focus of this work are thin film SiGe materials obtained by laser-sintering of Si and Ge NPs. The laser-sintering process and the obtained thin film morphology are discussed in Chap. 5. Those thin films show many of the above mentioned hierarchical structures and are as thus a promising thermoelectric materials class.

The used NPs are synthesized by the collaborating group of Hartmut Wiggers at the University of Duisburg-Essen. The films then are prepared at the Walter Schottky Institut at the Technische Universität München within the framework of this thesis, and are there further investigated concerning their morphology and their thermoelectric properties. Apart from laser-sintering at the Walter Schottky Institut, bulk-nano-crystalline Si(Ge) thermoelectric materials were made from the same initial NPs by current-activated pressure-assisted densification by the group of Gabi Schierning at the University of Duisburg-Essen. Those bulk materials serve as a benchmark and as a test system for the characterization methods used in this thesis.

The major difference between laser-sintered thin films and bulk-nano-crystalline material is the density of the resulting material. While the latter is almost perfectly dense, the laser-sintered NP films are porous with a typical feature size of several

hundred nm, which offers an additional potential scattering mechanism for phonons of a larger mean free path. Both materials consist of small grains which are intended to scatter phonons with a small mean free path. Whilst the grain growth for bulk-nano-crystalline materials made by current-activated pressure-assisted densification is only minor, laser-sintering leads to a significant grain growth.

The morphology of the materials is mainly responsible for their thermal conductivity, whose experimental determination is discussed in Chap. 8, while doping effects dominate the electrical conductivity and the Seebeck coefficient, as will be shown in Chap. 6 in more detail. In the standard doping procedure the dopant atoms are added during the synthesis of the NPs already. This doping method will be referred to as *gas-phase doping* in the following. Since this approach has some drawbacks concerning flexibility and safety, this thesis discusses an additional way to apply the dopants to the thin films in a wet chemical step. This method, which is discussed in Chap. 7, offers a high degree of flexibility with many other dopant elements being available, apart from boron and phosphorous, which are virtually the only available dopant species during the NP gas phase synthesis.

Figure 1.3 schematically summarizes important work flows for the fabrication of both thin films and bulk-nano-crystalline materials. The indicated chapters of this work cover the most important aspects. For the thin films three possible scenarios to achieve a defined doping density in the final film are shown. All routes start from gaseous precursors, which are silane (SiH_4) and germane (GeH_4). For simplicity only silane is shown here. Depending on the route, dopant gases such as phosphine (PH_3, red in Fig. 1.3) or diborane (B_2H_6) are added during the NP synthesis. By microwave decomposition of the precursor gases and the following cooling of the constituents, the NPs are formed. The standard way to obtain porous thin films from those NPs is to disperse the powder, so that a processable ink is formed. By coating this ink onto a substrate a film of more or less loosely packed NPs can be obtained. However, the electrical performance of such films is poor, so that a post-deposition treatment becomes necessary. Sintering by a high intensity pulsed laser leads to the formation of a well connected structure which exhibits a typical meander-like morphology on the substrates which are used in this thesis.

The second and third column in Fig. 1.3 illustrate two alternative ways to define the doping concentration in thin films, apart from adjusting the doping level in the initial gas phase synthesis as in the first column. In the *digital doping* approach two inks are mixed: one with undoped NPs and a second one with NPs with a rather high doping level. By the mixing ratio the effective doping in the film can be defined because the grain growth leads to a sufficient intermixing and distribution of the dopants. The third approach, which is discussed in detail in this work, is called *laser-assisted wet-chemical doping* and completely avoids doping of NPs in the gas phase, which is especially interesting with respect to the risks related to gases such as phosphine. Here, an ink of undoped NPs is deposited on a substrate. The film is then brought in contact with a doping liquid which contains suitable dopant species, e. g., phosphoric acid or boric acid. The dopant species

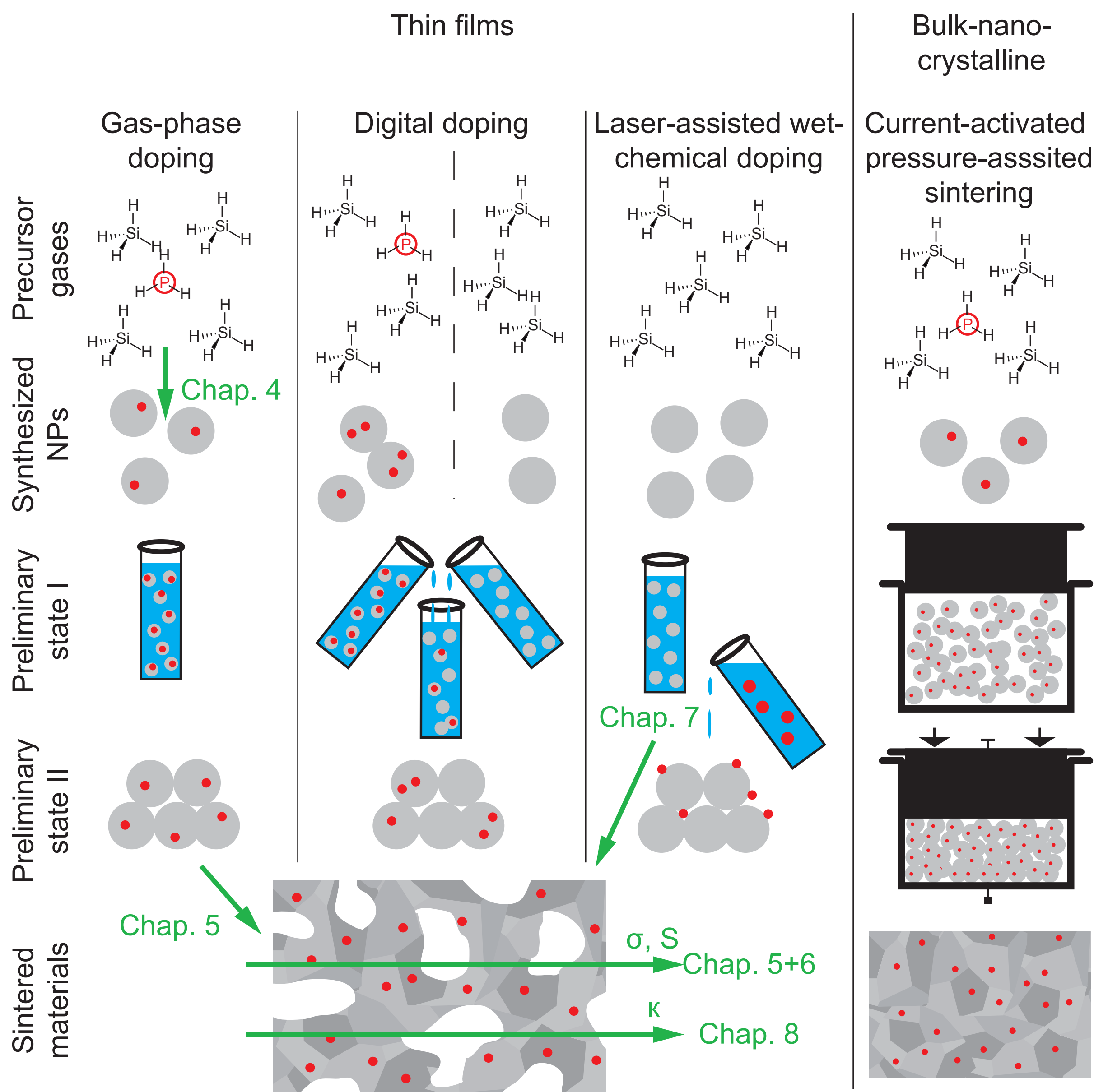

Figure 1.3. Schematic illustration of fabrication work flows for thin films and bulk samples discussed in this thesis: All NP powders used in this work are synthesized by decomposition of silane or germane and, if needed, dopant gases such as phosphine or diborane. This yields doped (symbolized by grey NPs including a red sphere) or undoped NPs (grey only). For the fabrication of thin films, the NPs are dispersed and deposited on a substrate. For digital doping dispersions of doped and undoped NPs are mixed, for laser-assisted wet-chemical doping the dopants are applied to the deposited film of undoped NPs by a doping liquid. Laser-sintering of all those films yields mesoporous granular material with comparable doping distribution. For bulk samples the NPs are compressed and sintered by the help of current and pressure, resulting in dense nano-crystalline material. The figure also indicates the chapters of this thesis dealing with the different steps in the fabrication and analysis of the NPs before and after laser-sintering.

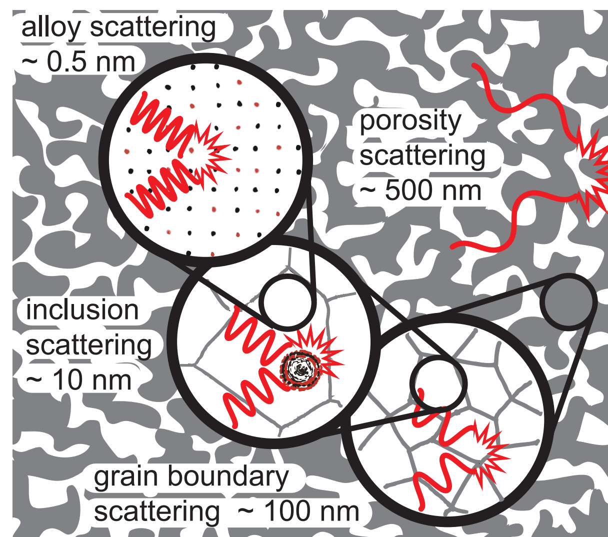

Figure 1.4. Hierarchical phonon scattering: Laser-sintered thin films made of NPs comprise potential scattering centers for phonons (symbolized as waves) of different wavelengths. Alloy scattering, scattering at NP inclusions, at grain boundaries and at mesoscopic pores span approximately 3 orders of magnitude in geometrical size, which is potentially beneficial for thermoelectric applications.[Bis12, Vin10]

attach to the NPs and are incorporated during the following laser-sintering step.

For the sake of completeness the fourth column of Fig. 1.3 illustrates the work flow for the fabrication of bulk-nano-crystalline samples at the University of Duisburg-Essen. There, the NP powder is filled in a die and is precompacted manually by a punch. Supported by external heating a uni-directional current is then injected through the powder so that Joule heating leads to a sintering and a densification due to the applied pressure. For this approach only gas-phase doped NPs are used in the framework of this thesis, although digital doping as well as the wet-chemical approach are in principle also suitable.

The resulting morphology of the bulk-nano-crystalline samples is characterized by small grains constituting a dense nanostructured bulk material. In contrast, after laser-sintering of NP films a porous network is obtained, which is the same independent of the doping approach applied. The hierarchy of potential scattering centers for phonons are depicted in the sketch in Fig. 1.4, where the background is an illustrative image of the porous meander network. The typical feature size of the porosity is approximately 500 nm so that long wavelength phonons, which have a larger mean free path, are affected most by this kind of disorder. For the part of the phonon spectrum with smaller wavelength, the granular substructures of the meanders become relevant as scattering centers. The grains have a typical size of 100 nm. Characteristic for the short pulse laser-sintering process some initial NPs withstand the grain growth and are embedded in the grains or at grain boundaries. With a typical size of slightly more than 10 nm phonons of even shorter wavelengths are prone to scatter there. The ultimate disorder for phonons of the shortest wavelength is a solid solution of atoms in an alloy. Using Si

and Ge as constituents the mass difference between the atoms leads to poorly defined vibrational modes and thus a lower thermal conductivity in the alloy compared to the pure materials.

With a variety of possibilities to define the electronic properties and their hierarchical morphology with feature sizes ranging from Å to the µm-range, laser-sintered NP films are proposed as a candidate for efficient thermoelectric materials. Fabrication, morphology, thermoelectrical and thermal properties therefore are the main aspects of the present thesis.

1.3. In Brief: The Content of this Work

The work is structured as follows: Chapter 2 introduces the theoretical base for the discussion of thermoelectric transport properties. Data on thermoelectricity in SiGe materials taken from the literature is also reviewed in this chapter. The main experimental techniques are presented in Chap. 3. All following chapters cover results obtained during the experimental part of this work. Their relevance with respect to fabrication and characterization of thermoelectric materials is also indicated in Fig. 1.3. Chapter 4 shortly summarizes the fabrication and the surface vibrational properties of gas-phase synthesized NPs, as well as the deposition of thin films from inks of NPs. Results on the morphology are discussed in Chap. 5, where the sintering of NPs is one focus. Another focus is the impact of the porous thin film structure on the electrical conduction in the plane of the film. In Chap. 6 the Seebeck coefficient as well as the electrical conductivity of laser-sintered films of NPs are discussed. The wet-chemical approach to dope the resulting laser-sintered thin films is presented in detail in Chap. 7. The results part of this thesis closes with Chap. 8, where the thin films' thermal conductivity is measured by optical means. Finally, concluding remarks will be given in Chap. 9.

2
Thermoelectric Transport

In the years between 1821 and 1823 T. J. Seebeck, a german physicist, indirectly discovered that an electrical voltage, the thermovoltage U, develops between the two ends of a conducting material, if the ends are at two different temperatures.[1][See26a, See26b] Later it was discovered that the Seebeck coefficient, which is sometimes also called thermopower and which is defined as

$$S = \frac{U}{\Delta T}, \tag{2.1}$$

is much larger in semiconductors than it is in metals, where S is typically of the order of $10\,\mu\text{V}/\text{K}$.[Gol54] The use of semiconductors then made the Seebeck effect interesting for applications where electrical energy needs to be supplied from simple heating, for example for mobile military radio stations in remote areas in Russia.[Ved98] In 1909 E. Altenkirch was the first to correctly calculate the efficiency of a thermoelectric energy converter and thereby introducing the concept of the thermoelectric figure of merit ZT.[Alt09, Cal]

It is important to note that with thermoelectricity this conversion of heat energy into electrical energy is partly reversible. Not in the sense that electrical energy can be dissipated by Ohmic losses, but in the sense that there exists an inverse effect to the Seebeck effect. In 1834 J. C. A. Peltier discovered that a current I passing a conductor

1 Actually, he did not discover the voltage itself, but he observed what happened to a compass needle, which was placed inside of a loop made from two half rings of different metals. As he heated one junction of the two metals while keeping the other junction cold, the needle was deflected. The reason for this behavior is the magnetic field caused by the current in the ring according to Ampere's law. In turn, this current is driven by the net voltage that remains when adding the thermovoltages of the two metals.

heats up one end and cools the other end. In contrast to Joule heating, reversing the current direction also reverses the heat flux. The heat transported can be written as

$$\dot{Q} = \Pi\, I, \tag{2.2}$$

with the Peltier coefficient Π. Today, the Peltier effect is exploited for cooling applications.

This chapter is intended to more extensively introduce the most important theoretical aspects of thermoelectricity, starting with an illustrative explanation for the emergence of the thermovoltage in an n-type semiconductor. As a basis for the discussion of the experimental results obtained in this thesis the present chapter will also review the literature on thermoelectricity in Si and SiGe materials.

2.1. A Simple Picture of the Origin of a Thermovoltage

If one imagines an n-type semiconductor with the conduction band edge E_c, and the valence band edge E_v, and which is doped to an extent that the Fermi level E_F is located in the vicinity of the conduction band, then, for a finite temperature, the Fermi distribution function extends into the Density Of States (DOS) of the conduction band. This results in a certain local density of ionized donors and in a transfer of electrons into the conduction band. For a slab of semiconducting material at constant temperature with no potential difference applied this charge carrier density is the same throughout the whole material. If now one end is heated to a higher temperature, the Fermi distribution function adapts to this higher temperature, broadens and the overlap into the conduction band is larger. A sketch of this situation is drawn in Fig. 2.1 (a). This larger overlap increases the density of freely mobile electrons at the hot end. With respect to the cold end, a concentration gradient of electrons establishes and, according to Fick's law, diffusion of carriers from the hot end to the cold end will take place. Since the electrons carry charge this leads to a negative potential at the cold side with respect to the hot side, lifting the band structure high in energy until the net flow of electrons due to diffusion is compensated by a flow of electrons due to the electric field. The equilibrium situation is shown in Fig. 2.1 (b), where the temperature dependence of E_F due to the local statistics leads to the tilt of the dashed line indicating E_F compared to the conduction band.

In the above example a negative voltage emerges at the cold side, because electrons are the majority carrier type. In a p-type semiconductor the same arguments hold and holes accumulate at the cold side, generating a voltage of opposite sign. Thus, the sign of the voltage at the cold side, and thus of the Seebeck coefficient, reveals the majority carrier type. This simple test is extremely helpful, especially because the material only needs to be poorly conductive since no net current flows when measuring the thermovoltage.

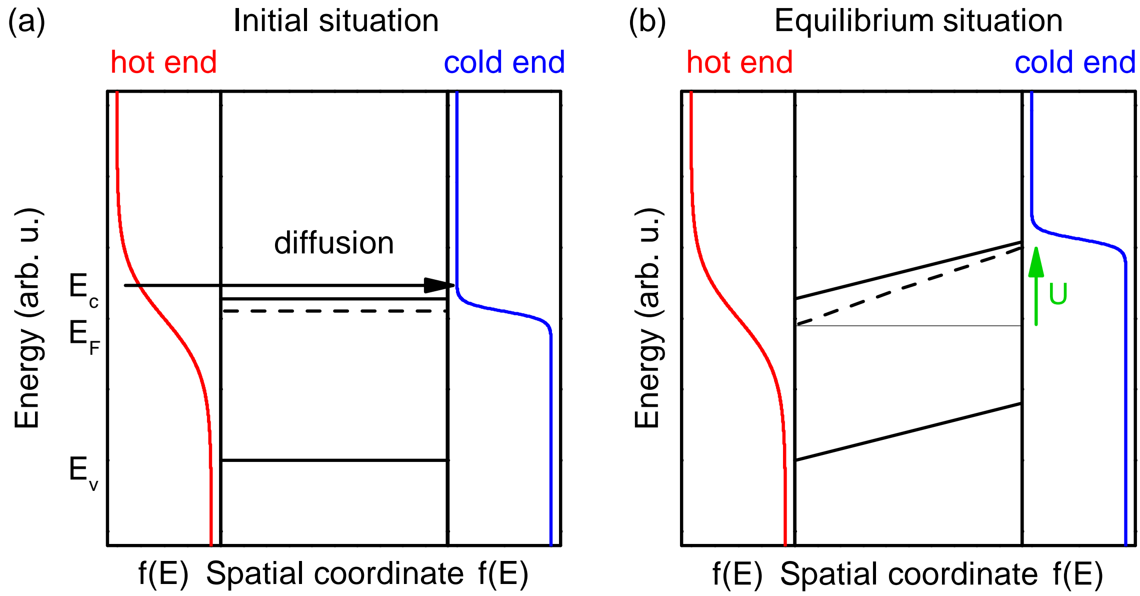

Figure 2.1. The formation of a thermovoltage in an n-type semiconductor: In the initial situation one end of the sample is hot, the other is cold, but no net diffusion of charge carriers took place yet. After diffusion of electrons from the hot to the cold end, the thermovoltage U ensures electrochemical equilibrium.

2.2. Thermoelectric Conversion Efficiency

Combining Two Materials for a Thermoelectric Generator

To assess the suitability of thermoelectric materials for energy harvesting applications it is necessary to study the conversion efficiency of a Thermoelectric Generator (TEG). As obvious from the above discussion, power can only be generated when contacting the hot and the cold side of the working material A with a Seebeck coefficient S_{A} to a load, which is at a temperature T_{load}. The cables made from a material B, leading to the load, however, also have a certain Seebeck coefficient S_{B}, so that the maximum voltage at the load is given by

$$U_{\mathrm{load}} = (S_{\mathrm{A}} - S_{\mathrm{B}})\,(T_{\mathrm{hot}} - T_{\mathrm{cold}})\,. \tag{2.3}$$

This consideration motivates to use two dissimilar materials for a TEG: an n- and a p-type leg. Then, the TEG can entirely be contacted at either the hot or the cold side and the cables themselves do not influence the voltage at the load. The different signs of the Seebeck coefficient for the two legs A and B lead to an enhanced voltage, which is the sum of the absolute values of the thermovoltage for the n- and the p-type leg. The typical appearance of a TEG is shown in Fig. 2.2.

The following calculations of the thermoelectric conversion efficiency are based on Ref. Iof57, assuming to a first instance temperature-independent material parameters. To be implemented in the same TEG, the two legs have the same length l and cross sections of A_{p} and A_{n} for the p- and the n-type leg, respectively. With the specific electrical

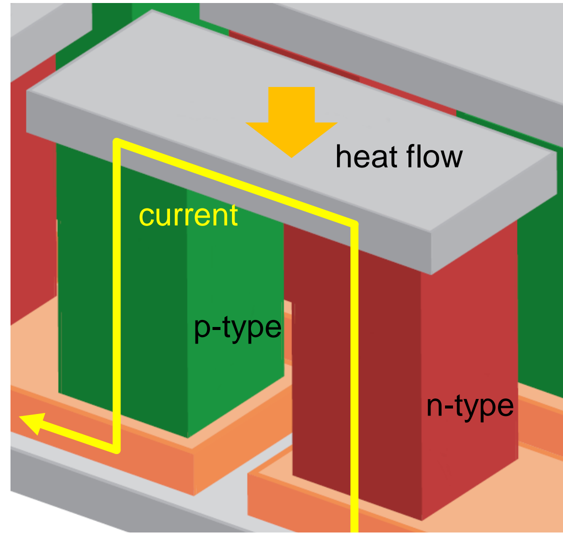

Figure 2.2. A thermoelectric generator (TEG): A p- and an n-type leg constitute the TEG. The heat is absorbed at the top surface and rejected at the bottom surface. When a load is connected, an electrical current results from the diffusion of electrons and holes to the cold side of the n- and p-type leg, respectively. The illustration is taken and adapted from Ref. Sny08.

conductivities σ_p and σ_n and the specific thermal conductivities κ_p and κ_n, the total electric resistance r of the TEG is

$$r = l\left(\frac{1}{\sigma_\mathrm{n}\,A_\mathrm{n}} + \frac{1}{\sigma_\mathrm{p}\,A_\mathrm{p}}\right), \tag{2.4}$$

and the total thermal conductance is

$$K = \frac{1}{l}\left(\kappa_\mathrm{n}\,A_\mathrm{n} + \kappa_\mathrm{p}\,A_\mathrm{p}\right), \tag{2.5}$$

since the legs are connected in series for the current but in parallel for heat transport. Considering the TEG as an effective device, also an effective Seebeck coefficient

$$S = S_\mathrm{p} - S_\mathrm{n} \tag{2.6}$$

can be assigned.

Defining the Efficiency of a Thermoelectric Generator

The efficiency η of a TEG for energy harvesting is defined as

$$\eta = \frac{P_\mathrm{load}}{\dot{Q}_\mathrm{lost}}, \tag{2.7}$$

where P_{load} is the electrical power consumed by the load and $\dot{Q}_{\text{lost}}$ is the heat flux taken from the hot bath (which in most cases is the "rare" source whereas the cold bath is abundant). With the resistance of the load R, P_{load} can be written as

$$P_{\text{load}} = R\frac{(\Delta T\ S)^2}{(r+R)^2}. \tag{2.8}$$

There are three different heat transport mechanisms: $\dot{Q}_{\text{Peltier}}$, $\dot{Q}_{\text{conduction}}$ and $\dot{Q}_{\text{Joule}}$, of which the first two are completely lost for the hot bath, whereas Joule heating also heats the hot bath, so that half of $\dot{Q}_{\text{Joule}}$ is fed back. Therefore

$$\eta = \frac{P_{\text{load}}}{\dot{Q}_{\text{Peltier}} + \dot{Q}_{\text{Conduction}} - \frac{1}{2}\dot{Q}_{\text{Joule}}} \tag{2.9}$$

$$= \frac{S^2\ \Delta T^2\ \frac{R}{(r+R)^2}}{S^2\ T_{\text{hot}}\ \Delta T\ \frac{1}{r+R} + \kappa\ \Delta T - \frac{1}{2}\ S^2\ \Delta T^2\ \frac{r}{(r+R)^2}}, \tag{2.10}$$

which can be rewritten as

$$\eta = \frac{\Delta T}{T_{\text{hot}}} \frac{\frac{R/r}{1+R/r}}{\frac{K\,r}{S^2}\frac{1+R/r}{T_{\text{hot}}} + 1 - \frac{\Delta T}{2\,T_{\text{hot}}}\frac{1}{1+R/r}}. \tag{2.11}$$

In this equation all external parameter, which essentially are the hot and cold side temperature, are marked in red. Although not based on mechanics, a thermogenerator's efficiency is still limited by the Carnot efficiency, which is the first term in Eq. 2.11. Interestingly, all material parameters accumulate in a single expression which is marked in green. This expression is called $\frac{1}{Z}$ and is the main subject of the following discussion.

Optimizing the Efficiency

The efficiency is optimized by matching the load resistance. The ratio of external load resistance to the resistance of the TEG is marked in blue in Eq. 2.11. As it is the case also for other energy sources the load must match the source in a certain way. For solar cells or batteries the internal resistance at the working point should be equal to the load resistance. This condition is slightly adapted for thermoelectric energy conversion, where η can only reach its maximum for

$$\left(\frac{R}{r}\right)_{\text{optimum}} = \sqrt{1 + Z\,\bar{T}}, \tag{2.12}$$

with Z being the material specific quantity alread defined in Eq. 1.1 and $\bar{T}$ being the mean operating temperature between the hot and the cold side temperature. With this

optimization the best efficiency of a TEG is

$$\eta_{\text{optimum}} = \eta_{\text{Carnot}} \frac{\sqrt{1 + Z\,\bar{T}} - 1}{\sqrt{1 + Z\,\bar{T}} + \frac{T_{\text{cold}}}{T_{\text{hot}}}}. \tag{2.13}$$

It is important to note here that Eq. 2.11 was not optimized with respect to maximum output power but to maximum efficiency. There may be applications where this is not the best optimization so that a different load resistance has to be chosen.

The Figure of Merit

As η rises monotonously with ZT, the holy grail of thermoelectrics is the characteristic combination of material parameter $\frac{S^2}{K\,r}$. Although deduced for a two-leg TEG, it can be shown that Z can be defined with similar meaning for each leg separately.[Iof57] Then, it can be written in terms of the material-specific quantities σ and κ

$$Z = \frac{S^2\,\sigma}{\kappa} \tag{2.14}$$

which enters the figure of merit as defined in Eq. 1.1. ZT is a dimensionless positive number and shall be maximized to maximize η. It is the long lasting quest of thermoelectric research to boost ZT. However, the quantities S, σ and κ are strongly interrelated so that a maximization of one easily leads to the reduction of another.

One of the most important parameters to influence the figure of merit is the charge carrier concentration. As an example, Fig. 2.3 shows the dependence of S, σ and κ on the carrier concentration n in single-crystalline bulk Si.[Sla91, Gla64, Sze81] As will also be treated in Sec. 2.3, the Seebeck coefficient decreases with increasing n, while the electrical conductivity strongly increases with n. This contradictory behavior is universal and it must be kept in mind for all further considerations that it is hardly possible to maximize S without decreasing σ or vice versa. The nominator in Eq. 1.1, $S^2\sigma$, is called the power factor, which is also plotted in Fig. 2.3.[2] At room temperature the power factor exhibits a maximum for a carrier concentration of approximately $5 \times 10^{19}\,\text{cm}^{-3}$. At these conditions, bulk single-crystalline Si has a thermal conductivity κ of $145\,\text{W/m\,K}$.[Gla64] This value is rather independent of n, unless the thermal conductivity added by the motion of charge carriers becomes significant above $n = 10^{20}\,\text{cm}^{-3}$, where, according to the Lorenz law, charge carriers contribute to thermal conductivity.[3] The resulting room temperature figure of merit for Si with a high crystal quality then also peaks at $n = 5 \times 10^{19}\,\text{cm}^{-3}$ but reaches only a rather low maximum value of $ZT = 3 \times 10^{-3}$.

---

2 As a very intuitive argument why S enters the power factor in the power of two is, that the power consumed by the load is proportional to I^2, with I in turn is proportional to the voltage U supplied by the TEG. The Seebeck coefficient linearly enters U, so that all power-related quantities are proportional to S^2.

3 Here it is neglected that heavy doping also reduces the lattice thermal conductivity.

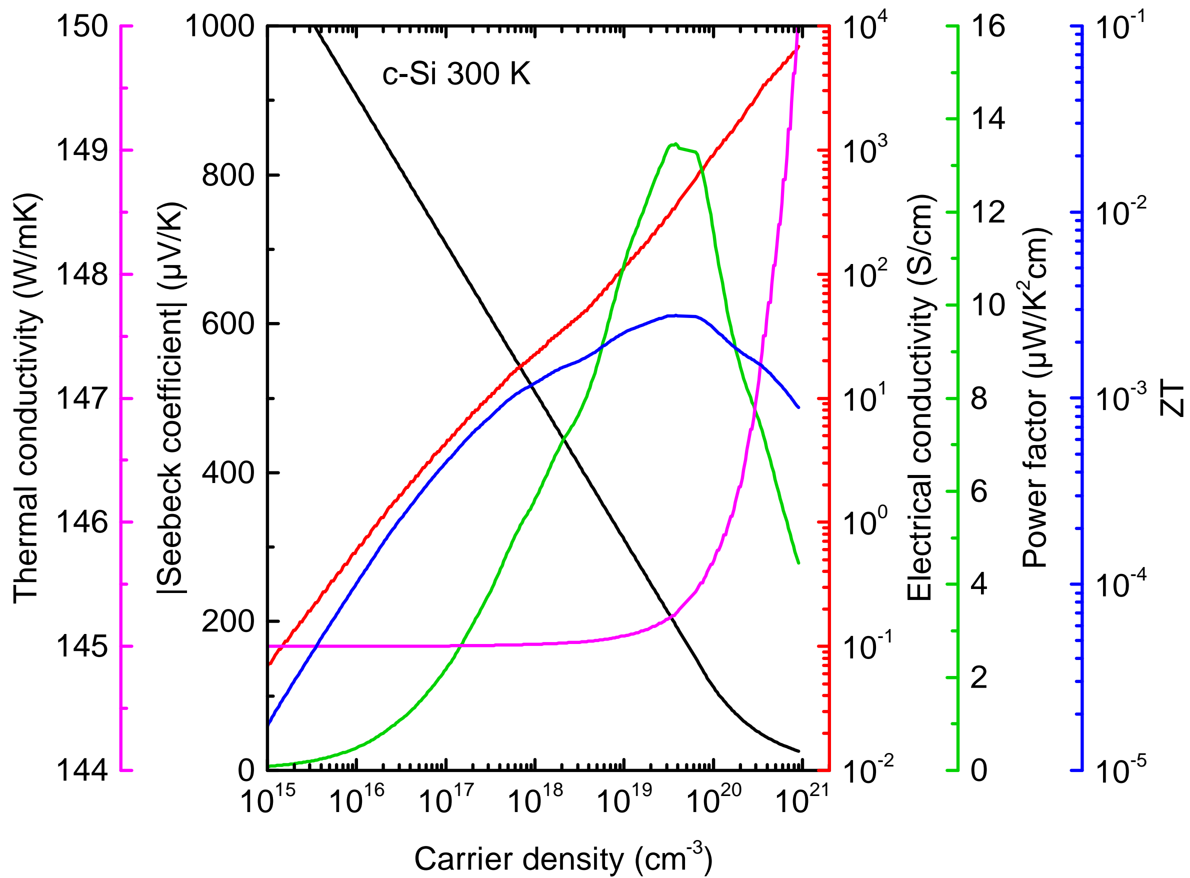

Figure 2.3. Thermoelectric figure of merit for single-crystalline n-type Si at room temperature: Realistic thermoelectric parameters are shown with respect to the carrier density. The Seebeck coefficient is taken from Ref. Sla91, the electrical conductivity is taken from Ref. Sze81 and the thermal conductivity is composed of a phonon contribution with 145 W/mK from Ref. Gla64 and an electronic contribution according to a Lorenz number of $2.44 \times 10^{-8}\,\mathrm{V^2/K^2}$ according to metal theory.

For a fixed doping concentration the second major parameter that determines ZT is the temperature. Figure 2.4 summarizes the figure of merit with respect to the temperature for some n- and p-type materials. This selection demonstrates several universal aspects.[4] First, all data sets of ZT for a given material rise with temperature, reach a maximum and decrease afterwards. As will become clear in the following discussions of thermoelectric transport, the reason for this observation is that usually the conductivity and the Seebeck coefficient rise with temperature until the material begins to become intrinsic, where both electrons and holes contribute, and the total Seebeck coefficient goes to zero. This becomes clear if one calculates the total Seebeck coefficient for two parallelly connected

4 A more complete selection of figures of merit including recently published data materials can, e. g., be found in Refs. Min09 and Zeb12.

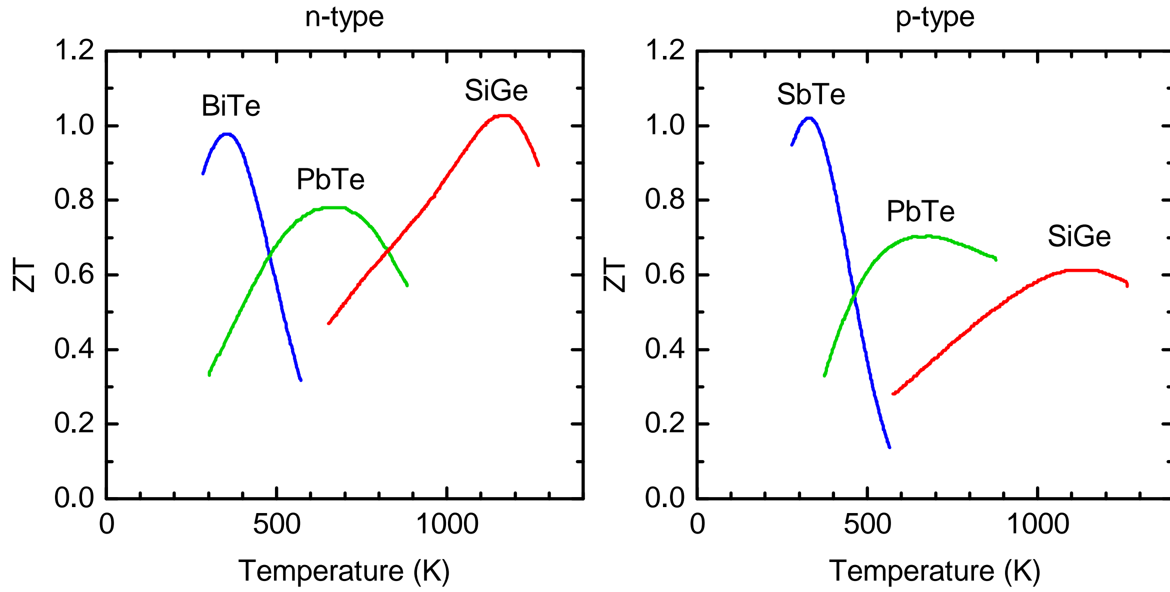

Figure 2.4. Figures of merit for different material classes: For n-type and p-type materials the figure of merit is shown versus the temperature. The data is taken from Ref. Sny08.

transport channels, here denoted by indices n and p,

$$S_{\text{total}} = \frac{S_{\text{n}}\, n\, \mu_{\text{n}} + S_{\text{p}}\, p\, \mu_{\text{p}}}{p\, \mu_{\text{p}} + n\, \mu_{\text{n}}}, \tag{2.15}$$

where n and p are the electron and hole densities and μ_{pn} and μ_{p} are the electron and hole mobilities, respectively. Second, the temperature of the maximum of the ZT curve is at higher temperatures when the bandgap of the material is higher.[Gol99] This fact is directly correlated to the first statement, because high bandgap materials need higher temperatures to become intrinsic. Third, in most material classes the p-type counterpart is less efficient than the n-type material, which can be explained by the often higher mass, and thus lower mobility, of holes compared to electrons.

The selected data in Fig. 2.4 are representative in the way that one can typically discriminate materials which are efficient at room temperature, at medium and at high temperatures. Low temperature materials often are based on Bi as main element, whereas medium temperature materials contain Pb. Also Te and Sb are commonly found in thermoelectric materials suitable for this temperature range. All the mentioned elements are rather heavy, which makes the materials poor thermal conductors, mainly due to the reduced group velocity in such heavy element materials.[Jai14] However, all these elements are either poisonous, rare or expensive. Only SiGe, the typical high temperature thermoelectric material, is based on rather abundant and non-poisonous elements.

The discussion of the efficiency of a TEG so far neglected that ZT depends on temperature, which is not justified as shown by Fig. 2.4. However, it is desirable to maximize

the temperature difference for maximum power output. As a consequence, a TEG made from a homogeneous material cannot be the optimum choice. To avoid this, good TEGs are graded and the doping density is adjusted to the local mean operating temperature. This motivates the search for a method that allows to flexibly tune the spatial distribution of the doping density. For thin films, such a method is presented in Chap. 7.

2.3. Theoretical Description of Thermoelectric Transport

The previous section derived an expression of the thermoelectric conversion efficiency, involving the figure of merit $ZT = \frac{S^2\,\sigma}{\kappa}T$. Now, a more basic discussion of thermoelectric parameters and thermoelectric transport shall be given. For the electric parameters semiclassical statistics will be employed, essentially following the books of Chen and Gross.[Che05, Gro12] The interested reader is directed to the books of Harman and Ioffe which treat these issues much more thoroughly.[Har67, Iof57] Thermal transport by phonons will also shortly be summarized using the analogy of gas theory according to arguments in the books of Gross and Weißmantel.[Gro12, Wei79]

2.3.1. General Transport Coefficients for Transport of Charge Carriers

The derivation of microscopic descriptions for S and σ starts by assuming a gas of charge carriers. Without loss of generality, the following derivation is valid for an n-type semiconductor and all energies are measured with respect to the valence band edge. Electrons are moving in an environment where electric fields, temperature and concentration gradients are small. The electrons obey Fermi-Dirac statistics with their undisturbed distribution function f_0

$$f_0 = \frac{1}{\exp\left(\frac{E-E_\mathrm{F}}{k_\mathrm{B}\,T}\right)+1}, \tag{2.16}$$

where E is the electron's energy, E_F is the Fermi level[5], and k_B is the Boltzmann constant. Within the relaxation time approximation the Boltzmann transport equation for electrons in an electric field $\vec{E}$ reads

$$\frac{\partial f}{\partial t} + \vec{v}\cdot\nabla f + q\vec{E}\cdot\frac{\partial f_0}{\partial \vec{p}} = \frac{f_0 - f}{\tau}, \tag{2.17}$$

where $\vec{v}$ is the velocity of an electron in the electron gas, q is the electron's charge, $\vec{E}$ is the electric field, $\vec{p}$ is the momentum of the electron and τ is the electron cloud's

5 There is a confusion in the literature about the meaning of E_F. Here, it is identified with the chemical potential, although the author is aware that the Fermi level is an energetic position rather than a potential in the sense of classical gas theory.

relaxation time. Applying the usual assumptions for a small disturbance and using $\frac{\partial f}{\partial \vec{p}} \approx \frac{\partial f_0}{\partial \vec{p}} = \frac{\partial f_0}{\partial E}\frac{dE}{e\vec{p}} = \vec{v}\frac{\partial f_0}{\partial E}$, Eq. 2.17 can be simplified to

$$\vec{v} \cdot \left[\nabla f_0 + q\vec{E}\frac{\partial f_0}{E}\right] = \frac{f_0 - f}{\tau}. \tag{2.18}$$

Now, the abbreviation

$$\zeta = \frac{E - E_{\mathrm{F}}}{k_{\mathrm{B}}T} \tag{2.19}$$

is introduced since, both, T and E_{F} can depend on spatial coordinates in a TEG, one obtains

$$\nabla\zeta = -\frac{1}{k_{\mathrm{B}}T}\nabla E_{\mathrm{F}} - \frac{E - E_{\mathrm{F}}}{k_{\mathrm{B}}T^2}\nabla T, \tag{2.20}$$

which consists of two terms: one with a gradient of the Fermi energy and one with a gradient of the temperature. As a result, the simplified Boltzmann transport equation now reads

$$\vec{v} \cdot \left[-\nabla E_{\mathrm{F}} - \frac{E - E_{\mathrm{F}}}{T}\nabla T + q\vec{E}\right]\frac{\partial f_0}{\partial E} = \frac{f_0 - f}{\tau}. \tag{2.21}$$

The electric field is related to the electrostatic potential φ_{e} by

$$\vec{E} = -\nabla\varphi_{\mathrm{e}}. \tag{2.22}$$

Thus, the electrochemical potential Φ is

$$\Phi = E_{\mathrm{F}} + q\varphi_{\mathrm{e}}. \tag{2.23}$$

With that one finally obtains

$$f = f_0 - \tau\,\vec{v} \cdot \left(-\nabla\Phi - \frac{E - E_{\mathrm{F}}}{T}\nabla T\right)\frac{\partial f_0}{\partial E}. \tag{2.24}$$

To derive expressions for transport coefficients the above term for f can be used. For example the electrical current density $\vec{j}_{\mathrm{e}}$, which is the integral of the product of charge density, charge carrier velocity, DOS and occupation probability f over all electron energies, can then be written as

$$\vec{j}_{\mathrm{e}} = \frac{1}{V}\int e\,\vec{v}(E)\,f(E)\,\mathrm{DOS}(E)\,\mathrm{d}E, \tag{2.25}$$

where V is the sample's volume. Using Eq. 2.24 it follows that

$$\vec{j}_{\mathrm{e}} = \frac{1}{3V}\int\frac{\partial f_0}{\partial E}\mathrm{DOS}(E)qv^2\tau\left(\nabla\Phi + \frac{E - E_{\mathrm{F}}}{T}\nabla T\right)\mathrm{d}E. \tag{2.26}$$

In a similar fashion, the energy flux density associated with the transport of electrons

can be derived to be

$$\vec{j}_\mathrm{E} = \frac{1}{3V} \int \frac{\partial f_0}{\partial E} \mathrm{DOS}(E) E v^2 \tau \left(\nabla\Phi + \frac{E - E_\mathrm{F}}{T} \nabla T \right) \mathrm{d}E. \tag{2.27}$$

The latter two equations can be written using the so-called general transport coefficients[6]

$$\vec{j}_\mathrm{e} = L_{11} \left(-\frac{1}{q} \nabla\Phi \right) + L_{12} \left(-\nabla T \right) \tag{2.28}$$

$$\vec{j}_\mathrm{E} = L_{21} \left(-\frac{1}{q} \nabla\Phi \right) + L_{22} \left(-\nabla T \right) , \tag{2.29}$$

with L_{ij} resulting from the above equations.

It is now interesting to relate these transport coefficients to physical phenomena. Having in mind the semiclassical expression

$$E = \frac{1}{2} m^* v^2, \tag{2.30}$$

with the effective mass of the charge carrier m^*, and knowing that electrical conduction is driven by a gradient of the electrochemical potential, the electrical conductivity σ is

$$\sigma = L_{11} = -\frac{2q^2}{3m^*} \int \frac{\partial f_0}{\partial E} \mathrm{DOS}(E) E \tau \, \mathrm{d}E. \tag{2.31}$$

For open circuit conditions, i. e., $\vec{j}_\mathrm{e} = 0$, the Seebeck coefficient is $S = \frac{L_{12}}{L_{11}}$. For vanishing temperature gradient and current flowing, the Peltier coefficient is $\Pi = \frac{L_{12}}{L_{11}} T$ and the thermal conductivity of electrons (not of the lattice, of course) is $\kappa_\mathrm{e} = L_{22} - \frac{L_{12} L_{21}}{L_{11}}$.

In the following, the expression for the Seebeck coefficient shall be discussed in further detail. Explicitly, S can be written as

$$S = -\frac{1}{qT} \frac{\int \frac{\partial f_0}{\partial E} \mathrm{DOS}(E) E (E - E_\mathrm{F}) \tau \, \mathrm{d}E}{\int \frac{\partial f_0}{\partial E} \mathrm{DOS}(E) E \tau \, \mathrm{d}E} \propto (E - E_\mathrm{F}). \tag{2.32}$$

This is one of the central equations in this work. The proportionality indicated hand-wavingly at the end (which strictly speaking is only true for each subensemble of charge carriers with the same energy) shows that the Seebeck coefficient measures the energetic distance of the energy where transport occurs to the Fermi level. An equivalent interpretation is that the Seebeck coefficient is the entropy carried by 1 A of current.[Hum05]

It is worth to notice that the Seebeck coefficient is a state function, such as it is the

6 Of course, also magnetic effects can be included in the most general form of transport coefficients.

conductivity in contrast to the conductance. Thus, the Seebeck coefficient does not depend on the sample geometry or the current path. This is reflected by the fact that the integrals in the above equation do not contain any sample dimension.

The main work to do when calculating the Seebeck coefficient for a certain material with known DOS is to evaluate the derivative of the distribution function. The results differ, depending on whether the material is considered a non-degenerate semiconductor, where the Fermi level lies deep in the band gap and the distribution function in the valence or conduction band can be approximated by an exponential tail, or whether the material is degenerate. In the latter case, the Fermi level is very close or even in the band, so that degenerate statistics need to be employed.

Assuming that the relaxation time can be written as

$$\tau \propto E^r, \tag{2.33}$$

with the scattering factor r, and after approximating the Fermi-Dirac integrals appropriately, the Seebeck coefficient for a non-degenerate semiconductor reads

$$S = \frac{1}{q\,T}\left(E_\mathrm{c} - E_\mathrm{F} + (r + \frac{5}{2})\,k_\mathrm{B}\,T\right), \tag{2.34}$$

or, using the charge carrier density n instead of the Fermi energy as a parameter,

$$S = \frac{k_\mathrm{B}}{q}\left(r + 2 + \ln\left(\frac{2(2\pi\,m^* k_\mathrm{B}\,T)^{3/2}}{h^3\,n}\right)\right). \tag{2.35}$$

Here, h is the Planck constant and m^* again is the effective mass of the charge carrier.

Using degenerate statistics for a metal or a heavily doped semiconductor, the Seebeck coefficient is commonly written as

$$S = \frac{\pi^2\,k_\mathrm{B}^2 T}{2qE_\mathrm{F}}, \tag{2.36}$$

or again, using the charge carrier density instead of the Fermi level [Sny08]

$$S = \frac{8\,\pi^2\,k_\mathrm{B}^2}{3\,q\,h^2} T\,m^*\,\left(\frac{\pi}{3\,n}\right)^{2/3}. \tag{2.37}$$

With knowledge of the effective mass, Eq. 2.37 allows to determine the charge carrier concentration if the Seebeck coefficient linearly rises with temperature. In many cases, the data sets cannot be extrapolated to the origin, so that it seems wise to use the slope $\frac{\partial S}{\partial T}$ instead of the absolute values. A possible reason for offsets in the Seebeck coefficient data sets are additional transport mechanisms which add a contribution to the metallic conduction.

To summarize, for heavily doped semiconductors the Seebeck coefficient behaves like

in a metal, with $S_{\text{metal}} \propto T$, whereas for a semiconductor with low doping $S_{\text{semic.}} \propto \frac{1}{T}$ is generally observed. However, also an implicit dependence of S on T due to the temperature dependence of E_{F} is contained in Eq. 2.34 and Eq. 2.36. The materials used for TEG are typically doped to a degree that falls in between these limiting cases, which often makes an evaluation simply along the lines of the above equations hard. In both cases, semiconductor-like and metal-like, the Seebeck coefficient decreases with increasing charge carrier concentration.

Finally, the importance of the DOS for the thermoelectric parameters shall shortly be mentioned. For the metallic case the Seebeck coefficient can also be written in a different form, which is known as the Mott formula and which reads, e. g. according to Ref. Fri71,

$$S = \frac{\pi^2\, k_{\text{B}}^2\, T}{3\, q} \left(\frac{\mathrm{d}\ln(\mu\ \text{DOS})}{\mathrm{d}E} \right) |_{E=E_{\text{F}}}, \tag{2.38}$$

where μ is the charge carrier mobility. Since the Seebeck coefficient in Eq. 2.38 rises with increasing modulation of the DOS with respect to energy, physics on the nanoscale can enhance the Seebeck coefficient when bunching the DOS from 3 dimensions to 2, 1 or even 0 dimensions.[Dre07, Min09b, Her08] A bunching of the states necessarily increases the energy dependence of the DOS and thus, according to Eq. 2.38, the Seebeck coefficient. This can be done by stacking layers in quantum well structures (2 dimensions), growing nanowires (1 dimension) or embedding nanoparticles into bulk material (0 dimensions).

2.3.2. Thermal Transport by Phonons

The thermal conductivity $\underline{\kappa}$ is a key parameter in materials research and device optimization. It relates the heat flux density $\vec{q}$ to the temperature gradient $\vec{\nabla} T$ by

$$\vec{q} = -\underline{\kappa}\ \vec{\nabla} T, \tag{2.39}$$

and is usually expressed in units of W/m K. In general, $\underline{\kappa}$ is a tensor quantity, reflecting the anisotropy of a material. In the following, conduction of heat parallel to the temperature gradient is assumed. If a distinction is drawn for conduction in specific directions, e. g., in- or cross-plane conduction in a thin film, this will be pointed out in such a case, so that only the scalar thermal conductivity κ is used from now on.

In many materials the majority of heat is conducted by phonons. For each spectral phonon mode of wavelength λ_{m} the conditions in a sample, such as its physical dimensions, its isotopic purity, its nano- and microstructure, and the sample temperature, limit the specific mean free path Λ_{m} of this mode. Λ_{m} can be understood as the mean distance between scattering events of the quasiparticle. The fraction this mode contributes to the total phonon thermal conductivity can be written as

$$\kappa_{\text{ph,m}} = \frac{1}{3}\, C_{\text{v}}\ \Lambda_{\text{m}}\ v_{\text{g}}, \tag{2.40}$$

where C_v is the specific heat for constant volume of the material and v_g is this phonon mode's group velocity.[Gro12]

The total thermal conductivity is the sum of all modes' contributions. As phonons obey Bose statistics the number of modes is not constant but increases with temperature. Thus, phonon-phonon scattering becomes increasingly important at higher temperatures which is the reason for the $1/T$ dependence of the thermal conductivity observed in the limit of high temperatures. At low temperatures, however, the thermal conductivity is limited by scattering events at defects as well as by the decreasing number of active modes. Usually, in the limit of very low temperatures, the temperature dependence of $C_v \propto T^3$ is also observed for κ then.

Apart from phonons, heat can also be carried by, e. g., charge carriers, magnons or spin waves.[Hoh14, An13] The total thermal conductivity κ is then the sum of all those contributions. For thermoelectric materials, with their usually high electrical conductivity σ, the electronic part of the thermal conductivity κ_{el} contributes according to the Wiedemann-Franz law

$$\kappa_{el} = \sigma \, L \, T, \tag{2.41}$$

where L is the Lorenz number. However, apart from metals and perfectly optimized thermoelectric materials, the phonon contribution to κ dominates. In the rest of this thesis, the minor contributions are neglected and the manipulation of κ is discussed in the sense that mostly phonons are affected.

2.4. Thermoelectric Parameters in Group-IV Materials

After the theoretical derivation of thermoelectric transport parameters in the previous section, thermoelectric data in Si-based materials shall be reviewed. This serves as a basis for the discussion of the results obtained on the materials developed in this work.

2.4.1. Conductivity and Mobility in Poly-Crystalline Materials

The literature data on the electrical conductivity of semiconducor materials is vast, so that this section will not discuss the general characteristics, such as intrinsic conduction or dopant freeze out. Also, this work takes the behavior of the Fermi level as a function of the temperature as given.[Gro12] As a special case which is relevant for the materials discussed in this thesis, the impact of grain boundaries on the electrical transport according to the model of Seto shall shortly be discussed.[Set75, Upr91]

In a poly-crystalline material one finds unsaturated bonds at the grain boundaries, so-called dangling bonds, which give rise to a density of states of trap states in the bandgap. Freely mobile charges get trapped there and pin the Fermi level at the energy of the trap states as long as there are still singly occupied orbitals of dangling bonds available. On the one hand this reduces the density of mobile charges because part of the charge carriers are trapped. On the other hand this reduces the mobility for the

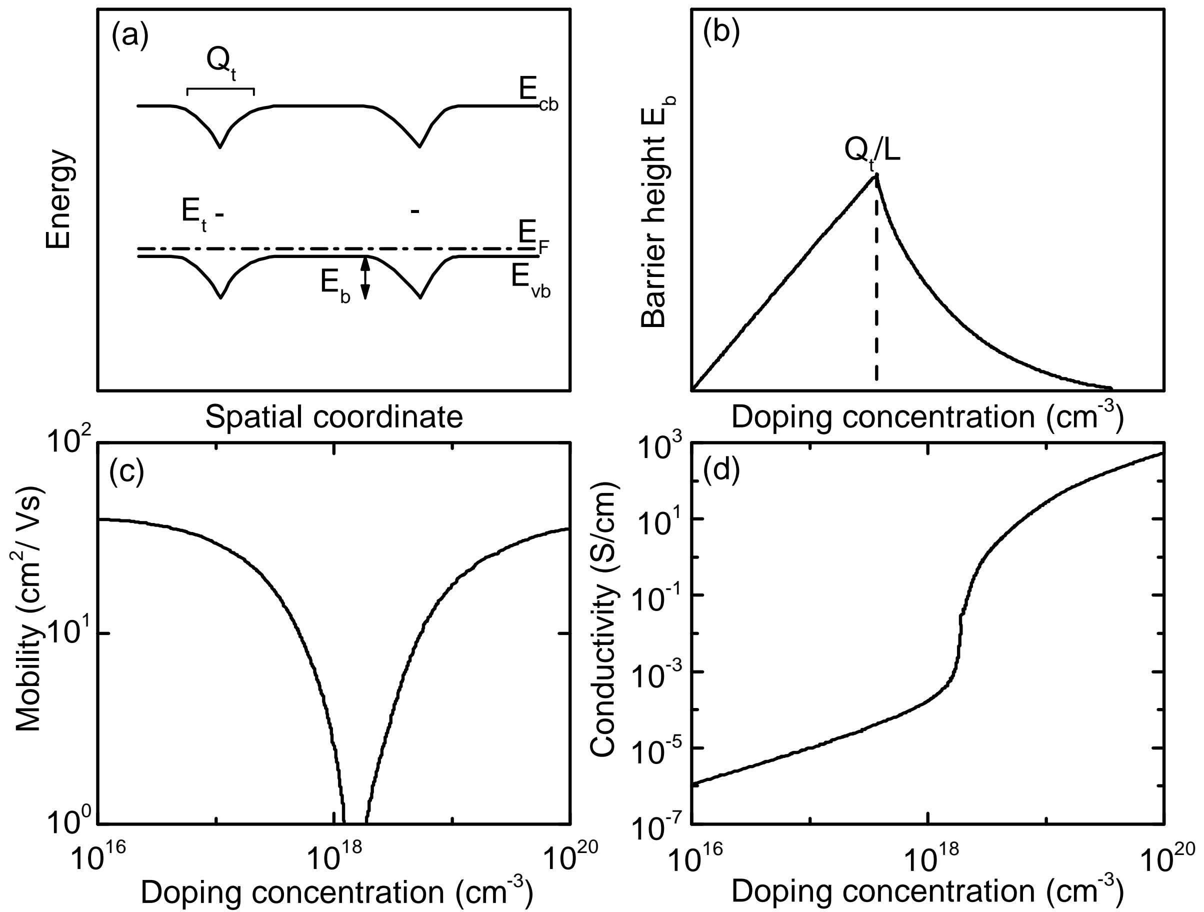

Figure 2.5. Transport of charge carriers across grain boundaries following the Seto model: (a) The energy landscape in poly-crystalline silicon is characterized by trap states, which pin the Fermi level at the grain boundary, resulting in barriers for holes. (b) The height of the energy barrier depends on the doping concentration. (c) The mobility for macroscopic transport through the poly-crystalline material is especially low when the doping concentration is equal to the trap state density. (d) The electrical conductivity rises several orders of magnitude when the doping concentration is higher than the trap state density.[Set75]

remaining charge carriers due to band bending. Figure 2.5 (a) schematically illustrates the energy landscape of a p-type poly-crystalline semiconductor. Holes encounter energy barriers in their transport path across the grain boundary. The barrier height E_B, shown in panel (b), is a function of the doping concentration with two regimes. For doping below the density of trap states the barrier height rises with doping while for doping above the trap state density the barrier height decreases due to increased screening effects. As a consequence of the barrier height being maximal when doping is equal to the trap state density, the mobility undergoes a minimum there, as shown in panel (c). The macroscopic electrical conductivity (not that within a grain), shown in panel (d), increases sharply for doping above the trap state density because all traps are filled and each additional dopant contributes with one mobile charge.

It is often observed that a situation discussed in the context of Fig. 2.5 leads to a convex behavior of the temperature-dependent conductivity in an Arrhenius plot. The reason is that transport is thermally activated with respect to the charge carrier concentration and also with respect to the mobility. Especially the mobility across the barrier is dependent on the temperature, because high energy charge carriers are easily emitted across the grain boundary. The percentage of carriers with enough energy increases strongly with temperature.[Yan80] The convex behavior of σ versus $1/T$ is even more pronounced for a distribution of barrier heights, as it will be the case in most realistic materials.

2.4.2. The Seebeck Coefficient in Group-IV Materials

From Eq. 2.35 and 2.37 it is obvious that the Seebeck coefficient decreases with the charge carrier concentration. This relation, known as the Pisarenko relation, is shown for Si in Fig. 2.6 (a) at room temperature with experimental data from Ref. Sla91. The two models for a semiconductor and a metal are shown as solid lines. At room temperature the two regimes cross at a carrier concentration of approximately $10^{20}\,\mathrm{cm}^{-3}$. This characteristic relation has also been reported for numerous other systems. As examples, data for thin film p-type Ge from Ref. Hui67 are shown in panel (b), for p- and n-type SiGe from Ref. Yam00 in panel (c) and for n-type GaAs from Ref. Pic11 in panel (d).

The data in Fig. 2.6 are valid for room temperature. More physical information is contained in the data of temperature-dependent Seebeck coefficients, because this allows to assign a semiconductor- or a metal-like model. Figure 2.7 shows a collection of some data from the literature on the temperature dependence of S for Si and Ge materials. In panel (a) B-doped Si has a positive Seebeck coefficient for low and moderate temperatures. The sample doped with $10^{15}\,\mathrm{cm}^{-3}$ shows an approximate $1/T$ behavior for temperatures up to 500 K and, thus, behaves according to the prediction of Eq. 2.34. Similarly, the n-type sample with a P concentration of $4 \times 10^{14}\,\mathrm{cm}^{-3}$ behaves like $-1/T$ up to a temperature of 450 K. Increasing the temperature above 500 K, the Seebeck coefficient of both samples changes to one characteristic for intrinsic Si. For those temperatures, the thermally activated charge carriers outnumber the ones caused by doping. The Seebeck coefficient of intrinsic Si is negative, because according to Eq. 2.15 the more mobile species, in this case electrons, dominate. Also for intrinsic Si, the Seebeck coefficient decreases in magnitude with temperature, following approximately a $-1/T$ law. Compared to the low B-doping, increased B-doping leads to a smaller positive Seebeck coefficient. Interestingly, for low temperatures these curves increase with temperature. Especially the sample doped with $1.5 \times 10^{19}\,\mathrm{cm}^{-3}$ shows a pronounced metallic behavior proportional to T according to Eq. 2.37. This is the only data set that still rises with temperature around room temperature, consistent with the transition between semiconductor- and metal-like model in Fig. 2.6. The green dashed line in Fig. 2.6 (a) is the expected behavior for the sample doped highest with B. The increased doping density leads to a transition to intrinsic behavior at higher temperatures compared to low-doped samples.

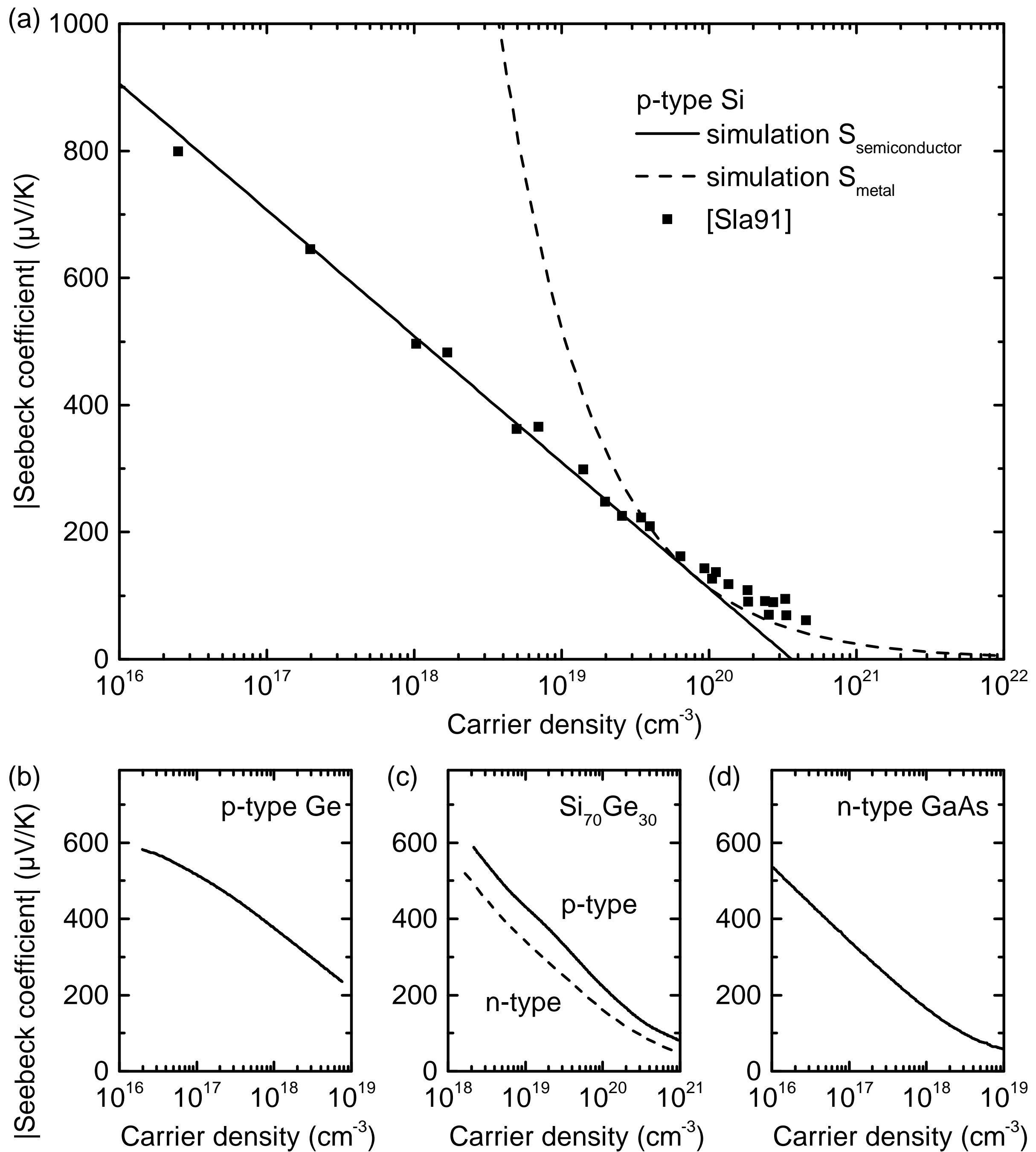

Figure 2.6. The Pisarenko relation for Si, Ge, SiGe and GaAs: The room temperature Seebeck coefficient is plotted versus the charge carrier concentration for (a) p-type Si from Ref. Sla91. The model for a semiconductor follows Eq. 2.35, the one for a metal Eq. 2.37. The lower panels show similar experimental results obtained on (b) p-type Ge from Ref. Hui67, (c) n- and p-type SiGe from Ref. Yam00 and (d) n-type GaAs from Ref. Pic11.

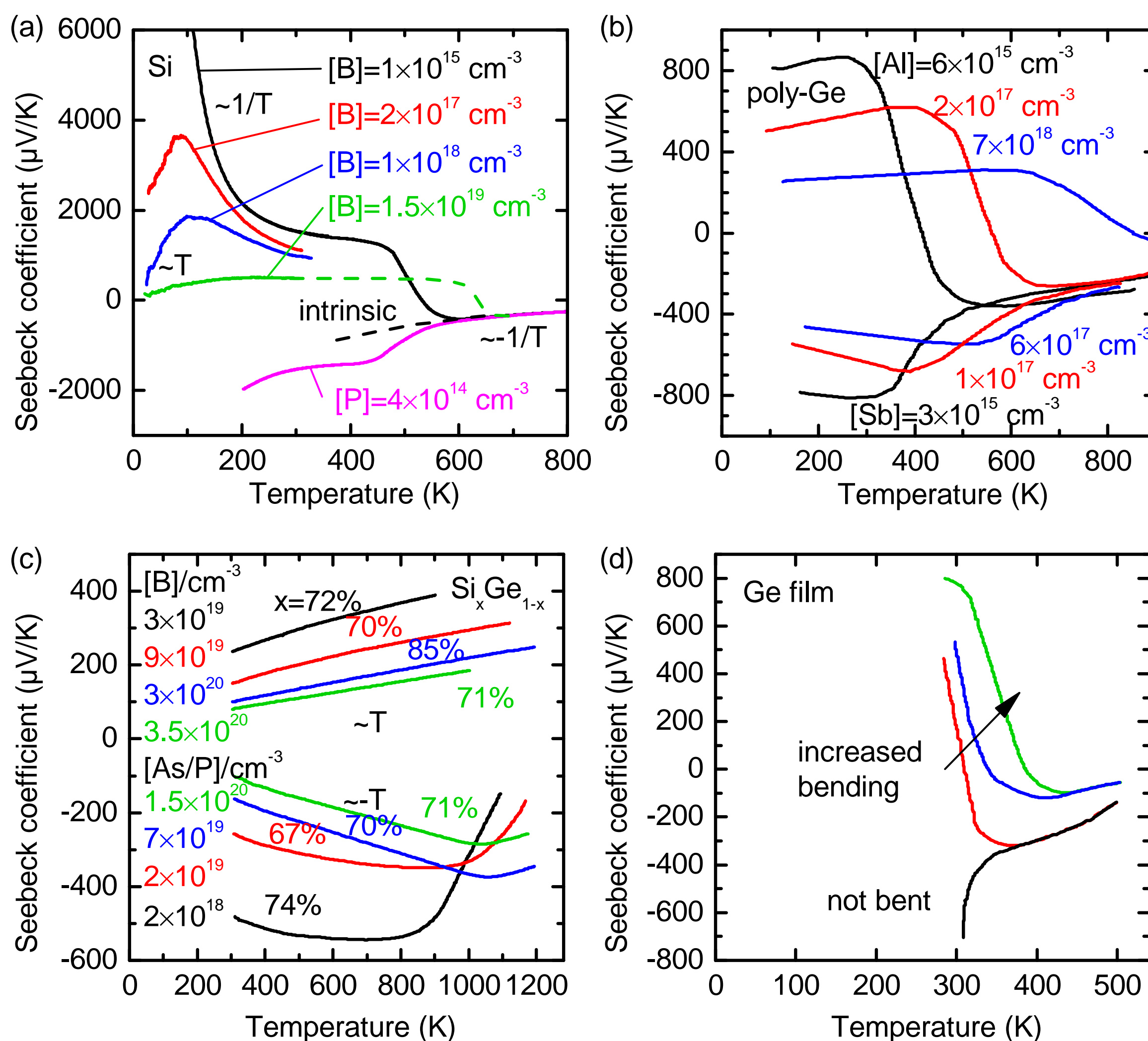

Figure 2.7. Temperature-dependent Seebeck coefficients for group-IV materials: The panels show the Seebeck coefficients for (a) B- and P-doped Si from Ref. Geb55, (b) Al- and Sb-doped Ge from Ref. Mid53, (c) p- and n-type SiGe of various Si contents from Ref. Dis64 and (d) plastically bent Ge thin films from Ref. Yam61. The dashed lines in panel (a) are schematically extrapolated.

This prediction is confirmed by the data in panel (b) where Al- and Sb- doped polycrystalline Ge samples are investigated. As expected, for low temperatures Al-doped samples have a positive and Sb-doped samples have a negative Seebeck coefficient. For all samples the Seebeck coefficient rises with temperature first, and then approaches that for intrinsic Ge. The higher the samples are doped, the higher the temperature needed for intrinsic conduction. Again, electrons are more mobile in crystalline Ge than holes, so that the intrinsic Seebeck coefficient is negative.

In Fig. 2.7 (c) the Seebeck coefficients of SiGe alloy materials doped heavily with B and As or P are shown. Compared to panel (a), the Seebeck coefficient is generally much lower, as expected from the high doping level. The rising Seebeck coefficient

with increasing temperature indicates a fully metallic behavior up to even highest temperatures. As already discussed in the last two panels, also here the sample doped lowest with donors is the first to leave its characteristic metallic behavior followed by the Seebeck coefficient tending to that of intrinsic material. The exact alloy composition indicated by the percentages in panel (c) seems to be of minor relevance for the Seebeck coefficient compared to the influence of the different doping levels.

As a last example which is relevant for the discussion of the samples prepared in this work, the Seebeck coefficient of thin films of crystalline Ge is shown in panel (d). Consistent with the data in panel (b), the Seebeck coefficient for the undoped sample marked with "not bent" is negative. A series of thin film samples underwent plastic bending, which increases the density of crystal defects such as twins or dislocations. Interestingly, the heavier the bending, the more pronounced the samples become p-type conducting. The most likely reason is that these lattice imperfections give rise to a density of states near the valence band of Ge, pinning the Fermi level there at low temperatures. Later, in Chap. 6, this behavior will be discussed in detail.

2.4.3. The Thermal Conductivity of Si-Based Materials

The Range of Thermal Conductivities in Solids

Similar to its electrical counterpart σ, the magnitude of the thermal conductivity κ spans a range of many orders of magnitude. The highest thermal conductivity of bulk materials is reported in single-crystalline diamond with more than 10 000 W/m K at $T = 100$ K.[Ber75] With 30 000 W/m K, isotopically purified diamond even outperforms its natural counterpart.[Ols93] At room temperature, isotopically enriched graphene has been measured to exhibit a thermal conductivity of > 4000 W/m K, which is even higher than the value obtained in bulk diamond for that temperature.[Che12] On the other side of the range of thermal conductivities, electrically insulating and highly disordered materials are found. Assuming that Λ must at least be comparable to λ, according to Eq. 2.40 a minimum of the thermal conductivity can be expected for dense materials. Many glasses, e. g., behave according to this assumption.[Cah92, Tri04] Of course, in the case of a solid with voids, the apparent thermal conductivity, i. e., normalized by the outer physical dimensions of a sample and not by the atomic density, exhibits practically no lower limit for extremely high porosities or vanishing material density.[Hop12] An example for such a material class with superb thermal isolation properties are silica aerogels, with values of the thermal conductivity down to 10^{-6} W/m K at $T = 0.1$ K.[Sch91]

Approaches to Lowering the Thermal Conductivity

Whereas enhancing the thermal conductivity of a material is virtually only possible by very expensive approaches, such as reducing crystallographic defects, chemically purifying the material and enriching certain isotopes, lowering the thermal conductivity

is a comparatively easy task, namely by a reduction of Λ. In the case of thermoelectric materials, however, care has to be taken not to degrade the electronic properties similarly. The fact, that the mean free path of charge carriers usually is already much smaller than that of phonons, makes micro- and nanostructuring a reasonable method for optimizing thermoelectric materials.[Web91, Qiu15] Figure 2.8 summarizes several aspects on the manipulation of κ in Si systems, based on reports from the literature.

The influence of isotopic purity: Figure 2.8 (a) shows the temperature dependence of κ for bulk single-crystalline Si with natural isotope composition as the curve labeled number 1.[Iny04] As already shortly described in Sec. 2.3.2, for low temperatures κ rises due to the increasing number of phonons with temperature. Phonon-phonon scattering processes decrease κ for high temperatures, which theoretically follows a power-law dependence with an exponent of -1. The overlap with other scattering processes around the maximum of the curve usually leads to an even steeper decrease of κ with T. Curve 2 shows experimental data on κ for isotope enriched ^{28}Si,[Iny04] which outperforms natural Si by an order of magnitude around the maximum of the curve. At higher temperatures, however, enriched Si shows approximately the same behavior as natural Si, because phonon-phonon scattering events are similarly likely in both materials.

The influence of boundary scattering: Curve 3 in Fig. 2.8 (a) shows the data of an undoped single-crystalline thin film of 1.6 μm thickness.[Ash97] Especially at low temperatures, where phonon-phonon scattering not yet dominates but boundary scattering at the sample surface is important, κ is reduced compared to bulk Si, approaching its value at around room temperature. An undoped single-crystalline thin film of 420 nm thickness (curve 4) shows a further reduced κ.[Ash97] In this case, also at room temperature a significant reduction is observed. For an undoped single-crystalline thin film of only 20 nm thickness (curve 5) κ is reduced further by an order of magnitude.[Liu04]

The influence of poly-crystallinity and doping: Curve 6 and 7 in Fig. 2.8 (a) denote the data of poly-crystalline thin films with grain sizes of 400 nm and 1.06 μm film thickness, B-doped with $2 \times 10^{18}\,\mathrm{cm}^{-3}$ and $1.6 \times 10^{19}\,\mathrm{cm}^{-3}$, respectively.[McC01] Compared to the curves discussed so far, the poly-crystallinity and the doping density reduce κ significantly. But even an undoped poly-crystalline thin film with a grain size of only 190 nm and 1 μm film thickness in curve 8 shows a thermal conductivity of half an order of magnitude lower, so that in this regime doping seems to be less important compared to the poly-crystallinity.[Uma01] Once the crystallite size is much smaller than the film thickness, the effect of thinning the sample becomes less important.

The influence of nano-crystallinity: Curve 9 in Fig. 2.8 (a) shows data of bulk-nanocrystalline Si with grain sizes of 550 nm, which shows a thermal conductivity comparable to a thin film with approximately the thickness of the grain size of the latter

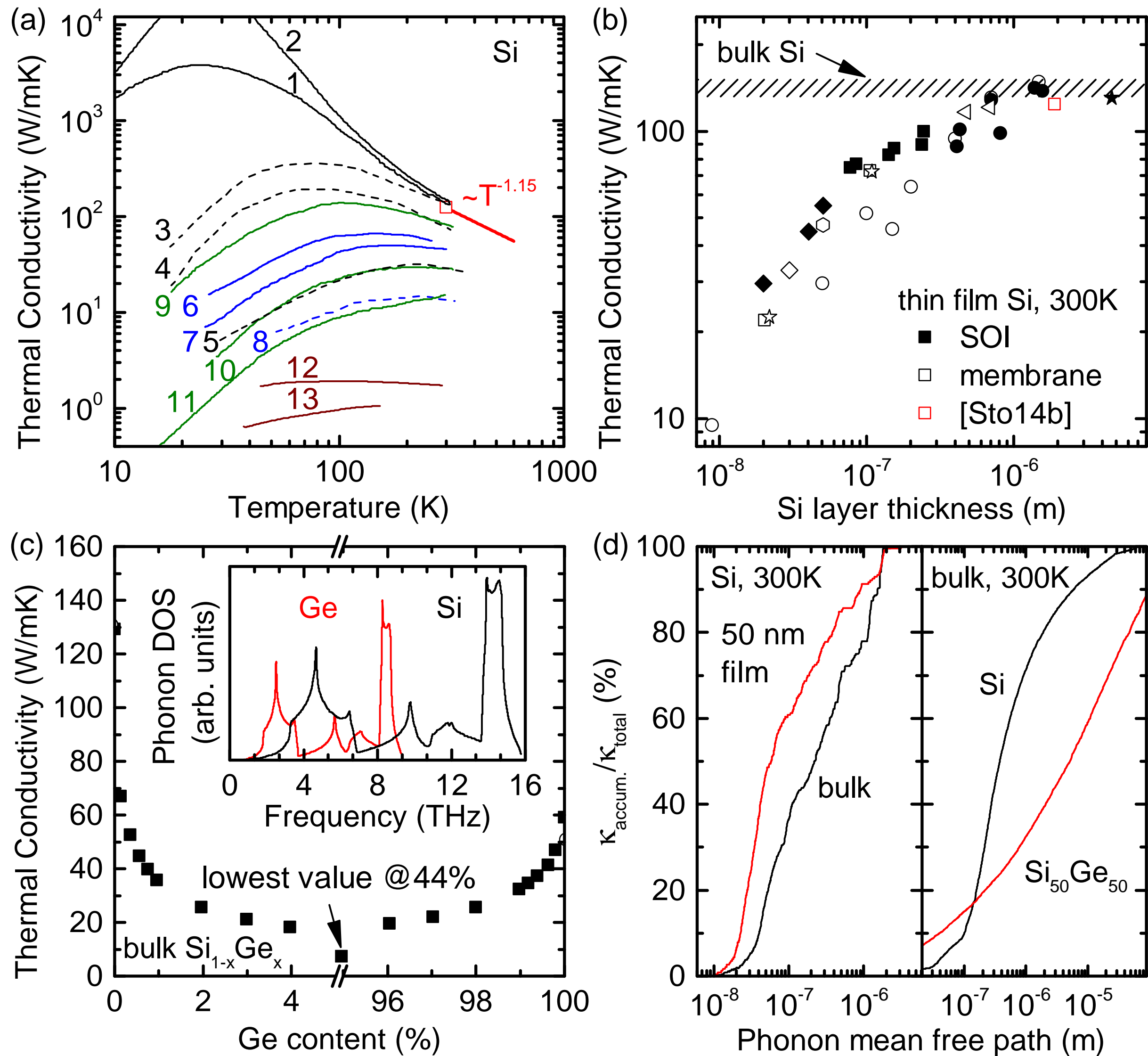

Figure 2.8. Manipulation of the thermal conductivity κ in Si systems: In panel (a) influences on the temperature dependence of κ in Si materials are shown.[Iny04, Ash97, Liu04, Wan11, Cla13, McC01, Uma01, Cah89] The open red symbol and the attached red line are discussed later in the context of Fig. 8.5. Panel (b) shows room temperature values of κ for silicon-on-insulator (SOI, closed symbols) and free standing membranes (open symbols) as a function of the film thickness. The data are taken from different references as indicated by the different symbols.[Ash98, Ju99, Liu04, Son04, Ju05, Liu05, Liu06b, Liu06a, Liu11, Chá14, Sto14b] In panel (c) the bulk thermal conductivity of $Si_{1-x}Ge_x$ is shown versus the alloy composition.[Gar11] The inset shows the phonon DOS of Si and Ge.[Web77] Theoretical calculations of the accumulated thermal conductivity $\kappa_{accum.}$ at room temperature, i. e. the thermal conductivity contribution of all phonons with mean free paths smaller than the value on the abscissa, are shown in panel (d). The left part shows normalized calculations for a thin film and bulk Si,[Jai13] the right part shows calculations for bulk Si and $Si_{50}Ge_{50}$.[Ber10] Details of all panels are discussed in the text.

sample.[Wan11] Further reducing the grain size to 76 nm in curve 10 shows the expected influence on κ.[Wan11] Bulk-nano-crystalline Si with with grain sizes of 30 nm in curve 11 shows the lowest thermal conductivity discussed so far.[Cla13]

The influence of amorphous disorder: Disorder on an even smaller scale is present in amorphous material. Hydrogenated amorphous Si with a hydrogen content of 20% is shown in curve 12 in Fig. 2.8 (a), and purely amorphous Si in curve 13, having a supremely low thermal conductivity.

Notably, the temperature dependence of systems with low dimensionality or a high degree of disorder is much less pronounced compared to single-crystalline material. This fact will become important when discussing the results obtained on laser-sintered thin films in Sec. 8.2.3.

The influence of the film thickness at room temperature: In Fig. 2.8 (b) the room temperature in-plane thermal conductivity of single-crystalline Si thin films is plotted versus the thickness of the membrane. Closed symbols denote silicon-on-insulator samples, whereas the open symbols are data for freely suspended membranes.[Ash98, Ju99, Liu04, Son04, Ju05, Liu05, Liu06b, Liu06a, Liu11, Chá14, Sto14b] The dashed region marks the range of literature values found for bulk single-crystalline Si at room temperature.[Gla64, May67] For films thicker than 2 µm virtually no difference is found compared to bulk Si. For decreasing film thickness below 2 µm κ starts to deviate from the bulk value. Values up to one order of magnitude lower than that of bulk Si are found for films of a thickness of the order of 10 nm. A reduction of the density of phonon modes that can be excited in physically restricted system, as well as the enhanced phonon scattering at the surface of the sample, lead to a decrease of κ not only in membranes but also in other small-scale systems, such as nanowires.[Li03, Doe10, Tan11, Mal12] In addition, if reflection at these surfaces is not specular due to an enhanced roughness of the surface, the thermal conductivity reduction is even more pronounced.[Hoc08, Lim12]

The influence of local density variation: The reduction discussed so far arises from shrinking a system and eliminating thermal transport by long wavelength phonons. Increased phonon scattering for short wavelength phonons is exemplarily shown in Fig. 2.8 (c), where Ge atoms are isovalently exchanged at random places in the Si lattice.[Gar11] The higher mass of Ge compared to Si leads to a defect in the vibrational chain and phonons adapted to the Si lattice are scattered by the alloy. The thermal conductivity decreases strongly even for smallest admixtures of Ge. Already for 1% Ge κ is reduced by a factor of 4. The lowest value of κ in the $Si_{1-x}Ge_x$ alloy system is found for roughly equal parts of Si and Ge, with a reduction by a factor of roughly 25. A related concept is the so-called phonon mismatch, where phases of, e. g., pure Si alternate with phases of pure Ge. The inset in panel (c) shows the phonon DOS of Si and Ge versus the phonon frequency.[Web77] Both DOS have little overlap, so that phonons coming from the one material find a low DOS behind the grain boundary, leading to enhanced

phonon reflection. A similar situation occurs for grain boundaries within material of the same composition, but with different crystal orientation of the grains. The symmetry of the Si lattice leads to an orientation-dependent DOS and an additional thermal resistance is found at the grain boundary, known as the Kapitza resistance.[Mai97, Phi05]

The cumulative thermal conductivity: The effect of selectively excluding a certain part of the phonon spectrum from heat transport is shown in calculations in Fig. 2.8 (d), where the normalized cumulative thermal conductivity, i. e., the fraction of thermal conductivity carried by phonons with a mean free path smaller than the value at the abscissa, is plotted versus Λ. A similar plot has already been discussed in Fig. 1.2. Both black solid lines represent Si, taken from different publications.[Jai13, Ber10] On the left half of the panel pure bulk Si is compared to a 50 nm thick membrane of pure Si. As already discussed, this eliminates phonons with mean free paths much larger than the film thickness. Thus, the curve of the normalized cumulative thermal conductivity shifts to lower mean free paths. Contrary, if pure Si is compared to $Si_{1-x}Ge_x$ where phonons of short mean free paths carry less heat, the curve shifts to higher mean free paths. Experimental knowledge of such kind of graphs is extremely helpful in optimizing κ. To further reduce κ in a material, additional scattering mechanisms need to be introduced. Thereby, the characteristic feature size of this scattering mechanism needs to match the abscissa value where the curve in Fig. 2.8 (d) rises fastest. Panel (d) also motivates that the introduction of a microscale porosity in laser-sintered thin films is much more useful in $Si_{1-x}Ge_x$ thin films than in pure Si or Ge films, because in the alloy system, long mean free path phonon contribute relatively more than in the pure materials.

3
Selected Experimental Techniques

For the sake of readability of the sections on the experimental results, the most relevant experimental techniques are introduced separately here in this chapter. Among these techniques are Fourier Transform Infrared Spectroscopy (FTIR), the determination of the electrical conductivity and the Seebeck coefficient/thermovoltage, as well as Raman spectroscopy. Wherever measurements include special details, such as for example the Fano effect in Raman spectroscopy, these are covered in the respective results section. Also, important measurement parameter are mentioned directly before discussing the measurements.

Apart from the major techniques, this work also presents results obtained by methods which are used less frequently in this work, such as Photothermal Deflection Spectroscopy (PDS), Laser-Ablation Inductively-Coupled Plasma Mass Spectrometry (LAICP-MS) or X-ray Photo-electron Spectroscopy (XPS). A very short introduction of these techniques' principles is given in the context of discussing the results obtained.

3.1. Fourier Transform Infrared Spectroscopy

FTIR investigates the absorption of infrared light due to interaction with a molecular dipole, which results from different electronegativities of the elements constituting the sample. One advantage of FTIR is that a whole spectrum can be measured at one time, using a broad-band thermal radiation source and by making use of Fourier transformation of a modulated interferometer signal. For that, the infrared beam is separated by a beam splitter. In conventional FTIR spectrometers one part of the beam is reflected by a fixed mirror, the second one by a movable mirror. By use of a reference laser (e. g. a HeNe laser) the position of the movable mirror can be monitored exactly.

The two beams are then superimposed again and are directed onto the sample before reaching the detector. Fourier transformation of the signal intensity as a function of the mirror position yields a spectrum as a function wavenumber. By comparison to a spectrum recorded without sample, the absorbance of the sample can be obtained. A more detailed introduction to FTIR can for example be found in Refs. Gün02, Hoe10.

In this work a Bruker Vertex 70v spectrometer with a SiC globar is used in combination with an L-alanine-doped triglycine sulfate (DLTGS) detector. For this spectrometer a slightly different optical system is used which is less prone to vibrational disturbances. Since the NP surface termination is most relevant directly before laser-sintering the thin NP films, the most widely used measurement geometry in this work is a thin film of as-deposited NPs, spin-coated onto a gold-coated substrate. As a reference sample, a gold-coated substrate by itself is used. The infrared radiation penetrates the film under a 45° angle, is reflected by the gold mirror and penetrates the NP film for a second time, before leaving the film and entering the detector. This geometry is often called *transflection*, which is a portmanteau, describing the fact that the radiation is reflected by the mirror, but still the thin film is measured as if in two-fold transmission.

3.2. Measurement of the Electrical Conductivity

The room temperature electrical conductivity of thin film samples in this work is obtained by recording a current-voltage characteristics at ambient conditions and calculating the conductivity according to

$$\sigma = \frac{I}{U} \frac{l}{w\,d}, \tag{3.1}$$

where $\frac{I}{U}$ is the slope of the current-voltage characteristics and w and l are the width and the length of the sample, respectively. The height of the film is denoted by d. Although not stated explicitly, σ is a macroscopically defined quantity, i. e. not accounting for height corrugations and porosity effects.

For temperature-dependent measurements the sample is placed within an evacuated dark chamber onto a heated steel element. The temperature is monitored by a type K thermocouple glued either onto the sample itself or directly next to it using silver paste. A Eurotherm 3500 temperature controller ramps the temperature while the current through the sample is recorded by a Keithley 2400 for a constant bias voltage of for example 1 V. If major differences of heating and cooling curves are noticed, the cooling curve is used for calculation of the electrical conductivity.

3.3. Measurement of the Seebeck Coefficient

Temperature-Dependent Seebeck Coefficient Setup

The Seebeck coefficient is measured for temperatures ranging from approximately 350 K to 670 K in an in house-built steel setup, which is inserted into a vacuum chamber. The setup which is schematically shown in Fig. 3.1, consists of two posts, which can be heated separately by two heating cartridges, each of them controlled by a Eurotherm 3500 temperature controller. On both posts a steel platform is attached, so that a gap of approximately 5 mm between the platforms remains. As a solid carrier placed onto the platforms across the gap a 0.5 mm thick piece of sapphire is used, which is a passable trade-off with respect to a good thermal conductance from the steel platforms through the carrier to the sample and a small thermal conductance across the gap. Furthermore, sapphire is an electrical insulator and offers high mechanical stability. Onto this carrier the thin film samples are placed and attached by silver paste. The electrical contacts of the samples are sputtered or evaporated metal contacts, which typically have a distance of 7 mm, so that the electrical measurement of the thermovoltage picked between these contacts is placed completely above the platforms, where also the temperatures are measured by type K thermocouples.

For the determination of a Seebeck coefficient at a mean temperature of, e. g., 400 K,

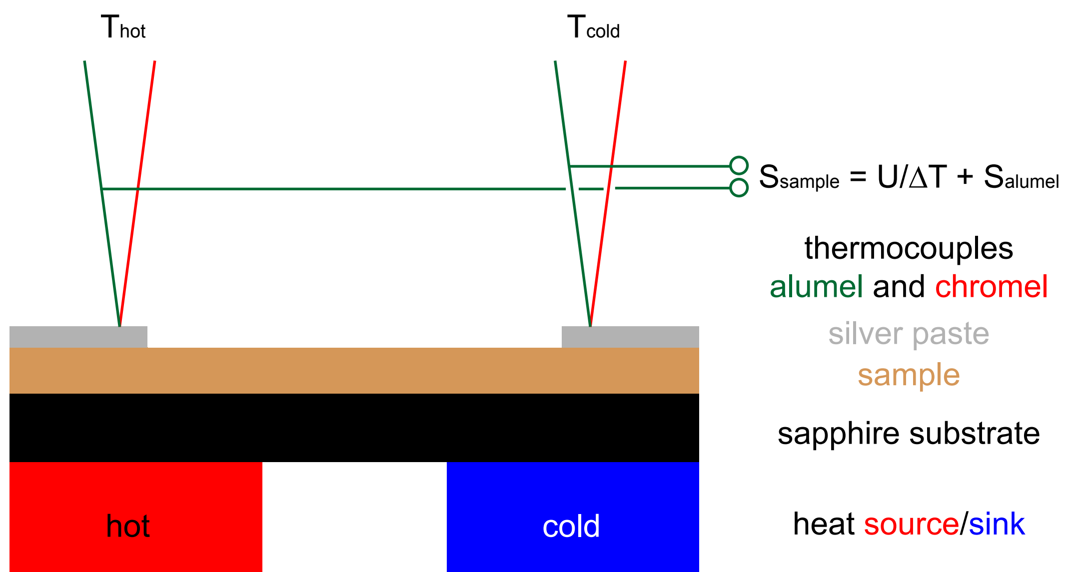

Figure 3.1. Setup for the determination of the Seebeck coefficient: The sample is placed on a mechanically stable and thermally conducting sapphire substrate, which in turn is placed with its two ends on a hot and a cold steel post. The temperature of the sample ends is measured by two alumel/chromel thermocouples onto the sample. The thermovoltage is picked between the alumel cables. The Seebeck coefficient of the sample is deduced from this voltage and the measured temperature difference and the Seebeck coefficient of alumel.

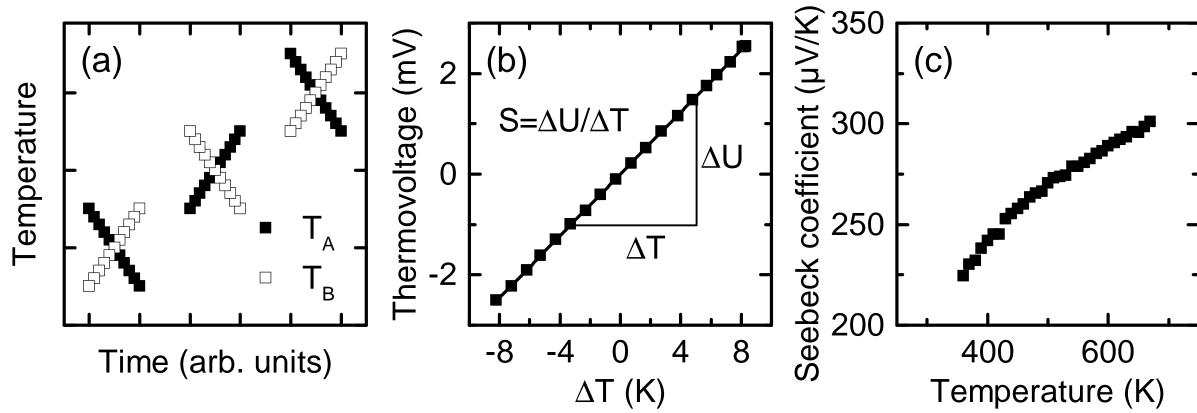

Figure 3.2. Principle of the determination of Seebeck coefficients: (a) Sequence of temperatures T_A and T_B at the two ends of the sample. (b) For one mean temperature, the thermovoltage is plotted versus the temperature difference. The slope yields the Seebeck coefficient of the system. (c) From several such measurements at different mean temperature, the temperature dependence of the Seebeck coefficient can be obtained.

typically a temperature difference ΔT between the two posts, named A and B, of 10 K is set, so that $T_A = 395\,\text{K}$ and $T_B = 405\,\text{K}$. The thermovoltage U of the system consisting of the first measurement wire, the sample and the second measurement wire is recorded by a Keithley 6517 electrometer with a high input impedance. To eliminate the disturbing effect of offset voltages in the calculation of S from a single measurement of the thermovoltage and the temperature difference, the temperature difference is inverted in several steps, maintaining the mean temperature, so that finally $T_A = 405\,\text{K}$ and $T_B = 395\,\text{K}$. Figure 3.2 (a) shows the temperature sequences for three consecutive Seebeck coefficient measurements. For each mean temperature the thermovoltage is plotted versus the temperature difference, as shown in panel (b). From this slope, the Seebeck coefficient can be obtained for that specific mean temperature. Repeating such a measurement for many mean temperatures yields the temperature dependence of the Seebeck coefficient as exemplarily shown in panel (c).

In most cases in this work, the measurement wire is one of the legs of the type K thermocouple used to determine the temperature on each side of the sample. Type K thermocouples consist of chromel and alumel, both of them having a separate Seebeck coefficient which is included in the thermovoltage. Thus, finally the Seebeck coefficient of the measurement wire S_{wire} has to be added to the effective Seebeck coefficient S_{eff} measured for the whole system to get the Seebeck coefficient S_{sample} of the sample itself according to

$$S_{\text{sample}} = S_{\text{eff}} + S_{\text{wire}}. \tag{3.2}$$

The temperature dependence of alumel and chromel are shown in Fig. 3.3. For the temperature range of interest in this work, S_{alumel}, which is mostly used for wiring, can be approximated by $S_{\text{alumel}} = -17\,\mu\text{V/K}$.

In the determination of the Seebeck coefficient there are two major sources of un-

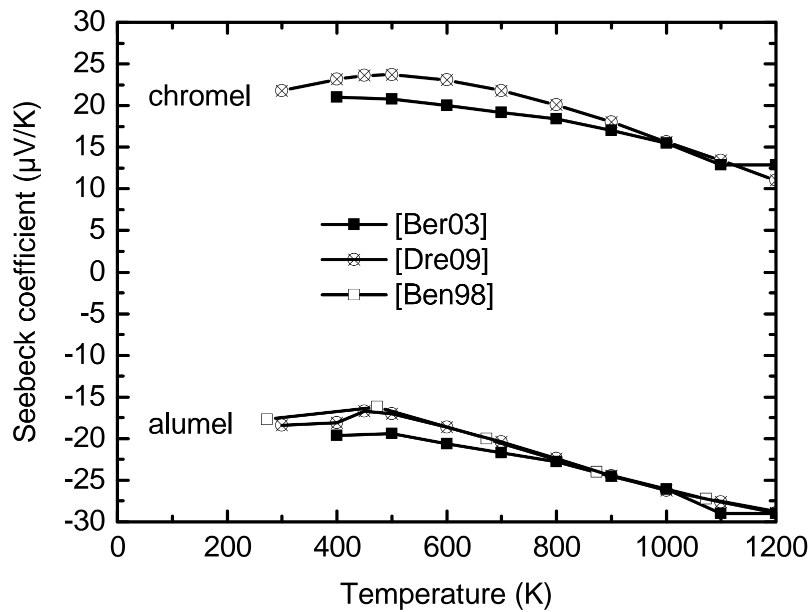

Figure 3.3. Seebeck coefficients of alumel and chromel: The data are taken from Refs. Ben98, Ber03, Dre09.

certainty. The first are inaccurate measurements of T_A, T_B or U due to deteriorated thermocouples or voltage offsets caused by non-Ohmic contacts. The effect of offset voltages as well as of wrongly measured temperatures is mainly eliminated due to the fact that only the slope of U vs. ΔT is considered. However, throughout this thesis data sets with a voltage offset larger than 1 mV in the U-ΔT-diagram have been rejected. The second source of uncertainty is a misinterpretation of these quantities due to the geometrical configuration of the sample and its electrical and thermal contacts. This can be caused by misplaced contacts and can lead to either an over- or an underestimation of S. Ideally, temperature and potential should be measured at identical points or at least at points where a defined geometrical relation is known. Two possible scenarios of deviations from this ideal situation are depicted in Fig. 3.4 (a) and (b), where silver paste with its negligible Seebeck coefficient of a few µV/K is assumed to be an equipotential body throughout.[Cus58] In both cases the spot where the thermocouples measure temperature are too far away from the decisive electrical contact to the sample because in panel (a) the silver paste is too high. The temperature difference measured will be too small, which leads to an overestimation of S. In panel (b), the thermocouple measure too far behind the electrical contact and measure too large a temperature difference, leading to an underestimation of S. Both errors can be minimized by placing the thermocouple as close to the innermost electrical contact as possible. An Scanning Electron Microscopy (SEM) micrograph of a thermocouple attached to a sample is shown in Fig. 3.4 (c). The spot where temperatures are measured is approximately 300 µm from the innermost electrical contact and some hundred µm above the sample surface.

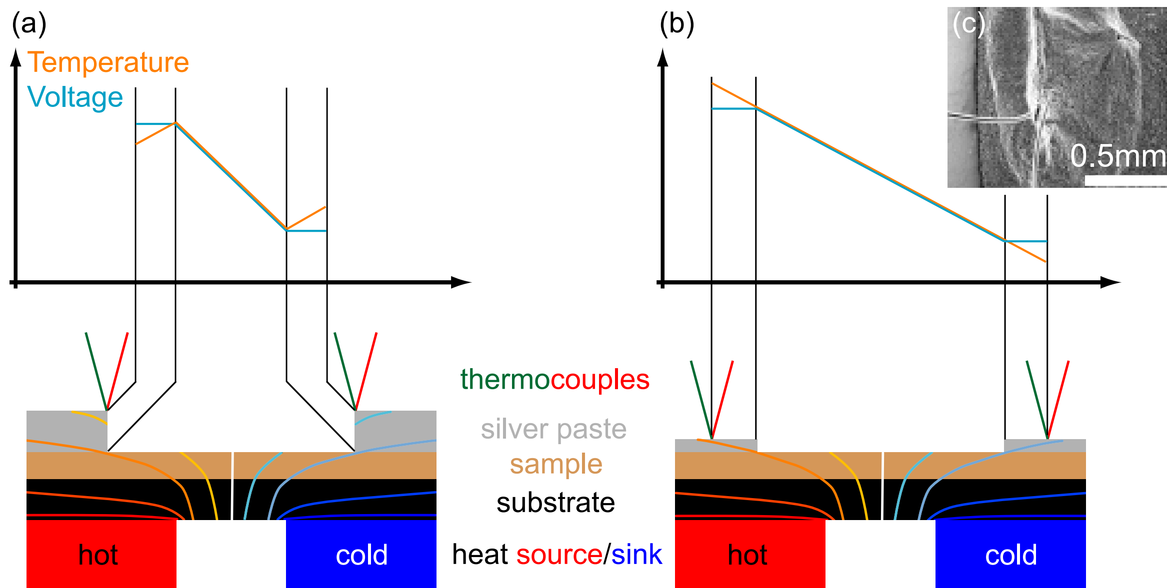

Figure 3.4. Geometrical sources of uncertainty in the determination of S: Isotherms are sketched qualitatively in the schematical depiction of the measurement geometry in panel (a) and (b). The SEM micrograph in (c) shows a realistic thermocouple placed in silver paste.

Room Temperature Measurement of the Thermovoltage

Temperature-dependent measurements of the Seebeck coefficient as discussed above are time consuming with one data set requiring one to two days. For experiments where a large number of samples have to be scanned, this is not appropriate. Thus, a setup for a quick and yet reliable investigation of the thermopower is needed. In this work, two Peltier elements placed next to each other and operated in a way that one surface is hot and the other element's surface is cool serve as such a setup. The samples of approximately 5 mm width and 8 mm length are placed at ambient conditions across the border between the two Peltier elements, so that the two electrical contact of a sample exhibit a temperature difference of approximately $\Delta T = 45\,\mathrm{K}$ at a mean temperature of 325 K. In contrast to the setup mentioned above, the temperature difference is kept fixed, but offset voltages can be neglected due to the high temperature difference. The voltage is measured using the two tungsten tips of a probe station. The quantity measured is called the *thermovoltage* U and is related to the temperature-dependent Seebeck coefficient $S(T)$ according to

$$U = \int_{T_{\mathrm{low}}}^{T_{\mathrm{high}}} S(T)dT. \tag{3.3}$$

In principle, the Seebeck coefficient could be obtained by dividing the thermovoltage by the temperature difference, however, since ΔT is rather large, a temperature dependent Seebeck coefficient falsifies the result. Because of that, the thermoelectrics community prefers to state the thermovoltage in such a case.

3.4. Raman Spectroscopy

As does infrared spectroscopy, Raman spectroscopy investigates vibrational modes by interaction of electromagnetic radiation with the material. In contrast to FTIR, no permanent dipole is needed in Raman spectroscopy. Rather, the selection rules require that during vibration, the polarizability changes with respect to the spatial coordinates. In solid state Raman spectroscopy light interacts with the optical phonon modes in a material. Involving virtual intermediate states, energy can either be absorbed by the material or emitted. The Raman-scattered light can, thus, be red-shifted (Stokes) or blue-shifted (Anti-Stokes). Further details and literature on the fundamentals of Raman scattering can for example be found in Ref. Zar10.

All Raman experiments in the following are performed using a Dilor spectrometer equipped with a 1800 l/mm grating and a liquid nitrogen-cooled CCD detector. To map samples, an x-y stage is used. Lasers operating at a wavelength of 514.5 nm or 647 nm are used to excite Raman scattering. Various objectives are used for the micro Raman experiments, and their nearly Gaussian spots were characterized by scanning the laser beam across the sharp edge of an evaporated Au film on top of a Si wafer, recording the decreasing Raman intensity of the Si LO mode. The spot width was obtained by deconvolution. The beam profile can be written as

$$H(r, z = 0) = \frac{P}{2\pi w^2} e^{-\frac{r^2}{2w^2}}, \tag{3.4}$$

with the power P and the standard deviation w of the beam. The latter quantity relates to the also often used full width at half maximum (FWHM) via

$$\text{FWHM} = 2w\sqrt{2\ln(2)}. \tag{3.5}$$

The objective used and the beam width is mentioned in the discussion of the respective experiments.

3.5. Scanning Electron Microscopy

A lot of knowledge on the morphology of the studied samples in this work is obtained by Scanning Electron Microscopy (SEM). The signal used is that of secondary electrons, which are a product of the local ionization of the material by the scanning electron beam. These secondary electrons leave the sample and are detected. As a consequence the signal intensity, and thus the image contrast, is enhanced for a high emission rate of secondary electrons. The ionization rate is increased with the energy of the scanning electron beam, which range from 2 keV to 30 keV. The image contrast also results from differences in the scattering cross section of the sample's atoms, which increases with the atomic number.[Sak99] Since electrons are also generated in the depth of the sample, the emission rate depends on the local charging of the surface. A high sample conductivity

leads to a low signal intensity. An important effect in secondary electron microscopy is the field enhancement at sharp features, which increases the emission rate. Edges and tips appear brighter than flat areas of the surface.[Sei83]

4

Group-IV Nanoparticles and Thin Film Deposition from Nanoparticle Inks

4.1. Gas-Phase Growth of Crystalline Nanoparticles

Starting from gaseous precursors such as silane (SiH_4) or germane (GeH_4) the NPs used in this work are synthesized by microwave-assisted decomposition of the precursors and subsequent agglomeration of the constituting atoms.[Kni04, Pet11] To this end, these

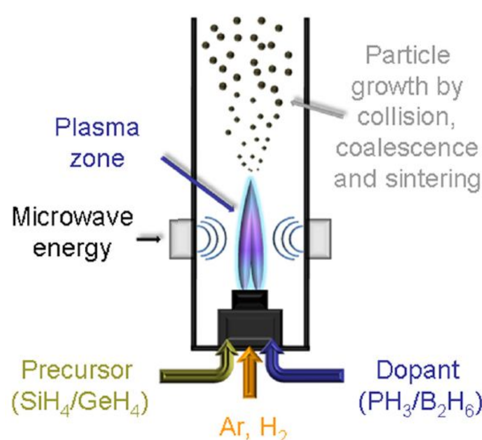

Figure 4.1. Schematic illustration of the microwave plasma reactor for NP synthesis: Precursor gases such as H_2, Ar, silane, germane and the dopant gases PH_3 and B_2H_6 are mixed and introduced into a low pressure tube around which a microwave generator is placed. The gas constituents, fractionized in the microwave zone, heat up there and cool downstream where they form the NPs. The figure is taken from Ref. Sch11a.

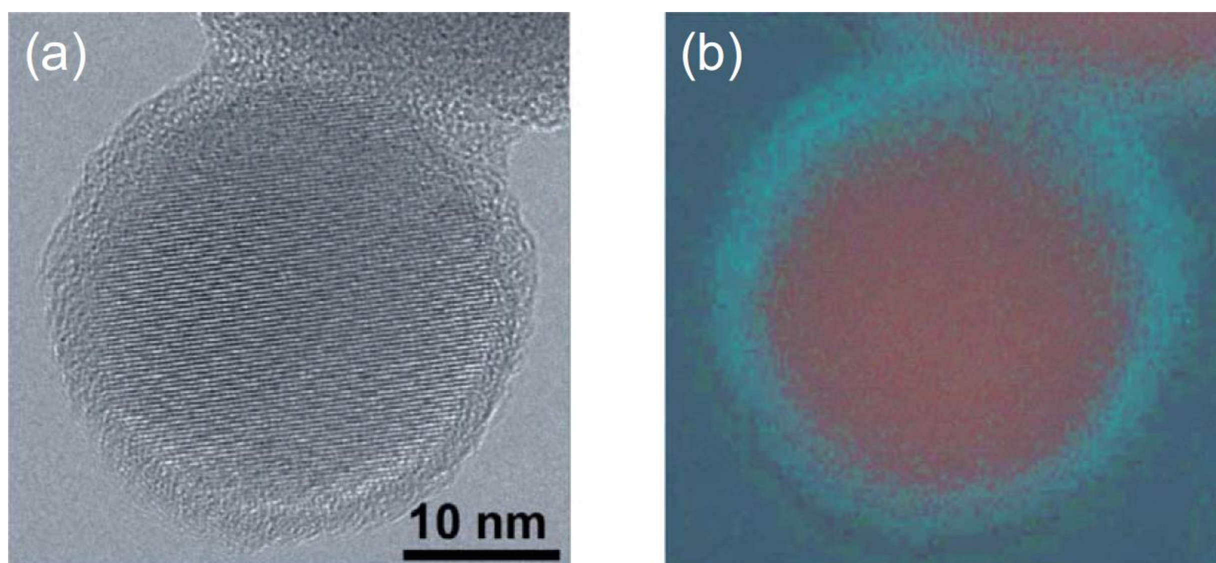

Figure 4.2. Spherical crystalline NP from the gas phase: (a) The high resolution TEM micrograph shows the high crystalline quality of the core and an amorphous oxide shell of the NPs used in this work. In the energy-filtered micrograph of the same NP in panel (b) the oxide shell is visible in blue. The figure is taken from Ref. Ste10.

gases are first mixed with additional process gases such as Ar and H_2. Injected by a nozzle, this mixture is led into a vacuum reactor, where the gas molecules are soon fractionized into their atomic constituents by a 2.45 GHz microwave plasma downstream of the nozzle. To control the growth kinetics additional Ar and H_2 nozzles form a shielding ring around the silane or germane gases. After leaving the plasma zone, the Si and Ge atoms agglomerate and form the NPs. Collected in a filter, the resulting powder is filled in bottles. The design of the reactor unavoidably involves an at least short contact of the NPs to ambient atmosphere during their removal from the reactor. This has significant implications for the surface properties.

Gas flow rate, reactor pressure, SiH_4/H_2 ratio and the microwave power are the main process parameters to control the shape, quality and size of the resulting NPs. A detailed discussion of the relation between process parameters and the resulting NPs can, e. g., be found in Refs. [Kni04, Lec09, Ste10, Pet11, Nie12]. Here, only a few basic structural properties will be discussed.

The NPs used in this work have a spherical shape and exhibit a highly crystalline core. Typical mean particle diameters that can be obtained by this gas phase synthesis approach are between 5 nm and 50 nm. Only for NPs larger than that, facets can occur. The collisions during the growth of the particles follows statistics, hence, also the resulting size of the NPs is distributed according to a log-normal size distribution with a mean diameter d.[Kni04] For most of the NP powders used in this work the mean diameter was determined by the Brunauer-Emmett-Teller (BET) method using the adsorption of gases to the NP surface.[Bru38] Some of the powder batches were also additionally characterized by TEM, which confirmed the results obtained by BET. Those

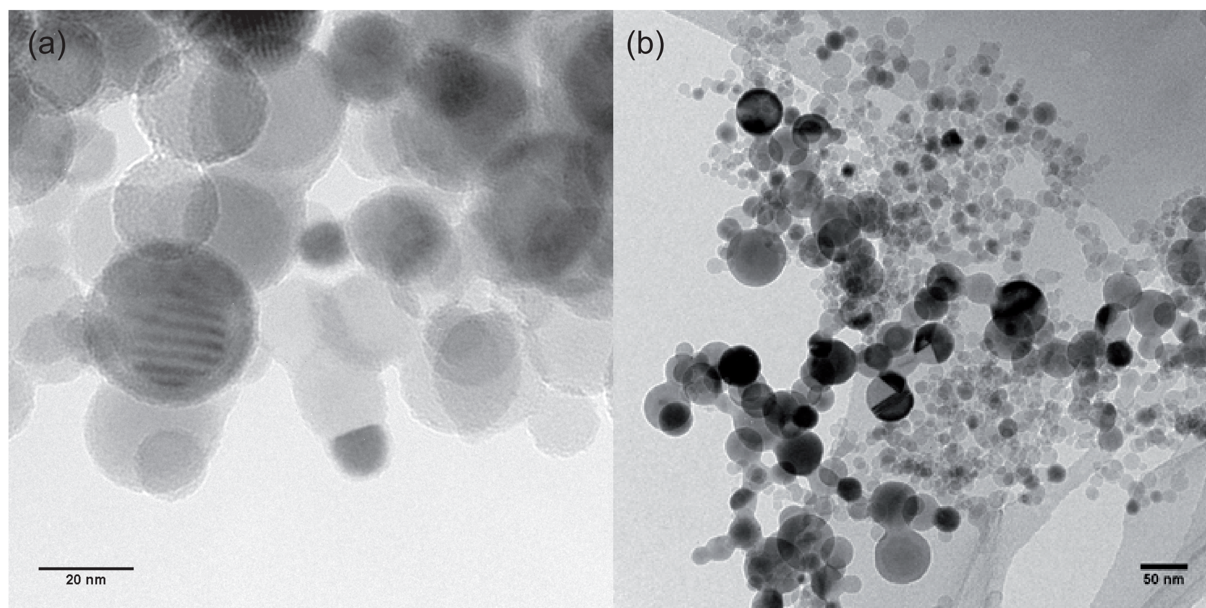

Figure 4.3. Alloy and composite SiGe NPs: (a) The TEM micrograph shows $Si_{80}Ge_{20}$ alloy NPs. (b) The larger and darker sub-ensemble of this SiGe 80:20 composite powder in this TEM image are Ge NP with a larger mean diameter compared to the Si NPs, which are brighter here. These micrographs were taken at the University of Duisburg-Essen within the collaboration.

TEM studies also reveal that the crystalline NP core is surrounded by an amorphous oxide shell, which is a result of the contact to ambient atmosphere. The micrographs in Fig. 4.2 show a high resolution TEM image of a Si NP in panel (a), with a clearly visible amorphous outer oxide shell. The same NP is also shown in panel (b), which is color-coded according to the energy loss of the electron beam. This energy loss is specific for the material and allows to distinguish the oxide shell (blue) from the crystalline core (red). The NP shown in Fig. 4.2 is not fully freestanding, as it is attached to a neighboring NP on the upper right side of the micrograph. This so called soft-agglomeration naturally occurs during the gas phase synthesis, however, is no handicap for further processing to NP inks and the laser-sintering process applied in this work.

Gas phase-grown NPs can be doped successfully by adding gases such as phosphine (PH_4) or diborane (B_2H_6) to the precursor gases. Similar to silane or germane these molecules are decomposed in the plasma zone and P or B are incorporated on substitutional lattice sites. Doping concentrations between $10^{18}\,cm^{-3}$ and $10^{20}\,cm^{-3}$ can be achieved, depending on the gas ratio. It was found by Stegner et al. that B is distributed homogeneously throughout the NP, whereas P tends to segregate towards the outer shell during the NP growth.[Ste09] The oxidation occurring during removal from the reactor leads to an electronic deactivation of large amounts of the P atoms. Up to 90 % of P can be lost by this self-purification.

By addition of germane to silane to the gas mixture injected by a single nozzle, $Si_{1-x}Ge_x$ NPs with an alloy composition x are formed. A homogeneous distribution of Si and Ge atoms is found by X-Ray Diffraction (XRD) for the whole composition range

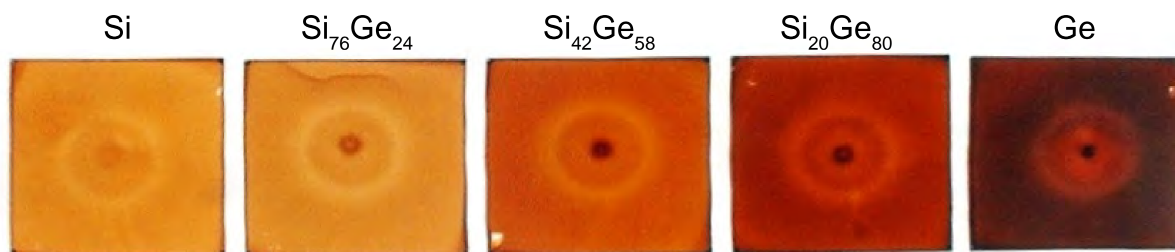

Figure 4.4. Change of NP color with SiGe alloy composition: This series of photographs shows thin films of SiGe NPs, spin-coated on 1" × 1" large transparent substrates. From left to right the Ge content of the alloy NPs increases as indicated. The ring structure visible is a result of the spinning process.

$0 < x < 1$, which is measured by Energy-Dispersive X-ray spectroscopy (EDX).

Similar to NPs of pure Si or Ge, alloy NPs also are of spherical shape with a crystalline core and an amorphous oxide outer shell, as can be seen in Fig. 4.3 (a). Increasing the Ge content of the NP also reduces the bandgap of the material, which leads to an enhanced optical absorption. Figure 4.4 shows photographs of thin NP films, spin-coated onto transparent substrates. From left to right, the Ge content increases and the transparency decreases.

By designing a special microwave growth reactor with two independent plasma zones it is possible to synthesize Si NPs and Ge NPs separately. Merging the particle flow downstream of the plasma zones where the NPs have already formed, both types of materials can be mixed within the reactor, so that the powder collected in the filter contains a well mixed powder of Si and Ge NPs. In Fig. 4.3 (b) a TEM micrograph of such a mixture of Si NPs with a mean diameter of 19 nm and Ge NPs with a mean diameter of 34 nm is shown. Although the intermixing of both types of materials is not perfect on the NP level, this is not of significant relevance for further processing steps.

A powder containing two types of NPs will be called a composite of Si and Ge and will be denoted SiGe $1 - X/X$ in contrast to an alloy powder, which will be denoted as $Si_{1-x}Ge_x$. Also materials processed from such powders, e. g., by laser-sintering, will be called composite or alloy.

4.2. The Nature of the Nanoparticle Surface and its Manipulation

The NP surface termination is of major importance for the success of further processing the powders. For deposition of thin films, in this work NPs are admixed to a dispersant after receiving the powder from the collaborators in Duisburg. As will be discussed in more detail in Sec. 4.3, the polarity of the NP surface is the main parameter for the dispersability and, thus, the basis for successful materials synthesis in this work.

To more clearly define at which stage of the work flow the status of the NP surface is

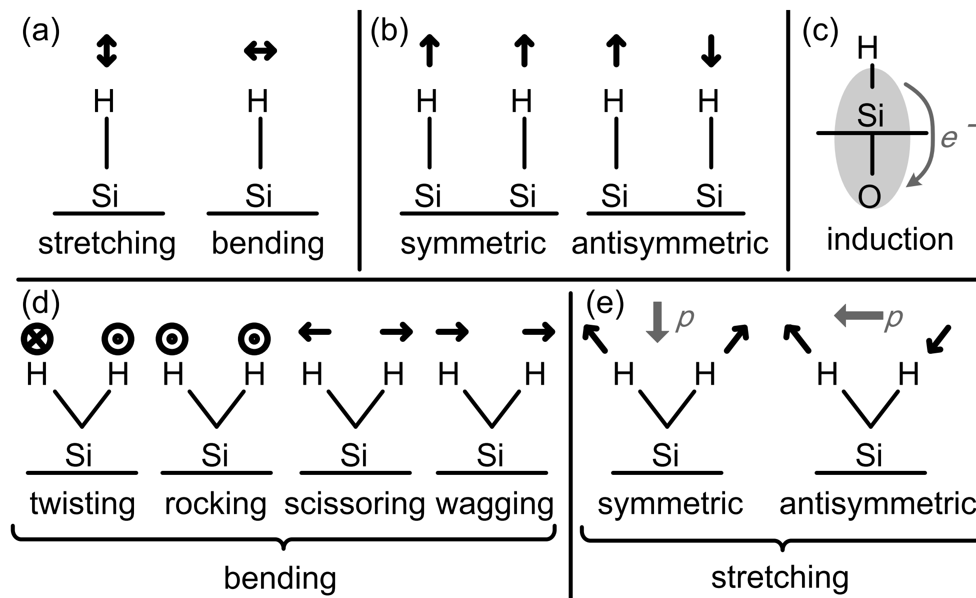

Figure 4.5. Hydrogen-related vibrational modes: For the case of a single hydrogen bound to a Si (or Ge) atom on the surface, panel (a) depicts the stretching and bending mode. (b) Coupling can occur between neighboring hydrogen. (c) Back-bonded oxygen changes the force constant between Si and H by induction. For the case of two hydrogen bound to each surface atom, panel (d) and (e) depict the possible bending and stretching modes.

discussed, the terminology is defined as follows: Directly after growth, i. e., still within the microwave plasma reactor, the powder will be called *as-grown*. After removal from the reactor and exposure to ambient atmosphere the powder will be called *as-received*. After deposition of a thin film by spin-coating from dispersion, the NPs will be called *as-deposited*. Immediately after removing the surface oxide by a wet chemical etching step, the NP surface will be called *as-etched*.

In the course of this work only two types of NP surface terminations play a role. The contact to ambient atmosphere during the removal of the powder from the reactor leads to oxidized surfaces. Typically, this oxide is removed wet-chemically using hydrofluoric acid (HF), which renders a hydrogen-terminated surface on Si as well as on Ge NPs. This is done by immersing deposited films of NPs into the respective etching solutions. Both, oxygen and hydrogen terminations are infrared-active so that they can be characterized by investigating the specific vibrational modes by FTIR.

In contrast to well defined wafer surfaces which are often investigated in detail in literature, spherical NPs exhibit hardly any defined surface orientation. However, many signals observed by FTIR can be identified with known stretching and bending modes of mono-, di- or tri-atomic surface termination groups and also with absorption signals from *s*- or *p*-polarized infrared radiation. Figure 4.5 schematically summarizes those relevant modes.

4.2.1. As-Deposited and As-Etched Si and Ge Nanoparticles

The oxygen and hydrogen coverage of as-deposited NPs can quantitatively vary significantly between different types and even batches of particles. Nevertheless, most NPs qualitatively show similar characteristic signatures. Exemplary FTIR signals of as-deposited and as-etched Si and Ge NPs are shown in Fig. 4.6, where important peaks are labeled for a clearer identification in the following discussion. Corresponding assignments and suitable references are given in Tab. 4.1. The observed signals are identified

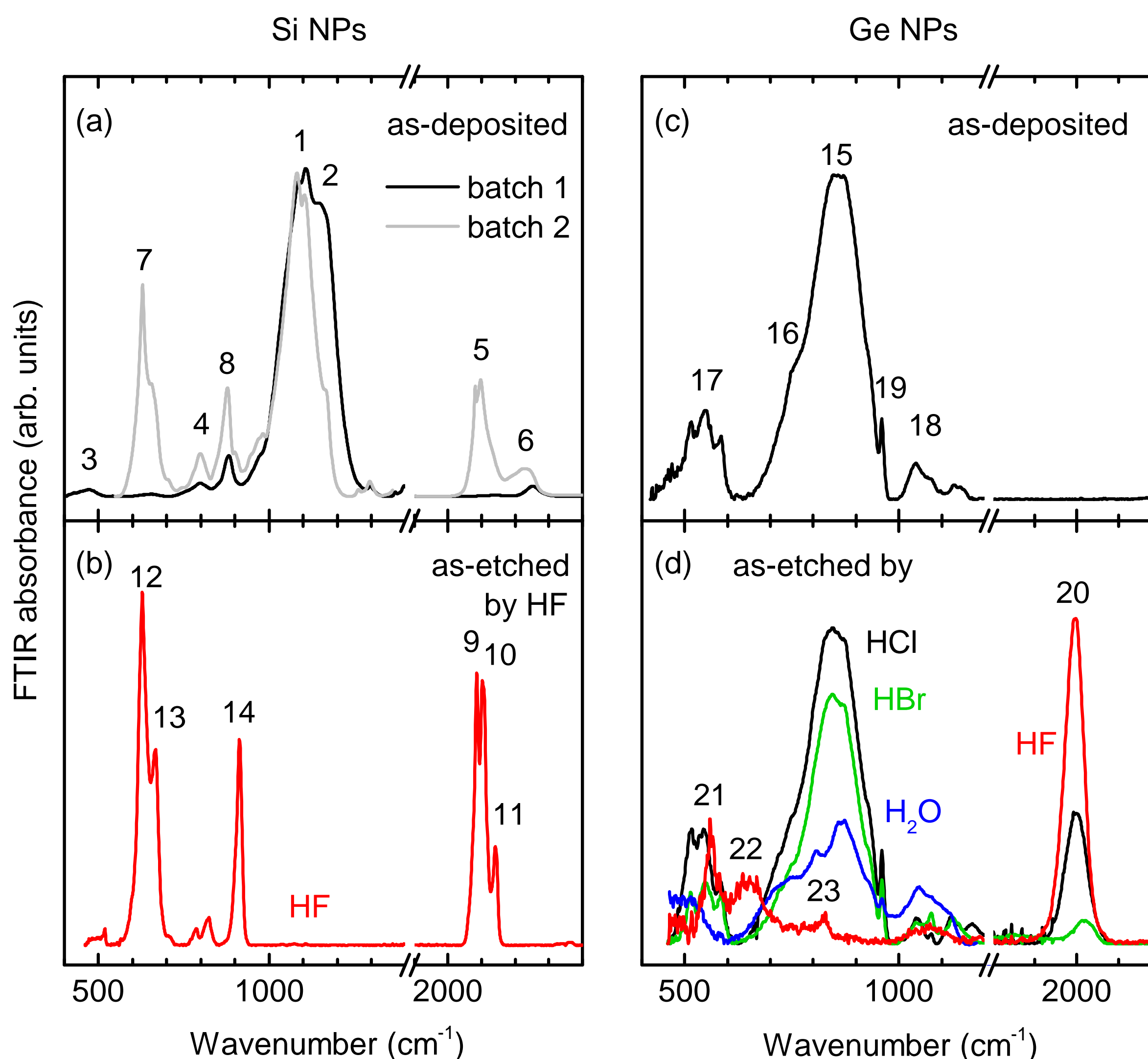

Figure 4.6. Vibrational modes of Si and Ge NPs before and after etching: (a) The Fourier Transform Infrared Spectroscopy (FTIR) absorbance of two batches of as-deposited Si NPs shows oxygen- and hydrogen-related peaks, which are labeled for discussion in the text. (b) Hydrogen-related signals are observed after etching the Si NPs with an aqueous solution of 5 % HF. (c) Only oxygen-related signals are found on as-deposited Ge NPs. (d) Oxygen- and hydrogen-related peaks are observed after etching the Ge NPs with an aqueous 20 % solution of HCl, of HBr, with deionized water and with a 10 % solution of HF.

in the following by comparison to data from the literature on well defined wafer surfaces with defined polarity of the incoming infrared radiation and by comparison to data on amorphous (hydrogenated) systems and on porous Si. The latter material has many similarities to thin films of NPs, as there internal surfaces have a largely undefined orientation and contain hydrogen.

In Fig. 4.6 (a) two batches of as-deposited Si NPs are compared. Batch 1 and 2 exhibit the most prominent absorption around 1080 cm^{-1} (peak 1), which is related to stretching vibrations of Si-oxide as a result of the NP's contact to ambient atmosphere. Not observed for all batches of Si NPs, the absorption at 1170 cm^{-1} (peak 2) is also caused by Si oxide. Probably this band is related to the LO mode of a-SiO_2 or SiO_x. A much lower absorbance is then observed around 470 cm^{-1} (peak 3), which can be identified as a Si-O-Si rocking mode. Similarly, around 800 cm^{-1} (peak 4) Si-O-Si bending modes can be observed. Due to the hydrogen gas involved in the growth process as-grown Si NPs have a partially hydrogen-terminated surface, which is stable enough to be detected even after dispersion of the particles. Around 2100 cm^{-1} (peak 5) the Si-H stretching region is characteristic for such a coverage. Shifted to higher wavenumbers hydrogen stretching modes with oxygen backbonded to the Si atom are typical for partly oxidized surfaces (peak 6). As a rule of thumb, each additional oxygen backbonded to Si shifts the Si-H stretching mode by 50 cm^{-1} to higher wavenumbers.[Niw94] The reason is the (negative) inductive effect of the electronegative oxygen, which removes negative charge between Si and H and by that increases the force constant. The higher oxide-related signal of batch 2 compared to batch 1 is also confirmed by a lack of peak 5 in batch 2, where only strongly oxidized Si-H vibrations are visible. Related to bending modes of H the structure around 630 cm^{-1} (peak 7) exhibits a substructure, similar to peak 5. Peak 8 around 880 cm^{-1} is most probably the stretching vibration of Si-OH.

To remove the surface oxide of Si an established procedure is the immersion of the material in hydrofluoric acid, which renders the Si surface hydrogen-terminated.[Tru90, Pi07] In Fig. 4.6 (b) the FTIR absorbance of an as-etched Si NP film is shown. The oxide related structures of panel (a) are no longer observed. Instead peak 5 is more pronounced and reveals a distinct substructure with peaks at 2087 cm^{-1}, 2105 cm^{-1} and 2143 cm^{-1}, which are usually identified as stretching vibrations of Si-H, Si-H_2 and Si-H_3 species. However, there is a controversy in the literature whether the substructure can also be a result of angle dependent absorption of *s*- and *p*-polarized infrared light by the Si-H_x species.[Cha89, Car83a, Gla96] The system which shows the most comparable absorption spectra to that of as-etched Si NPs is porous Si. The structural complexity of both systems makes it impossible to resolve the controversy here. After HF etching also the substructure of peak 7 can be separated into a contribution of Si-H bending (peak 12) and Si-H_2 wagging (peak 13). Scissor vibrations of Si-H_2 can be observed at 910 cm^{-1} (peak 14).

Many of the discussed signals on Si NPs can equivalently be observed in films of Ge NPs. The FTIR signatures of as-deposited Ge NPs are shown in Fig. 4.6 (c). The most prominent absorption (peak 15) is due to, both, antisymmetric stretching modes from

Table 4.1. Correlation of peaks observed in FTIR spectra of Si and Ge NPs with the modes related to oxygen and hydrogen species on the surface.

Label in Fig. 4.6	Related to	Mode	Reference
1	O	Si-O-Si stretching	[Luc87, Inn03]
2	O	LO mode of a-SiO_2 or SiO_2 or related to SiO_x	[Kir88, Que01, Inn03, Bat00]
3	O	Si-O-Si rocking	[Luc87, Inn03]
4	O	Si-O-Si bending or symm. stretching	[Kir88, Luc87, Inn03]
5	H	Si-H_x stretching (see peaks 9-11)	[The97, Gla96]
6	H	(O_x-Si)-H stretching	[Bor94, Niw94, Maw97, Oga95b, Zha01]
7	H	Si-H_x wagging (see peaks 12, 13)	[The97, Oga95a, Bro77]
8	O/H	Si-OH	[Oga95b]
9	H	Si-H stretching	[Bro77, Car83a, Cha85, Cha86, Cha89, Gla96]
10	H	Si-H_2 stretching	[Bro77, Car83a, Cha85, Cha86, Cha89, Gla96]
11	H	Si-H_3 stretching	[Bro77, Car83a, Cha85, Cha86, Cha89, Gla96]
12	H	Si-H bending	[The97, Oga95a]
13	H	Si-H_2 wagging	[The97, Oga95a]
14	H	Si-H_2 scissoring	[The97, Oga95a]
15	O	Ge-O-Ge antisymm. stretching and GeO_x	[Cor64, Riv05, Lee08]
16	C/O	covalent C, tetrag. GeO_2	[Lip58, Dim07]
17	O	hex. GeO_2	[Lip58]
18	O?	oxide-related	
19	O	hex. GeO_2 ,LO of GeO_2	[Lip58, Dim07]
20	H	stretching of Ge-H, Ge-H_2 Ge-H_3	[Riv05, Zah07, Bud96, Dim07]
21	H	Ge-H bending	
22	H	Ge-H_2 rocking	[Riv05, Dim07]
23	H	Ge-H_2 scissoring	[Riv05, Und08, Dim07]

Ge-O-Ge configurations in GeO_2 regions and due to GeO_x in non-stoichiometrically oxidized regions. Further, the weak high wavenumber shoulder at approximately 933 cm^{-1} could be identified as the LO mode in GeO_2. The low wavenumber shoulder (peak 16) could be a signature of tetragonal GeO_2, but could also originate from covalently bound C due to the ethanol dispersion. The triplet structure at 514 cm^{-1}, 547 cm^{-1} and 583 cm^{-1} (peak 17) is a signature of hexagonal GeO_2. Peak 18 could not be identified by comparison to the literature, but is always observed in as-deposited Ge NPs and must, thus, be related to oxidic Ge. The distinct feature at 960 cm^{-1} (peak 19), which scales with the pronounced oxide signal (peak 15) is also related to hexagonal GeO_2.

The discussion of the oxide related Ge signals in panel (c) suggests that the as-deposited Ge NPs carry hexagonal as well as tetragonal GeO_2, but also suboxides GeO_x. Hexagonal GeO_2 is soluble in water, but the tetragonal phase as well as the suboxide cannot be removed with a simple rinse in pure water.[Lau32, Zha93, Dim07] A native oxide on Ge surfaces should, however, be etched by hydrohalogenics such as HF, HCl, HBr and HI, rendering the surface hydrogen-, chlorine-, bromine- or iodine-terminated, respectively.[Kim08, Bod03, Los06, Mer07] Investigated on clean and well defined Ge wafer surfaces, the ambient stability of the termination should increase with the mass of the terminating atom. Figure 4.6 (d) shows the results obtained after attempts to etch and terminate the Ge NPs films by H_2O, HCl and HBr. Whereas the water treatment at least partly removes the oxide from the particles, HCl and HBr did not show the expected results on the NPs.[Sun08] However, the spectra reveal a hydrogen coverage after these treatments, as evident from the Ge-H stretching signal around 2000 cm^{-1} (peak 20).

Obviously not only the oxide was not removed as expected, but also a termination with hydrogen instead of the halide is observed. In contrast, etching the Ge particles by HF completely removed the oxide-related contributions to the spectrum, accompanied by a pronounced Ge-H stretching signal. This important finding leads to the use of HF as an oxide etch also for Ge NPs in this thesis. Where Si shows a substructure in peak 5, Ge does not in peak 20. However, the peak is slightly asymmetric as the literature ascribes this to the contribution of stretching modes by Ge-H, Ge-H_2 and Ge-H_3 at 1987 cm^{-1}, 2020 cm^{-1} and 2060 cm^{-1}. In addition to these stretching modes the spectra also show the bending mode of Ge-H (peak 21), the rocking mode of Ge-H_2 (peak 22) and the scissor mode of Ge-H_2 (peak 23).

4.2.2. As-Deposited and As-Etched SiGe Alloy Nanoparticles

So far the discussion concentrated on the vibrational signals observed on NPs of pure Si and pure Ge. As already mentioned in Sec. 4.1, also SiGe alloy NPs are available for the fabrication of thermoelectric thin films. Their surface vibrational modes are shown in Fig. 4.7. Panel (a) depicts the FTIR absorbance of as-deposited pure Si NPs, of as-etched Si NPs after exposure to ambient air for two days. In panel (b) through (e) the respective signals are shown for various SiGe alloy compositions. Finally, panel (f) shows the

fingerprints of pure Ge NPs again.

As already discussed in the last section, as-deposited Si NPs exhibit a strong oxide-related band and Si-H stretching modes with and without backbonded oxygen. Increasing the Ge content to 24 %, the oxide mode does not change qualitatively in position nor shape. However, the hydrogen stretching mode shifts by 100 cm^{-1} to lower wavenumbers, towards that characteristic for Ge. The hydrogen stretching mode with backbonded oxygen does not change its position with respect to pure Si. Increasing the Ge content to 58 % adds an oxide signal at the position of the Ge oxide band at 860 cm^{-1}. The hydrogen stretching mode further looses its substructure, but its position as well as that of the hydrogen stretching mode with backbonded oxygen do not change compared to the signals of NPs with lower Ge content in panel (b). The trend of increasing Ge-related oxide and decreasing Si-related oxide persists up to pure Ge particles, where no Si bands cn be detected any more. For Ge contents as high as 80 % only hydrogen stretching signals with backbonded oxygen are observed, whereas pure hydrogen stretching modes are not found for the as-deposited films.

After etching the NPs the oxide-related bands have disappeared for the whole composition range. Interestingly, the prominent hydrogen stretching mode is at the position characteristic for that of pure Ge. This is already found for Ge contents as low as 24 %. Additionally, the substructure indicative of mono-, di- and trihydride is smeared out.

After two days of exposure to ambient air, the as-etched NPs show the signal of a regrown oxide throughout the whole composition range. The data in Fig. 4.7 allow to speculate that alloy NPs are more prone to reoxidation than the pure materials. Also of interest for further processing the powders is the remaining hydrogen coverage. As obvious from Fig. 4.7 (a), Si NPs exhibit virtually no decrease in the absorption strength at the hydrogen stretching region. For NPs with 24 % Ge in panel (b), the hydrogen stretching signal is slightly reduced and also some signal from hydrogen stretching with a backbonded oxygen atom appears. The spectrum shown for the alloy NPs in panel (c) reveals a significant loss of hydrogen after two days in ambient atmosphere. By integration of the area under the peaks it becomes evident that the hydrogen coverage after etching and storage in air for 2 days is even less than that observed on as-deposited NPs. Nanoparticles with 80 % of Ge or more loose all hydrogen present on their surface after etching within two days in air. This important finding implicates that for further processing of the etched films the time has to be kept as short as possible.

The experimental results mentioned above are indicative of an alloy NP surface which is not of the same composition as the core and which changes upon HF etching. Assuming that hydrogen can only be found at the very surface of the particles and that an oxide reaches deeper into the NP, a possible model would be that as-deposited SiGe alloy NPs are enriched of Ge at the outermost shell. Such an inhomogeneity on the scale of a monolayer cannot be detected by TEM, XRD or EDX as they were used to investigate as-received powders. From studies on SiGe structures grown by molecular beam epitaxy it is known that Ge tends to segregate to the surface.[God94] An experiment where the present NPs were reoxidized using H_2O_2 and this oxide again

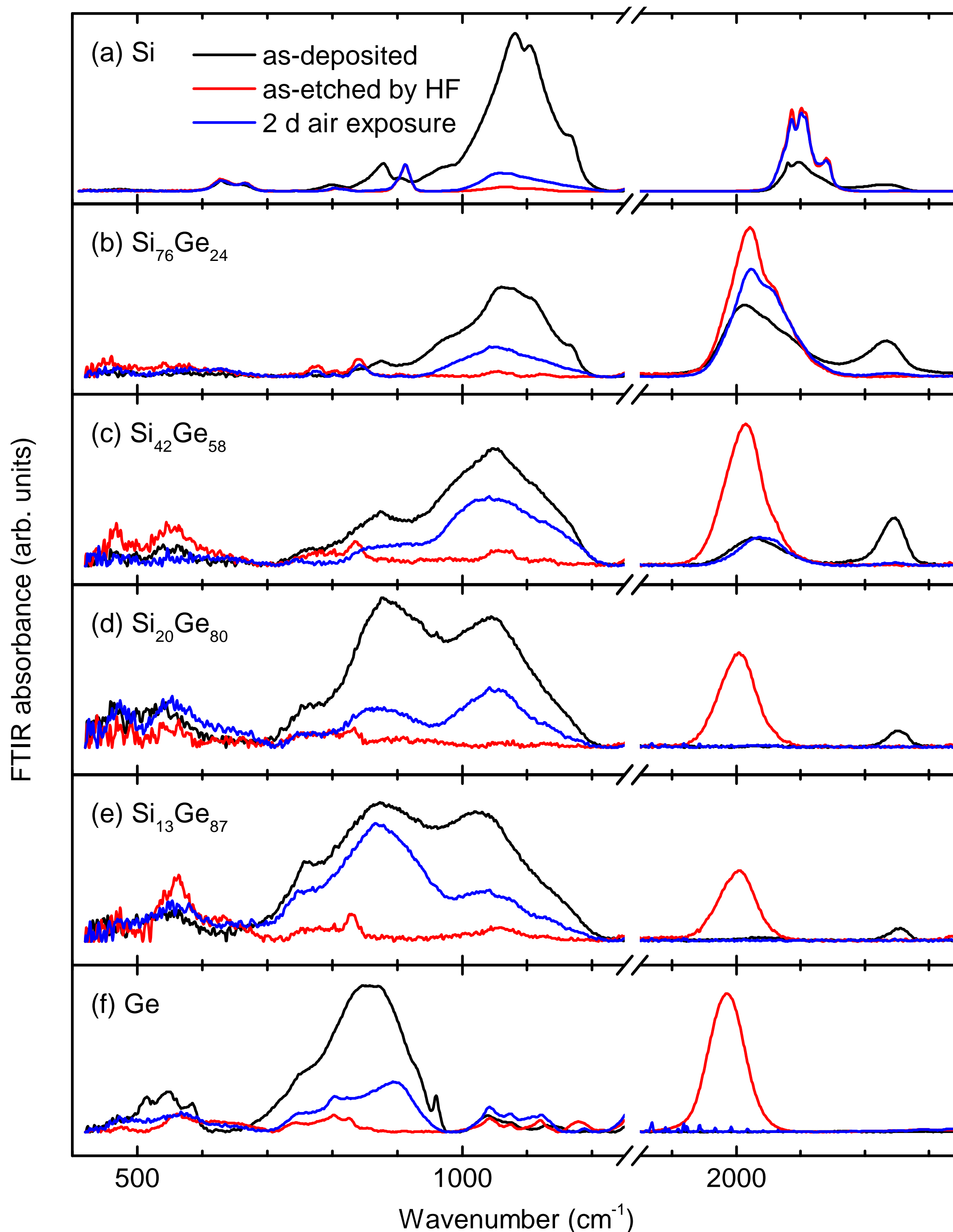

Figure 4.7. Oxygen- and hydrogen-related vibrational modes on SiGe alloy NPs: The oxide and hydrogen stretching region are shown as observed by FTIR of SiGe alloy NPs for the whole composition range, as determined by EDX. Signals are shown for as-deposited and as-etched NPs, as well as after etching followed by a 2 d exposure to ambient air.

was removed again by HF confirms the hypothesis of Ge enriched surfaces on alloy SiGe NPs by EDX measurements.[Gre13] The FTIR results in Fig. 4.7 could then be explained by an initially Ge enriched surface, so that the majority of hydrogen stretching vibrations is similar to that on pure Ge NPs. With an oxide reaching deeper into the NP where Si and Ge are abundant similar to the concentration measured for the whole NP, the relative oxide contributions of Si and Ge in Fig. 4.7 reflect the composition of the alloy.

Interestingly, although as-deposited alloy NPs show the signature of hydrogen coverage even for long times of up to many months after their synthesis, the hydrogen found after HF etching is much less stable with respect to time. The aspect of hydrogen stability is thus also part of the discussion in the following sections.

4.2.3. Influence of Etchant Concentration and Etching Duration on the Hydrogen Coverage

Focussing only on the hydrogen stretching mode near $2000\,\text{cm}^{-1}$, in this section the influence of the HF concentration used for etching on the stability of the hydrogen bond are investigated. Starting with pure Si NPs, Fig. 4.8 shows the hydrogen stretching region of the FTIR spectrum for different concentrations of HF used for the 2 min etch. Although the ordinate is given in arbitrary units, the fact that the samples investigated were cut from a single larger sample allows to quantitatively compare the spectra. All panels show the already discussed triplet structure, independent of the HF concentration, which ranges from 0.5 % to 20 %. As obvious from the areas under the peaks, the hydrogen coverage cannot be correlated to the HF concentration. It can, thus, be argued that already tiny amounts of HF in the etching solution are sufficient to completely remove the native oxide and all panels shown here show the signals observed on a virtually H-saturated Si surface. The variation of the hydrogen coverage observed in Fig. 4.8 is very likely caused by NP agglomerates which resided in the dispersion used to fabricate the thin films. As already mentioned in the discussion of Fig. 4.7 (a), the hydrogen coverage on Si NPs is very stable with respect to storage in ambient air.

A similar experiment with different HF concentrations for etching is shown for Ge NPs in Fig. 4.9. As already seen in the previous section, the hydrogen coverage of Ge NPs is not stable in ambient atmosphere. This becomes also evident in Fig. 4.9, where several spectra are shown per panel. The most intense spectrum, which can well be fitted by a Gaussian peak as plotted by solid lines, is taken immediately after transfer into the spectrometer, so that the sample was exposed to ambient air for approximately 25 s. After an additional exposure to air for the time indicated in the figure caption the same samples were measured again, which then showed a decreased hydrogen coverage. In contrast to the Si samples discussed previously, here, the samples were free of agglomerates, so that the direct comparison of the intensity between different panels is justified. With increasing HF concentration, the hydrogen coverage is enhanced.

A detailed investigation of the data in Fig. 4.9 reveals an approximately exponential desorption of hydrogen from the Ge surface with time. Notably, the character-

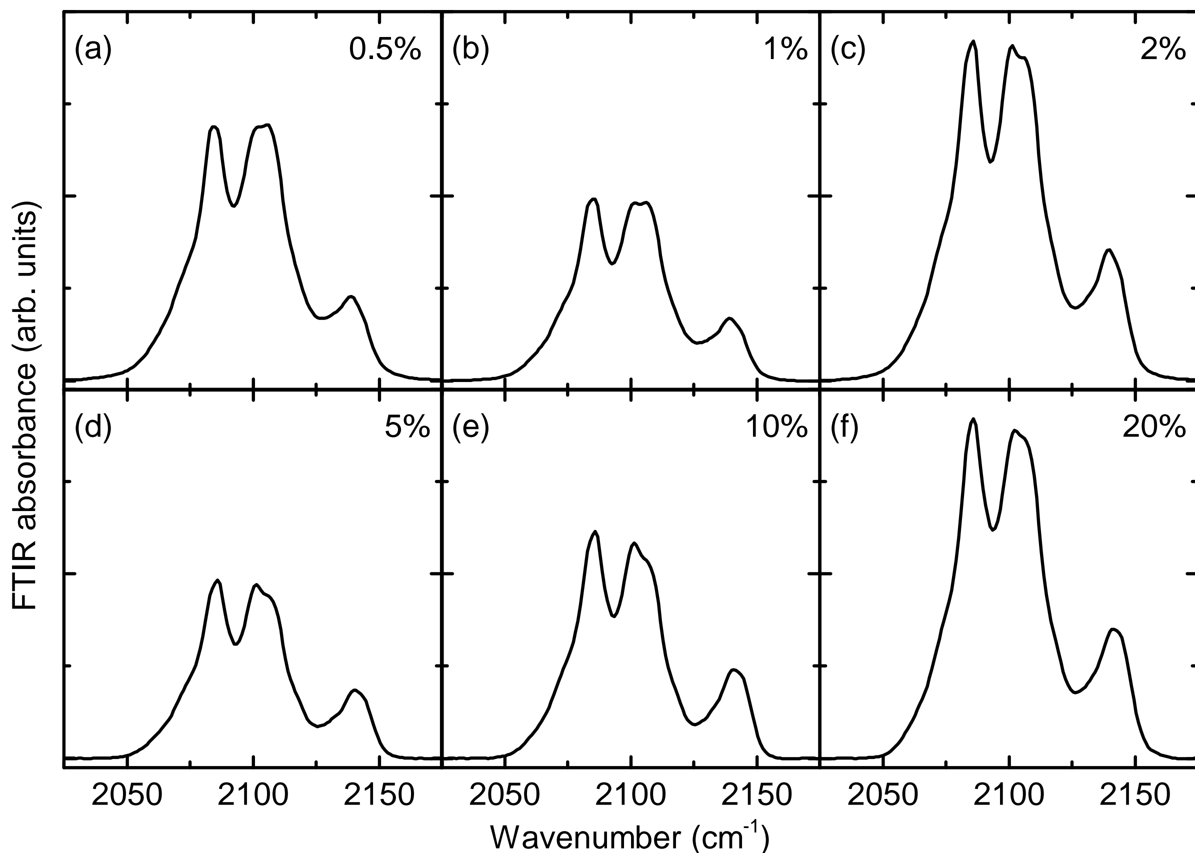

Figure 4.8. Hydrogen stretching signals for Si NPs etched with aqueous solutions of different HF concentration: Panel (a) through (f) show the hydrogen stretching FTIR signal of Si NPs immediately after etching with the indicated concentrations of HF, each for 2 min. The substructure is discussed in the context of Fig. 4.6 (b).

istic decay time is higher after etching with higher HF concentrations, ondicating a higher stability. This behavior was also found in the literature on HF-treated Ge wafer surfaces.[Par08b, Par08a] In view of further processing the Ge NP powder, for which a hydrogen termination is desirable, the shortest decay time found is approximately 10 min, so that any fabrication step in air should follow within some minutes. Interestingly, no detectable oxide related signal arises, even for samples which lost all the hydrogen, which excludes a competitive bonding to oxygen instead of hydrogen. The reduced stability of Ge-H in contrast to Si-H can be explained by a lower bond energy of Ge compared to Si.[Bey91] Still, typical desorption temperatures found on amorphous Ge films as well as on crystalline Ge are not below 500 K.[Bey91, Tok04, Eve93]. Thus, the found room temperature instability of Ge-H_x bonds seems to be characteristic for NP surfaces.

The observation that the hydrogen coverage depends on the HF concentration when applying an etching step of 2 min could also mean that the termination chemistry is slow and no equilibrium was reached yet. Thus, Fig. 4.10 shows experiments where the Ge

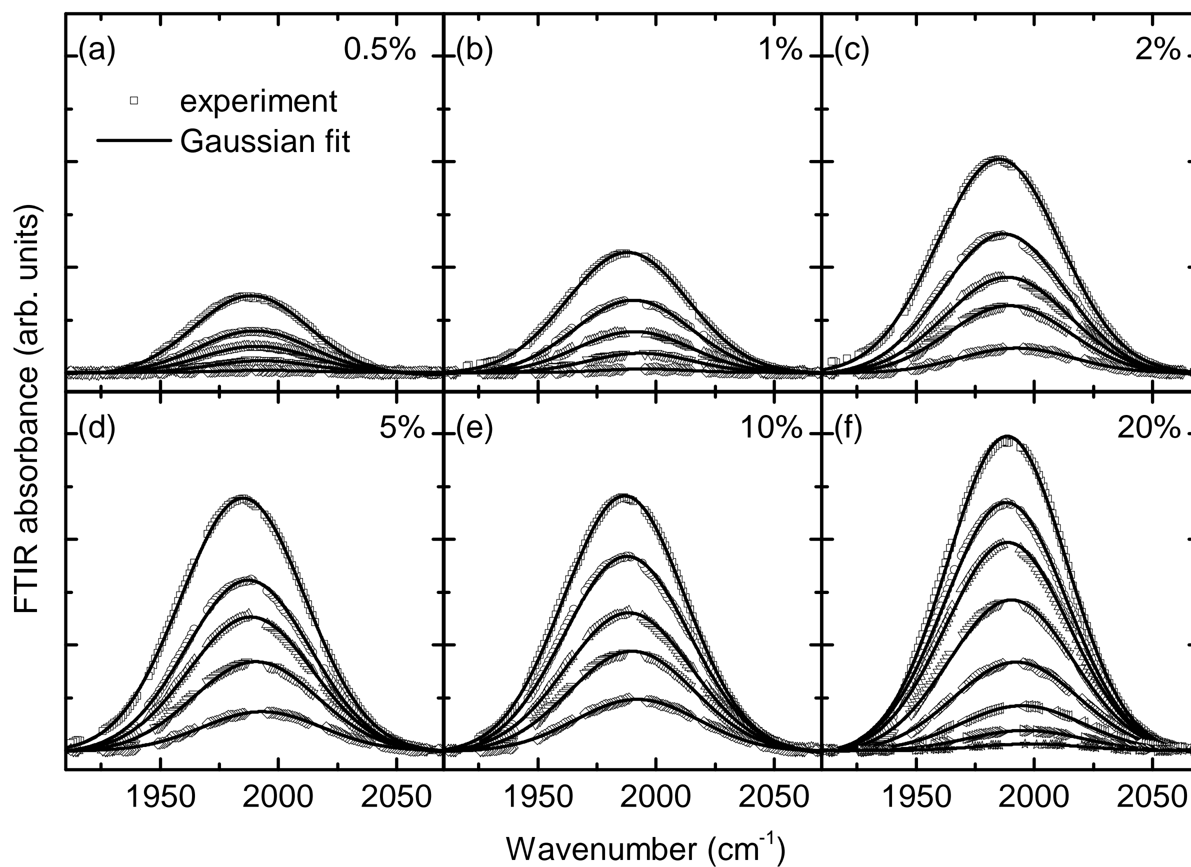

Figure 4.9. Influence of the HF concentration on the hydrogen coverage of Ge NPs after etching: Each panel shows the hydrogen stretching FTIR signal after 2 min of etching the NPs with HF of the indicated concentration for different times of exposure to ambient air. Beginning from the top, the data shown are signals observed after 15 s, 5 min, 10 min, 20 min, 40 min, 60 min, 80 min, 120 min. Missing experimental data are related to residual water absorption lines in the FTIR measurement, which were removed for clarity.

NPs were etched in a 5 % aqueous solution of HF and the etching time was varied from 25 s to 1500 s. However, the little variation of the initial hydrogen coverage shown in all panels as well as the very similar desorption kinetics suggest, that this is not the case. The HF concentration rather than the etching time seems to be the important parameter for the resulting hydrogen coverage of Ge NPs.

4.3. Nanoparticle Inks

The approach taken in this work to deposit thin films of NPs is to spin-coat them from a suitable ink. The general term *dispersion* classifies systems where one particulate phase is distributed in another, continuous phase, i. e., the dispersant. In the case where the dispersed phase is a solid and the continuous phase is a liquid, the system is called a *suspension*. Often, the size of the dispersed phase is important for the stability of the

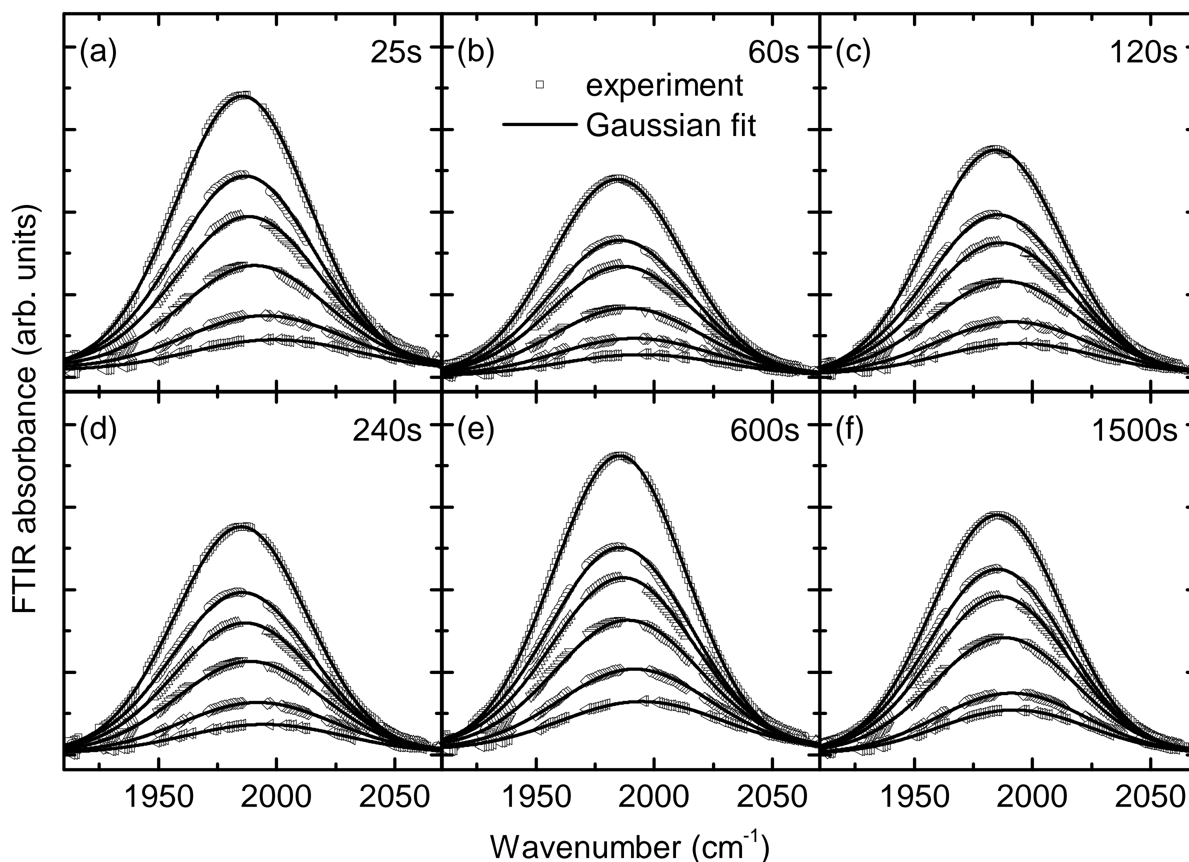

Figure 4.10. Influence of the HF etching time on the hydrogen coverage of Ge NPs: Ge NPs were etched in a 5 % aqueous solution of HF for the indicated time. The data shown are the observed hydrogen stretching FTIR signals after 15 s, 1 min, 5 min, 10 min, 20 min, 40 min exposure to ambient air.

suspension due to the opposing trends of gravity, which leads to sedimentation, and Brownian motion, which drives the system towards homogeneity. For particle sizes between approximately 1 nm and 1 µm the system is called a *colloid*, which is defined also for other than solid-liquid systems. The NP inks aimed for in this work should be a colloid, but depending on the batch of NPs, sedimentation of at least a part of the NPs is observed sometimes. Such inks must be called suspensions. Thus, for simplicity, in the following, all inks will be called dispersions.[Lev83, Wib95]

A necessary condition for successful dispersion of a powder in a dispersant is that the particles are wetted.[Tad12] This wetting behavior is mainly determined by the hydrophobic/hydrophilic properties of both the dispersant and the dispersed phase. The results obtained in the previous section can be summarized by the fact that oxygen- as well as hydrogen-terminated surfaces are found on the NPs used. Whereas oxidized surfaces are hydrophilic, hydrogen-terminated surfaces are hydrophobic in the case of Si. As found above, Ge-H is not stable in ambient air, and should, thus, also not hinder the use of hydrophilic dispersants.

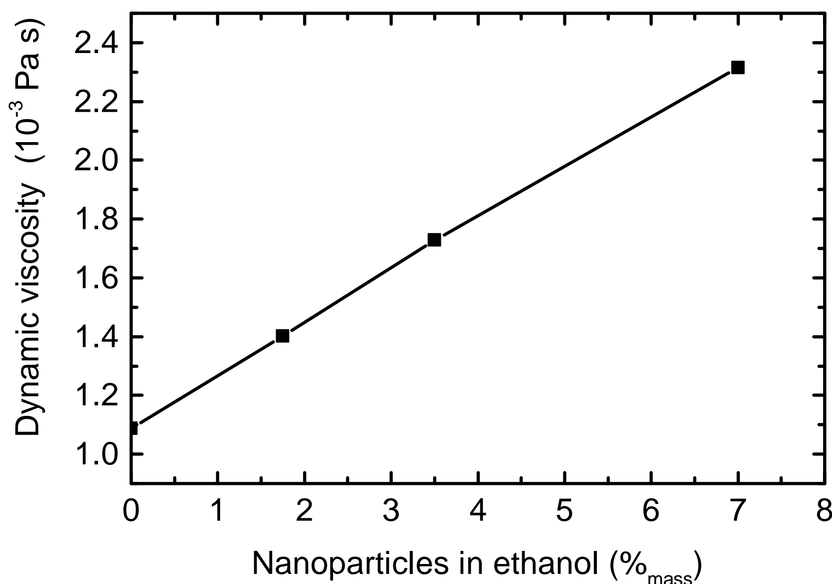

Figure 4.11. Viscosity of inks depending on the NP mass concentration: For Ge NP with a mean diameter of 27 nm the dynamic viscosity of ethanol-based dispersions is shown.

Apart from wetting, which is a necessary precondition, there are some further considerations that play a role when selecting the dispersant. First, the boiling point should be high enough, so that the concentration of the dispersion does not increase too much within the time needed for the thin film preparation. The boiling point should, however, also be low enough to allow drying of the deposited films. Second, the viscosity and the surface energy of the final dispersion must be compatible with the spin-coating process and the substrate itself. Third, especially in view of a commercialization of the processes, it is desirable that the dispersant is not harmful, neither for the environment nor for the equipment used.

A suitable compromise that well matches the above mentioned aspects for a dispersant is ethanol. With a boiling point of 78 °C, a viscosity of 1.1 mPa s and a surface energy of 22.1 mJ/m^2 ethanol is technologically suitable.[Ada97] The health risks of ethanol are not essentially based on its inhalation. Ethanol is volatile, so that no significant remnants can be found by FTIR in NP films dried on a hot plate.

With increasing concentration of NPs in ethanol the dynamic viscosity η increases, as it is shown exemplarily in Fig. 4.11. Here, the dynamic viscosity was measured using a micro-Ubbelohde viscosimeter. The mass concentration cannot exceed certain limits because agglomeration becomes more likely for highly concentrated dispersions. Typical dispersions used in this work contain $5 - 7\,\%_{\mathrm{mass}}$ of NPs. If a higher viscosity is needed as can be obtained by increasing the mass concentration, a second dispersant phase must be added. This second phase also must meet some criteria, e. g., it must be miscible with the first phase and its boiling point should not deviate too much from that of the first phase. Otherwise, the ink decomposes upon drying. Polyethylene glycol (PEG) is an

appropriate additive because the viscosity can be adjusted by selecting the chain length of the molecule.

A major challenge for the production of inks is their stability against agglomeration and sedimentation. The growth conditions of the NPs used here naturally causes the powder to form soft agglomerates. If such larger particles turn out to be problematic for the thin film formation, sonication of the dispersion in a cooled ultrasonic bath and/or shaking the dispersion with zirconia milling balls usually lead to homogeneous inks in this thesis.

4.4. Thin Film Deposition by Spin-Coating

The standard way to deposit thin films of NPs in this work is by spin-coating from pure ethanol dispersions with a mass concentration of 5 %. As a substrate, typically 125 µm thick foils of polyimid are used, which are compatible with further HF etching steps and can withstand the thermal stress during sintering of the NP films. Further, polyimid has a surface energy of approximately 40 mJ/m^2, which is compatible with the ethanol NP dispersion.[Bra89] For cleaning of the substrates acetone and isopropanol baths in the sonicator are used. A standard substrate is of 2.5 cm $\times$ 2.5 cm size and rotates with 32 rounds per second on the spin-coater, before 80 µl of the dispersion is pipetted in the center of the substrate while rotating. To drive out the ethanol dispersant the samples are placed on a hot plate of 100 °C for approximately 2 min.

As a result of remaining agglomerates and the centrifugal force during spin-coating radial inhomogeneities occur on some samples. Further, a central ring as can also be seen in the photographs in Fig. 4.4 is a result of the suction power of the spin-coater to fix the substrate. For further processing only the regions outside the central ring, which are homogeneous in thickness, are used by cutting appropriate sample pieces.

Depending on the rotation speed, the mass concentration and, thus, the viscosity of the dispersion, the NP film can reach thicknesses between 100 nm and 1 µm. The majority of films used in this work had a thickness of approximately 300 nm.

The spin-coated film of NPs is not packed to the maximum density as a result of the size distribution of the particles and the rather fast evaporation of the solvent on the hot plate. For spheres of the same diameter the theoretic maximum packing density is 74 %.[Hal10] Random packing is less dense and fills the space to approximately 60-64 %.[Sco69] An increased inhomogeneity of the diameter distribution leads to an increase of the maximum packing density again.[Far09] However, SEM studies, as the one later discussed in Fig. 5.2, of the films deposited here showed that the NPs are not packed densely, so that a fill factor of 50 % will be assumed in the following.

5 Enhancing the Nanoparticle Interconnection

The thin films of NPs deposited from dispersion by spin-coating, as discussed in the previous section, exhibit a rather poor electrical performance if no further measure is taken. Electrical in-plane conductivities as low as 10^{-10} S/cm to 10^{-7} S/cm are found, depending on the type of NPs investigated. Even for doped NPs the conductivity of the as-deposited film cannot be enhanced beyond these values.

There are two main reasons for the observed low electrical conductivities. First, current passing an ensemble of spherical particles is spatially constricted to the tiny contact between them. This significantly reduces the effective area through which current is transported. Second, if the device is to be operated in ambient air, two neighboring NPs will oxidize again so that charge carriers not only need to pass through the small contact area but even more, they need to cross an oxide barrier there. Transport processes found in such systems include space-charge limited current and hopping, coming along with rather low electrical conductivities.[Ros55, Bur97, Raf06] If the degree of interconnection of the NP ensemble could be enhanced, e. g., by allowing the formation of necks around the touching points,[Pan08] the geometric drawback can be overcome. Such a contact would further have a reduced surface-to-interface ratio and would, thus, be less prone to oxidation.

The formation of necks, i. e., the coalescence of NPs, can be achieved by heating them to temperatures where the atomic constituents become mobile.[Sch08a] Such processes are generally classified in *melt* and *sub-melt* processes, depending on whether the material is heated above its melting temperature. If no special care is taken that the subsequent cooling is sufficiently fast, so that the material is quenched into an amorphous state, usually crystalline phases result. In the case where the initial substance is already

crystalline, such as the NPs used here, an appropriate term would be *recrystallization*. If in sub-melt processes the movement of the atoms is purely based on diffusion, this is called *sintering*. A related term is *annealing*, which is often used for steel and describes the formation or rearrangement of certain phases within the materials. Annealing can also refer to curing crystal defects which often requires only a few hundred degrees. In the following sections the applicability of these terms to the process studied in this work will be discussed.

The present thin films are deposited on flexible organic substrates, such as polyimides, which are sensitive to high temperatures. A possible compromise to limit the thermal stress for the substrate while on the same time reaching sufficiently high temperatures in the thin film are pulsed excitations. High intensity flash lamps or pulsed lasers can be used to optically heat the film by the absorption of light in the film. Lasers are especially attractive because their use would also allow to simultaneously write electronic structures into the material.[Chr00, Reg07, Mit11]

The use of light for heating restricts the material's thickness due to the finite absorption depth. For bulk materials a homogeneous heating also within the sample can be reached by the use of Joule heating. Dissipation due to the initially high resistance of uncompacted powder in combination with pressure leads to dense bulk material.

In the following two methods, namely short pulse laser-sintering of thin films of NPs and Current-Activated Pressure-Assisted Densification (CAPAD) for bulk samples are discussed and experimental details for the processes used in this work are given. The subsequent sections concentrate on the relation of morphology and electrical conductivity of material obtained by these methods.

5.1. Pulsed Laser-Sintering of Nanoparticle Films to Fabricate Thin Film Materials

This section covers the most important aspects of the sintering Si or Ge NPs by a high intensity short pulse laser. After an introduction to experimental details, the section will put special emphasis on the evolvement of the thin film morphology during sintering and its effect on electrical conduction.

5.1.1. Experimental Setup and Sintering Procedure

After deposition and HF treatment of the as-deposited NP thin films on a substrate the samples are transferred into a vacuum chamber, typically within less than 5 min. This ensures that oxidation of the particles is limited. The chamber is pumped to a pressure of less than 10^{-5} mbar, which takes approximately 10 min. After that, the laser-sintering takes place by illuminating the samples through a borosilicate window of the vacuum chamber.

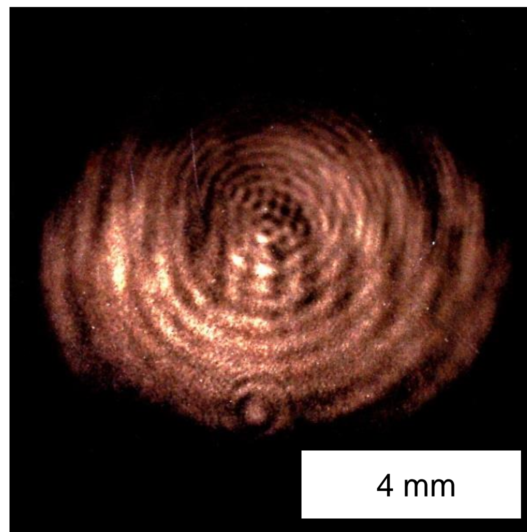

Figure 5.1. Shot image of the sinter laser: A photographic paper was exposed to the sinter laser operated at $\lambda = 532\,\text{nm}$ at a fluence low enough to visualize the intensity variations.

The system used to treat as-deposited or as-etched NPs thin films is a Quanta Ray GCR 230 Nd:YAG laser, which operates at the fundamental wavelength of $\lambda = 1064\,\text{nm}$. The duration of the Q-switched pulses is 5-8 ns. For convenience a frequency doubled operation at te visible $\lambda = 532\,\text{nm}$ is preferred, since no marked difference on sintering either Si or Ge NPs was observed compared to the fundamental wavelength. An image of the laser beam for operation at $\lambda = 532\,\text{nm}$ is shown in Fig. 5.1. The system is capable of a fluence, i. e., energy per shot and area, of $F = 650\,\text{mJ/cm}^2$, which is monitored by coupling out some percent of the beam to a bolometer and which can be reduced by limiting the power of the flash lamps pumping the Nd:YAG rod. Spatial inhomogeneities are caused by the long coherence length of the laser, which prohibits any reasonable attempt to obtain a homogenized spot. Such inhomogeneities of the spot are visible in Fig. 5.1 and of course are detrimental for the performance of the final thin films. Thus, the sample is illuminated not once but several times in sequence, while the sample is moved beneath the laser spot. With a typical velocity of 0.5 mm/s and a shot repetition rate of 10 Hz the beam of 8 mm diameter illuminates each position on the sample approximately 160 times. By this, at least in one dimension the inhomogeneity with respect to the so-called sinter-direction can be reduced substantially. With the energy density being highest in the beam center, the local fluence first rises in magnitude for the first 80 shots and then decreases again for the last 80 shots. For the hydrogen-terminated NPs used here this is advantageous, because shots with low fluence first drive out the hydrogen slowly, so that for the shots with maximum fluence no hydrogen gas is cast out. This would otherwise lead to ruptures of the film.[Len01, Lec09] In the following the fluences states for a certain experiment need to be understood as averaged over the total area of the beam, whereas the local fluence may deviate from that value.

Although the laser pulses are only some ns long, the temperature of the film is

increased for a much longer time. Experiments on laser-crystallizing thin films of a-Si:H on quartz substrates reveal typical times of 300 ns for this type of sample.[Sch96] For the loosely deposited NP films here, this time scale is probably increased up to µs due to the less dense material and a higher thermal resistance to the polyimid substrates.

5.1.2. Thin Film Morphology and its Dependence on the Laser Fluence

The Evolvement of a Meander Structure

As a representative example, the effect of short pulse laser treatment of Ge NPs on the morphology of the films obtained shall first be discussed. The films are 300 nm thick and the NPs are undoped with a mean diameter of 27 nm. An SEM micrograph of an as-deposited film is shown in Fig. 5.2 in the first panel indicated by $0\,\mathrm{mJ/cm^2}$. As already discussed in Sec. 4.4 the film is not densely packed and exhibits some larger pores. Increasing the sinter fluence the light is absorbed by the NP film and heats it. The value from the literature for the absorption coefficient of bulk Ge is $\alpha_{\mathrm{Ge}} = 63 \times 10^4\,\mathrm{cm^{-1}}$.[Hum89] According to the Lambert-Beer law the majority of the heat is introduced near the film surface. In the panel indicated by $9\,\mathrm{mJ/cm^2}$ a slight coalescence of the NPs can already be observed. The very surface is slightly compacted without substantial grain growth. For $F = 17\,\mathrm{mJ/cm^2}$, the surface layer of the film already exhibits a characteristic structure, which will be called *meander structure* or *meander network* in the following discussion. This remarkable self-organized morphologic feature is characteristic for all laser-sintered NP films in this work. It consisting of grains which are larger than the initial NPs. Beneath the meanders still unsintered NPs occur. Increasing the fluence, the size of the meander structure grows. The characteristic structure size, which can for example be defined as the width of the narrow constriction, steadily increases with F. The meander structure reaches down to the substrate for $F \gtrsim 50\,\mathrm{mJ/cm^2}$. Now all the material contributes to the electrical conduction by being part of the meander network, so that this fluence is typically used in this thesis. For $F \gtrsim 100\,\mathrm{mJ/cm^2}$ the meander structure disintegrates so that no percolating path across the substrate can be found anymore.

The evolvement of the effectively two-dimensional meander network and the growth of the structures with increasing laser fluence is not only observed for the Ge NPs discussed in Fig.5.2. Very similar behavior is found for films of Si NPs and for SiGe alloy NPs of any composition and even for composite powder of Si and Ge NPs. Of course the different absorption coefficient and the different melting temperature of these materials changes the fluence for which a certain morphology is observed.

Though the morphology discussed above is probably not expected a priori, the characteristic network formed by the laser-sintered NP film is not unique. Very similar structures have been reported in the literature, many of them in the context of (pulsed) laser-sintering.[Pen04, Her07, Kam10, Zha10, Lee11b, Beh12, Pen12, Pae14] Naively, one would probably expect a simple compaction of the present NP film with increasing fluence, so that the observed film thickness decreases. For a high fluence a dense, non-

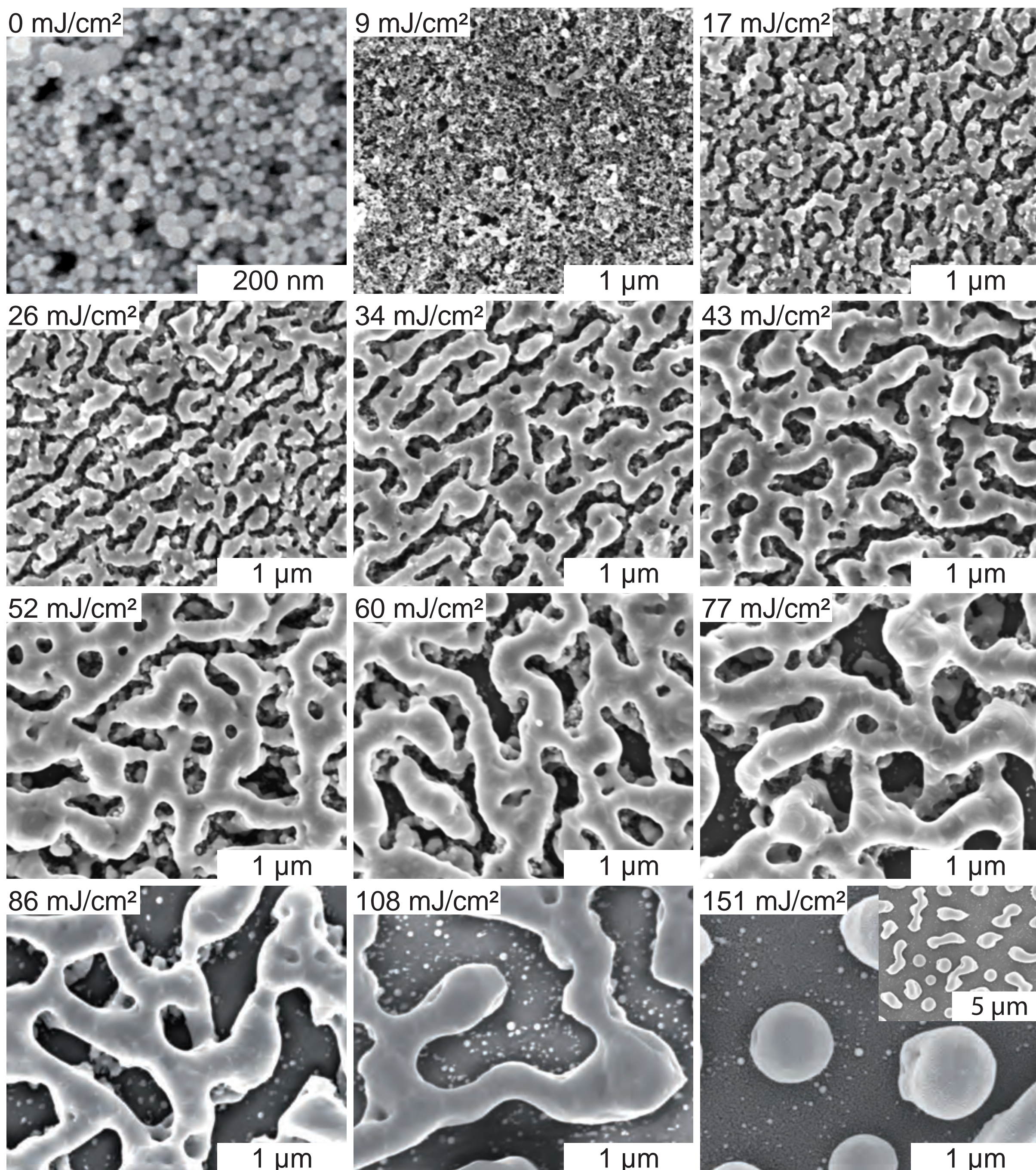

Figure 5.2. Dependence of the morphology of laser-sintered NP films on the laser fluence: This series of Scanning Electron Microscopy (SEM) micrographs shows the morphology of laser-sintered Ge NP films for increasing sinter laser fluence F. Details are discussed in the text.

porous film covering the substrate planely may be the final state in this way of thinking. However, this is not the case, because this picture neglects the inhomogeneous temperature distribution across the depth of the film and, most importantly, the effect of surface

tension, which drives every system to minimize the surface energy.[1] Assuming that the uppermost NPs melt, their surface energy should be around 0.6 J/m^2 for Ge and around 0.7 J/m^2 for Si.[Kec53, Mil08, Eus13] Depending on the crystal orientation, solid Ge has a surface tension between 1.3 J/m^2 and 1.845 J/m^2, and solid Si between 1.51 J/m^2 and 2.13 J/m^2. Thus, molten layers of NPs should theoretically wet the solid unsintered NPs beneath them to minimize the total surface energy. However, the unsintered particles of only a few nm in diameter constitute an effective surface of a high roughness, which leads to a dewetting of the molten parts on the unsintered NPs.[Qué08] If the meanders reach down to the substrate, the low surface energy of polyimid of only 0.043 J/m^2 again prohibits wetting.[Woh09] Thus, the molten material forms tubular structures within the short time it is mobile.

Non-porous films can be obtained using a Si wafer as a substrate and applying very high fluences. For oxide free NP films the above mentioned argument holds and liquid Si spreads homogeneously across the solid substrate. This technique is nowadays used to form very thin heavily doped contacts on solar cells or high power electronics.[Beh12, Mes13] One of the advantages is that the total thermal budget introduced by pulsed laser treatment is low compared to other techniques.

Limits to the Film Thickness

The samples discussed in the context of Fig. 5.2 were prepared from a single larger sample of as-deposited Ge NPs, so that the initial film thickness was identical for all smaller samples. The thickness of the unsintered film is of course important for the final thickness of the laser-sintered film, but cannot be varied without limits, as it is shown in the photographs of samples with varying initial film thickness and varying sinter laser fluence in Fig. 5.3. The films of Si NPs have an identical thickness in each row of the figure and were sintered with identical fluences in each column. The evolvement of the meander structure occurs at higher fluence for Si compared to Ge, thus, the samples sintered with 65 mJ/cm^2 still appear in red, which is caused by the polyimid substrate used. For all film thicknesses, sintering with 75 mJ/cm^2 leads to closed films which shine metallically. This is correlated with the evolvement of the meander structure, consisting of larger grains and having optical properties similar to bulk Si. For the thinnest film the fluence can be increased up to approximately 120 mJ/cm^2, until during the sintering process flakes peel off the substrate. Further increasing the fluence lowers the film adhesion even more. The observed delamination of the laser-sintered film occurs at already much lower fluence for thicker films, as can be observed for the second row in Fig. 5.3. Interestingly, for very thick films this trend is inverted and peeling off occurs at higher fluences again. As discussed above increasing the fluence is accompanied by an increase of the structure size, so that it may be desirable to sinter the NPs with a certain fluence. If this is not compatible with the film thickness, the samples cannot be used for

1 Surface tension and surface energy are identical quantities, although defined differently. Old units of 1 $dynes/cm = 10^{-5}$ N/m and 1 $erg/cm^2 = 10^{-3}$ J/m^2, respectively are often used in the literature.

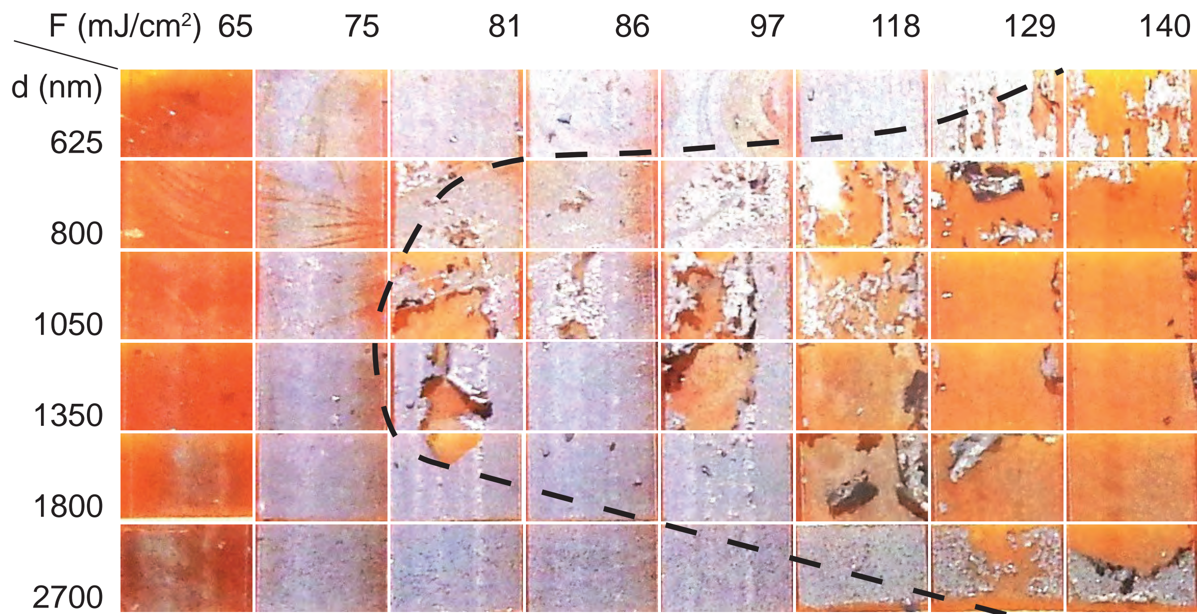

Figure 5.3. Delamination of films during laser-sintering: Each row are samples cut from the same substrate with Si NP films having the same thickness d and each column are samples laser-sintered with the same laser fluence F. The polyimid substrate appears in red. The dashed line marks the approximate transition of films showing no delamination to films exhibiting cracks and severe delamination.

application.

The reason for the behavior observed in Fig. 5.3 most likely is the thermal gradient between the surface of the film during sintering (hot) and the deeper regions of the substrate or unsintered NPs (cold). The thinner the film, the more homogeneous the temperature of the film, so that the remaining stress is small after solidification of the meander structure. The thickest films in Fig. 5.3 are less prone to cracking and delamination because the thermal stress is released into the underlying film of NPs, which act as a kind of ball bearing.

There is an alternative to increasing the final film thickness by increasing the initial film thickness. Therefore in a first step an optimized layer with respect to the film thickness, the fluence and, hence, the meander structure size is deposited. Then, a second film of NPs is spin-coated onto the already sintered film. Repeating all fabrication steps of HF-etching and sintering leads to the formation of thicker films. Figure 5.4 compares the results of depositing and sintering a single layer of Si NPs in panel (a) and of three such layers in panel (b). To more clearly depict the morphology the samples were cut by a Focussed Ion Beam (FIB) and the cross-cuts are viewed under an angle 54°. The typical meander structure can be seen for the single layer, which covers the substrate to approximately 60 %. For many applications the fill factor of the thin film needs to be higher, so that filling the remaining pores would be desirable. The single layer shown in panel (b) is effectively a two-dimensional material. In 2-D, the percolation threshold

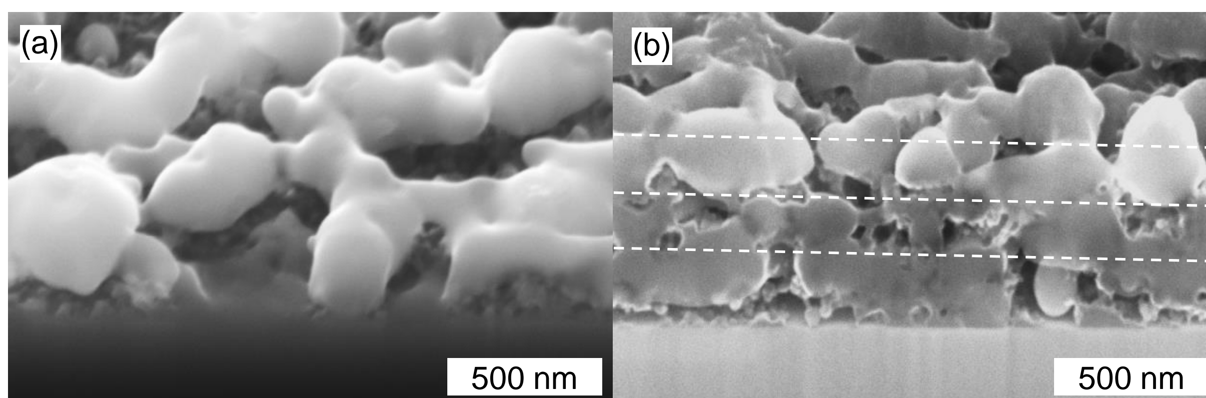

Figure 5.4. Tilted angle SEM view of a laser-sintered NP film: In panel (a) a single layer of Si NPs was deposited and laser-sintered. In panel (b) three cycles of NP deposition, HF-etching and laser-sintering were conducted sequentially.

for in-plane conduction is between 50 % and 64 %,[Las71, Kir73, Win81] which is very near the value of the surface coverage observed for the laser-sintered films in this work. Thus, the conduction in the plane can be expected to be limited by percolation to a large extent, as will be discussed in detail in Sec. 5.1.4. The morphology of a triple-layer is shown in panel (b). The approximate junction of the different layers are indicated by dashed lines. Indeed, the coverage of the substrate is greatly enhanced and the total film is thicker compared to a single layer. Also connections between the layers have formed. Current can now also bypass dead-ends, so that the percolation should increase. In three dimensions the percolation threshold is only 15 %. The fill factor in panel (b), however, is much higher, approximately 80 %, so that the conductivity is reduced to only roughly 90 % compared to complete filling. Thus, the trend of the material in panel (b) towards three dimensions helps to overcome the deficiencies of a single layer. Still, the material is highly porous and the typical structure size of the meanders is not changed compared to panel (a).

Despite the expected improved performance of the multi-layer approach the following experiments are performed depositing only single layers, first, because optimizing the stability of multi-layers requires significant engineering effort, and second, because many physical properties are the same for single and multiple layers.

Insight into the Grain Structure of Laser-Sintered Nanoparticle Films

In the previous discussions of this section only the outer appearance of the meander structure was covered. In the following also the substructure of the grains that form during laser-sintering will be investigated, concentrating on films sintered with an optimal fluence. In this context optimal means that the meander structure is fully developed and the meander reach down to the substrate.

To first estimate the degree of grain growth initiated by the sintering process, SEM micrographs of a film of unsintered NPs and of a detail of a sintered film are shown in

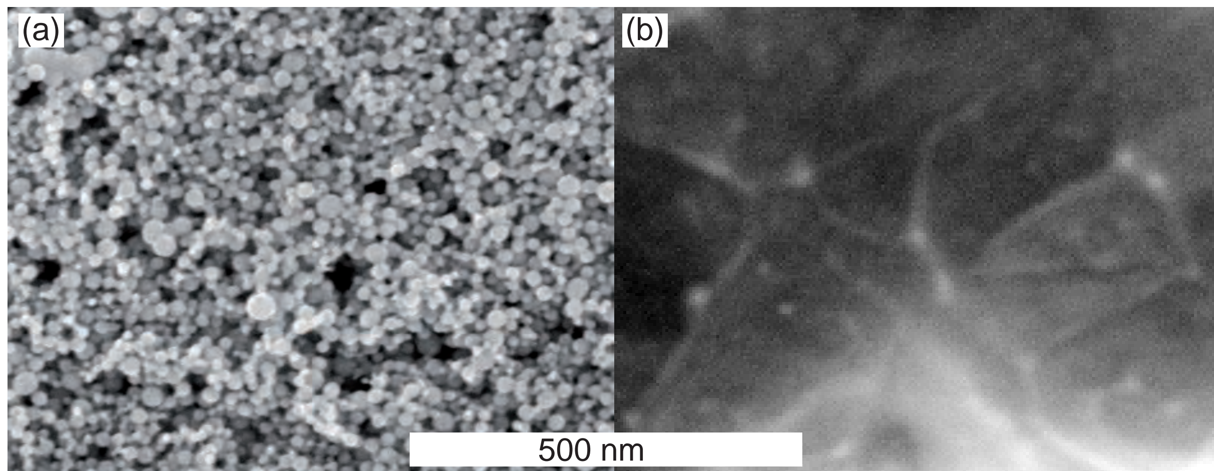

Figure 5.5. Grain growth induced by laser-sintering: Comparison of a Ge NP film (a) before and (b) after laser-sintering. For both SEM micrographs the same magnification is used.

Fig. 5.5 using the same scale bar for better comparison. As obvious from panel (b), within the meanders the material is dense and consists of several grains, visible by the white grain boundaries in the micrograph, which are much larger than the initial NPs. The common scale bar used in the SEM micrographs allows to estimate that one grain in a sintered meander consists of 10^2 to 10^4 initial NPs. The substantial grain growth as well as the apparent density of the material after laser-sintering suggests a complete melting of the deposited NPs, rather than a diffusion-based sintering. However, sintering is observed for lower laser fluence, so that the term used to describe the fabrication process cannot be determined without explicitly stating the fluence. For the sake of convenience, however, the term *laser-sintering* will be used throughout the rest of this work.

Apart from the growth of larger grains, also some point-like white structures of approximately the size of the initial NPs are visible in Fig. 5.5, both, at the grain boundaries as well as within the grains. From this top-view SEM micrograph it cannot be concluded whether these structures are initial unsintered NPs, which survive the sintering process, or oxidic precipitates, which would appear white in SEM.

A more suitable possibility of investigating the inner structure of the grains is to cut a thin lamella of the sample by FIB and to investigate it by Scanning Transmission Electron Microscopy (STEM). Several selected micrographs of such a lamella, cut from a laser-sintered film of $Si_{80}Ge_{20}$ NPs, are shown in five panels in Fig. 5.6. The cross-cut meander in panel (a) consists of three grains, separated by grain boundaries. As one example, such a grain boundary is indicated by the dashed line. In STEM the gray scale can be caused in principle by a locally different Si/Ge composition or by channeling effects caused by the different crystal orientations of the grains with respect to each other. Using different quadrants of the dark field image it was cross-checked that in Fig. 5.6 the gray scale indeed is caused by different crystal orientations. The object in panel (b) shows another interesting feature. Indicated by the dashed circle a couple of small objects of approximately the size of the initial NPs can be observed within

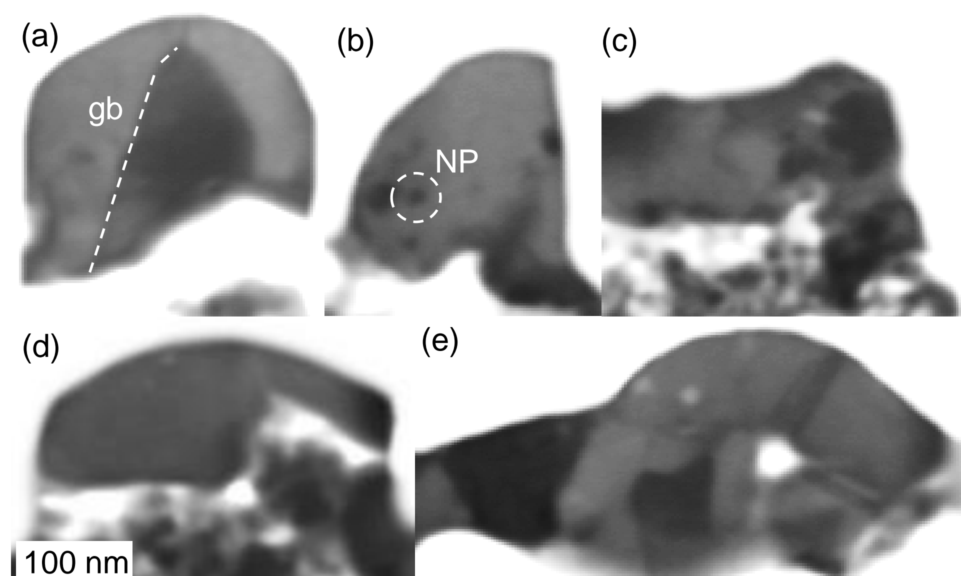

Figure 5.6. STEM micrographs of laser-sintered SiGe NP film: The micrographs show cross-cut lamellas of selected areas of a laser-sintered $Si_{80}Ge_{20}$ NP film. The dashed line in panel (a) marks a grain boundary (gb), the dashed circle in panel (b) indicates a NP surviving the laser-sintering process. In panel (c) and (d) unsintered NPs lay beneath the sintered meanders. The gray scale of the grains is caused by a different orientation of the crystal lattice with respect to the probe electron beam.

the grain. These inclusions are most likely NPs that did not take part in the sintering process and were incorporated into the meander structure. Energy-Dispersive X-ray spectroscopy measurements of this lamella during TEM investigations did not show an enhanced oxygen content in these structures. The micrographs in panel (c) to (e) further confirm that the meanders are composed of smaller grains. Especially in panel (c) and (d) beneath the larger meanders the underlying unsintered NPs can be seen.

Effective Film Thickness

From the micrographs in Fig. 5.5 and Fig. 5.6 a considerable height corrugation of the films can be concluded. Although the deposited film of NPs is very homogeneous in thickness [Lec09], the surface tension of the molten material leads to an uneven height of the resulting meanders. In most of this work the thickness of the resulting film is interpreted as the maximum height above the substrate, as it is measured by profilometry using probe needles with a tip diameter of 3 μm, although, the effective height that is relevant, e. g., to calculate the specific conductivity from the resistance is smaller. This fact will be of importance for the discussion of electrical and thermal properties of the sintered films.

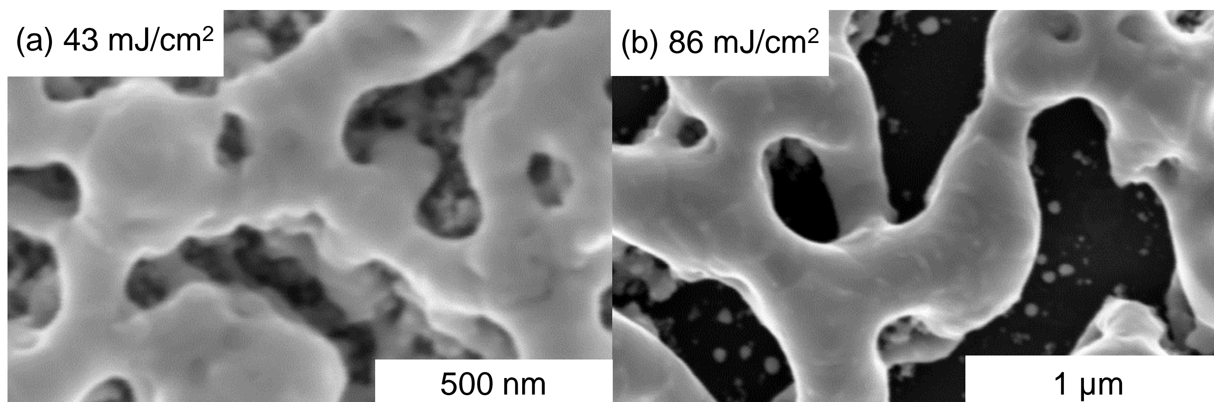

Figure 5.7. Similarity of the meander structure for different laser fluence: The laser-sintered Ge NP film in panel (a), sintered with 43 mJ/cm^2, exhibits meanders which look similar to those on a film sintered with 86 mJ/cm^2. The structure sizes of the latter is roughly twice as large as of the first.

Similarity of Structures Sintered with Different Fluences

In the following the growth of the meander structures with respect to the sinter fluence will be discussed. It is a remarkable feature of the SEM micrographs in Fig. 5.2 that as soon as this characteristic morphology is developed, the general appearance is similar for all sinter fluences, only the size of the structures depends on the fluence. The structures are similar in the sense that the diameter of the meanders, the width of necks and the size of the pores between the meanders grow in an identical manner. This observation can be confirmed by comparing two SEM micrographs using an adapted magnification. Such a comparison is shown in Fig. 5.7. In panel (a) a detail of a structure laser-sintered with a fluence of 43 mJ/cm^2 is shown. In panel (b) the corresponding structure, sintered with twice the fluence, is shown. The scale bar in panel (b) is similarly long as compared to panel (a), but represents a length of 1 µm in contrast to 500 nm in panel (a). In the images the structures look very similar regarding the diameter of the meanders, the pores and the necks between meander nodes, so that doubling the sinter fluence seems to double the characteristic structure size of the resulting film.

This conjecture is verified by the data shown in Fig. 5.8, where the characteristic structure size is plotted versus the sinter laser fluence. Here, the structure size is defined as the diameter of necks between meander nodes, as shown in the inset of the figure. Each data point is an average of at least 15 measurements per structure, taken from SEM images. The dashed line is a fit of the data and illustrates the linear growth of the meander structure with the sinter laser fluence. Although only shown for Ge NPs in Fig. 5.8, this behavior is also observed for Si and SiGe NPs as well.

In Fig. 5.8 the structure size ranges from 100 nm to more than 500 nm. This makes it hard to categorize the structures either as nano-, micro- or macro-scale. As most of the features are larger than atomic distances or even the initial NPs, but smaller than length scales which are relevant for phenomena in the macro-world, such as e. g. convection, a

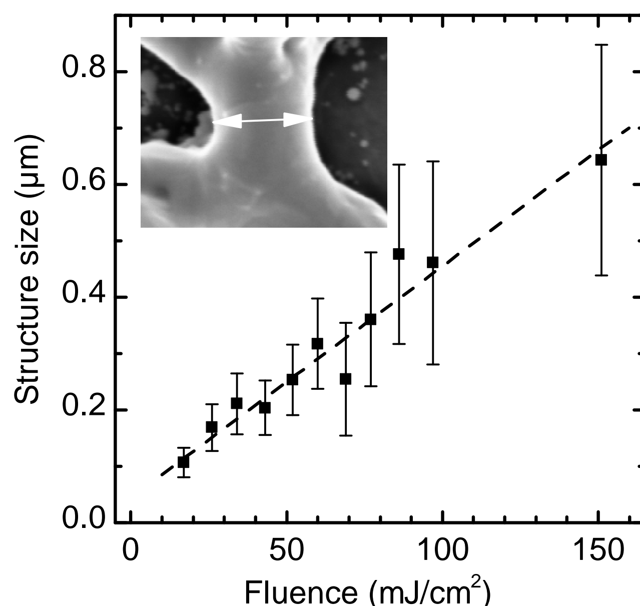

Figure 5.8. Influence of laser-sintering on the structure size of undoped Ge NP films: The structure size, in this case defined as the width of the necks between two meander nodes as depicted in the inset, grows linearly with the sinter laser fluence.

probably suitable term to describe the meander structure is mesoporous.

The observance of meander structures has already been discussed to be caused by surface tension effects. To explain the dependence of the meander size on the laser fluence, transient effects need to be taken into account. The higher the fluence, the higher the energy deposited in the material, so that the melt is hotter at the end of the laser pulse is higher. Thus, it takes a longer time for the melt to solidify and the surface tension can act longer to minimize the total surface energy, resulting in larger structures.

5.1.3. Laser-Sintering Nanoparticle Films and its Effect on the Electrical In-Plane Conductivity

As discussed in Chap. 2, for thermoelectric materials the electrical conductivity is a major parameter in the conversion efficiency. Here, in this section, the effect of the meander structure's incomplete substrate coverage on the electrical in-plane conductivity σ is discussed. The conductivity here is defined as the effective macroscopic in-plane conductivity at ambient conditions. Effective means that the maximum height h of the meander structure, measured from the substrate, enters Eq. 3.1.

As a representative example, σ of the samples already discussed in the context of Fig. 5.8 is shown in Fig. 5.9. Since these Ge NPs are not doped the change of σ with the laser fluence should mostly originate from morphologic effects, such as the evolvement of the meander structure.[2] The conductivity of the film of as-deposited NPs is

2 For doped NPs the lifting of dopant deactivation in the NPs may also increase σ with laser-sintering.

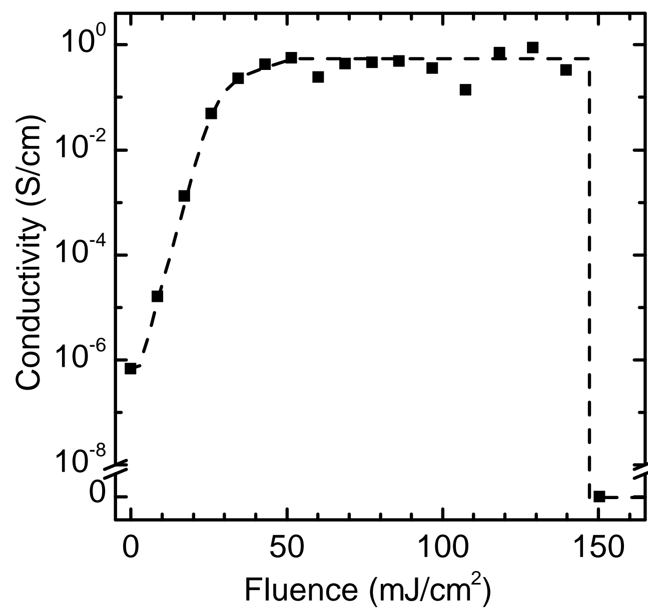

Figure 5.9. Influence of laser-sintering of undoped Ge NP on the electrical in-plane conductivity: For the samples also discussed in Fig. 5.8 the effective macroscopic conductivity σ is shown versus the sinter laser fluence in a semi-logarithmic plot.

$\sigma = 10^{-6}\,\mathrm{S/cm}$. Already lowest fluences of $9\,\mathrm{mJ/cm^2}$ give rise to an increase of the conductivity by an order of magnitude, although in the SEM micrograph in Fig. 5.2 hardly any change of the morphology is visible. However, such a low fluence most likely leads to real sintering of neighboring NPs with the formation of necks. With the onset of meander formation σ rises further rapidly, in an approximately exponential manner, with increasing fluence. As soon as the meander network at the sample surface is well connected for a fluence of approximately $34\,\mathrm{mJ/cm^2}$ the conductivity reaches a value of $0.5\,\mathrm{S/cm}$, which is 5 to 6 orders of magnitude higher compared to the unsintered film. With further increased fluence, however, the conductivity is rather constant. This plateau of σ persists up to a fluence of $140\,\mathrm{mJ/cm^2}$, where the conductivity breaks down suddenly. As is also obvious from the last SEM micrograph in Fig. 5.2, no percolating path for in-plane conduction exists any more.

It is remarkable to see that between $30\,\mathrm{mJ/cm^2}$ and $140\,\mathrm{mJ/cm^2}$ the structure size steadily increases, as shown in Fig. 5.8, while the electrical conductivity stays rather constant. This behavior originates from the similarity of the morphology for different fluences, as discussed in the context of Fig. 5.7. In Eq. 3.1 the quotient $\frac{l}{w}$ is independent of the fluence, so that the constant macroscopic effective conductivity suggests a microscopic conductivity of the grainy structure which is also independent of the fluence.

In view of thermoelectric applications, this independence of electrical conductivity and morphology is promising, because it allows the independent optimization of the two, in particular allowing to tune the thermal conductivity κ by selecting the structure size.[Son04, Yu10, Hop11, Dec12] In many of the following experiments the samples are

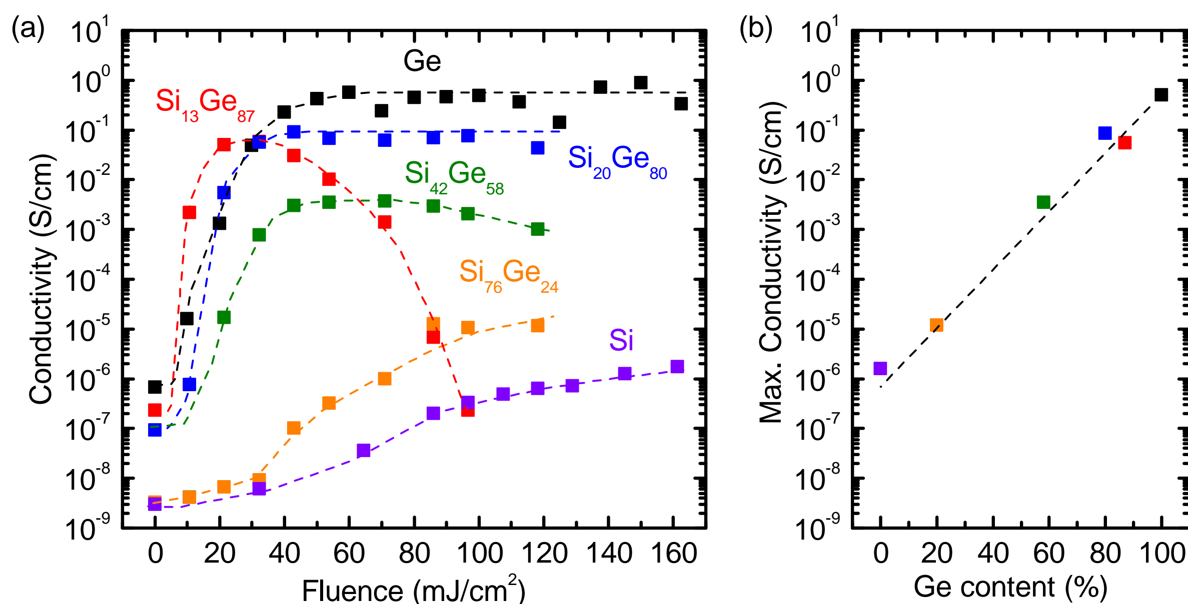

Figure 5.10. Series of laser-sintered undoped SiGe alloy NP films with varying sinter fluence: In panel (a) the electrical conductivity of NP films for compositions ranging from pure Ge to pure Si are shown versus the sinter fluence. Panel (b) shows the maximum electrical conductivity depending on the Ge content of the used NPs.

prepared to maximize the electrical conductivity while still limiting the grain growth. Thus, in the example of Ge, typically a fluence slightly higher than that necessary to reach the plateau in Fig. 5.9, i. e., 50 mJ/cm^2, are used for laser-sintering.

A similar dependence of the effective in-plane electrical conductivity on the sinter laser fluence is observed for Si and SiGe materials as well. Using exclusively undoped NPs, the results obtained for the whole range of available alloy NPs are summarized in Fig. 5.10. For as-deposited films the conductivity decreases with increasing Si content of the NPs. One of the reasons for that is the larger bandgap of Si-rich alloys.[Joh54, Lev55] For all alloy compositions, the conductivity increases with laser-sintering. However, the increase occurs at lower fluences for Ge-rich alloys compared to Si-rich alloys. Two facts account for that. First, the optical absorption coefficient for light with $\lambda = 532$ nm is higher for Ge, so that Si NP films transmit part of the impinging power. Second, and more importantly, the melting temperature of Si is 1687 K compared to 1211 K for Ge.[Thu53] Thus, a higher fluence is needed for Si-rich materials to rise the temperature above that required for neck formation or the evolvement of the meander structure. In general, all materials exhibit a plateau of the conductivity. The $Si_{13}Ge_{87}$ films, however, show an early decrease of σ without having a plateau. In this specific case, the films were too thin to allow a continuous growth of the meanders. Instead, dewetting occurred already at low fluences which results in the decrease of σ. For all other materials sintered with a fluence at the beginning of the plateau, the morphology is similar, i. e., it consists of meander structures. The higher bandgap of Si is also partly responsible for the lower plateau conductivity of Si compared to Ge. Panel (b) shows the maximum electrical

conductivity at the plateau region versus the alloy composition. The extraordinary high conductivity of sintered Ge will again be part of the discussion of the thermoelectric properties in Sec. 6.2.

5.1.4. Current Paths Through the Meander Structure

Concerning in-plane electrical transport, the side view in Fig. 5.4 (a) suggests that the laser-sintered films should be regarded as effective two-dimensional networks. As already mentioned in the context of Fig. 5.4, an incomplete coverage of the substrate has severe consequences on the effective electrical conductivity. In Fig. 5.11 (a) the results of a theoretical calculation of the probability that there is a percolating path across a 2-D sample is plotted versus the coverage of the 2-D lattice.[Win81] In this specific example the lattice is a Voronoi lattice. The exact threshold values where percolation begins vary from 50 % to 65 %, depending on the lattice assumed. The dashed line marks the results which would be valid for an effective medium. In panel (b) the electrical conductivity is shown for the respective coverages. If the structures do not percolate, the sample

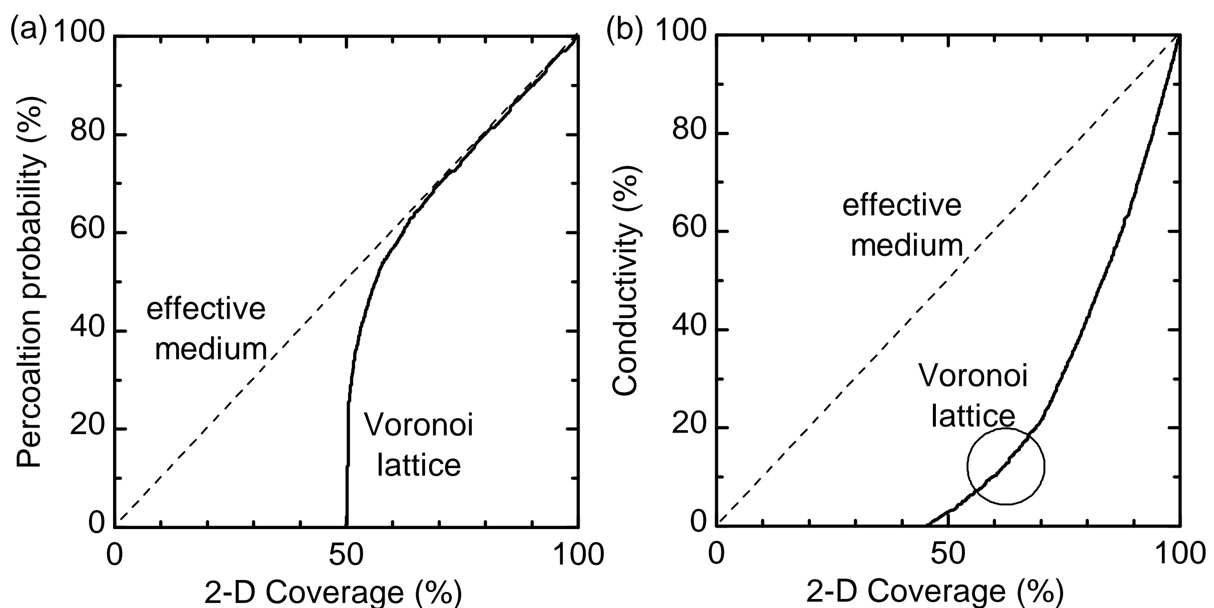

Figure 5.11. Relation of substrate coverage and effective conductivity for a two-dimensional percolating network: (a) For a Voronoi lattice the probability for percolation follows the solid line. The result for an effective medium approach is shown as dashed line. (b) The corresponding electrical conductivity of the Voronoi lattice is reduced compared to the effective medium. The circle marks the regime which is relevant for the meander structures of laser-sintered NP films. The data is reproduced from Ref. Win81.

is an insulator. As soon as the first percolation path opened, the sample begins to conduct. However, the conductivity rises only slowly first, because the probability for *one* percolating path is high, but still not many paths have formed. The circle marks the approximate region of 2-D coverage which is relevant for the laser-sintered structures

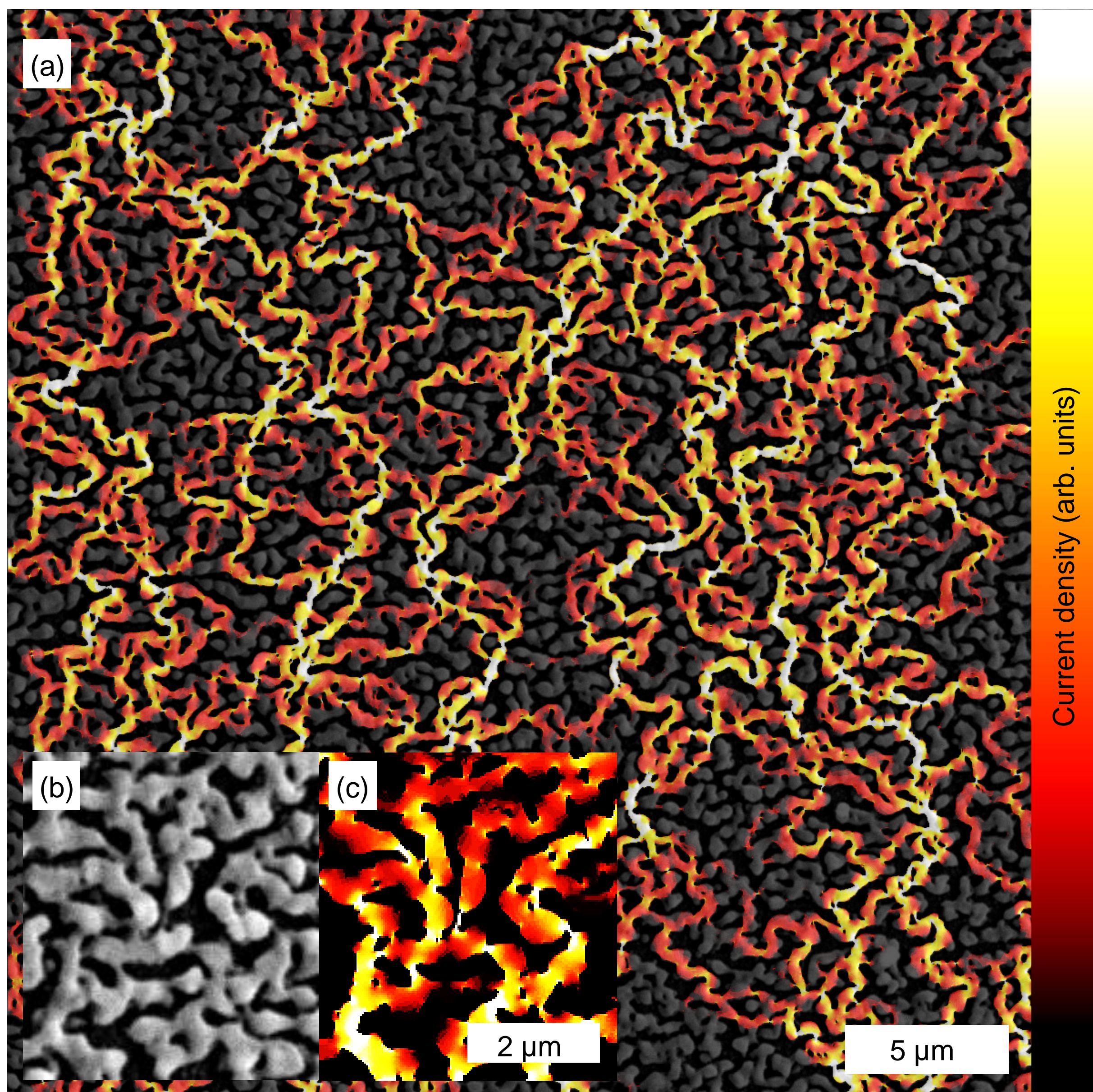

Figure 5.12. Color-coded current density through a laser-sintered NP film as obtained by numerical simulation: (a) An SEM micrograph of a laser-sintered film (background) was converted to a conductivity matrix filled only with conductive and non-conductive pixel. This resistor network was fed to a simulation which applied a bias between the top and the bottom line of the network representing the image. The resulting current density is shown semi-transparently overlaid on the SEM micrograph. A zoom-in of the structure and the corresponding current density is shown in panel (b) and (c), respectively.

discussed here. For a coverage below 70 % the conductivity is reduced at least by a factor of 5.

Although the lattice assumed in Fig. 5.11 is of course not reflected by the laser-sintered films, the general behavior of the conductivity is very similar. To test the

degree of reduced conductivity by the porous morphology a simulation based on a real sample was conducted. Therefore, an SEM micrograph was converted into a resistor network on a square lattice in which every pixel which is on the meander structure is set as conductive and every pixel belonging to the substrate or unsintered NPs is set as insulating. Assuming an external current passing from the top line to the bottom line of the network, the local potentials are calculated. The local current densities are then obtained from the corresponding potential differences.[Knu06] The result of this procedure is shown in Fig. 5.12 in a false color image. For comparison the original SEM image is shown semi-transparently in the background of the current density. The illustration shows that electrical conduction is mainly carried by a few percolating conduction paths. Some few nodes exist where the current density is extraordinary high. The insets (b) and (c) show a detail of the structure in the original SEM micrograph and the corresponding current density, respectively. In this example, the macroscopic conductivity is decreased by a factor of 14 compared to a fully conductive layer. Other simulations based on different SEM micrographs yielded a reduction of factors 3 to 15. On average, the meander structure reduces the effective macroscopic conductivity by one order of magnitude compared to the microscopic conductivity of the material. Having in mind the improved connectivity of multi-layers of laser-sintered NPs already shown in Fig. 5.4, such structures should have an effect on the electrical conductivity which exceeds the effect of simple addition of the conductivities of the respective individual layers.

5.1.5. Importance of HF Etching for the Morphology of Laser-Sintered Nanoparticle Films

As a last section in the discussion of laser-sintering NP layers for the fabrication of thin films, the importance of oxide removal prior to laser-sintering shall be demonstrated in an example. Section 4.2.1 argued in detail that as-deposited NPs exhibit an oxide shell, which is removed upon HF etching, rendering Si as well as Ge NPs hydrogen-terminated. To test the influence of oxide removal on the morphology of the sintered layers a sample of as-deposited Ge NPs was immersed only with the half of its area in a 5 % aqueous solution of HF. After that, the sample was sintered with a fluence of $60\,\mathrm{mJ/cm^2}$. Figure 5.13 (a) shows an optical micrograph of the sample. The left half was HF-etched, whereas the right half was not. The oxide free area exhibits a metallic appearance after laser-sintering, indicating optical properties similar to bulk Ge. The right halt appears brownish as if not sintered at all, much like the Ge sample in Fig. 4.4. Observing this sample region in panel (b) by SEM, the borderline is again clearly visible. In SEM, the oxidic part at the right part is much less conductive, as can be seen by the brighter appearance which is caused by charging effects. The zoom-in in panel (c) and (d) reveals the reason for this difference in conductivity. The oxide free NPs formed a much better connected network compared to the oxidic layer in panel (d), where the residual meander are rather isolated. It is remarkable that the structures contain

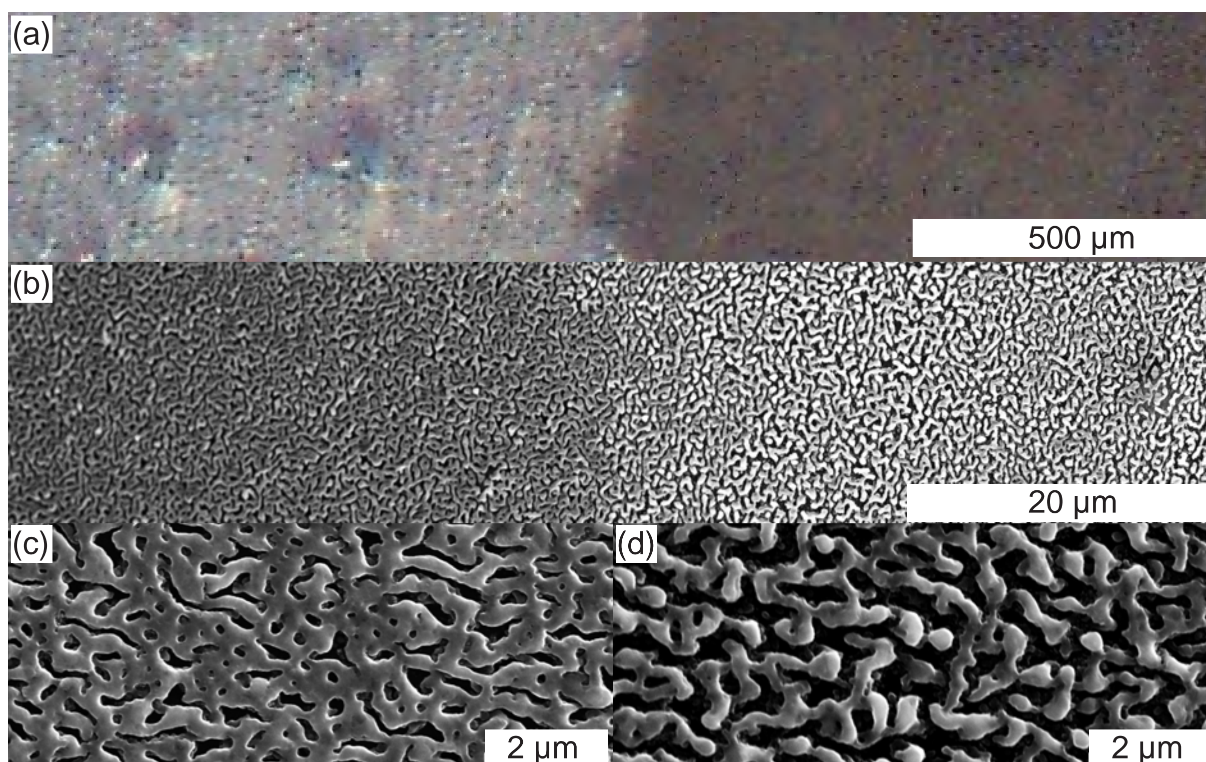

Figure 5.13. Importance of oxide removal for the evolvement of the meander structure by laser-sintering: (a) Optical micrograph of a laser-sintered Ge NP film. Prior to sintering, the left half of the film was dipped in hydrofluoric acid for oxide removal, whereas the right side was sintered as-deposited. The same is shown in panel (b) in an SEM image. Panel (c) and (d) show SEM images of higher magnification of the left and the right halfs of panel (b).

certain areas which appear whiter than neighboring parts of the meanders, although they are directly connected. A generally low conductivity cannot explain that. However, such features, which often are shaped like a dome, also result from laser-sintering at ambient conditions. Here, a locally high oxygen content can be presumed, which traps charges and leads to the enhanced signal in SEM investigations. Similar observations as discussed above can be found for Si NP films when residues of oxygen are present on the NPs surface. Concludingly, the fact that a NP layer is free of oxygen is of paramount importance for the formation of a well connected meander structure.[Beh12]

5.2. Current-Activated Pressure-Assisted Densification of Nanoparticles to Fabricate Bulk Materials

In this work several experiments are conducted on samples fabricated by Current-Activated Pressure-Assisted Densification (CAPAD), which have a fundamentally different morphology compared to the thin films obtained by laser-sintering. Within the collaboration with the University of Duisburg-Essen, the group of Gabi Schierning

provides these samples made from the same gas-phase synthesized NPs also used for the thin film approach. For this work, the CAPAD samples with their well investigated state-of-the-art thermoelectric properties serve as a benchmark for the laser-sintered films. Furthermore, the measurement equipment and techniques used in this work can be validated by comparison of the experimental results with those obtained on these reference samples in Duisburg using industrial metrology systems. This short section summarizes the synthesis method and the morphology of the samples obtained by CAPAD. Further, more detailed information, can be found in Refs. [Pet11, Sch11a, Ste11, Mes12, Sch14].

As sketched in Fig. 1.3, to obtain bulk-like samples via CAPAD the NPs powder is filled (often in ambient conditions) into a die around a punch and is precompacted by hand using the counter punch.[Gra09] The precompacted powder is inserted into an Spark Plasma Sintering (SPS) machine, which is then evacuated. The interior is heated to an increased temperature of, e. g., 1060 °C, to ease sintering. While still exerting a pressure of typically 10 to 100 MPa onto the sample by the punches, a dc-current is then injected from one punch through the powder to the other punch.[Sch11b] Joule heating due to the high electrical resistance of the powder heats it above the temperature needed for further compaction and sintering. As the sample is fully compacted to a density of up to 98 % of the theoretical maximum after a process time of typically several minutes, the sample is cooled down.[Pet11] Finally a typical sample can have dimensions of several mm in height and some cm in diameter.

The micrographs in Fig. 5.14 show the resulting morphology of the sintered samples on different length scales. In panel (a) elongated porous precipitates within the otherwise dense material can be seen. As investigated by EDX, these precipitates are rich in oxygen and, for the case of phosphorous-doped initial NPs, rich in phosphorus. Oxygen entered the process since the NPs were handled in air for precompaction. In this top view on a surface cut perpendicular to the direction of the sinter current, the disk-shaped precipitates look cigar-shaped. Simulations of the compaction process suggest the formation of such disk-shaped structures, which result in an incomplete compaction and which form morphological barriers for current and heat transport.[Sch11b, Sto14b] Concentrating on the almost pure silicon areas of panel (a), panel (b) shows a TEM micrograph of the grainy substructure. Compared to the initial NPs the grain growth is less pronounced as in the case of laser-sintering. Such areas as shown in panel (b) are almost perfectly dense and exhibit no holes. However, also these regions are not free of oxygen as can be seen in panel (c). The enhanced temperature during the process leads to a mobilization of the silicon oxide, which relocates at grain boundaries (larger structures 1) and also within grains (smaller structures 2). The silicon grains themselves are highly crystalline with well defined grain boundaries, as the high resolution TEM image in panel (d) demonstrates.

Interestingly, the dc current applied during sintering leads to a considerable asymmetry of the temperatures reached at the anode and the cathode side. The doped NPs typically used for thermoelectric materials exhibit the Peltier effect, introduced in Chap. 2, which carries heat from one end to the other. The different temperatures result

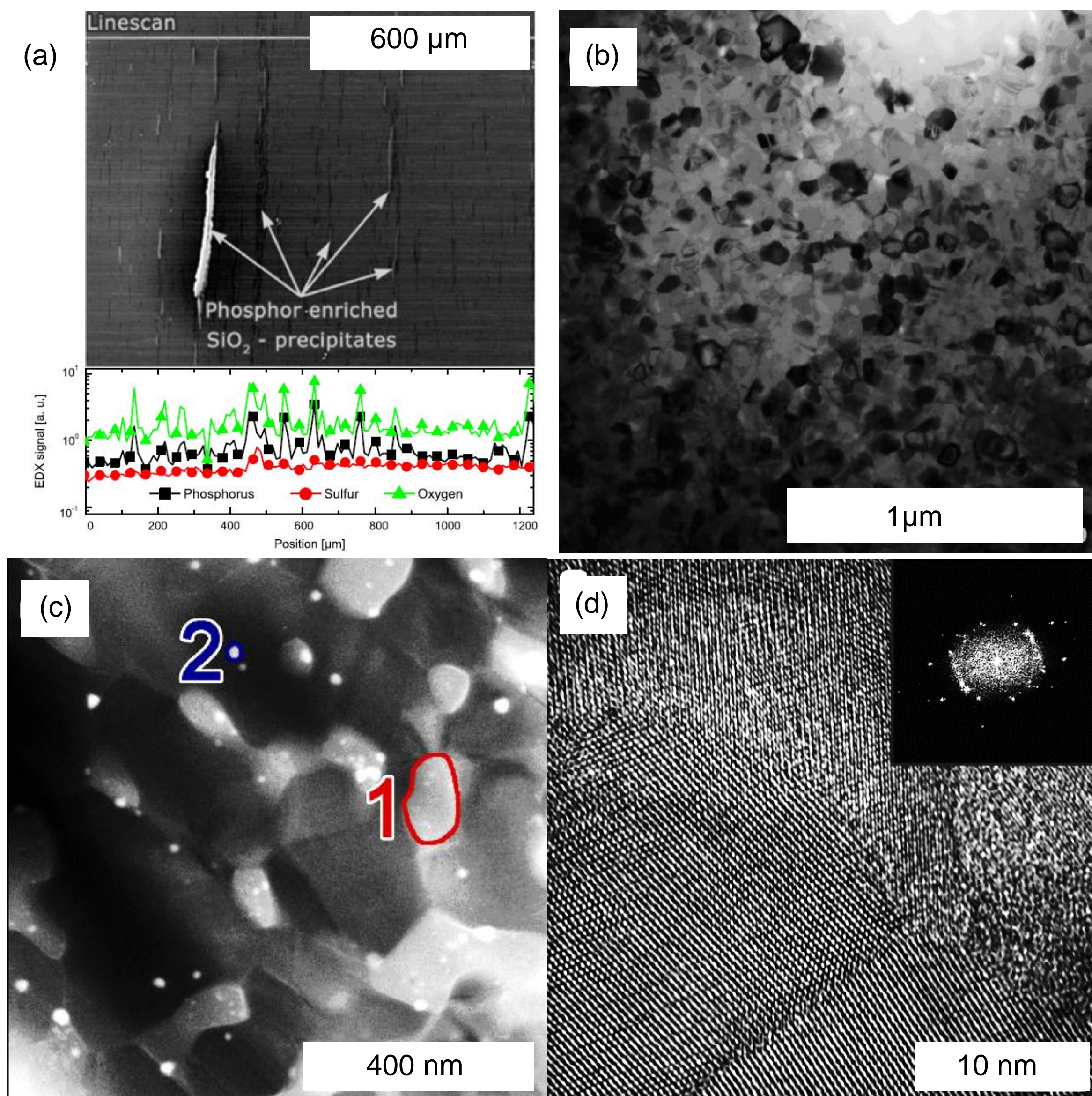

Figure 5.14. Morphology of bulk-nano-crystalline samples prepared by CAPAD: (a) SEM micrograph showing elongated precipitates which are rich in oxygen and phosphorus. (b) Bright field TEM image of the dense grainy structure. (c) Energy-filtered TEM micrograph discriminating silicon (dark) from silicon dioxide (bright). Different oxidic precipitates are marked with 1 and 2. (d) High resolution TEM image of the crystallinity of the grains. The micrographs are taken from Refs. Mes12 and Sch11a.

in different grades of compaction and grain sizes.[Bec12]

The terminology for the above mentioned process is subject of a decade-lasting controversy.[Gra09] Since analytical methods lack to characterize the powder during sintering, the interplay of current, temperature and pressure remains rather unclear. Other abbreviations used in this context are Current-Assisted Sintering (CAS), Spark-Plasma Sintering (SPS) or Electric Current Activated/Assisted Sintering (ECAS).

6 Thermoelectric Properties of Sintered Nanoparticles

In this chapter the macroscopic electrical conductivity σ and the Seebeck coefficient S of thin laser-sintered NanoParticle (NP) films are investigated. If not stated otherwise, the samples are laser-sintered with a fluence leading to a well connected meander structure, which results in a conductivity at the beginning of the plateau region as discussed in the context of Fig. 5.9 and Fig. 5.10.

The chapter starts with the thermoelectrical properties of undoped laser-sintered Si and Ge NP films. Then, digital B-doping is discussed for Si. Finally, SiGe alloy and composite NPs, which are heavily P-doped, are characterized and compared to bulk-nano-crystalline material, made from the same NPs.

6.1. Thermoelectricity of Laser-Sintered Undoped Si Nanoparticle Films

Undoped Si films are not relevant for thermoelectric applications, but they serve as a basis for the understanding of doped Si films. In Fig. 6.1 (a) the electrical conductivity of a laser-sintered undoped Si NP film is shown and plotted in an Arrhenius-type graph, i. e., σ vs. $1/T$. In such a graph a straight line indicates

$$\sigma \propto \exp\left(\frac{E_c - E_F}{k_B\, T}\right), \tag{6.1}$$

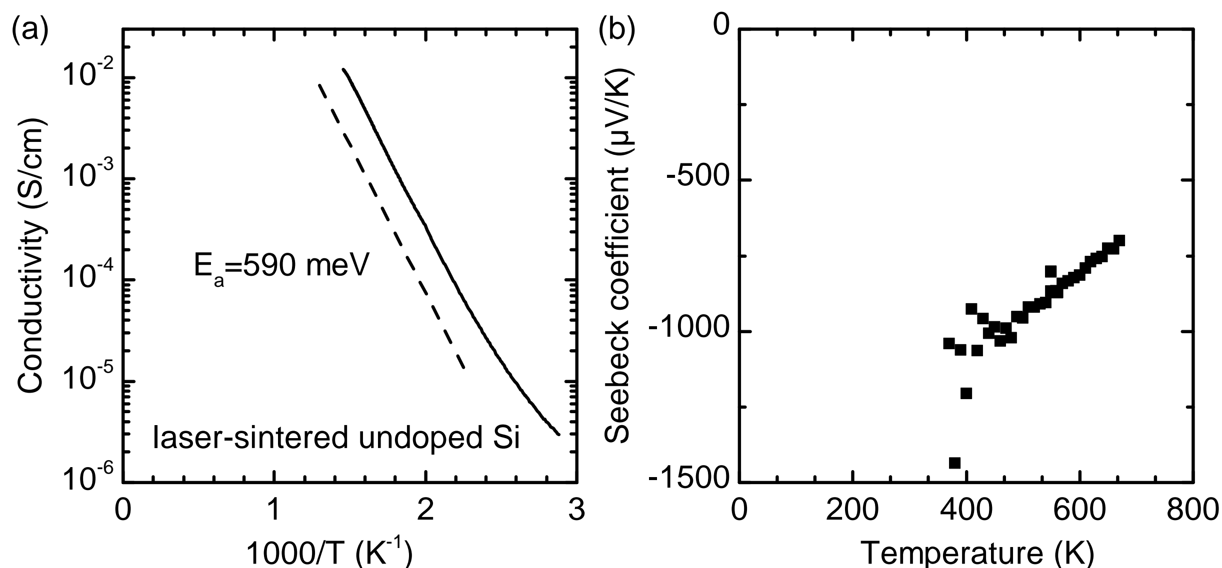

Figure 6.1. Thermoelectric properties of laser-sintered undoped Si NPs: In panel (a) the electrical conductivity is shown in an Arrhenius plot. The dashed line indicates a thermal activation energy of 590 meV. The Seebeck coefficient of this sample is shown in panel (b).

where k_B is the Boltzmann constant and $E_a = E_c - E_F$ is the thermal activation energy. In undoped Si the Fermi level is expected to be close to the middle of the bandgap, so that an activation energy of half of the bandgap energy should be measured. With a slope corresponding to $E_a = 590$ meV and an approximate bandgap of 1.1 eV, the data set in panel (a) confirms this notion.

The corresponding data set on the Seebeck coefficient is shown in Fig. 6.1 (b). Due to the higher mobility of electrons compared to holes the Seebeck coefficient is negative, according to Eq. 2.15. As expected for an intrinsic material and as predicted by Eq. 2.34, the Seebeck coefficient decreases in magnitude for higher temperatures. Compared to the dashed line in Fig. 2.7 (a) which approximately indicates intrinsic Si, the measured data in Fig. 6.1 (b) is in good agreement. From the above data it can be concluded that laser-sintered Si NP thin films behave very similar to bulk crystalline Si with respect to the qualitative behavior of the Seebeck coefficient and the electrical conductivity.

6.2. Thermoelectricity of Laser-Sintered Undoped Ge Nanoparticle Films

Similar to the properties discussed for Si, the electrical conductivity and the Seebeck coefficient of laser-sintered Ge NP films are discussed now.

Figure 6.2 (a) shows the electrical conductivity of a representative sample in an Arrhenius plot. In contrast to the Si data in the previous section, the data set here can be divided into two regions. For high temperatures, an activation energy of 260 meV

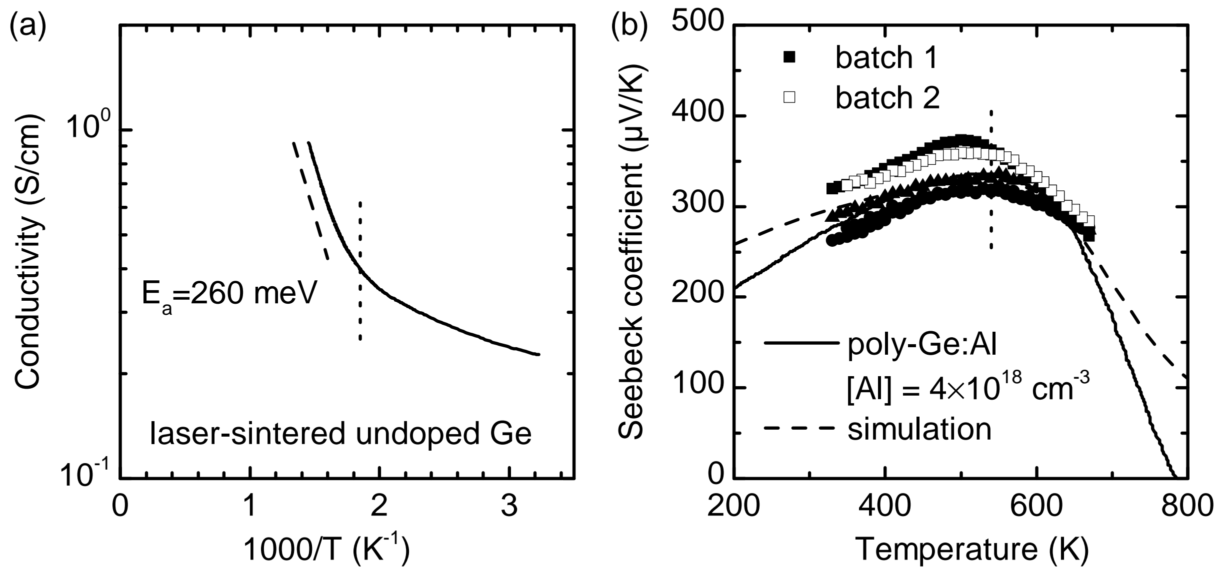

Figure 6.2. Thermoelectric properties of laser-sintered undoped Ge NPs: Arrhenius plot of a representative thin film of laser-sintered, nominally undoped Ge nanoparticles. In agreement with the Seebeck coefficient in panel (b), two regimes can be distinguished. The vertical dashed line indicates $T = 540\,\mathrm{K}$ in both panels. The identically prepared films in panel (b) are of two NP batches, closed symbols correspond to NP batch 1 and open symbols to batch 2. All samples have a positive Seebeck coefficient, rising with temperature for $T < 540\,\mathrm{K}$. Above that temperature the Seebeck coefficient of all samples decreases with increasing temperature. The data for poly-crystalline Ge is taken from Ref. Mid53.

can be deduced, which is again close to half of the bandgap of Ge, so that the material can be regarded as intrinsic there. However, for lower temperatures the conductivity is much higher compared to the thermally activated transport with the Fermi level in the middle of the band gap, as would be extrapolated from the high temperature data.

Correspondingly, the Seebeck coefficient, shown in panel (b), is also characterized by two transport regimes. For low temperatures, the Seebeck coefficient is positive and rises with temperature, whereas for higher temperatures the Seebeck coefficient decreases. To exclude spurious doping, several samples were prepared and even two different batches of undoped Ge NPs were used. These different samples in panel (b) vary only slightly and show the same characteristic behavior. The transition between those two regimes happens at approximately the same temperature in, both, the conductivity and the Seebeck data. The vertical dashed lines in both panels indicate a temperature of 540 K.

The following model is able to explain the observed transport data: The sintered film consists of grains which are separated by grain boundaries. Those grain boundaries contain unsaturated bonds. According to the literature, the dangling bond level in Ge is in the vicinity of the valence band, either some tens of meV above or even below the valence band edge.[Bro08, Kuz09, Bro10, Bro12, Web13] Both Weber at al. and Broqvist et al. provide results from super cell simulations but use slightly different functionals

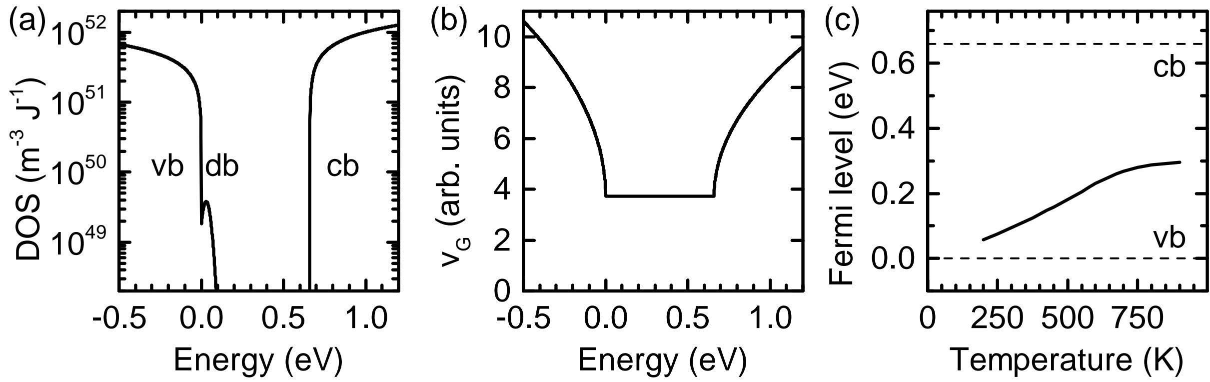

Figure 6.3. Assumptions for the simulation of the Seebeck coefficient of laser-sintered undoped Ge NPs: (a) The DOS of poly-crystalline Ge used for the simulation. (b) The corresponding group velocity of charge carriers in the material. (c) The Fermi level as obtained from the charge neutrality condition.

and cell sizes. Weber et al. states that $\epsilon^{+/0} \approx -220\,\text{meV}$, $\epsilon^{+/-} \approx -165\,\text{meV}$ and $\epsilon^{0/-} = -110\,\text{meV}$ with respect to the valence band edge and Broqvist states that $\epsilon^{+/0} = 50\,\text{meV}$, $\epsilon^{0/-} = 110\,\text{meV}$ and $\epsilon^{+/-} \approx 90\,\text{meV}$ above the valence band edge. More heuristically, the literature reports on acceptor states of Ge grain boundaries.[Ell53, Twe55, Hob57, Log59, Ree59, Ham62, Bro81, Lab91] At moderate temperatures the Fermi level is pinned at these states near the valence band and gives rise to a positive Seebeck coefficient.[Yam61, Pőd71] Furthermore, transport via these states has a much lower activation energy compared to intrinsic Ge. If the temperature is high enough to lift electrons into the conduction band, the Fermi level shifts towards midgap, the Seebeck coefficient decreases according to Eq. 2.15, and the electrical conductivity is thermally activated with the observed activation energy.

A simulation based on Eq. 2.32 will back up this model. This now requires quantitative assumptions for the physical quantities in this equation. For the sake of simplicity an energy-independent relaxation time τ is assumed. The DOS used for the simulation is shown in Fig. 6.3 (a) with a square-root function for the valence and conduction bands representing the effective masses for charge carriers in bulk Ge outside the energy gap. A dangling bond density near the valence band serves as a model for the acceptor states due to the grain boundaries. To express E in Eq. 2.32, v is identified as the group velocity in Eq. 2.30. For transport via sub-bandgap states v is assumed to be constant with a rather arbitrarily chosen value, as shown in panel (b). However, this value is adapted to best describe the following experiments. The resulting temperature dependence of the Fermi level, which is obtained from charge neutrality considerations, is shown in panel (c). As expected, for low temperatures the Fermi level is pinned near the valence band. With increasing temperature, it shifts into the middle of the bandgap. To clarify it, the model is not able to yield quantitative results on the Seebeck coefficient and the electrical conductivity due to the very much simplifying assumptions on the scattering time and the group velocity. However, since the DOS outside the bandgap is modelled

carefully using data from the literature on the effective masses, the additional dangling bond feature inserted into the band gap can deduced quantitatively by adapting the simulation to experimental results. More information on the assumptions and the effect of variations of input parameters to the simulation results can be found in App. A.

This model is now used to describe the experimental data on the Seebeck coefficient in Fig. 6.2 (b). For a dangling bond density of $2 \times 10^{17}\,\mathrm{cm}^{-3}$ the resulting curve is shown as dashed line there. The main parameter to adapt the simulation is the temperature at which the maximum Seebeck coefficient occurs. Regarding the experimental variation of the Seebeck coefficient, the data can well be reproduced and the dangling bond density lies in a realistic order of magnitude. Additionally, Fig. 6.2 (b) contains data of poly-crystalline Ge doped with Al to $4 \times 10^{18}\,\mathrm{cm}^{-3}$, which shows that although the laser-sintered Ge NP films are undoped, they behave as if doped almost to a metallic extent. This result backs up the assumption that indeed dangling bonds which are energetically located near the valence band are the origin of the typical Seebeck coefficient data of undoped laser-sintered Ge NP films.

The Seebeck Coefficient of Ge Films for Different Sinter Fluences

Coming back to the discussion following Eq. 2.32, the Seebeck coefficient does not depend on the sample geometry or, in other words, the exact current path. However, if the morphology of the NP films changes with laser-sintering and the current passes through regions of different local Seebeck coefficients, also the net Seebeck coefficient of the laser-sintered sample changes.

In Ge NP films it can be found that indeed the overall Seebeck coefficient depends on the laser fluence used for sintering. Figure 6.4 summarizes the thermoelectric properties as well as vibrational properties obtained by Raman spectroscopy for these films. Panel (a) shows Raman spectra of the Ge-Ge LO phonon mode near $300\,\mathrm{cm}^{-1}$ with respect to the sinter fluence. The shape of this line is suited to assess the degree of grain growth induced by laser-sintering. The Raman spectrum of unsintered Ge NPs shows a large peak slighly below $300\,\mathrm{cm}^{-1}$ which originates from the highly crystalline core of the NPs. On the low wavenumber side a shoulder is observed around $285\,\mathrm{cm}^{-1}$, which stems from amorphous regions of the NP shell.[Yan97] The spectra also show a laser plasma line at $266.3\,\mathrm{cm}^{-1}$, which is used for calibrating the spectrometer.[Cra79] For increased sintering of the NPs this shoulder dissappears. This finding reflects the fact that in laser-sintered films virtually no amorphous phase is present any more. By fitting the peaks with a Lorentzian and a Gaussian lineshape, respectively, the relative intensity of crystalline and amorphous contributions to the spectra can be assessed. This fitting procedure also reveals that the crystalline peak sharpens as the amorphous peak disappears. In Fig. 6.4 (b) the electrical conductivity of the films is plotted versus the sinter fluence. The data set indicated by circles is identical to the one shown in Fig. 5.9. Squares denote the samples of which the Raman spectra in panel (a) were taken. In addition to the conductivity, panel (b) also shows the thermovoltage for all samples. Unsintered films exhibit a large negative thermovoltage which becomes positive for

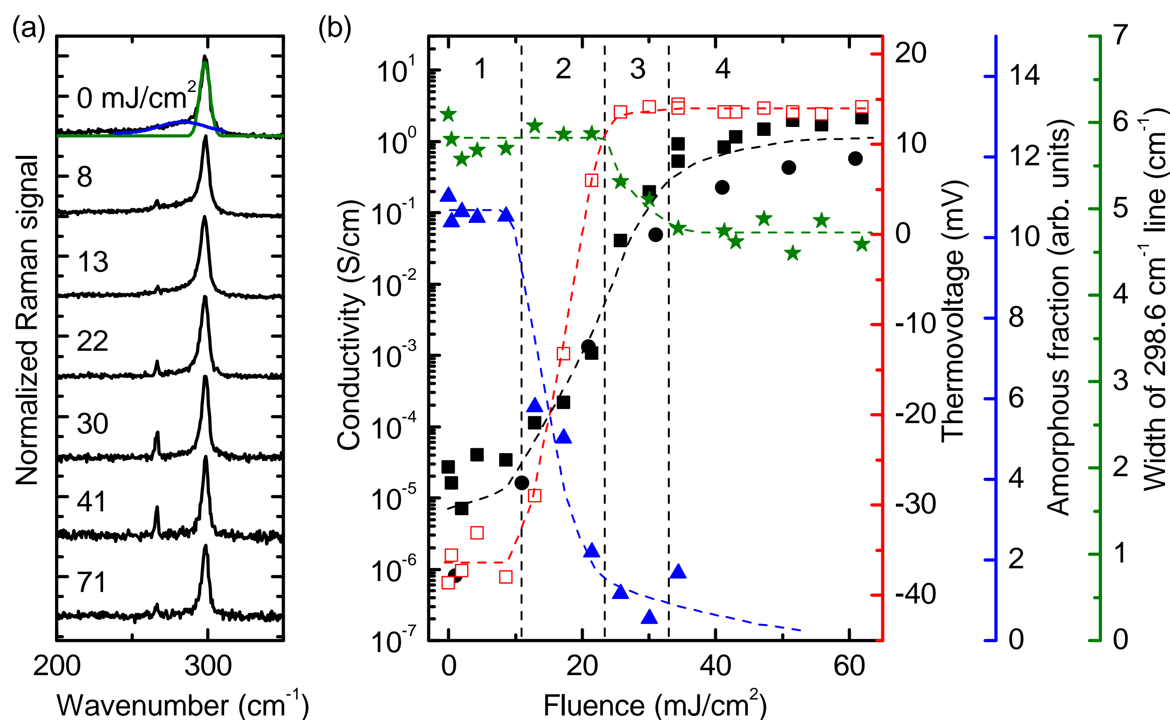

Figure 6.4. Correlation of Raman characteristics and thermoelectric parameters of laser-sintered undoped Ge NP films: Panel (a) shows the normalized Raman spectra of samples, laser-sintered with varying sinter fluence. The spectra contain a crystalline Ge peak centered at 298.6 cm^{-1} and an amorphous shoulder, at approximately 285 cm^{-1}. Panel (b) correlates the electrical in-plane conductivity (full squares and circles) and the thermopower (open squares) at $\Delta T = 45\,\mathrm{K}$ with the amorphous fraction (triangles) and the width of the crystalline peak (stars), both obtained from fitting the Raman spectra in panel (a). The regions 1 to 4 are discussed in the text.

completely sintered films. To correlate the thermoelectrical data to the microstructure, the amorphous fraction, i. e., the peak intensity ratio of the amorphous shoulder to the crystalline peak, is shown, as well as the width of the crystalline line.

The combination of Raman and thermoelectrical data allows to distinguish four regimes, which are separated in panel (b) by vertical dashed lines. In region 1 the electrical conductivity is not yet significantly enhanced, because the impinging optical power of the sinter laser cannot heat the film to temperatures sufficient for sintering. The thermopower there is negative, the amorphous fraction is rather high and the crystalline peak is slightly broadened. In region 2, above a fluence of 10 $\mathrm{mJ/cm^2}$, sintering begins, so that the electrical conductivity rises. At the same time, the amorphous fraction begins to decrease and the thermopower becomes positive. For a fluence above 25 $\mathrm{mJ/cm^2}$ in region 3, the thermopower satturates at a positive value while the amorphous fraction already disappeared to a level which cannot be detected any more for this signal-to-noise ratio. Also, in region 3 the crystalline peak begins to narrow until in region 4 all discussed parameters are stable with an electrical conductivity in the plateau region, a

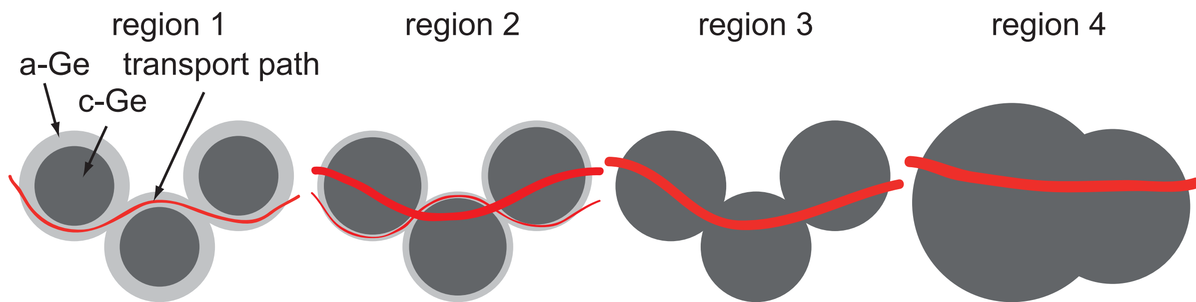

Figure 6.5. Schematic model for changes in the current path upon laser-sintering undoped Ge NP films: In region 1 of Fig. 6.4, the film consists of particles with a crystalline Ge core, surrounded by an amorphous shell. Current transport occurs via the amorphous network. Increasing the sinter fluence in region 2, the amorphous regions crystallize and current is transported across the crystalline parts as well. In region 3 no amorphous material is left and the temperature induced by laser irradiance reaches the melting/sintering temperature, leading to grain growth up to region 4.

positive thermopower, a vanished amorphous fraction and a narrow crystalline peak.

To explain the observed correlation of thermoelectrical parameter and Raman spectra, the following transport mechanism is proposed. The corresponding current paths are schematically depicted in Fig. 6.5. The as-deposited NPs in region 1 have a crystalline core and are surrounded by an amorphous shell. Since the unsintered spheres have contact only via this amorphous part, current passing the ensemble is also carried to a significant extent by the amorphous material. Reports from the literature on the Seebeck coefficient of amorphous Ge state negative values.[Lew76, Bar76, Hau92] After the beginning of sintering in region 2, the amorphous shells are annealed and improve their crystallinity, so that the crystalline cores touch each other. Now, the main portion of the current is carried in the crystalline Ge phase. The increased interconnection enhances the electrical conductivity and the discussed acceptor states in the poly-crystalline material lead to a more and more positive thermovoltage. Since the temperature during sintering reaches higher values in region 2, the fraction of amorphous shells decreases but the average size of the NPs is still similar to that of unsintered ones. In region 3 the amorphous shells have completely disappeared, so that only poly-crystalline Ge remains with a positive thermovoltage. Since the grains now start to grow significantly, the nano-size effects leading to a broadened crystalline peak in the as-deposited film becomes less important.[Cam86, Pis03] This grain growth still enhances the electrical conductivity somewhat due to the improved percolation of larger structures. The final state is reached then in region 4, with purely crystalline grains constituting the poly-crystalline material.

6.3. Thermoelectricity of Laser-Sintered B-Doped Si Nanoparticle Films

The materials systems discussed so far were undoped, and as such suitable for not classical thermoelectric applications. Below, a digital doping approach as discussed in the context of Fig. 1.3 is used to dope Si films with B. The nominal B concentration is calculated according to the mixing ratio of doped and undoped NPs and ranges from $8 \times 10^{17}\,\mathrm{cm}^{-3}$ to $5 \times 10^{20}\,\mathrm{cm}^{-3}$.

The electrical conductivity and the Seebeck coefficient obtained from those samples are shown in Fig. 6.6. The undoped sample is the same as already discussed in Fig. 6.1 with a thermal activation energy of the conductivity of 590 meV. Increasing the B concentration leads to a slightly lower activation energy and a slightly higher conductivity. The changes in the conductivity are not pronounced until the samples are doped higher than $3 \times 10^{18}\,\mathrm{cm}^{-3}$. A boron concentration of $8 \times 10^{19}\,\mathrm{cm}^{-3}$ leads to an almost temperature independent electrical conductivity already. This is even more true for the sample doped highest with $5 \times 10^{20}\,\mathrm{cm}^{-3}$ B atoms. In these samples transport occurs purely in an acceptor band.

The corresponding Seebeck coefficient data are shown in panel (b). The undoped sample was again already discussed in Fig. 6.1 and can be interpreted as intrinsic with the Fermi level within the band gap. An increased B concentration of $2 \times 10^{18}\,\mathrm{cm}^{-3}$ already leads to a pronounced shift of the Seebeck coefficient towards small negative values. In contrast to the conductivity data, at this doping concentration small variations of the nominal B-doping results in a significant change of the Seebeck coefficient. Already at a B concentration of $3 \times 10^{18}\,\mathrm{cm}^{-3}$ the Seebeck coefficient is positive for the whole measured temperature range, as expected for doping with a group-III acceptor element. However, the magnitude of the Seebeck coefficient decreases with increasing temperature. This changes when the doping concentration is increased to $8 \times 10^{19}\,\mathrm{cm}^{-3}$, where the slope of the data set in panel (b) allows to assign metallic conduction according to Eq. 2.37. As expected, in this doping regime the Seebeck coefficient decreases with increased B concentration.

In Fig. 6.7 the discussed data are summarized with respect to the doping concentration for two temperatures, 300 K and 650 K. The Seebeck coefficient switches sign at a doping concentration of approximately $2 \times 10^{18}\,\mathrm{cm}^{-3}$, while for this concentration the conductivity and the activation energy stays unchanged. For slightly higher B concentrations the activation energy at 650 K begins to decrease and the conductivity increases.

The fact that the Seebeck coefficient is sensitive to lower B doping compared to the conductivity can be explained as follows: The band edges in poly-crystalline material are not spatially constant because of local strain, bond disorder at grain boundaries or inhomogeneous distribution of dopants. The measurement of the Seebeck coefficient does not require a net current flow and if the measurement is slow enough a thermovoltage establishes although the Fermi level is still too far away to allow macroscopic transport. For current transport the carriers must have a energy that allows transport

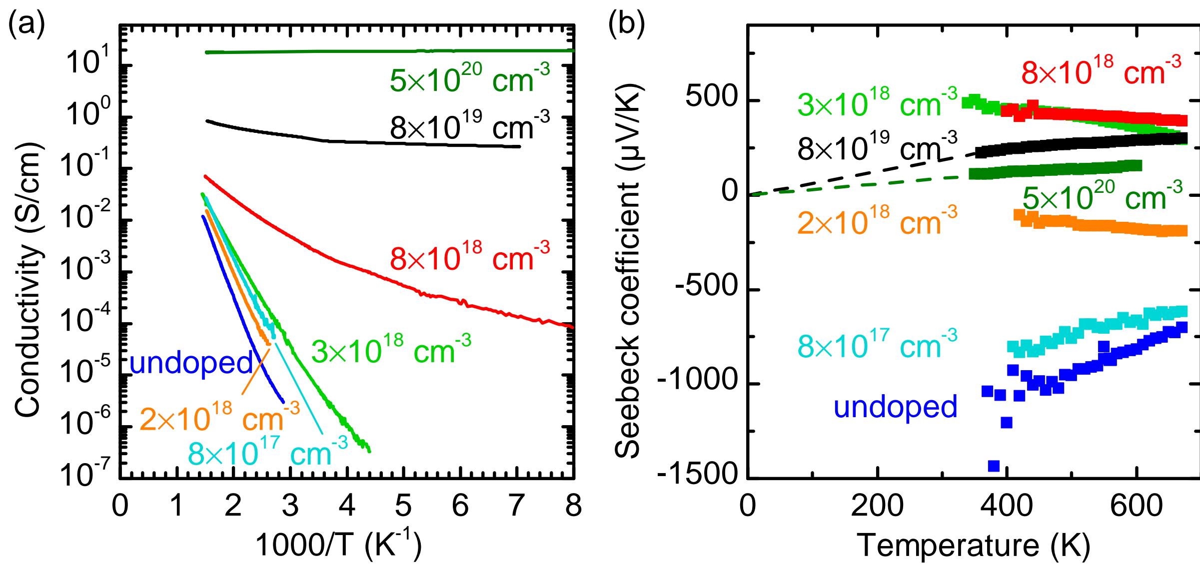

Figure 6.6. Laser-sintered digitally B-doped Si NP films: Panel (a) shows the electrical conductivity of a series of samples with different nominal B concentration in an Arrhenius plot. Panel (b) shows the Seebeck coefficient of the same samples. The dashed lines extrapolate the experimental data to the origin, indicating metallic transport.

also in the valence band regions low in energy. Thus, the Seebeck coefficient reacts to p-type doping at lower acceptor concentrations than the conductivity. Such potential fluctuations and different activation energies for conductivity and Seebeck coefficient due to trap states and the resulting band bending have already been reported in the literature for poly-crystalline thin films.[Tan80]

The doping concentration where the Seebeck coefficient switches sign is an indicator for the density of midgap states that pin the Fermi level there for low B doping. Such dangling bond states of approximately 2×10^{18} cm^{-3} are realistic, as already reported in Ref. Lec08. Effective doping of laser-sintered films can only occur if these trap states for charge carriers are overcompensated by the dopants.

6.4. Thermoelectricity of Heavily P-Doped Sintered SiGe Nanoparticles

In contrast to the materials discussed in the previous sections of this chapter, now materials of high interest for thermoelectric applications will be investigated. One characteristic feature of such Si-based materials is that they also contain a considerable amount of Ge, which is mainly introduced to suppress thermal conduction. Another feature is their heavy doping, which typically is introduced by B or P.

This section is mainly aimed at discussing the Seebeck coefficient and the electrical conductivity of several laser-sintered films of such composition. Beyond, there are three

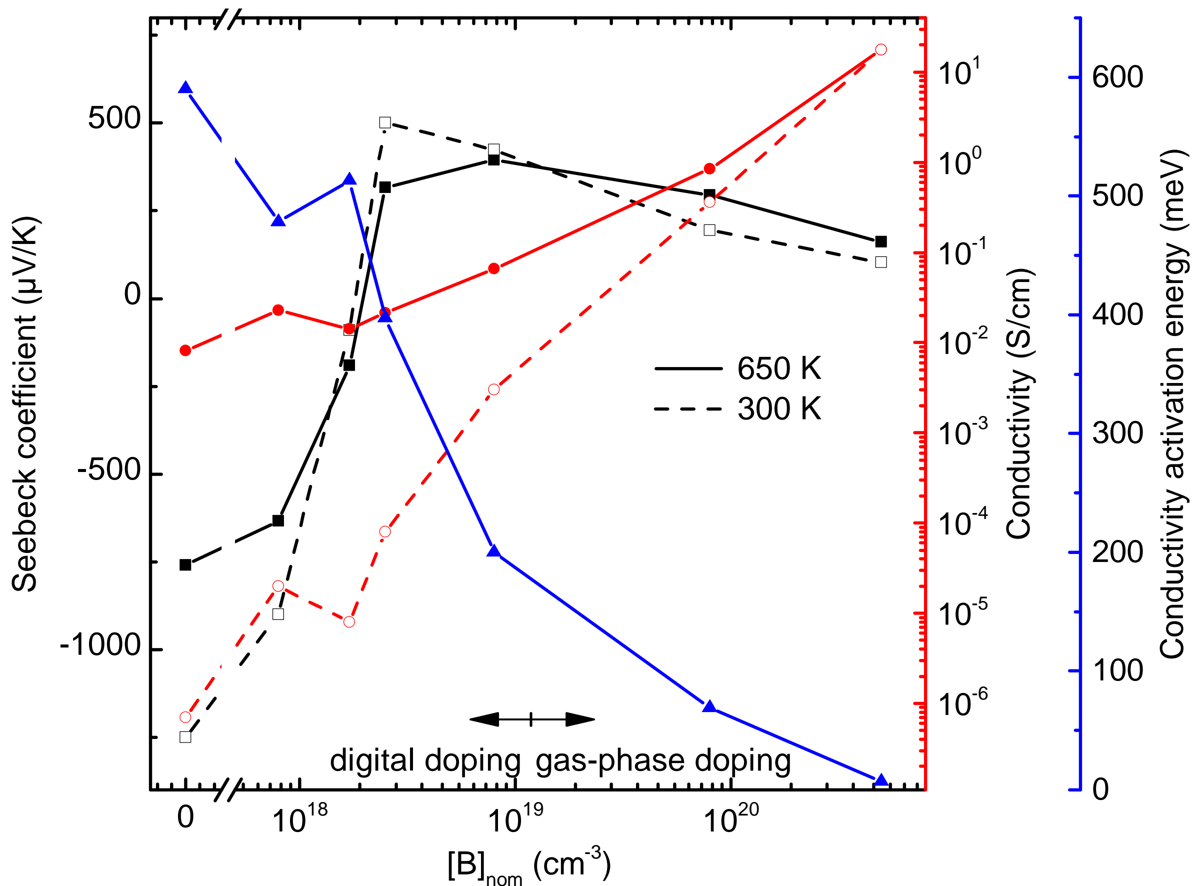

Figure 6.7. Thermoelectric parameters for digitally B-doped Si films: For 300 K and 650 K the Seebeck coefficient, the electrical conductivity and the activation energy of the conductivity at high temperatures are shown as a function of the nominal B concentration.

aspects that are also treated here:

1. the two sintering approaches which were already mentioned in Sec. 1.2, laser-sintering and CAPAD,
2. the setup, used mainly in this thesis to determine σ and S, with a commercial setup, a ZEM-3 (ULVAC Technologies, Inc.), and
3. the two concepts of introducing Ge, summarized in Sec. 4.1, yielding alloy und composite materials.

In Fig. 6.8 the Seebeck coefficients of laser-sintered $Si_{80}Ge_{20}$ and $Si_{95}Ge_{05}$ alloy NPs and of laser-sintered Si-Ge 91:09 and Si-Ge 60:40 composite NPs are shown together with the results of the corresponding CAPAD samples of the same initial raw materials. For the experiments described here, the P content in the silane flow was 1 %. This is a concentration leading to electron densities around 10^{20} cm^{-3}, as found in many SiGe thermoelectric materials.[Dis64] The degenerate doping with P is reflected by the negative Seebeck coefficient, with its absolute value increasing with rising temperature. Assuming Si-like effective masses m^* also in these SiGe materials,[Gre90] the n-type

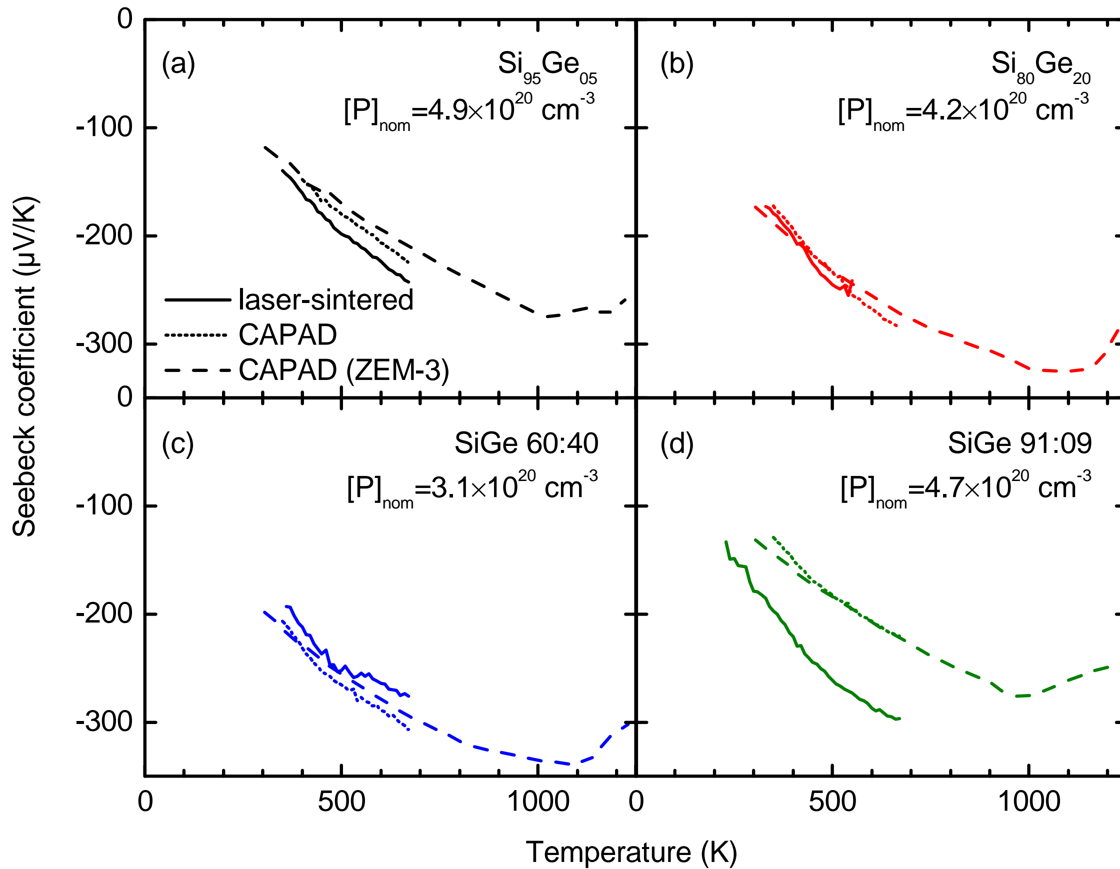

Figure 6.8. Seebeck coefficient of sintered alloy and composite SiGe NPs: Comparison of the data obtained on laser-sintered NPs and data obtained from CAPAD samples made from the same initial raw material. Also, for CAPAD samples the data measured at the Walter Schottky Institute dan be compared to the results obtained from a commercial setup (ZEM-3) located at the University of Duisburg-Essen. Panel (a) and (b) show the data of the alloy NPs, panel (c) and (d) show the results obtained on the composite materials.

carrier concentration n can be evaluated via Eq. 2.37. Irrespective of the the type of initial NPs, all laser-sintered samples show a carrier density of $n \approx$ 4-9 $\times 10^{19}$ cm^{-3}. Since in laser-sintered samples the grain size can be expected to be much larger than the grain boundary region and thus the temperature gradient along the sample mainly drops across the grain interiors, the T-dependence of S suggests a rather T-independent carrier concentration within a grain. The depletion of carriers at the grain boundary regions cannot be accessed by these Seebeck coefficient measurements.

Comparing laser-sintered and CAPAD samples and taking into account the differences in their microstructure discussed in Chap. 5, it is encouraging to see that the Seebeck coefficients of alloys and composites treated by these two sintering methods agree well. This confirms the statement that mainly the doping and not so much the morphology of a material determine the Seebeck coefficient.

The data shown as dashed line in Fig. 6.8 reaching to temperatures of up to 1200 K

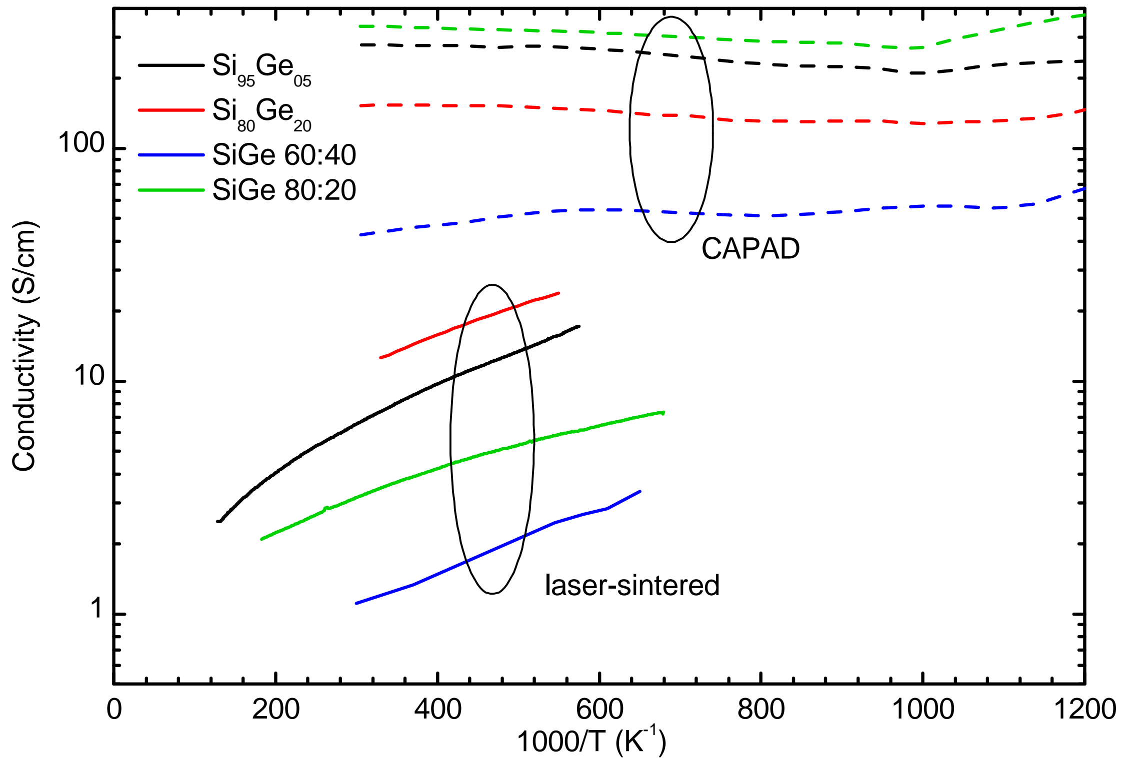

Figure 6.9. Electrical conductivity of sintered SiGe NPs: Made from the same initial NPs, laser-sintered as well as CAPAD samples are compared with respect to the temperature dependence of σ. Note that the macroscopic conductivity defined in Eq. 3.1 is shown. The type of initial NPs is indicated in the legend and follows the convention given in Sec. 4.1.

has been measured in Duisburg on the CAPAD samples using the ZEM-3 setup. The results obtained on these same samples by the two Seebeck setups quantitatively agree well, demonstrating the high reproducibility of the measurements.

Corresponding to the data in Fig. 6.8, Fig. 6.9 shows the T-dependence of the macroscopic electrical conductivity σ of laser-sintered and CAPAD samples. For laser-sintered samples the absolute value of σ is approximately one order of magnitude lower than for bulk-nano-crystalline CAPAD samples. This can mainly be ascribed to the percolation effects discussed in Chap. 5, which were not corrected for in Fig. 6.9. Morphological variations between individual samples dominate the ordering of σ here. The ordering among the CAPAD samples with respect to σ corresponds well to the slight differences observed in the Seebeck coefficient measurements obeying the anticorrelation of S and σ, as already discussed in the context of Fig. 2.3.

The CAPAD samples show a conductivity which is rather independent of T, as expected for such degenerate doping. Regarding the T-dependence of σ for laser-sintered samples, the observed increase of σ with T can empirically be described by a power-law with $\sigma \propto T^{\sim 1.2}$. Plotted in a classic Arrhenius-diagram, power-law dependencies $\sigma \propto T^{\alpha}$ appear curved upwards for $\alpha > 0$. Qualitatively this upward bending can be interpreted as an activation energy E_a increasing with temperature, arising, e.g., from a distribution

of barrier heights as already discussed in the context of the digitally B-doped Si samples in Sec. 6.3.

For all samples discussed here, the heavy P doping is introduced via admixing phosphine to the silane gas flow during gas phase growth of the NPs. This implicates that for samples of different Ge content also the overall P concentration slightly varies. Also, there is can be a difference between alloy and composite NP powder due to a different degree of dopant segregation in pure and in alloy NPs. As already discussed in Sec. 4.1 Stegner et al. found that for pure Si NPs doped with P, approximately 90 % of the dopants reside in the oxide shell. For $Si_{80}Ge_{20}$ alloy NPs a similar Secondary Ion Mass Spectroscopy (SIMS) experiment in the framework of this thesis yields a dopant loss of 60 %. This reduced loss for alloy NPs may be explained by the already pronounced mass and bond strength difference introduced by Ge, so that P atoms tend to segregate less. Arithemtically, this should lead to an enhanced loss of dopants in composite NPs compared to alloy NPs, when the oxide shell is removed by HF, as it is the case for the laser-sintering process. In the CAPAD process, however, no etching is performed and P is mainly contained in the oxide precipitates. For high temperatures P becomes mobilized and can act in the Si phase as a dopant again.

7 Laser-Assisted Wet-Chemical Doping of Sintered Nanoparticle Films

In Fig. 1.3 different ways to fabricate doped thin films from laser-sintering NP films were introduced. In this chapter the principle of *laser-assisted wet-chemical doping* will be discussed in detail. The basic mechanisms are studied for As-doped Ge, which was chosen as a model system. Further, the method will be transferred to other group-III and -V dopants as well as to SiGe and Si films. In the course of this chapter, the dopant incorporation and doping efficiency will also be analyzed quantitativly.

7.1. The Principle of Laser-Assisted Wet-Chemical Doping

In contrast to conventional doping of gas-phase synthesized NPs during their gas-phase growth,[Kni04, Pet11] laser-assisted wet-chemical doping uses undoped NPs as precursors. The method yields doped films when the undoped film is immersed in a dopant liquid, dried and subjected to a sintering step. In this thesis, laser-sintering is used, but other treatments may be used as well, such as CAPAD,[Pet11] thermal annealing [Lec09] or microwave sintering.[Dra14] The term *laser-assisted wet-chemical doping* refers to two facts: One one hand, that the method combines both the enhancement of the film morphology in terms of connectivity and the incorporation and electrical activation of the dopants in the film, so that doping by this method can be done without an extra processing step, and, on the other hand, that the dopants are applied to the film in a wet-chemical step via a liquid, the so-called doping liquid.

Figure 7.1 schematically illustrates important processes of laser-assisted wet-chemical doping. The doping liquid contains suitable dopant species in the form of ions or

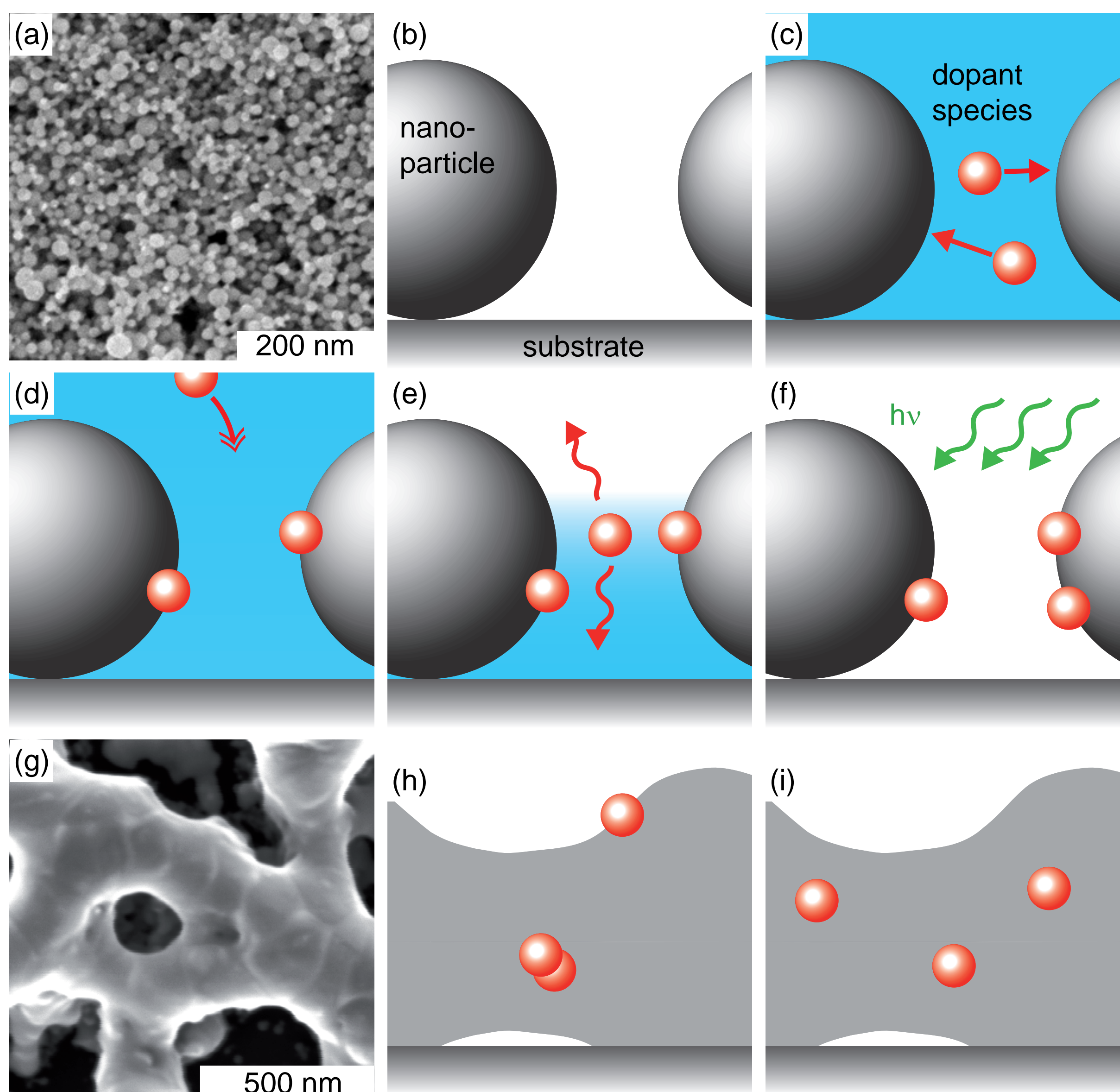

Figure 7.1. Schematic illustration of the work flow of laser-assisted wet-chemical doping: (a) SEM micrograph of an as-deposited Ge NP film, which panel (b) represents schematically. (c) The NP film is immersed in a liquid containing dopants, which adsorb to the NP surface. (d) The depleted liquid is refilled with dopants from the free outer liquid. (e) During drying, the dopants can remain in the film or evaporate. (f) Laser-sintering incorporates the dopants. (g) SEM micrograph of the mesoporous film after laser-sintering. (h) In the sintered matrix the dopants can occupy surface states or precipitate, leaving them electrically inactive. (i) Ideally, the dopants occupy dilute substitutional lattice sites and become electrically active.

molecules. As visible in the top-view SEM micrograph in panel (a), after deposition the loosely packed NPs constitute a film, sketched in the side-view in panel (b), with a very large internal surface area. As illustrated in panel (c), the NP film is immersed in the doping liquid. Depending on the interaction of the NP surface and the dopant

species, adsorption of the dopants to the NP surface takes place. Because the adsorbed dopants reduce the concentration of dopants in that part of the doping liquid which initially penetrated the NP film, successive diffusion of dopants from the outer liquid into the interior of the film will take place, as shown in panel (d). This diffusion through a nanometer-sized porous film can be slow and thus a time- and efficiency-limiting process. As sketched in panel (e), the film is dried next. The dopants that are not yet adsorbed can either evaporate in an unspecified manner together with the doping liquid, or be retained in the film during evaporation of the liquid phase. Then, also those dopants that did not yet adsorb to the NPs are available for doping. To form the desired interconnected and doped semiconductor film, the loosely packed NP ensemble with adsorbed dopants is then subjected to the sintering step, as indicated in panel (f). The typical morphology of the film after laser-sintering discussed extensively in Sec. 5.1 is shown in the top-view SEM image in panel (g). During laser-sintering the morphology evolvement induced by laser-sintering as discussed in Sec. 5.1 is not influenced by the wet-chemical treatment in the doping liquid. The NPs are at least partly molten and, upon solidification, larger grains are formed. Those can be seen in panel (h) and (i) as constituents of the meander network. Panel (h) schematically shows that dopants in the sintered film can occupy surface states or even cluster, both rendering the dopants electrically inactive.[Sol96, Bai99, Tak02, Mue04] The ideal situation is shown in panel (i), where the dopants occupy dilute substitutional lattice sites and are electrically active.

7.2. Doping Liquids for Laser-Assisted Wet-Chemical Doping

The doping liquids into which the as-deposited NP films are immersed in this thesis are pure or diluted solutions usually used as standards for calibration in Inductively-Coupled Plasma (ICP) mass spectrometry. All pure doping liquids contain 10 g/l of the respective dopant element. As group-III elements, B, Al, Ga and In were tested. From group V, P, As, Sb and Bi were available for the doping experiments. The matrix of pure doping liquids is acidic in most cases. The pure liquids typically have concentrations of trace impurities in the ppb-range, except for the elements Ni, Os, P and Se, which are found in concentrations of up to ppm.[Car]

In many experiments discussed here, the concentration of dopants in the doping liquid is reduced, which is achieved by diluting the pure ICP solution, as shown in Fig. 7.2, with a diluent such as deionized water or an aqueous solution of 5 % hydrofluoric acid. The resulting doping liquids are then called HF-free and HF-containing doping liquids, respectively. The dilution is typically achieved by mixing, e. g., 1000 µl of the diluent with 500 µl of the doping liquid with the next higher concentration of dopants inside 2 ml cuvettes (3:1 dilution steps). Proper vortexing of this mixture, typically for some minutes, ensures a homogeneous distribution of the dopants within the doping liquid. The next dilution step then uses 500 µl of this doping liquid and mixes them with 1000 µl

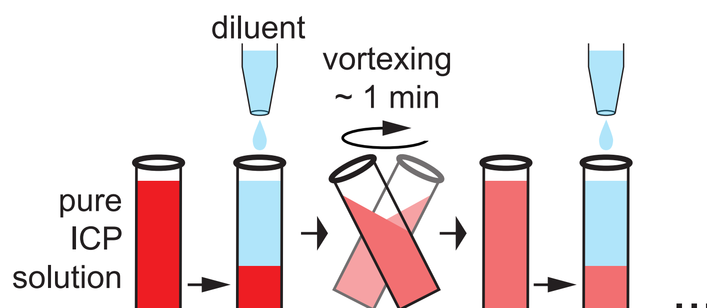

Figure 7.2. Dilution of doping liquids: Starting from pure Inductively-Coupled Plasma (ICP) standard solutions, doping liquids with a reduced concentration of dopants can be obtained by mixing with a diluent. To ensure a homogenous distribution of dopants in the doping liquids, vortexing is used.

of the diluent again. This procedure ensures that the relative uncertainty of the pipetting steps are small.

7.3. Selectivity of Laser-Assisted Wet-Chemical Doping

To first prove the selectivity of laser-assisted wet-chemical doping and to exclude cross-contamination, HF-etched Ge NP films are immersed for 2 min prior to the laser-sintering step in pure doping liquids containing 10 g/l of either P, As, Sb or Bi. Figure 7.3 shows X-ray Photo-electron Spectroscopy (XPS) spectra of the doped films. The laser-sintered Ge thin films only contain the intended elements at the surface, which demonstrates the selectivity of the doping method. A similar composition of surface-near and sub-surface

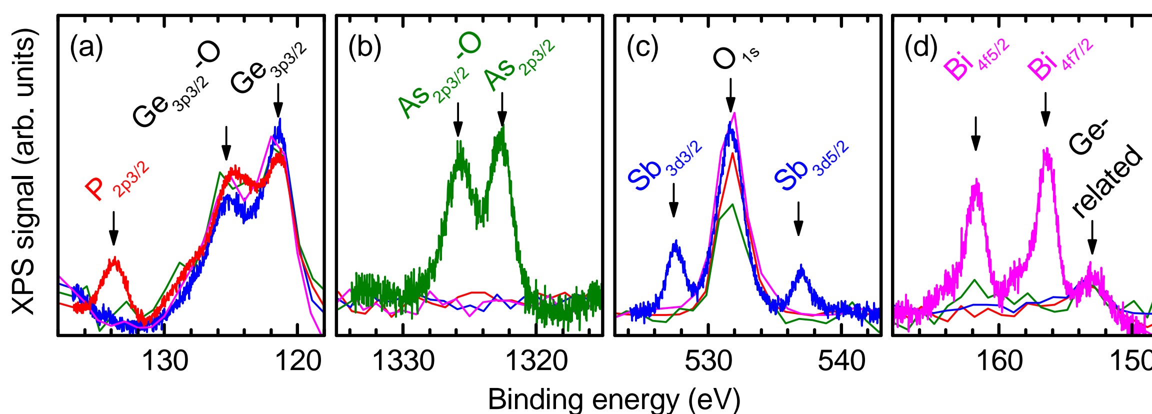

Figure 7.3. Selectivity of laser-assisted wet-chemical doping: X-ray Photo-electron Spectroscopy (XPS) spectra of four laser-sintered Ge NP thin films after laser-assisted wet-chemical doping. Only samples intentionally doped with P, As, Sb or Bi show the XPS signature of the respective element. The concentrations of the dopant element in the solution were (a) $2 \times 10^{23}\,l^{-1}$ of P, (b) $8 \times 10^{22}\,l^{-1}$ of As, (c) $5 \times 10^{22}\,l^{-1}$ of Sb, (d) $3 \times 10^{22}\,l^{-1}$ of Bi. Since the samples were not kept under inert atmosphere, oxide-related signals are also observed.

regions is assumed due to the quenching during the fast recrystallization. Oxide-related signals are also present because the samples were not kept in inert atmosphere after their fabrication.

7.4. A Model System for Laser-Assisted Wet-Chemical Doping

The XPS study in Sec. 7.3 only proved the presence of the dopant atomsin the host material and not yet the element's impact on the electric properties. To influence those, the dopants must be electrically active, i. e., they must release their charge carriers into the host material. To study the effect of laser-assisted wet-chemical doping on the electrical properties of the doped material, a model system is useful.

Such a model system needs to fulfill some criteria: The electronic properties of undoped material needs to be understood reasonably well and should also be properly defined in terms of reproducibility. Further, the dopant used should be a shallow substitutional dopant in the host material used for the model system.

The mentioned criteria are met by As-doped Ge thin films. As discussed in Sec. 6.2, the p-type conductivity of undoped laser-sintered Ge NP films is accompanied by a rather high electrical conductivity and a positive Seebeck coefficient. These properties make undoped laser-sintered Ge a well defined and easy to measure material. Further, As is a shallow substitutional donor in Ge.[Geb54] In practice, it is found that As-doped Ge films can be fabricated very reproducibly and can be measured fast and with reasonable high accuracy in ambient atmosphere. Thus, in the following sections, laser-assisted wet-chemically As-doped Ge films are used as a model system to investigate important parameters of the method.

The pure ICP doping liquid for the model system is made from 10 g As(V)-oxide, dissolved in 1 l of a 2 % aqueous solution of HNO_3. To control the doping concentration in the final laser-sintered film, the doping liquid is diluted in a 5 % aqueous solution of hydrofluoric acid. Using this HF-containing aqueous diluent has the advantage that the native surface oxide, which typically covers the as-grown NPs used in this work, is also removed during the doping step. Due to the low pH of the doping liquid, the oxidation state of the initially present As(V) presumably persists also in less concentrated dilution liquids, so that the adsorbed dopant species should be dihydrogen arsenate ions $(H_2AsO_4)^-$.[Tak11]

7.4.1. Experimental Observations for n-Type Doping of Ge Films

The following sections use a specific type of diagram to show the results of investigations on the mechanism and the efficiency of laser-assisted wet-chemical doping. Such a diagram is shown on the right in Fig. 7.4. The abscissa represents the nominal concentration of the dopant element in the doping liquid in units of l^{-1}. These values

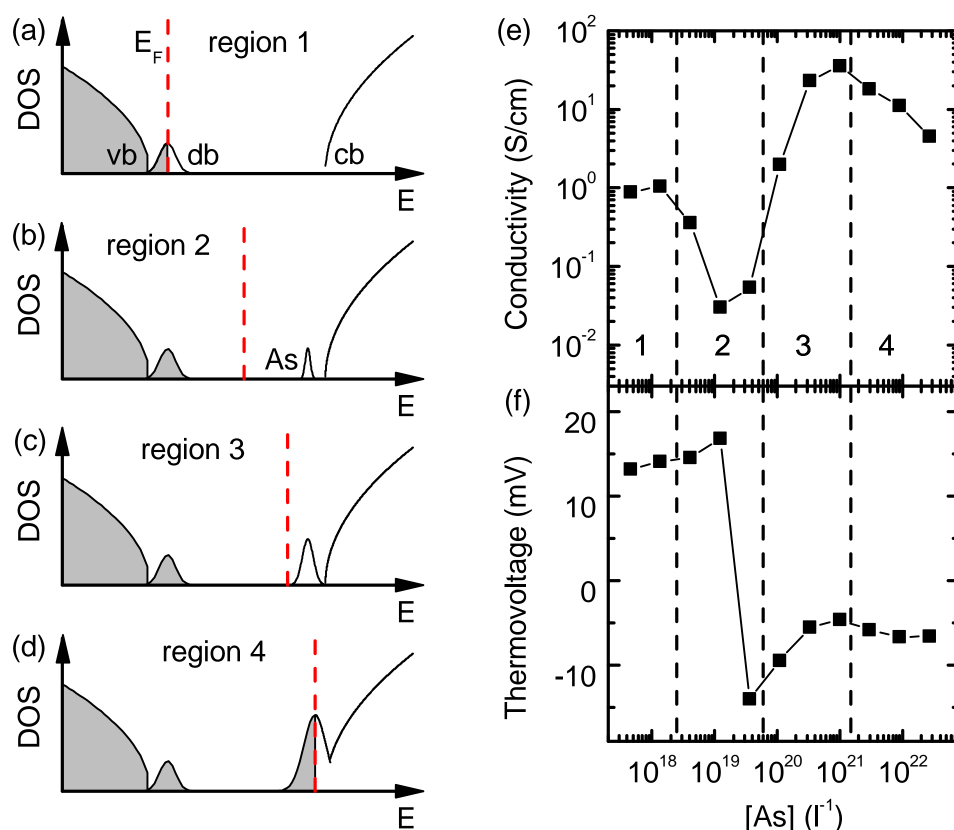

Figure 7.4. As-doped Ge as a model system for laser-assisted wet-chemical doping: Panels (a)-(d) sketch a scenario for the DOS with the valence band (vb), dangling bonds (db) and the conduction band (cb) with as a functio of the electrically active As donors, activated by laser-assisted wet-chemical doping. The shaded states are filled and the red dashed line represents the Fermi level E_F. Panel (e) shows experimental data of the in-plane electrical conductivity of Ge films, doped with different amounts of As. The corresponding thermovoltage is shown in panel (f). The regions 1 to 4 corresponding to the DOS sketches can be identified in the experimental data.

are calculated according to the concentration of the pure ICP solution of 10 g/l, the mass of the dopant element and the dilution steps as discussed in conjunction with Fig. 7.2. The ordinates of the two panels represent the thermovoltage and the effective electrical in-plane conductivity, both as a measure for the electrically activated As dopants. In particular, the thermovoltage, i. e., the product of the Seebeck coefficient and the temperature difference of $\Delta T = 45\,\mathrm{K}$ used to measure the thermoelectric effect, yields valuable information about the majority carrier type, which is especially helpful in a doping regime where the electrical conductivity is poor.[Bra98]

To illustrate the effect of doping on sintered Ge NP films with donors such as As, Fig. 7.4 shows a schematic DOS model of poly-crystalline Ge. More quantitatively such a DOS has already been shown in the discussion of Fig. 6.3, which is briefly repeated here. In Fig. 7.4 (a), the Fermi level E_F, indicated by the red vertical dashed line, of undoped laser-sintered films of Ge NPs is pinned at the charge transfer level of Ge

dangling bonds, which is located in the vicinity of the valence band in Ge.[Bro08, Web13] As a consequence, these films exhibit hole conductance (positive thermovoltage) and a considerably high conductivity. Such p-type behavior is typical for poly-crystalline Ge.[Sto13, Twe55, Yam61] Doping the Ge film with an increasing amount of As gradually transforms the material to an electron conductor, visible by the shift of E_F towards the conduction band as shown in panel (b) through (d).

Corresponding to the model discussed, typical experimental data of the conductivity and the thermovoltage of laser-assisted wet-chemically As-doped Ge thin films are shown in panel (e) and (f). The regions separated by vertical dashed lines correspond to the respective sketches in panel (a) through (d). In region 1 low doped laser-sintered Ge shows the p-type conductance with the positive thermovoltage discussed in Sec. 6.2. In region 2 the concentration of As in the doping liquid and thus the density of As in the sintered film increases. To fulfil charge neutrality, E_F shifts towards mid-gap. Since the DOS around mid-gap is practically vanishing, the overall number of carriers contributing to the electrical transport is reduced, which is reflected by a minimum of the conductivity in region 2 of panel (e). At the beginning of region 2 in panel (f), the thermovoltage, measuring mostly the energetic distance of E_F to the respective transport channel according to Eq. 2.32, slightly rises in magnitude as E_F moves away from the valence band. Adding more As donors, E_F approaches the conduction band and the conductivity rises again at the end of region 2. With electrons being the majority carrier type now, the thermovoltage changes sign within a rather narrow range of dopant concentrations in the doping liquid. It then decreases in magnitude as the conductivity increases further, indicating the shift of E_F towards the conduction band. In region 3 the trend of rising conductivity persists, until a maximum conductivity in panel (e) and a minimum in the magnitude of the negative thermovoltage in panel (f) is reached. Very high doping levels in region 4 reduce the conductivity in panel (e) again, accompanied by a slight increase of the magnitude of the thermovoltage in panel (f).

Although the incorporated amount of As should monotonically increase with the concentration of As in the doping liquid, at least three different processes will contribute to the conductivity reduction for the highest doping levels: First, increased impurity scattering becomes mobility-limiting.[Con52, Deb54] Second, the formation of vacancy-arsenic clusters which render the dopants electrically inactive competes with the formation of substitutional As atoms.[Chr14] Third, p-type germanium-arsenate precipitates counteract the n-type doping of As in Ge.[Stö40, Spi61]

7.4.2. Simulation of Laser-Assisted Wet-Chemical Doping

To back up the qualitative behavior discussed in the previous section, the dependence of the conductivity and the Seebeck coefficient on the concentration of electrically active donors can be simulated, applying a semi-quantitative Boltzmann formalism for (thermo)electric transport. Essentially, the simulation used in Fig. 6.3 is extended and donors are included.

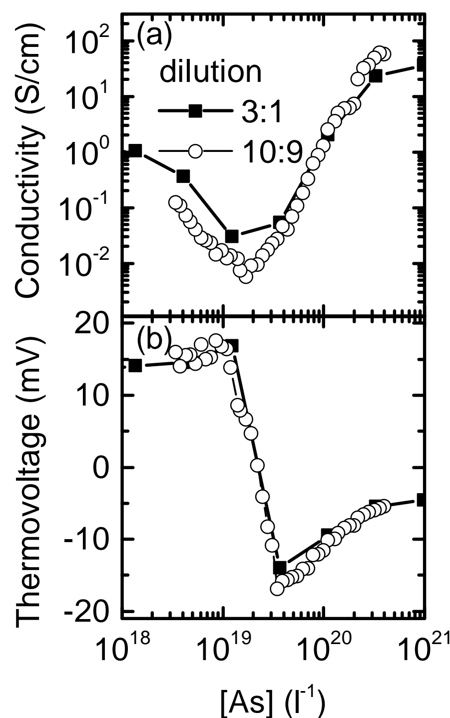

Figure 7.5. High resolution dilution series of laser-assisted wet-chemically As-doped Ge films: Panel (a) and (b) show the conductivity and the thermovoltage ($\Delta T = 45\,\mathrm{K}$) for the same experimental conditions as in Fig. 7.4, from which also the data for the 3:1 dilution series are taken. The highly resolved data sets result from diluting the doping liquid in steps of 10:9.

The data shown so far in Fig. 7.4 do not contain enough information for a full simulation of laser-assisted wet-chemical doping. Therefore, Fig. 7.4 additionally shows the data obtained from a doping experiment using doping liquids that were diluted in steps of 10:9 rather than 3:1 (see also Fig. 7.2). The data of the experiments with 10:9 and 3:1 dilution ratio match well. The concentration of dopants in the doping liquid where the thermovoltage changes sign is also reproduced within a few percent. Further, the highly resolved data set shows impressively little scatter, demonstrating the high accuracy with which the concentration of dopants in the doping liquid can be adjusted, as well as the high precision with which the doping method yields films of defined electronic properties.

The simulation of laser-assisted wet-chemical doping is an extension to the simulation of the temperature dependence of the Seebeck coefficient for undoped laser-sintered Ge NPs in Sec. 6.2. There, one result was that the experimental data can be reproduced well, assuming a dangling bond density of $2 \times 10^{17}\,\mathrm{cm}^{-3}$. To add As donors to the model, a sharp (delta-like) donor state 13 meV below the minimum of the conduction band is introduced.[Con58] Similar to Sec. 6.2, the model is not quantitative with respect to the values on the ordinate, since knowledge on the scattering rate and the group velocity lacks. Therefore, simulation data on the electrical conductivity will not be

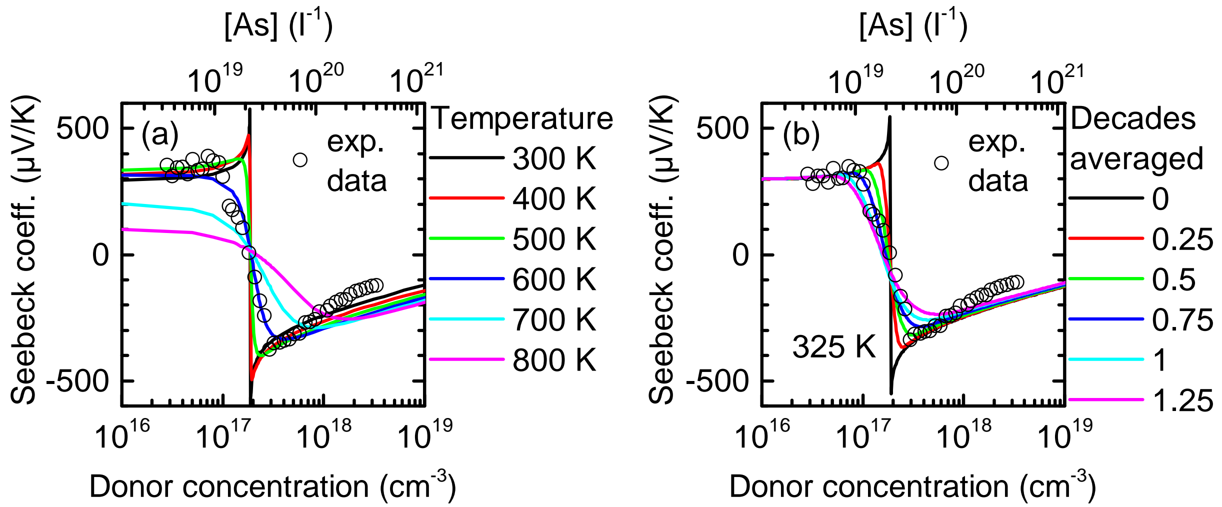

Figure 7.6. Simulation of the Seebeck coefficient in laser-sintered wet-chemically doped Ge films as a function of the As content: In panel (a), data obtained from the simulation are shown for different temperatures and homogeneous material. Panel (b) shows simulation data at 325 K, averaged over material with varying dopant concentration. The assumed dangling bond density in both panels is $2 \times 10^{17}\,\mathrm{cm}^{-3}$.

shown but the discussion will concentrate on the Seebeck coefficient since it is a much more defined measure due to the open circuit conditions. The Seebeck coefficient obtained from the simulation is scaled to the experimental room temperature data in Fig. 6.2 (b). Additionally, the density of (ionized) donors enter the simulation, rather than the concentration of dopant species in the doping liquid. However, it is assumed that those quantities are proportional to each other over a wide range of concentrations of dopants in the doping liquid, so that the experimental data are shifted along the abscissa to match the simulated data.

The black line in Fig. 7.6 (a) represents the results obtained from the simulation for a material having spatially homogeneous densities of dangling bonds as well as of donors and is calculated for room temperature. The most striking discrepancy between the experimental data and the simulated data is that the simulated data changes sign within a much narrower range of concentrations of dopants. Of course, the thermovoltage is measured for a temperature difference of 45 K, so that varying the temperature in the simulation seems to be advisable. However, to obtain agreement of experimental and simulated data, a temperature of 600 K has to be assumed in the simulation. Thus, the non-homogeneous temperature across the sample cannot explain the discrepancy observed.

Rather, it is reasonable to assume that neither the dangling bond density nor the donor density are homogeneous in space. To implement this fact in the simulation in a first approach, the dangling bond density will be fixed at $2 \times 10^{17}\,\mathrm{cm}^{-3}$, but the sample will be divided into several slices having different donor concentrations. These slices are then connected in parallel, so that the thermovoltage measured is a conductivity-weighted

average of the different slices. To adapt the simulation to the logarithmic abscissa, the material is averaged over certain fractions of a decade of donor densities. Panel (b) shows the results of such simulations at a mean temperature of 325 K, which is typical for the experimental situation. Now, the temperature difference of 45 K is neglected as a learning from panel (a). Taking the range of concentrations needed for the change in sign as a measure, an acceptable agreement of experimental and simulated data can be achieved when varying the donor concentration by approximately one order of magnitude while keeping the dangling bond density constant. A similar result would be obtained when varying both the donor and the dangling bond density by factors of 3, which seems to be the realistic scenario.

7.5. Parameters Influencing Laser-Assisted Wet-Chemical Doping

The model discussed so far showed that the degree of doping can be regulated by controlling the concentration of dopants in the doping liquid in a very controlled and repeatable fashion. However, this does not yield information about the efficiency of laser-assisted wet-chemical doping. To first get an idea which process parameters are relevant for the efficiency of the doping method, the NP diameter, the time which the as-deposited NP film is immersed in the doping liquid and the immersion temperature shall now be varied. The corresponding results are shown in Fig. 7.7. For each set of parameters curves as shown in Fig. 7.4 are recorded. Standard conditions were 300 nm thick films of Ge NPs, having a diameter of 27 nm, which are immersed for 25 min at 300 K. These standard conditions are indicated by black squares in all panels of Fig. 7.7. All the data sets show the features discussed in the context of Fig. 7.4 and only differ by a shift along the abscissa, observed most clearly by the different As concentrations where the thermovoltage changes sign. Important to note here, a shift of the data set to lower dopant concentrations implies an enhanced doping efficiency for these parameters.

Figure 7.7 (a) and (b) show data of experiments with two different NP diameters. Compared to the 27 nm data set, the data for 10 nm NPs is shifted by approximately half a decade to lower As concentrations in the doping liquid. Varying the immersion temperature in panel (c) and (d) between 270 K and 330 K shows that the doping efficiency increases with a higher immersion temperature. In panel (e) and (f) the time which the NP films are immersed in the liquid is varied from 10 s to 25 min. The longer the films are immersed, the lower is the concentration of dopants in the liquid required for similar doping effects.

In a further experiment, shown in Fig. 7.8, the aspect of in-diffusion, already addressed in Fig. 7.1 (b), is studied by immersing Ge NP films having film thicknesses ranging from 100 nm to 700 nm each for 2 min in equal HF-containing doping liquids with $8.9 \times 10^{21}\,\mathrm{l}^{-1}$ of As. All films were wetted instantaneously, ensuring a complete penetration of the doping liquid through the whole film. Without further laser-sintering

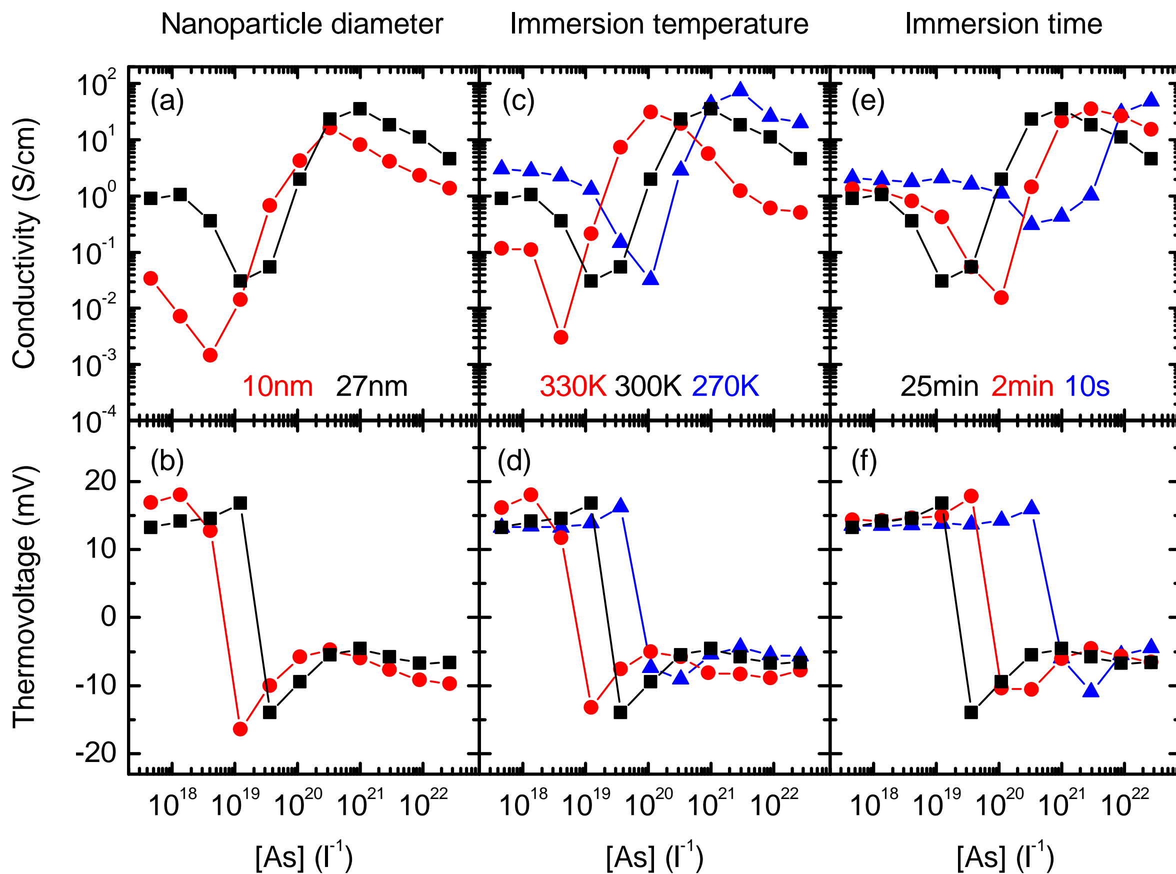

Figure 7.7. Variation of some parameters influencing the efficiency of laser-assisted wet-chemical doping of Ge with As: Standard parameters for laser-assisted wet-chemical doping were a NP diameter of 27 nm, an immersion time of 25 min and an immeersion temperature of 300 K. Those standard data are shown as black squares in all panels. In panel (a) and (b), the diameter of the NPs is varied by a factor of 3. In panel (c) and (d), the immersion temperature is varied from 270 K to 330 K. In panel (e) and (f), the time the films are immersed is varied by more than two orders of magnitude. The data, presented similarly to Fig. 7.4, show curves which are essentially only shifted along the abscissa. A shift to lower As concentration implies an increased efficiency of laser-assisted wet-chemical doping and vice versa.

treatment, an Energy-Dispersive X-ray spectroscopy (EDX) analysis was performed on the films. The substrate beneath the NP film was coated with a gold film. Experiments with an acceleration voltage of 5 kV reveal the Au M line for all films, which ensures that the film was probed also in its depth. To assess the As content of the immersed films, the spectra were normalized to the Ge L_α peak. Panel (a) shows EDX spectra of an undoped Ge film (black) and of immersed films of different thickness (colored). For the spectra of those films, the high-energy shoulder of the Ge L_α peak arises from the L_α line of As present in the doped film. A qualitative estimate of the As concentration in the films can be obtained by integrating the signal intensities of the Ge L_α and the As L_α line for all films. The results in panel (b) show that thick films contain less As,

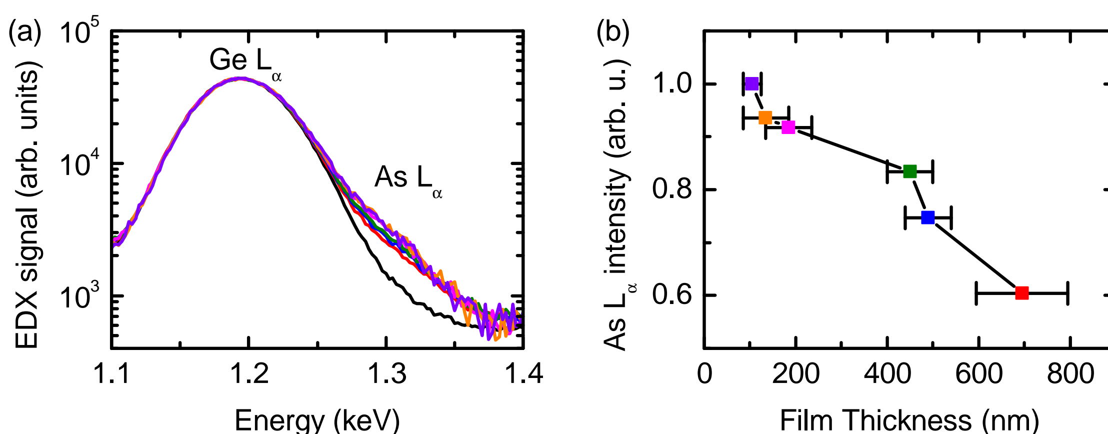

Figure 7.8. EDX investigation of the influence of the film thickness on the amount of adsorbed As in Ge NP films: (a) Normalized EDX spectra showing the Ge Lα and the As Lα line for films of as-deposited Ge NP films. The black line represents an undoped film. The colored lines show the signals for films with different thicknesses which were immersed for 2 min in an As-containing liquid with a concentration of $[\mathrm{As}] = 8.9 \times 10^{21}\,\mathrm{l}^{-1}$. For an increasing thickness of the Ge NP film the As content decreases. (b) The relative As/Ge EDX signal intensity. Error bars originate from the film thickness determination.

compared to thin films. This integral information on the As content versus the total film thickness also implies that a film of as-deposited Ge NPs contains more adsorbed As on the surface compared to deeper regions. However, the subsequent laser-sintering leads to the formation of a mesoporous structure, which, according to scanning and transmission electron microscopy in Sec. 5.1.2, in the direction of the film thickness essentially consists of single grains. The melting of the NP layer and the subsequent fast crystallization should therefore lead to a doping which is homogeneous in depth. A verification of this behavior, however, would require, e. g., mass spectroscopic methods with high lateral and depth resolution such as atom probe microscopy, which is beyond the scope of this investigation.

The results shown in Fig. 7.7 and Fig. 7.8 support the interpretation that the uptake mechanism of As in the NP layer is specific adsorption, where As species are attracted by the NP surface during immersion, rather than a simple retention of the dopants during drying. Here, the term specific adsorption is used in the sense that the adsorption is characteristic for a certain pair of adsorbent and adsorpt.[Lyk83] Thus, the method benefits from the large internal surface of the NP films used as a precursor. The amount of As in the NP layer is limited by As diffusion from the outer doping liquid into the porous layer. In detail, the data in Fig. 7.7 and Fig. 7.8 can be interpreted as follows:

An increase of the surface-to-volume ratio of the ensemble of NPs in Fig. 7.7 (a) and (b) by a factor of approximately 3 enhances the uptake and hence the doping efficiency by a similar factor. A mere retention of the dopants during drying should not change the uptake efficiency for films of comparable packing density, which was verified by SEM. The increased doping efficiency for higher temperature found in Fig. 7.7 (c) and

(d) agrees with the reported temperature dependence for adsorption of As species on a variety of other materials, e. g. activated carbon, magnetite nanoparticles or Fe(III)-Si binary oxide adsorbents.[Pay05, Zen04, Shi09] However, since diffusion was discussed above to play a significant role, an increased diffusion constant D due to an increase in temperature T according to the Stokes-Einstein relation [Ein06]

$$D = \frac{k_B\, T}{6\pi\, \eta\, r_{\text{eff}}}, \tag{7.1}$$

with the Boltzmann constant k_B, the viscosity of the liquid η and the effective radius of the diffusing dopant r_{eff}, may also at least partially account for the results of Fig. 7.7 (c) and (d). The pronounced time dependence in Fig. 7.7 (e) and (f) indicates that in-diffusion, proposed in Fig. 7.1 (b), is a limiting process. Finally, the dependence of the As uptake on the Ge NP film thickness in Fig. 7.8 further supports the hypothesis that in-diffusion from the outer liquid (which is reduced for thick films) is an extremely relevant process and governs the efficiency of laser-assisted wet-chemical doping.

7.6. Laser-Assisted Wet-Chemical Doping Transferred to Other Elements

After the discussion of As-doped Ge films as a model system, the suitability of other group-III and -V dopants for laser-assisted wet-chemical doping of Ge films will be discussed. Although not investigated in as many details as As-doped Ge, it is reasonable to assume similar dependencies on parameters such as temperature, time, film thickness or NP diameter as well, which would have to be properly investigated when the respective element shall be used to fabricate devices. The industrial relevance of Si, of course, is much higher compared to Ge, so that in this section the method is also investigated using Si NPs.

7.6.1. Group-III and -V Elements for Doping Ge Films

Room Temperature Observations of Laser-Assisted Wet-Chemical Doping of Ge

In all experiments discussed so far the diluent of the doping liquid was an aqueous solution of 5 % HF, to facilitate the simultaneous removal of the NP surface oxide and the dopant application. This is necessary since the NPs available for this study have a surface oxide shell, as discussed in Chap. 4. Should printing of NP thin films without oxides become possible, this HF-containing doping liquids would not be necessary, allowing a safer doping. Due to this safety issue concerning HF treatment, this section starts to compare As doping of Ge films via HF-containing and HF-free doping liquids. For the application of the latter, the NP thin films are immersed in 5 % aqueous solution of HF and dried by N_2 before exposure to the doping liquid, mimicking a hypothetical

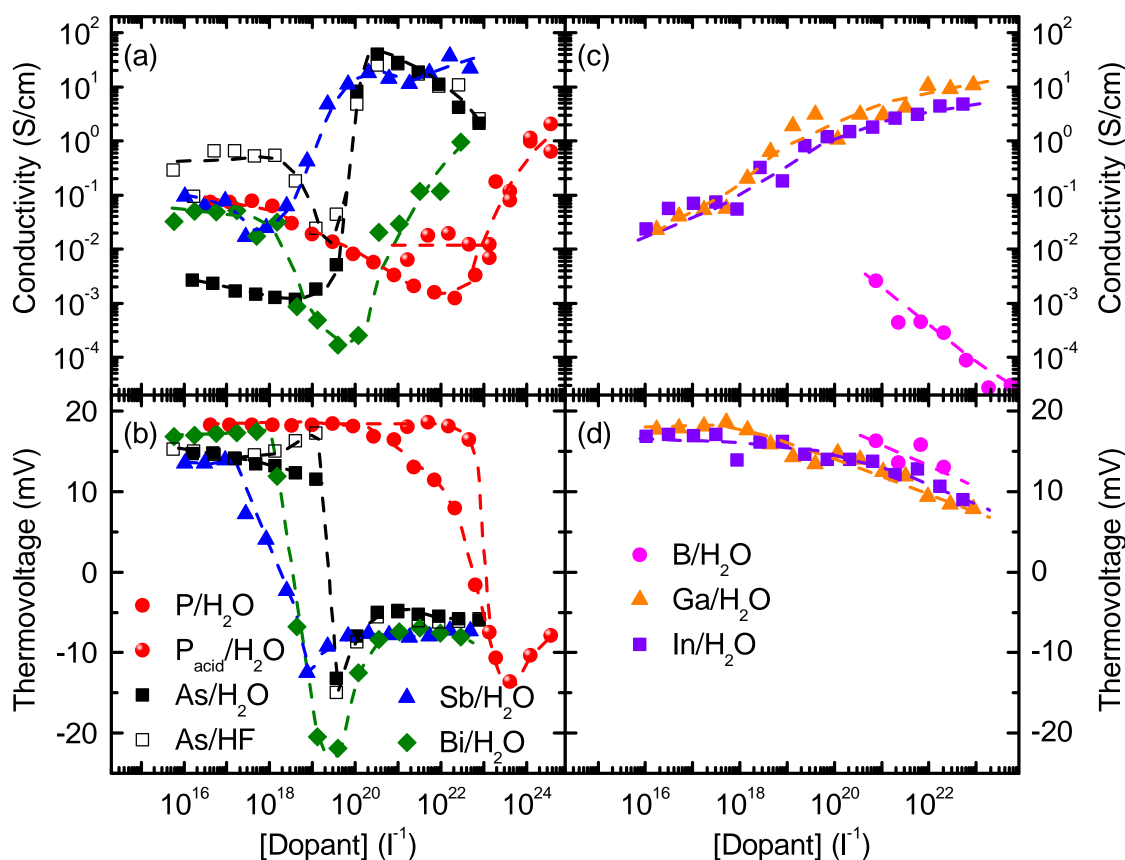

Figure 7.9. Laser-assisted wet-chemical doping of Ge films with group-III and -V elements: The electrical conductivity and the thermovoltage ($\Delta T = 45\,\mathrm{K}$) are shown for laser-assisted wet-chemically doped Ge films. Doping with group-V elements is shown in panel (a) and (b). High concentrations of P are obtained by using H_3PO_4 as a doping liquid. Doping with group-III elements is shown in panel (c) and (d). Closed symbols denote experiments with HF-free doping liquids and open symbols are used for HF-containing doping liquids.

source of unoxidized NPs. Square symbols in Fig. 7.9 (a) and (b) show the conductivity and the thermovoltage of As-doped Ge films, with open symbols corresponding to HF-containing and closed symbols to HF-free doping liquids, denoted by As/H_2O. While the conductivity in the samples doped with low concentrations of As in the doping liquid in HF-free liquids is smaller due to residual or regrown oxide, the As uptake is as efficient in HF-free as in HF-containing doping liquids, evidenced by the identical characteristic concentration of As in the doping liquid, where the thermovoltage changes sign. Also the effectiveness of both doping liquids is similar, as proven by identically high conductivities at high doping concentrations.

Figure 7.9 (a) and (b) further summarizes the results on laser-assisted wet-chemical doping of Ge films with the group-V elements P, Sb and Bi, all using HF-free doping liquids. The features of compensation, the change in sign of the thermovoltage and the rise in conductivity for high doping concentrations can also be observed for the other

group-V elements, demonstrating that laser-assisted wet-chemical doping is applicable to all those substitutional n-type dopants. The different characteristic concentrations where the thermovoltage changes sign are attributed to differences in the efficiency of adsorbate-specific diffusion and adsorption to the NP surface. This may also be the reason for the fact that in the case of P the characteristic concentration for the thermovoltage sign reversal is far beyond that for the other group-V elements. However, using H_3PO_4 higher concentrations of P in the doping liquid compared to the ICP solutions can be achieved. For P concentrations above $10^{23}\,l^{-1}$, these data merge with data obtained using ICP solutions as doping liquids. Apart from different adsorbate-specific adsorption effects, a different degree of ionization of the dopant in the laser-sintered matrix may further contribute to the variation of the doping efficiency found.

Figure 7.9 (c) and (d) shows the corresponding results on p-type doping of Ge films with the group-III elements B, Ga and In, again using HF-free doping liquids. For doping with Ga and In, the electrical conductivity steadily rises with increasing dopant concentration in the liquid and the positive thermovoltage decreases in magnitude correspondingly. Doping Ge films with B showed a similar decrease of the thermovoltage with increasing B concentration as observed for Ga and In. However, in this case the film morphology severely suffered from the treatment in the doping liquid, as was confirmed by SEM investigations, leading to the drastic decrease of the conductivity observed. Attempts to use Al as a dopant failed, irrespective of the starting agent and the Al concentration. A possible reason might be the large hydrate shell of $[Al(H_2O)_6]^{3+}$ ions in aqueous environments, prohibiting diffusion or the adsorption to the NP surface and possibly making Al incompatible with laser-assisted wet-chemical doping.[Cas06]

Temperature Dependence of Thermoelectrical Properties of Laser-Assisted Wet-Chemically Doped Ge

The discussion so far concentrated on the thermoelectrical properties of Ge films prepared by laser-assisted wet-chemical doping observed at room temperature. This already yields information on the applicability of the doping method and of the relative doping efficiencies of different dopants. More information on the transport properties of the doped films can be obtained by investigating the temperature dependence of the Seebeck coefficient and of the electrical conductivity. Figure 7.10 shows such data of the Seebeck coefficient for Ga-doped films with different concentrations of Ga in the doping liquid. A representative data set for undoped Ge taken from Fig. 6.2 (b) is also shown for comparison. The decrease of the room temperature Seebeck coefficient with increasing dopant concentration in the doping liquid is in agreement with Fig. 7.9. For increasing dopant concentration the shape of the curves continuously change in a way, which is in accordance with the literature and the data shown in Fig. 2.7.[Mid53] For the sample doped highest with Ga, the characteristic maximum of the Seebeck coefficient is not observed in the investigated temperature range, but the data can well be fitted linearly, typical for metallic transport. This clear indication of a single dominant transport mechanism allows the deduction of a carrier concentration n according to Eq. 2.37.

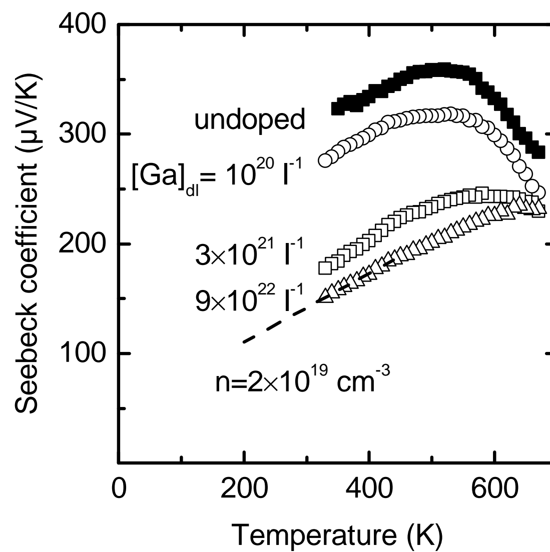

Figure 7.10. Temperature dependence of the Seebeck coefficient of laser-assisted wet-chemically Ga-doped Ge films: Using HF-free doping liquids containing the concentration of Ga stated in the figure, the Ge films are doped by with Ga applying an immersion time of 2 min. A representative undoped sample is also shown as a reference. The sample doped highest with Ga can be fitted according to Eq. 2.37 for temperatures around room temperature.

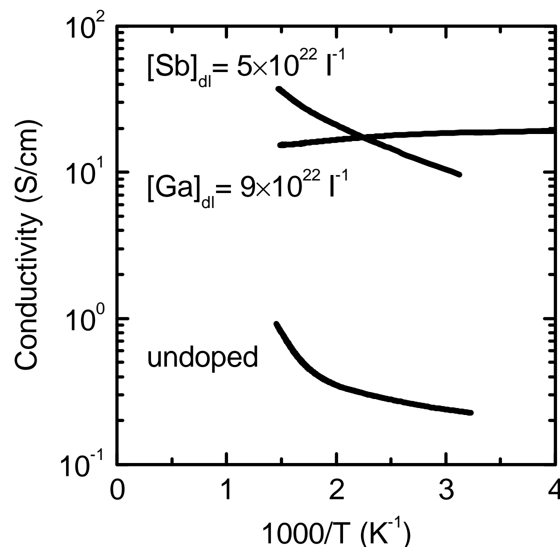

Figure 7.11. Temperature dependence of the electrical conductivity for laser-assisted wet-chemically Ga- and Sb-doped Ge films: As a reference, the results of an undoped sample is included. Both Sb and Ga doping with such high concentrations lead to a pronounced increase of the conductivity. High Ga doping leads to a decreasing conductivity with increasing temperature, as it is expected for degenerately doped Ge.

With an effective density of states mass for holes in Ge of $m^* = 0.355\ m_0$,[Jul73] a charge carrier concentration of approximately $n = 2 \times 10^{19}\ \mathrm{cm}^{-3}$ is found from the slope of S vs. T. In Fig. 7.10 the red dashed line represents a behavior according to Eq. 2.37 for this

carrier concentration.

Figure 7.11 shows the temperature dependence of the electrical conductivity of exemplary samples, doped with Ga and Sb at the highest available concentrations of $9 \times 10^{22}\,\mathrm{l}^{-1}$ and $5 \times 10^{22}\,\mathrm{l}^{-1}$ in the doping liquid, respectively. As already discussed in the context of Fig. 7.9, the room temperature conductivity of the doped samples is enhanced by approximately two orders of magnitude compared to the undoped reference. The highest available Sb doping does not yet lead to transport properties known for degenerately doped semiconductors, i. e., a decreasing conductivity with increasing temperature, but still gives rise to a convex curve in the Arrhenius plot. Consistent with the discussion of the Seebeck coefficient, the heavily Ga-doped sample exhibits a metallic behavior of the conductivity. The crossing of the Ga and the Sb curves most probably originates from macroscopic variations in the sample morphology which result from little differences in the sample preparation conditions. Similar variations can be found in Fig. 7.9 (b) at [Dopant] $= 0$, where nominally identical samples vary in conductivity by approximately one order of magnitude.

Sub-Bandgap Optical Absorption of Doped Ge Films

Apart from thermoelectric measurements where the impact of doping is evident in the sign and the magnitude of the Seebeck coefficient, the release of charge carriers from the incorporated dopant to the host material can also be detected by an enhanced optical absorption below the band gap due to free charge carrier.[Sch81, Aw91, Cha96] In Fig. 7.12 absorption spectra obtained by Photothermal Deflection Spectroscopy (PDS) are shown. Compared to the undoped sample, the absorption of the As-doped sample is

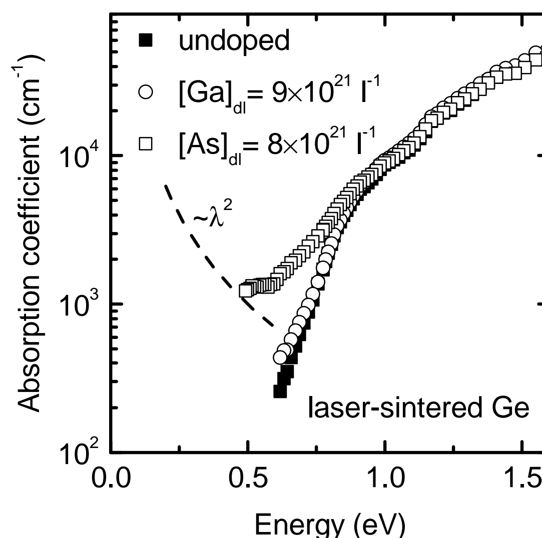

Figure 7.12. Free carrier absorption in laser-assisted wet-chemically doped Ge films: The optical absorption coefficient as measured by PDS in the sub-bandgap region is shown for undoped Ge and laser-assisted wet-chemically As- and Ga-doped Ge films.

enhanced at energies below the band gap. The concentration of As in the doping liquid and the experimental parameters used (an immersion time of 2 min and an immersion temperature of 325 K) lead to the highest electrical conductivities observed in laser-assisted wet-chemical As-doping of Ge and thus, also to the observed strong absorption of free charge carriers. In contrast, Ga-doping with a similarly high Ga concentration in the doping liquid does not yet lead to pronounced sub-bandgap absorption.

Although free carrier absorption of such complex materials such as laser-sintered Ge NPs can be used to compare the relative free carrier absorption between different samples, an absolute quantification is not possible. The theoretical dependence of the absorption coefficient α on the energy of the absorbed light in the Drude model is $\alpha \propto E^{-2}$, but this behavior is not observed strictly in all material systems.[Spi61] As can also be observed in Fig. 7.12 the energy range where this theoretical behavior should be visible most clearly is not accessible by the PDS spectrometer available.

7.6.2. Group-III and -V Elements for Doping Si Films

The doping method shall now be transferred to films of Si NPs. The results are shown in Fig. 7.13 (a) through (d). A typical dangling bond density in such laser-sintered films of Si NPs is on the order of $10^{18}\,\mathrm{cm}^{-3}$ to $10^{19}\,\mathrm{cm}^{-3}$.[Lec08] This makes the situation different from the experiments with Ge NPs, since the thermoelectrical properties of nominally undoped laser-sintered films is less well defined until the intentional doping outnumbers the dangling bonds. For low doping E_F of laser-sintered Si NP films is pinned at the dangling bond level in the middle of the band gap.[Bro08] Together with the larger band gap of Si compared to Ge, this results in a much lower electrical conductivity for laser-sintered Si films compared to Ge films. Thus, the thermovoltage can reliably be interpreted only for highly doped Si samples. In Fig. 7.13 (a) and (b) the conductivity and the thermovoltage are shown for n-type doping of laser-sintered Si NP films with P, As and Sb. For high doping levels the curves show a similar behavior as in the case of Ge films. They exhibit a negative thermovoltage and thus are electron conductors as expected. However, due to the intrinsic behavior of undoped Si with a large density of dangling bonds, the clear signature of compensation, a minimum of the conductivity, cannot be observed. The concentration dependence of the thermovoltage is very similar for all dopants tested, although the onset concentration at which the conductivity rises differs by up to one order of magnitude between different doping elements. The undiluted Bi doping liquid contains 20 % HCl, which dissolved the Si NPs, prohibiting successful doping experiments, whereas in diluted Bi doping liquids the doping concentration most likely was to low to show an effect on conductivity or thermovoltage.

Laser-assisted wet-chemical doping of Si films with group-III elements could successfully be shown for B and Ga. The data in Fig. 7.13 (c) and (d) show that the conductivity reached is lower than in the case of doping with group-V elements. The thermovoltage is positive as expected for doping with group-III elements, and decreases with increasing

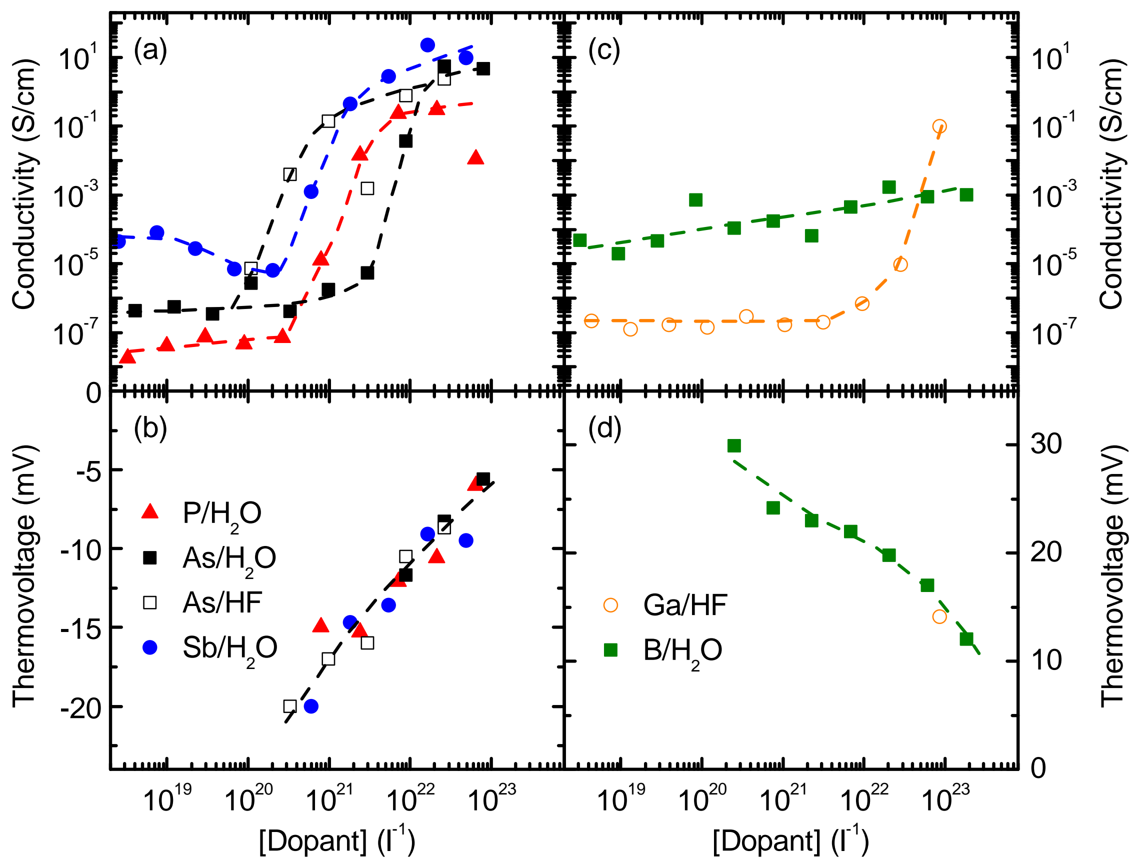

Figure 7.13. Laser-assisted wet-chemical doping of Si films with group-III and -V elements: The electrical conductivity and the thermovoltage for a temperature difference of $\Delta T = 45\,\mathrm{K}$ are shown for laser-assisted wet-chemically doped Si films. Doping with group-V elements is shown in panel (a) and (b), doping with group-III elements is shown in panel (c) and (d). Closed symbols denote HF-free dopping liquids, whereas open symbols denote experiments using HF-containing doping liquids.

doping concentration. Aluminum shows the same deficiency as discussed in the case of Ge in Sec. 7.6.1. Indium, in turn, is a deep acceptor in Si and not commonly used for doping in Si technology.[New55, Ont67]

As in the case of Ge, doping Si with As by HF-containing and HF-free doping liquids is also compared in Fig. 7.13 (a) and (b). Different from Ge, where in Fig. 7.9 (a) the As threshold concentration for a thermovoltage sign reversal and the corresponding rise in conductivity is the same for HF-free and HF-containing doping liquids, the corresponding data sets in case of Si are shifted by more than one order of magnitude (closed and open squares, respectively). In Si, HF-containing As doping liquids outperform HF-free ones in terms of doping efficiency. This finding shall further be investigated in the next section.

7.6.3. Arsenic-Doping of SiGe Alloy Films

HF-free and HF-containing doping liquids have different impact in Si and Ge concerning the As concentration, where the onset of effective doping occurs (see Fig. 7.9 and Fig. 7.13). Applying laser-assisted wet-chemical As-doping to $Si_{1-x}Ge_x$ alloy NPs is a suitable experiment to investigate the origin of this effect. Figure 7.14 (a) and (b) show the conductivity and the thermovoltage for laser-assisted wet-chemically As-doped $Si_{1-x}Ge_x$ alloy NPs of varying Ge content x. All samples were oxide etched by HF prior to the doping step, where HF-free doping liquids were used then. The resulting Ge-rich alloy films with Ge contents down to 60 % behave very similarly to pure Ge films. For films with a lower Ge content the onset concentration, i. e., the approximate concentration where the conductivity rises most steeply, is shifted to higher concentrations of As in the doping liquid. Thus, the doping efficiency decreases towards that characteristic of pure Si films. The dependence of the approximate onset concentration on the Ge content is shown in panel (c).

The surface of both, Si and Ge NPs used in this study, exhibits a native oxide shell after their synthesis due to unavoidable contact to ambient air, as discussed in Chap. 4. If HF-containing doping liquids are used for laser-assisted wet-chemical doping, the polarity of the oxidized NP surface allows the doping liquid to wet the film and instantaneously penetrate deeply into it. If, however, the immersion follows the oxide removal step by HF, the aqueous doping liquid needs to wet hydrogen terminated NPs, which result from the HF treatment as discussed in the context of Fig. 4.6. Therefore, reduced wetting of hydrogen terminated Si NP films by aqueous doping liquids compared to oxide etched Ge NP films is the reason for the different onset concentrations of Si and Ge observed in Fig. 7.14 (a) and (b). That the NP thin films used in this study indeed show this behavior is demonstrated in Fig. 7.14 (d). The contact angle of a water drop on HF-treated NP films is shown as a function of the Ge content. Si-rich films exhibit a high contact angle of up to 120°, whereas for Ge contents above 60 % the contact angle can be as small as 30°.

The contact angle of water on HF-treated Ge wafers was reported to be approximately 45°, which is less than in the case of Si, where it usually is larger than 70°.[Ada96, Bal10, Ma10] This means that Ge is more hydrophilic compared to Si in general. A second reason for the observed wetting of water on etched Ge NP films is that there the hydrogen termination is known to be unstable in ambient conditions, as has been shown in Fig. 4.7. This instability may be even more pronounced when the Ge NPs come in contact with the doping liquid.[Bod03] Then, the hydrogen termination is lost and the Ge NPs can reoxidize, making the surface hydrophilic again. As a result, easy penetration by the doping liquid is also possible for previously HF-treated Ge NP films.

Compared to the results in Fig. 7.14 (a) and (b) it can be concluded that the reduced doping efficiency of HF-free doping liquids in combination with Si NP films is due to the reduced tendency of the doping liquid to penetrate the film, caused by a stable hydrophobic hydrogen termination of Si NPs after oxide removal by HF.

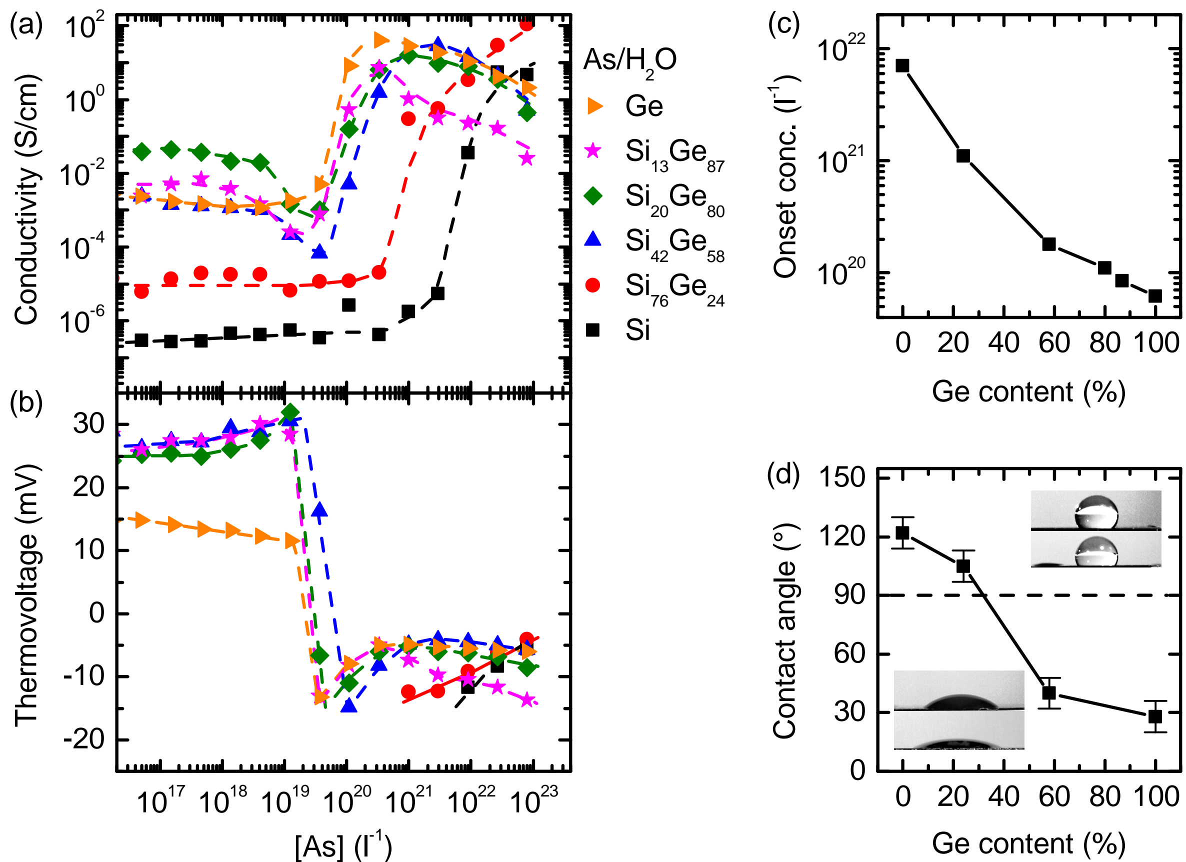

Figure 7.14. Laser-assisted wet-chemical doping of SiGe alloy films with As: In panel (a) and (b) the room temperature conductivity and the thermovoltage at a mean temperature of 325 K and a temperature difference of 45 K is shown for laser-assisted wet-chemical doping of $Si_{1-x}Ge_x$ films with As, using HF-free doping liquids. The Ge content is varied from 0 % to 100 %. Panel (c) shows the approximate onset concentration, where the conductivity rises steepest, versus the Ge content. Panel (d) shows the contact angle of a drop of H_2O on the films after oxide etching by HF, together with side-view photographs of water droplets on the respective $Si_{1-x}Ge_x$ NP films.

7.6.4. Solid Solubility and Laser-Assisted Wet-Chemical Doping

From experiments on ion implantation followed by laser-annealing it is known that carrier concentrations can exceed the values of the equilibrium solid solubility of the dopant element in the host material.[App79] Laser-assisted wet-chemical doping as it is presented here also exhibits a fast recrystallization of the material after the ns-laser pulse. It is thus interesting to compare whether solid solubility can be a reason for the different doping efficiencies observed. Figure 7.15 summarizes the temperature dependence of the equilibrium solid solubility for group-III and -V dopants in Si as well as in Ge according to the literature.[Tru60] The data for different elements vary by up to 4 orders of magnitude. In Si, the lowest solubility is reported for In (not shown), which precipitates already above concentrations of $4 \times 10^{17}\,cm^{-3}$.[Bac57] For the elements which led to successful doping in Fig. 7.13 no clear correlation between

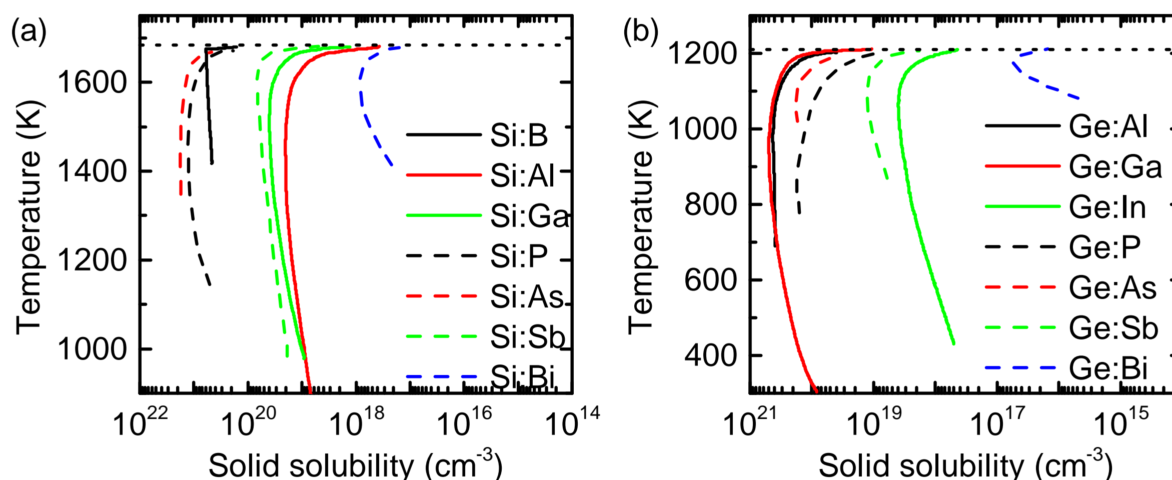

Figure 7.15. Solid solubility limits for various elements in Si and Ge: Data for (a) Si and (b) Ge are reproduced from Ref. Tru60. The horizontal dotted lines denote the melting temperatures of Si and Ge, respectively.

doping efficiency, deduced from Fig. 7.13, and the solid solubilty can be observed.

The doping experiments on Ge in Fig. 7.9 allow a more clear statement on the effect of the equilibrium solid solubility on the efficiency of laser-assisted wet-chemical doping. For example, the solubilities of Ga and In differ by two orders of magnitude. However, the thermoelectric data suggest very similar doping efficiencies. On the other hand, similar solubilities of P and As are not reflected in a similar doping efficiency. Most clearly, the solubility of Bi in Ge falls below the density of dangling bonds assumed in the experiments, so that quenching after laser-sintering is obvious from the doping experiments.

In conclusion, the experimental data in Fig. 7.9 and 7.13 do not suggest a major influence of the solid solubility in thermal equilibrium on the efficiency of laser-assisted wet-chemical doping.

7.7. Quantitative Dopant Analysis

The studies so far demonstrated the feasibility of laser-assisted wet-chemical doping of sintered NP films and that the doping level realized can be tuned by several parameters. This section discusses attempts to quantitatively determine the efficiency of the method concerning both, the physical incorporation of dopant atoms into the sintered host material, as well as the density of charge carriers released by the dopant atoms.

7.7.1. Elemental Abundance of Dopants

To study the elemental abundance of the dopants incorporated into the material by laser-assisted wet-chemical doping, Laser-Ablation Inductively-Coupled Plasma Mass

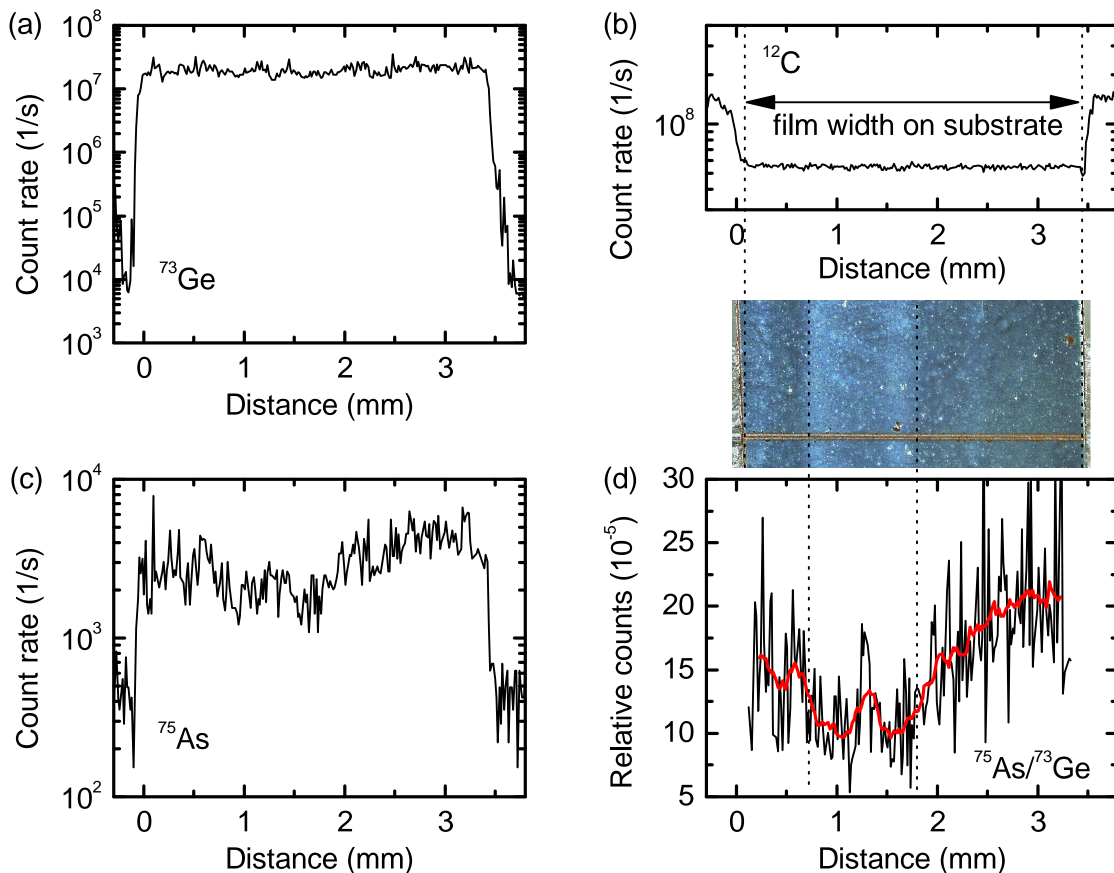

Figure 7.16. LAICP-MS measurement of a laser-assisted wet-chemically As-doped Ge film: Panel (a) shows the count rate for ^{73}Ge as the ablation laser is scanned across the sample. The count rate of ^{12}C, originating from the polyimid substrate, is shown in panel (b). The dopant-related ^{75}As count rate is shown in panel (c). The variation of the relative counts of ^{75}As to ^{73}Ge in panel (d) can be correlated to a variation of the sinter laser fluence by comparing with an optical micrograph of the respective sample. A high sinter fluence (between the dotted lines) corresponds to a low As content.

Spectrometry (LAICP-MS) is applied. A pulsed laser with $\lambda = 213\,\text{nm}$ (New Wave NWR213) of high fluence ($6\,\text{J/cm}^2$) and a repetition rate of 20 Hz ablates the film together with parts of the polyimid substrate in vacuum. The LAICP-MS system is capable of scanning across the sample, so that a spatial resolution of the order of the beam diameter of 50 µm can be achieved. This is sufficiently large to average out the meander structure of the laser-sintered films, but small enough to detect inhomogeneities resulting from the sinter laser which are shown in Fig. 5.1. The ablated particles are then injected into an ICP plasma and fractionized into their atomic components, which are then detected by a Perkin Elmer Nexion mass spectrometer.[Hil13, Hou80]

In Fig. 7.16 an exemplary LAICP-MS measurement of a Ge film prepared by laser-assisted wet-chemically As doping is shown. With the ablation laser scanning across the

sample perpendicularly to the direction of the sinter laser sweep, the ^{73}Ge count rate is shown in panel (a). Background and Ge film can be discriminated due to a Ge signal three orders of magnitude higher compared to the signal originating from the sample holder. The ^{12}C count rate in panel (b) allows to localize the borders of the sample and correlate them with an optical micrograph. Panel (c) shows the ^{75}As count rate. The relative count rate of ^{75}As and ^{73}Ge is shown in panel (d), together with a moving average plotted as red line.

The first point to note is that the As content is not constant throughout the sample. For the spatial resolution given by the spot size a local variation of the dopant molar fraction of up to a factor of 2 is found. This is in agreement with the discussion in the context of Fig. 7.6. The numbers discussed in the following are thus values averaged over one sample. The second point to note is that the variation of the As content can be correlated to the fluence of the sinter laser. In the optical micrograph above panel (d), regions of high sinter laser fluence exhibit a more metallic reflectivity (within the dotted lines). The high metallic brightness can well be identified with regions of lower As content. A possible reason is that during the time the NPs and the applied dopants are heated by the sinter laser pulse, the volatility of As is higher compared to that of Ge.

To translate the relative count rates of dopant elements and host element into dopant concentrations in the sintered film, a NIST 612 standard material is used to calibrate the instrument.[1] The molar fraction obtained from the LAICP-MS count rate is thus corrected for matrix effects, the element's isotopic composition and the sensitivity of the instrument.

Figure 7.17 shows the results obtained on the relative elemental abundances in As-doped Ge in panel (a) (the 270 K data set of Fig. 7.7), on Ga-doped Ge in panel (b) (HF-containing doping liquid, 330 K immersion temperature and 25 min immersion time), on As-doped Si in panel (c) (the data shown by open symbols in Fig. 7.13 (a) and (b)) and on B-doped Si in panel (d) (data set from Fig. 7.13 (c) and (d)). For all materials investigated in Fig. 7.17, the amount of incorporated dopant species rises monotonically with their concentration in the doping liquid. The apparent saturation that can be perceived for low doped films is attributed to the sensitivity limit of LAICP-MS. Notably, the uptake of As and Ga into Ge NP films shown in panel (a) and (b), respectively, approximately follows a power law with exponent 1, whereas the uptake of As or B into Si NP films in panel (c) and (d) exhibits a weaker dependence and also does not reach the same high concentrations in the thin film. Again, this difference of Ge and Si NP films strongly suggests specific adsorption as uptake mechanism. Assuming the atomic density of bulk Si ($5.02 \times 10^{22}\,\mathrm{cm}^{-3}$) and Ge ($4.42 \times 10^{22}\,\mathrm{cm}^{-3}$) in the diamond crystal structure for the sintered NP films as well as a homogeneous distribution of the dopants, the relative elemental abundances obtained from the LAICP-MS measurements can be converted to dopant densities. The corresponding highest obtained concentrations are $2 \times 10^{21}\,\mathrm{cm}^{-3}$

1 NIST 612 contains Si: 336.5 g/kg, Ge: 35 mg/kg, Ga: 36 mg/kg, As: 37 mg/kg and B: 33 mg/kg. With the high Si content and the low Ge content it has to be noted that this standard material is more suited for Si films than for Ge films.

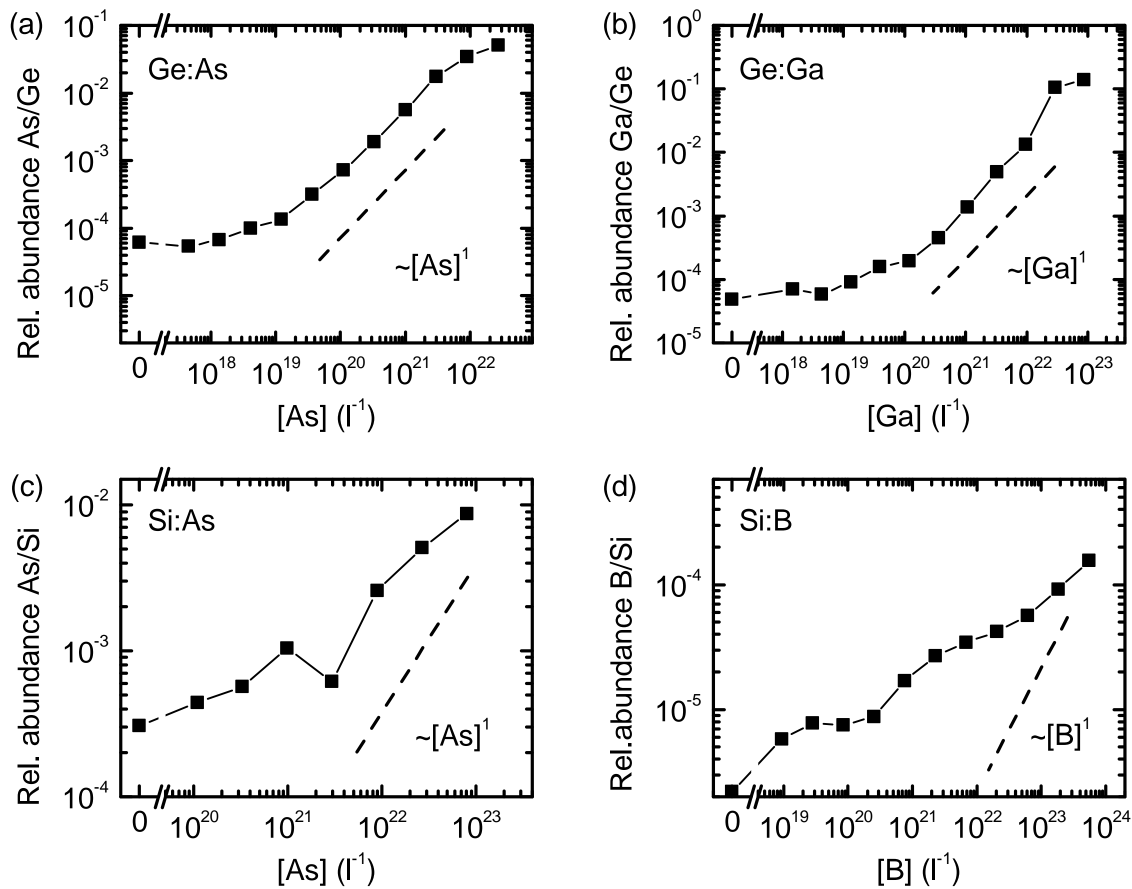

Figure 7.17. Results of LAICP-MS measurements for laser-assisted wet-chemically doped Ge and Si films: For all materials investigated, As or Ga dopants in the case of Ge films and As or B in the case of Si films, the relative abundance of the dopant in the host material rises with an increasing concentration of the dopant in the doping liquid. Panel (a) and (b) show an approximately proportional increase of the dopant concentration in Ge films with the concentration of the dopant in the doping liquid. For Si films the elemental concentration of the dopant in the film also increases with the dopant concentration in the liquid, but the exponent is smaller than 1.

for Ge:As, $6 \times 10^{21}\,\mathrm{cm}^{-3}$ for Ge:Ga, $4 \times 10^{20}\,\mathrm{cm}^{-3}$ for Si:As and $8 \times 10^{18}\,\mathrm{cm}^{-3}$ for Si:B.

Again, the importance of in-diffusion is emphasized by these numbers. Doping Ge with an As concentration of $2.7 \times 10^{22}\,\mathrm{l}^{-1}$ in the doping liquid in Fig. 7.17 (a) leads to a density of As in Ge of $2 \times 10^{21}\,\mathrm{cm}^{-3}$, which corresponds to one As atom per approximately 20 Ge atoms. One can estimate the porosity of the as-deposited NP film to be approximately 50 %. If for argument's sake one neglects in-diffusion and assumes that only As species in the doping liquid that initially penetrated the pores of the film are adsorbed and later incorporated by laser-sintering, then the corresponding density of As in Ge would be only $2.7 \times 10^{19}\,\mathrm{cm}^{-3}$, which is two orders of magnitude less than the density found by LAICP-MS. In conclusion, without the mechanism of in-diffusion only one percent of the As dopants could be incorporated.

These numbers further allow to assess whether the adsorption creates a monolayer of dopants on the NP surface or whether multiple layers are adsorbed. Using Ge NPs with a diameter of 27 nm and estimating the lower bound to the NP surface area occupied by an adsorbed dopant species to be $3 \times 3\,\text{Å}^2$,[Kis99][2] a monolayer of adsorbed arsenate would correspond to a concentration of As in the laser-sintered material of 5.3 %. The measured concentration of one As atom per 20 Ge atoms is very close to this estimate, so that under the mentioned assumptions, a multilayer adsorption would not yet be necessary. However, compared to the 270 K immersion temperature samples measured by LAICP-MS, the 330 K data set in Figure 7.7 (c) and (d) is shifted by more than a decade to lower As concentrations in the doping liquid, indicating an even stronger adsorption that includes multiple layers of adsorbed dopants.

7.7.2. Raman Scattering by Free Charge Carriers

The Fano Effect in Heavily Doped Semiconductors

It is necessary to measure the concentration of mobile charge carriers in the semiconductor material after laser-assisted wet-chemical doping because the mere physical incorporation, as it is studied in the previous section, is not equivalent to doping on an electronic level. Dopant deactivation is a common phenomenon in heavily doped semiconductors and also in nanostructured material.[Nob82, Kuz86, Bjö09, Chr07, Sim09] Conventional measurements of the charge carrier concentration by Hall measurements are limited in the case of the thin film samples discussed here, due to their porous morphology and the rather complicated mixed phase system. Hall measurements average over large sample areas, which might be undesirable for such samples, considering the local variation of the dopant distribution already discussed. Furthermor, for the present material it is unclear to which extent percolation effects and also the different mobilities of charge carriers inside a grain and across grain boundaries affect the results obtained by macroscopic Hall measurements.[Ort80]

As an alternative to Hall measurements of the carrier density a non-contact method based on micro-Raman spectroscopy shall now be applied. This method, which became popular in recent years for mapping doping distributions, e. g. in solar cells, exploits the impact of charge carriers on the lineshape of the Raman signal of semiconductors for rather high doping levels to determine the carrier density.[Bec09, Kun13, Gun10]

For high densities of charge carriers, phononic Raman scattering processes interact with electronic Raman scattering. With charge carriers populating an energetic continuum of states and phonons populating discrete states, the Lorentzian Raman lineshape of the non-interacting case changes to an asymmetric Fano-type lineshape

---

2 This is based on the As-O bond length in arsenate of 1.7 Å, which is roughly doubled for the estimation.[Kis99]

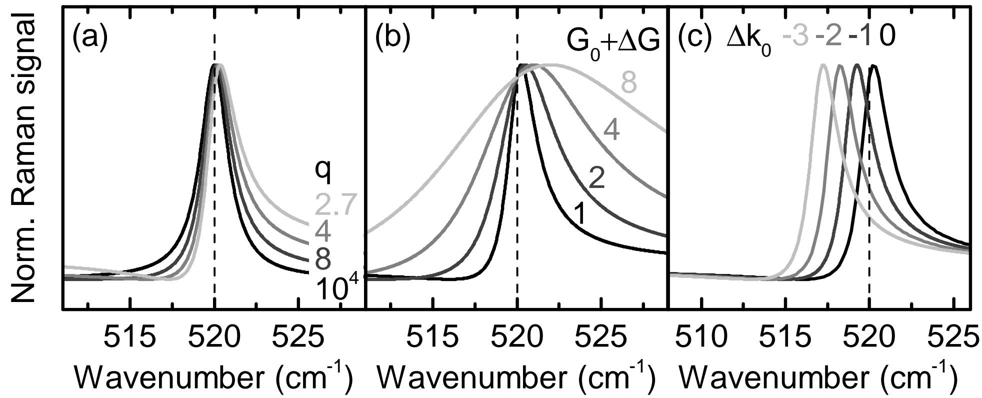

Figure 7.18. Change of a Raman spectrum with Fano parameters: Panel (a) shows simulated Raman spectra with Fano lineshape for different asymmetry parameters q. The width and the peak shift are fixed at $G_0 + \Delta G = 1\,\text{cm}^{-1}$ and $\Delta k_0 = 0\,\text{cm}^{-1}$, respectively. For negative values of q the asymmetry is inverted. Panel (b) and (c) show the corresponding line shapes for different $G_0 + \Delta G$ and Δk_0 with fixed $q = 4$.

[Fan61, Cha78]

$$I(k) = I_0 \frac{\left[q\left(G_0 + \Delta G\right) + k - \left(k_0 + \Delta k_0\right)\right]^2}{\left(G_0 + \Delta G\right)^2 + \left[k - \left(k_0 + \Delta k_0\right)\right]^2}, \tag{7.2}$$

where I is the observed signal intensity, I_0 is a scaling factor, q is the Fano asymmetry parameter, G_0 is the line width of the undoped material, ΔG is the additional linewidth induced by the interaction with free charge carriers, k is the wavenumber, k_0 is the peak position of the undoped material and Δk_0 is the softening of the Raman mode induced by the interaction with the charge carriers. Depending on the matrix elements of the Raman tensor, q can be positive as well as negative.[Cha80] [3] For $|q| \to \infty$, the Fano lineshape is identical to a Lorentzian lineshape.

In Fig. 7.18 normalized simulated Raman spectra with a Fano lineshape are shown. In panel (a) the asymmetry parameter q is varied for some positive values, leading to a shoulder at the high wavenumber side for small q. In panel (b) and (c) $q = 4$ is fixed and the linewidth $G_0 + \Delta G$ and the phonon softening Δk_0 is varied, respectively. Notably, in all panels the mode has $k_0 = 520\,\text{cm}^{-1}$, but the peak maximum shifts with variation of any one of the three parameters.

With the Fano effect in Raman scattering it is possible to determine a sample's carrier concentration via comparison to reference data with known carrier density. For that task, in principle all the quantities q, ΔG and Δk_0 can be used because they depend distinctively on the charge carrier concentration. Although no analytical expression for the relation between the Fano parameters and the carrier density is known, theory predicts two useful relations: $q \propto p^{-1}$, with p being the hole concentration in a p-type semiconductor and $q \propto \left(E_{\text{laser}} - E'\right)^{-1}$, where E_{laser} is the energy of the excit-

3 For example, using a laser with $\lambda = 1490\,\text{nm}$, heavily Ga-doped Ge changes the sign of q from negative to positive at 77 K.

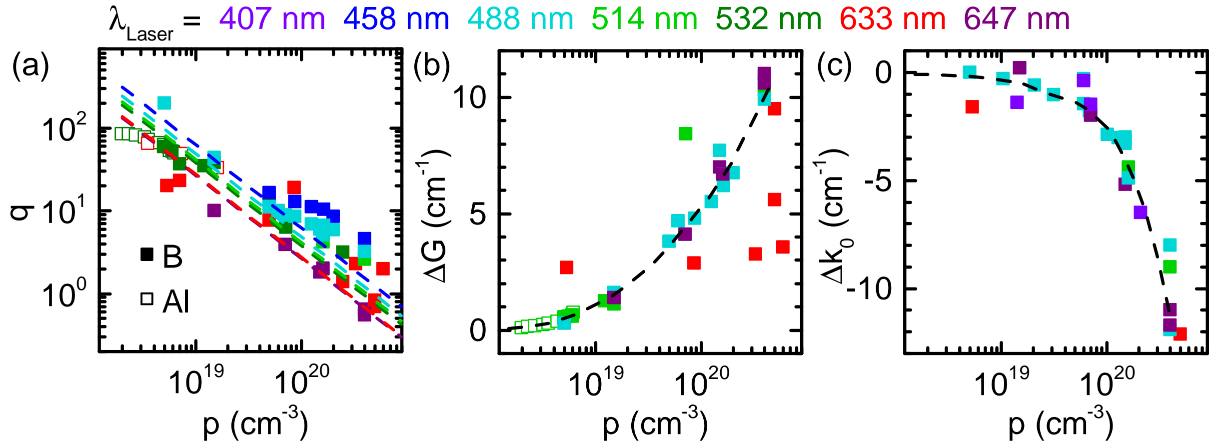

Figure 7.19. Literature data on the Fano effect in p-type Si: Panel (a) summarizes data from the literature on the asymmetry parameter q for B-doped (closed symbols) and Al-doped (open symbols) Si. The dashed lines in panel (a) obey $q \propto p^{-1}$ according to Ref. Cer73 for each laser wavelength and for a fixed hole concentration they also obey $q \propto (E' - E_{\mathrm{laser}})^{-1}$, where E_{laser} is the energy of the laser light and $E' = 3.3\,\mathrm{eV}$ is the energy of the critical point in Si.[Cer73a] Panel (b) and (c) show corresponding data on the additional linewidth ΔG and the wavenumber shift Δk_0, respectively. Dashed lines serve as a guide to the eye. The data are taken from Refs. Cer72, Cer73a, Bal75, Jou75, Cha78, Ole81, Com84a, Con84, Per96, Nic00, Len01, Len03, Bec09, Gun10, Rif11.

ing laser light and E' is the energy of a critical point, which is, e. g. $E' = 3.3\,\mathrm{eV}$ in Si.[Lau87, Cer73a] ΔG and Δk_0 are assumed not to be changed with the exciting laser wavelength.[Cer73a] The material studied most intensively in the literature is p-type Si.[Cer72, Cer73a, Cer73b, Bur10] Only some reports on similar experiments in n-type Si and p- and n-type Ge exist, which however do not contain enough information to systematically use them as a reference here.[Jou75, Cha77, Cha78, Com83, Com84a, Con84, Con85, Fuk10, Cer72, Ole81, Wag85, Len03, San13a, San13b]

A collection of data from the literature on B- and Al-doped Si is shown in Fig. 7.19. All data points, plotted versus the hole concentration p in Si, are color-coded according to the laser wavelength used in the experiment. In panel (a) the asymmetry parameter q is shown. The dashed lines obey the relations mentioned above. Spectra measured in experiments with red excitation exhibit a more pronounced asymmetry and are thus more reliable. Empirically the relation

$$p = \frac{3.74 \times 10^{20}\,\mathrm{cm}^{-3}\mathrm{eV}}{q\,(E' - E_{\mathrm{laser}})} \tag{7.3}$$

can be deduced from panel (a). The additional linewidth ΔG and the phonon softening Δk_0 are shown in panel (b) and (c), respectively. The latter parameters are not used for the determination of the carrier concentration here because nano-size effects and strain contribute to the spectra measured on laser-sintered NP films in a way which cannot be

assessed well enough. Additionally, the literature is not precise in stating whether the peak position or the peak maximum is taken.

The Fano Effect in Laser-Assisted Wet-Chemically Doped Ge and Si Films

To apply micro-Raman spectroscopy on samples prepared by laser-assisted wet-chemical doping and to maximize the asymmetry in the spectra observed, a Krypton laser with $\lambda = 647\,\text{nm}$ was used in a setup with a $20\times$ objective (numerical aperture 0.4) and a Dilor triple spectrometer. The power on the sample was kept below 350 µW to minimize the influence of temperature on the spectral lineshape. The wavenumber scale was corrected using the emission of a Neon lamp.

The samples investigated here are identical to those measured by LAICP-MS in Fig. 7.17. Figure 7.20 shows the micro-Raman results obtained on Ge films doped with As and Ga. In panel (a) the experimental data of the zone center optical mode in Ge are shown as open symbols. Additionally, the fit curves according to Eq. 7.2 are plotted as solid lines. The numbers indicate the concentration of As in the doping liquid. The undoped sample was only HF-treated. As a reference, the Lorentzian fitted line of a Ge wafer is also shown as black solid line. Compared to the Ge wafer reference, the undoped laser-sintered Ge NP thin film is slightly broadened and shifted to lower wavenumbers, both most probably caused by the poly-crystallinity of the film with a distribution of grain sizes. Increasing the As concentration in the doping liquid at first leads to a further shift of the mode to lower wavenumbers, accompanied by an increased linewidth. Characteristic for the Fano effect, a shoulder at low wavenumbers appears, which is described by negative values of q. Notably, the two samples doped highest with As show less interaction of phononic Raman scattering with free charge carriers.

The thermovoltage and the electrical conductivity of those samples are shown in panel (b) and the fit parameters $G_0 + \Delta G$, Δk_0 and q are presented in panel (c). For both panels the abscissa is deduced from the LAICP-MS measurements. The thermoelectric data follow the behavior for As-doping of Ge films already discussed in the context of Fig. 7.4. Starting from p-type undoped material, increased As-doping leads to a negative thermovoltage. For low As concentrations the conductivity is reduced (compensation) but largely enhanced for medium As concentrations. The highest conductivity occurs when the magnitude of the thermovoltage is smallest. For clarity this region is shaded in panel (b) and (c). High As concentrations reduce the conductivity again, as well as slightly increase the magnitude of the thermovoltage. The linewidth of the zone-center Raman mode is roughly $2.3\,\text{cm}^{-1}$ for undoped material. It increases then for increased As doping up to values of more than $3\,\text{cm}^{-1}$ for the sample showing the highest electrical conductivity. Similar to the thermoelectric data, the linewidth decreases again for highest As doping. Also the phonon softening Δk_0, measured with respect to the Ge wafer, reflects this behavior. The sample with the highest conductivity shifts by $-1.3\,\text{cm}^{-1}$ to lower wavenumbers, compared to $-0.6\,\text{cm}^{-1}$ for undoped or the highest doped material. The asymmetry parameter q shows a monotonic behavior with values as large as $q = -18$ for insignificantly doped material, which decreases in magnitude down to

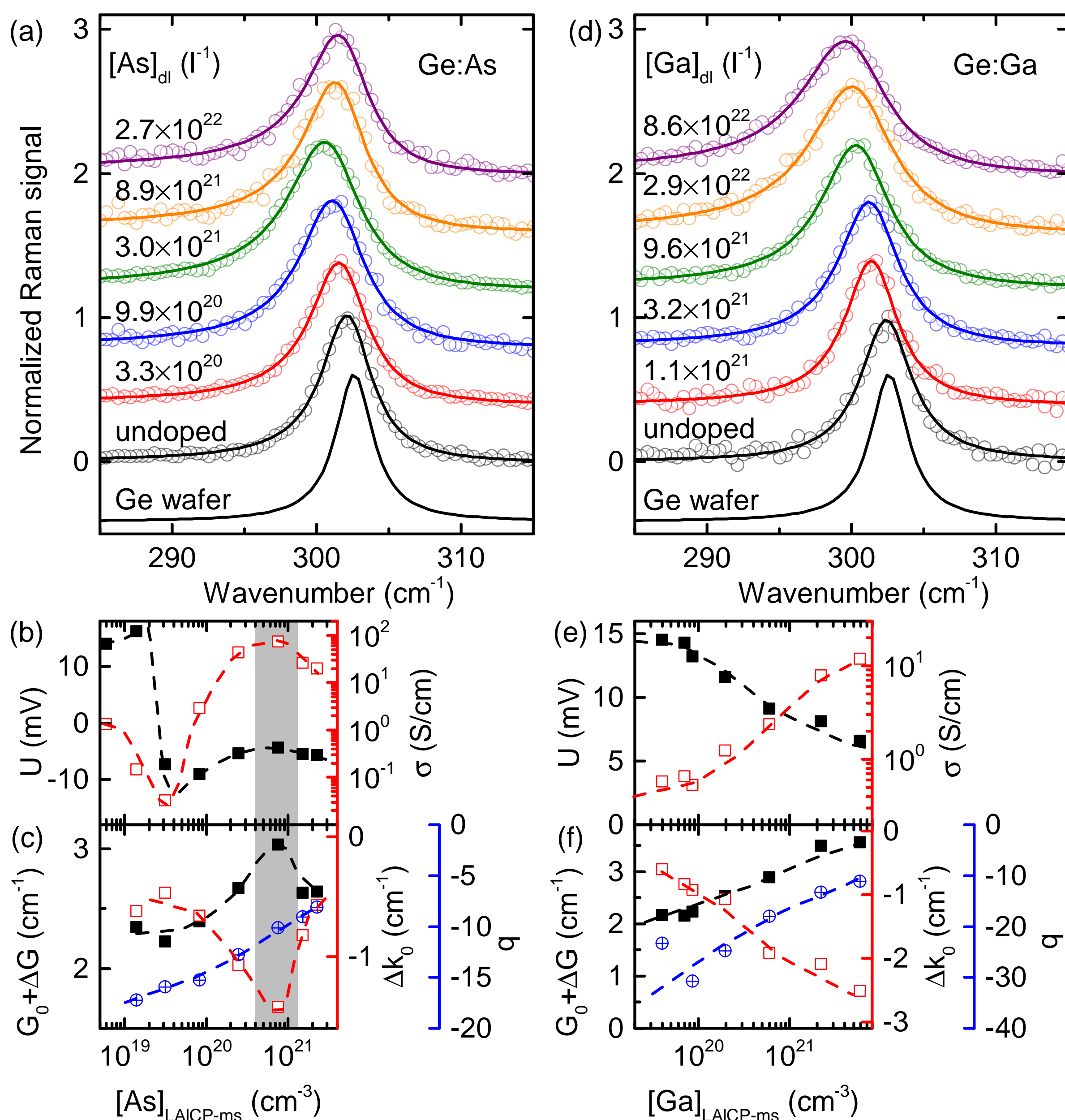

Figure 7.20. Raman spectra of laser-assisted wet-chemically doped Ge films: Panel (a) shows Raman spectra of Ge films, doped with different concentrations of As in the doping liquid. The experimental data (open symbols) can be fitted by a Fano lineshape according to Eq. 7.2. The spectrum of a Ge wafer is shown as solid line, too. The spectra were normalized and shifted vertically. Panel (b) shows the thermovoltage U at a mean temperature of 325 K and a temperature difference of 45 K and the rooom temperature electrical conductivity σ of the samples investigated in the Raman experiment. The abscissa is the abundance of the dopant in the host material, as determined by LAICP-MS. Panel (c) shows the Fano fit parameters in panel (a): total Fano linewidth $G_0 + \Delta G$, peak shift Δk_0 and asymmetry parameter q. The shaded region marks where the correlation of macroscopic thermoelectric data and micro-Raman fit parameter is most clearly observed. In panel (d) to (f) the corresponding data and fit values are shown for the case of Ge doped with Ga.

$q = -8$ for the sample doped highest with As.[4]

The obtained results on laser-assisted wet-chemically As-doped Ge films support the finding that, although the incorporated amount of As rises monotonically with the As concentration in the doping liquid, the carrier concentration decreases for very high As concentrations. This was found in macroscopic measurements of thermoelectric properties as well as in microscopic studies discussed here, demonstrating the high degree of validity of both experiments.

Figure 7.20 (c) through (f) show the corresponding data obtained on laser-assisted wet-chemically Ga-doped Ge films. Still, q is negative, in accordance with similar experiments in the literature on p-type Ge samples.[Fuk10] As already discussed in the context of Fig. 7.9, the thermovoltage and the conductivity follow a monotonic behavior with increasing Ga concentration in the doping liquid. The same is found for the Fano fit parameters. Both, the linewidth increase as well as the phonon softening are even more pronounced compared to the respective samples doped with As. The asymmetry parameter q reaches values similarly low, with $q = -10$ for the sample doped highest with Ga.

Corresponding data are shown in Fig. 7.21 for doping Si films with As and B. The undoped Si wafer reference can well be fitted by a symmetric Lorentzian lineshape with a width of $G_0 = 1.47\,\mathrm{cm}^{-1}$, centered around $k = 523.6\,\mathrm{cm}^{-1}$. The undoped laser-sintered Si NP film exhibits a slightly broadened Lorentzian signal with $G_0 = 2.0\,\mathrm{cm}^{-1}$, centered at a lower wavenumber of $k = 522.7\,\mathrm{cm}^{-1}$. This again is an indication for the degree of disorder in the sintered films due to their granular structure. Increased doping with As clearly transforms the films to n-type Si and gives rise to a low-wavenumber shoulder, which is in agreement with the literature.[Jou75, Cha77, Cha78, Con84, Con85] In the case of As-doping Si films both the thermoelectric data and the Fano fit parameters follow a monotonic behavior. The reduced variance of the microscopic fit parameter suggests that the rather large variation of the conductivity data is related to macroscopic features of the sample morphology, e. g. cracks of dewetting, rather than ineffective doping.

Finally, Fig. 7.21 also summarizes the results obtained on doping Si films with B. The spectra show that a shoulder appears on the high wavenumber side of the zone-center optical phonon mode, which is reflected by a positive q fit parameter. Increased B doping clearly increases the asymmetry as well as the width of the spectra. The peak shift does not follow such a clear behavior, which indicates that other effects, such as strain or slightly different thermal resistances to the substrate, have an additional influence. Concentrating on the samples doped highest with B during laser-assisted wet-chemical doping, the fitting of the spectra according to Eq. 7.2 yields q and, using the relation in

4 The fact that q does not show an extreme value for the sample with the highest electrical conductivity should not be overinterpreted. Although q is the parameter most characteristic for the interaction of Raman modes with charge carriers, it is also the one most prone to fitting errors as well as to the influence of residual small nanocrystals or amorphous regions to the overall Raman spectrum.[Len03] This is especially true for low wavenumber shoulders.[Iqb82, Pis03, Mei06]

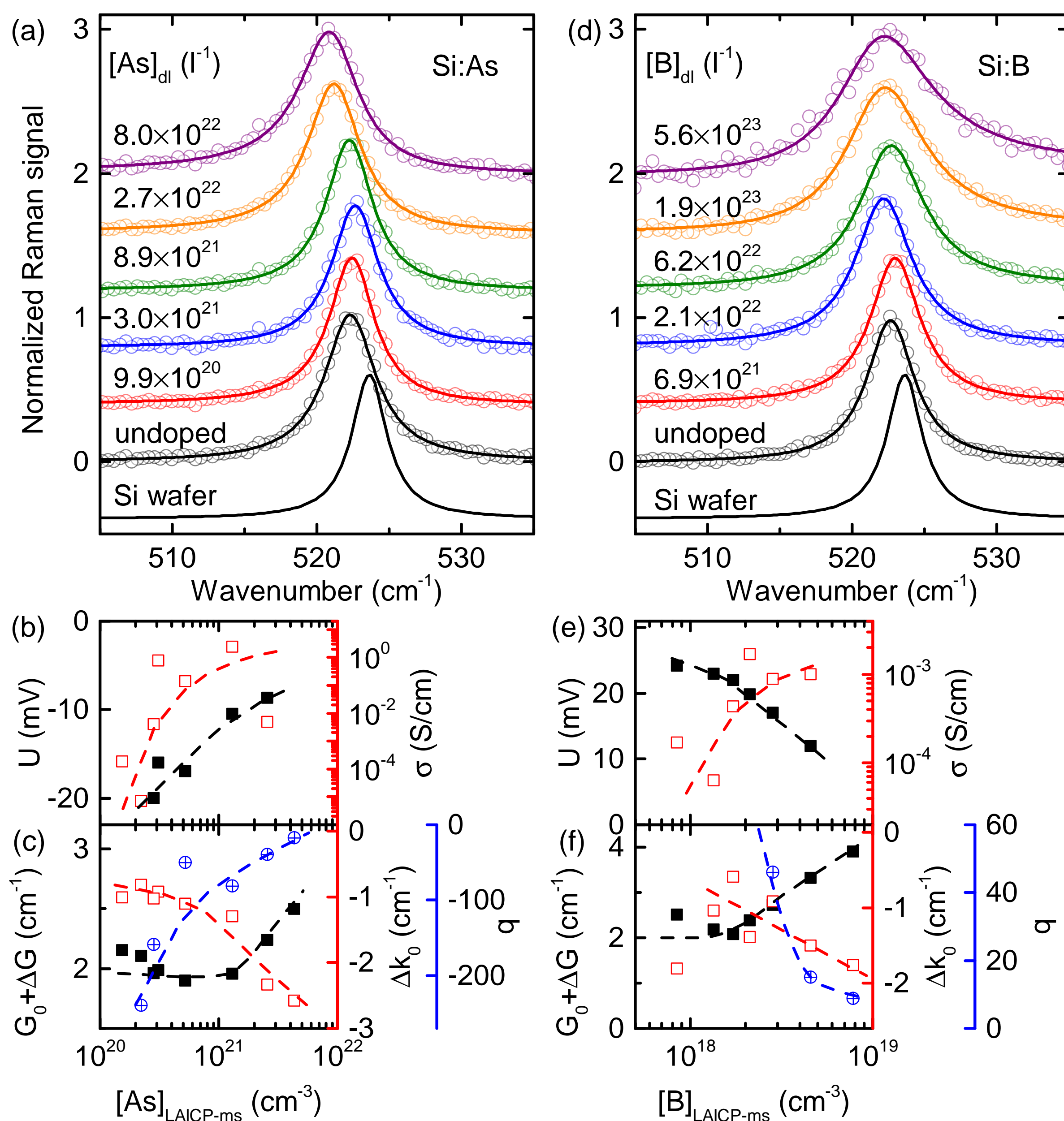

Figure 7.21. Raman spectra of laser-assisted wet-chemically doped Si films: Panel (a) shows the Raman spectra of Si films, doped with different concentrations of As in the doping liquid. The experimental data (open symbols) can be fitted by a Fano lineshape according to Eq. 7.2. The signal of a Si wafer is shown as a gray solid line. The thermovoltage U and the electrical conductivity σ of the samples are shown in panel (b), where the abscissa is obtained from the correlation in Fig. 7.17. The fit parameters of the Fano-lineshapes in panel (a) are shown in panel (c). Panels (d) to (f) show the corresponding data and fit parameters for Si films doped with B.

Eq. 7.3, the carrier concentration can be deduced. The hole concentration p determined by this is compared in Fig. 7.22 to the B concentration [B] determined by LAICP-MS.

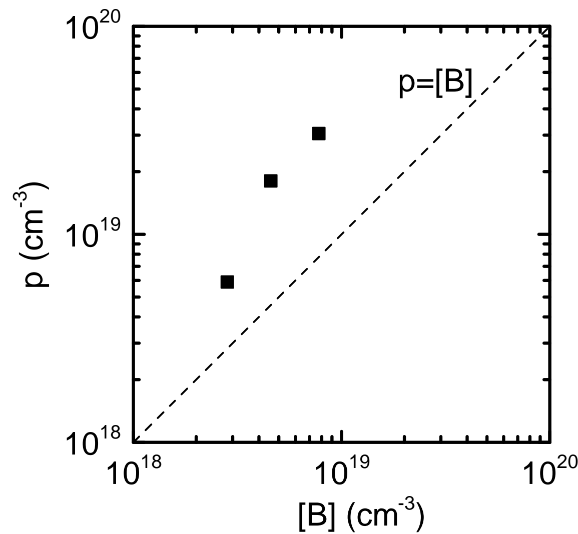

Figure 7.22. Correlation of hole concentration and acceptor concentration in laser-assisted wet-chemically B-doped Si films: The hole concentration is deduced from the Fano asymmetry parameter q via Eq. 7.3. The Boron concentration is measured by LAICP-MS.

Such an evaluation of the Fano data extracting numbers for the charge carrier densities is only possible for p-type Si films, as was already discussed in the context of Fig. 7.19. The dashed line in Fig. 7.22 indicates $p = [\mathrm{B}]$. The hole concentration rises with increasing B content, suggesting that clustering of dopants or dopant deactivation at high doping levels do not occur in this regime. However, all data lie above the dashed line indicating 100 % activation, which is unphysical as B is known to be a single acceptor state in Si. Errors involved in the LAICP-MS measurements are the rather low B content of the NIST 612 standard material. Further, in a CVD processes B has the tendency to stick to reactor walls, suggesting a similar effect for the LAICP-MS measurement after the plasma flame. Both effects would lead to an underestimation of the concentration of B incorporated in the laser-sintered film. The determination of p from the Fano asymmetry may be hampered by the scatter of the literature data in Fig. 7.19 and thus the accuracy of the constant in Eq. 7.3. For the sample doped highest with B the uncertainty of q can be estimated to be rather small, due to the pronounced Fano effect. Considering these sources of uncertainty, the values obtained on p still suggest a rather high percentage of activation.

Together with the conductivity of B-doped Si films shown in Fig. 7.13 a hole mobility in the sample doped highest with B can be estimated roughly. Extrapolating the data, the effective conductivity is $\sigma \approx 3 \times 10^{-3}\,\mathrm{S/cm}$, where the microscopic conductivity $\sigma_{\mathrm{mic.}}$ is typically reduced by percolation effects by an order of magnitude, caused by the mesoporous morphology, as discussed in Sec. 5.1.4. Since the Raman measurements determine microscopic carrier densities, this estimation uses $\sigma_{\mathrm{mic.}} = 3 \times 10^{-2}\,\mathrm{S/cm}$. This yields a conductivity mobility of $\mu = 10^{-3}\,\mathrm{cm^2/Vs}$, which is close to what has already been reported on laser-sintered Si NP films with gas-phase B-doping.[Lec08]

In single-crystalline as well as in poly-crystalline Si of comparable doping density the mobility usually is much higher reaching values of 4-40 cm^2/Vs.[Kim87, Ant07] An important argument for the low conductivity mobility found in the samples prepared by laser-assisted wet-chemical doping is the effect of trap states at grain boundaries, leading to barriers for charge transport.[Set75] As the doping density found roughly matches typical dangling bond densities, the dc-conductivity mobility can be drastically reduced. It can thus be concluded that within a grain the doping method leads to freely mobile charge carriers that evoke the Fano effect in the Raman signal, however their transport across grain boundaries is limited by barriers typical for poly-crystalline material with a high density of trap states.

8

Thermal Conductivity Measurements of Sintered Group-IV Nanoparticles

In Eq. 1.1 the figure of merit is determined by the power factor in the nominator and the thermal conductivity κ in the denominator. The previous chapters only concentrated on the nominator in Eq. 1.1. The last chapter of this thesis now adresses the determination of κ for sintered NPs is emphasized.

8.1. The Challenge to Determine Thermal Conductivities

The experimental and theoretical data in Si systems discussed in Sec. 2.4.3 highlighted that materials with low thermal conductivities often have a complex structure on a hierarchy of length scales, ranging from Å to several µm. The concept of an "all-scale hierarchical disorder" has been proposed and confirmed in other materials as well.[Bis12] With alloy scattering in the $Si_{1-x}Ge_x$ system, inclusions of pristine NPs of a typical size of 25 nm, a poly-crystallinity with grain sizes of 50 nm to 200 nm, a film thickness of approximately 300 nm and a meander-like mesoporosity with a characteristic distance between neighboring meanders of 500 nm, the laser-sintered materials studied in the context of this work exhibit many levels of disorder, which was already addressed in Fig. 1.4. The morphological complexity of such nano- and microstructured thin film materials implies that standard methods to measure the thermal conductivity are limited in their application.

Methods to measure κ used today include the laser flash method for samples of rather large dimensions and well defined thickness,[Cap63] the 3ω method for flat

thin films with a good thermal junction to the underlying substrate,[Bor01] microelectromechanical measurement platforms, e. g., for individual nanowires,[Völ10] or time or frequency domain thermoreflectance measurements for samples with well defined specular and temperature-dependent reflectivity.[Cah04] Force microscopy methods are suitable to extract local differences of the thermal conductivities, but the quantification remains difficult.[Non92, Fie99, Mec08, Maj99, Gom07, Zha10] Local measurements of the thermal conductivity perpendicular to the sample surface have also been reported using thermoreflectance methods.[Hux04, Zha12, Zhe07, Wei13] Applied to the materials discussed in this work the methods mentioned suffer from a hardly known heat capacity, rough sample surfaces, highly diffuse reflection, high electrical conductivity, poorly defined sample thickness or spurious thermal conductance by contacts, substrates or the ambient.

Before two alternative approaches are discussed in this chapter, fundamental requirements for methods suitable to measure κ of complex materials such as laser-sintered NP films shall be identified. Basically all concepts to measure κ have to provide a couple of needs, which arise from the fact that the net steady state heat flow in a sample obeys the heat diffusion equation

$$-H(\vec{r}) = \kappa(\vec{r})\,\Delta T(\vec{r}) + \vec{\nabla} T(\vec{r}) \cdot \vec{\nabla}\kappa(\vec{r}). \tag{8.1}$$

As obvious from this equation, a temperature gradient $\vec{\nabla} T(\vec{r})$ and a finite heating power density $H(\vec{r})$ are required, so that any method to obtain κ needs a suitable excitation source. The derivatives with respect to spatial coordinates in Eq. 8.1 translate into the necessity to know the geometry of the sample to be investigated. Either the vector field of the heat flux needs to be known a priori or it must be obtained by simulation. Otherwise only the thermal conductance, in contrast to the thermal conductivity, can be determined. Among the fundamental requirements for methods that are be able to provide insight into thermal transport of laser-sintered NP thin films is the need to determine local temperatures contactlessly. The signal used for that needs to originate from the interior of the material, rather than from the surface, which exhibits poorly defined optical properties due to its roughness.[1] It would also be desirable to time-efficiently obtain spatially resolved information, especially because the microstructure of the sample is expected to heavily influence thermal transport.

In the following, two optical methods to obtain κ will be discussed. First, the Raman shift method uses the temperature dependence of Stokes-scattered light to measure local temperatures, while the sample is excited by the Raman laser itself. The method is comparatively well developed and measures a sample spot after spot. Second, the near-infrared radiation emitted by the sample is proposed as a future tool to measure the temperature distribution for the whole sample simultaneously, and a proof-of-principle experiment is presented.

---

1 In contrast to thermoreflectance methods, where specular reflection of externally applied radiation is required.

8.2. The Raman Shift Method to Obtain Thermal Conductivities

The Raman shift method, which is also called Raman thermography, micro Raman method or optothermal Raman measurement technique, uses a strongly focused laser beam as a thermal excitation source, and by this potentially offers a spatial resolution on the sub-micrometer scale. In the past, this technique has been applied to low-thermally conducting porous Si,[Pér99, Pér00] as well as to high-thermally conducting graphene,[Bal08, Gho09, Tew10, Gho10, Cai10, Bal11, Lee11a, Che12, Nik12, Yan13] and has been adapted and extended to other materials, such as carbon nanotubes,[Li09b, Liu13] SiO_2 films,[Hua09] Si nanowires,[Doe10] Si membranes,[Liu11, Chá14] mesoporous films of SiGe and Ge[Sto14b, Sto14a] or GaAs nanowires.[Soi10]

To measure the local temperature, the temperature dependence of Raman active phonon modes is used. If this dependence is known, e. g., from calibration experiments with uniform external heating and very low Raman laser powers, the Raman spectrum obtained with higher laser powers contains quantitative information on how strongly the sample was heated by the Raman excitation laser during the measurement. For known excitation power this temperature increase contains explicit information on the thermal conductance of the structure or device investigated. Together with sufficient knowledge about the sample geometry and the path of heat flow in the sample, it is possible to obtain the thermal conductivity κ, the material specific intensive quantity of interest.

Deduction of the Raman Temperature

In harmonic approximation the energy of atomic vibrations in a solid is determined by the mass of the atoms and by the force constants between the masses. The anharmonicity of the potential leads to a change in the force constants with temperature and usually a crystal *softens* with increasing temperature. In Raman scattering light interacts with these vibrations. Hence, the wavenumber shift Δk of Stokes and anti-Stokes scattered light also usually decreases with an increasing temperature of the sample studied.[Car83b] In fact, the Stokes shift follows a distinct material specific dependence on temperature and can thus be used as a non-contact thermometer.[2] As a typical example, this dependence of the Stokes shift Δk of crystalline Ge and Si is shown in Fig. 8.1 for the longitudinal optical (LO) phonon mode.[Cow65, Har70, Bal83, Men84, Bur93, Bra00, Doe09] The choice of the phonon mode to be evaluated for temperature measurements depends mostly on the signal-to-noise ratio, but may also be influenced by the substrates available when

2 Apart from the softening of the phonon mode, the Stokes/anti-Stokes intensity ratio yields similar temperature information,[Com84b] but is, however, often more difficult to measure.[Her11] More importantly, it is extremely sensitive to variations of the signal intensity in time and space. The roughness of laser-sintered NP films, which is on the scale of the wavelength used for excitation, hinders the use of the Stokes/anti-Stokes ratio as a measure for temperature.

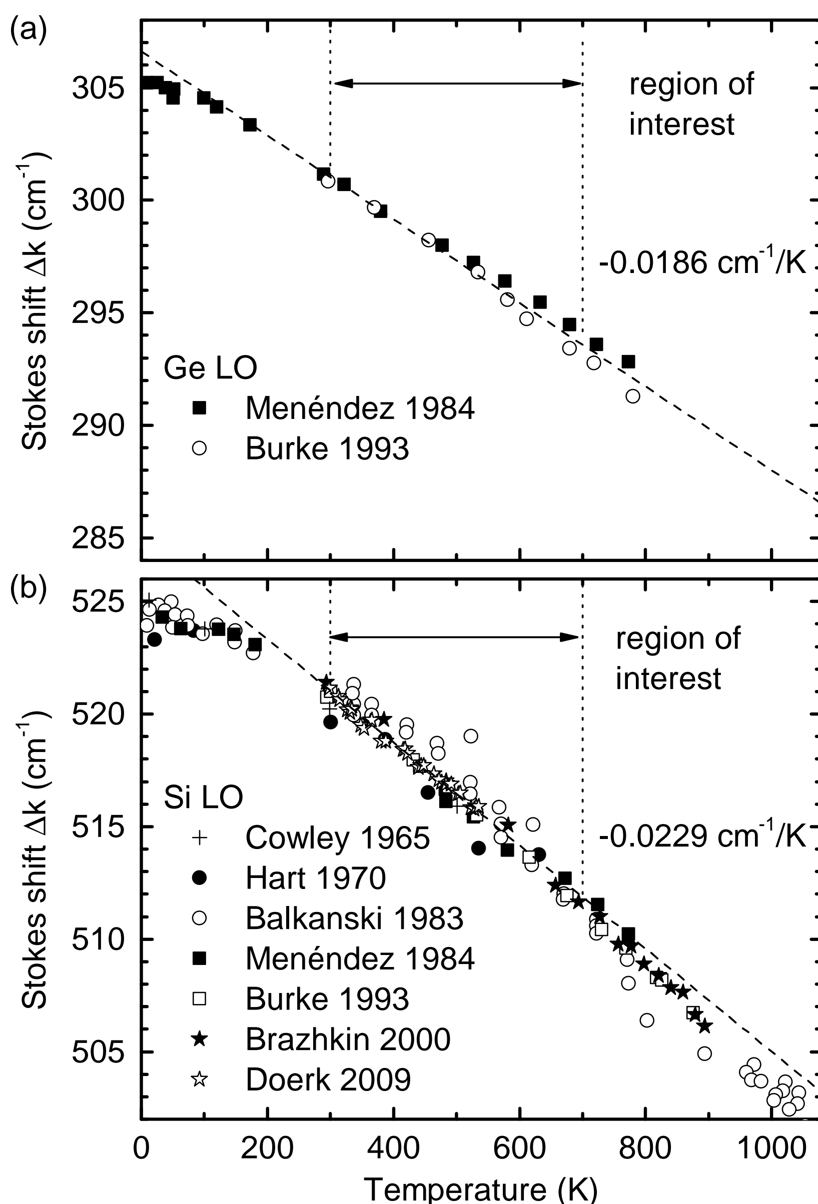

Figure 8.1. The temperature dependence of the Stokes shift Δk for the LO mode in crystalline Ge and Si: The data in panel (a) are reproduced from Refs. [Men84, Bur93], the data in panel (b) from Refs. [Cow65, Har70, Bal83, Men84, Bur93, Bra00, Doe09]. In the region of interest for this work between 300 K and 700 K, a linear dependence is assumed.

investigating, e. g., thin films, since the Raman signal from the substrate should not interfere. For experiments on Si or Ge around and above room temperature, $\partial \Delta k / \partial T$ can well be approximated by a linear fit through all published data in the temperature region of interest. Notably, the increasing slope with increasing temperature shown in Fig. 8.1 makes the method explicitly applicable at high temperatures.

Although in SiGe alloys the LO mode of the Si-Si vibration has a different energy than that in pure Si, for a wide range of Si contents $\partial \Delta k / \partial T$ is essentially the same in SiGe

as in Si,[Bur93] so that the pure Si value is also used for Si-rich alloys in the following. Dependencies similar to Fig. 8.1 are observed in other solids as well,[Men84, Liu99, Cui98, Li09a, Sah13] making the Raman shift method applicable to a large variety of materials systems.

In the great majority of Raman spectroscopy experiments, the temperature distribution $T(\vec{r})$ is not homogeneous in the sample region where the laser light is Raman scattered. This means that the Raman spectrum collected will contain contributions of hotter (e. g., in the beam centre) and colder (edge of the laser beam) regions of the sample.This is caused by the inhomogeneous excitation via, e. g., a Gaussian laser beam, such as the one also used in the following experiments. Thus, care must be taken when deducing a temperature from a Raman spectrum and the spectrum collected should be interpreted as a weighted average.[Her11, Liu11] To distinguish it from the local temperature $T(\vec{r})$ of the sample, the temperature deduced from the Stokes shift Δk measured will be called an effective Raman temperature T_{Raman}. In the most simple approach it can be assumed that every location $\vec{r}$ on the sample contributes to T_{Raman} by its local temperature $T(\vec{r})$, weighted by the local excitation power density $H(\vec{r})$, since the intensity of Stokes-scattered light is proportional to the latter quantity. Adding up all those contributions in the sample volume and normalizing the sum by the total absorbed laser power P one obtains

$$T_{\text{Raman}} = \frac{1}{P} \int H\left(\vec{r}\right) T(\vec{r}) c(T(\vec{r})) g(\vec{r}) \mathrm{d}\vec{r}, \tag{8.2}$$

where $c(T(\vec{r}))$ is the (in principle temperature-dependent) Raman scattering cross section and $g(\vec{r})$ is a function that accounts for the effect that Raman scattering of weakly absorbed light takes place deep in the sample and that such scattered light is less efficiently collected by the objective. In all following calculations and experiments $c(T)$ is assumed to be constant. Further assuming full surface near-absorption and Raman interaction, $g(\vec{r}) = 1$. Then, Eq. 8.2 simplifies to

$$T_{\text{Raman}} = \frac{1}{P} \int H(\vec{r}) T(\vec{r}) \mathrm{d}S, \tag{8.3}$$

where dS is a surface element on the sample.

An example for such a weighting procedure is shown in Fig. 8.2, where a hypothetical 2-dimensional thin square-shaped sample with lateral dimensions of 30 µm × 30 µm is excited by a Gaussian spot at $(x|y) = (5\,\mu\text{m}|15\,\mu\text{m})$. The material is assumed to have a thermal conductivity of 400 W/m K and its temperature is fixed to the temperature of a heat sink at the border of the sample. The temperature distribution results from the excitation by the laser beam and obeys Eq. 8.1. The static heat diffusion equation can be used in the context of the Raman shift method because typically the minimum acquisition time of a Raman spectrum is of the time scale of a second, so that for small samples the measurement conditions are close to equilibrium. The temperature distribution in panel (b) is not symmetric with respect to the center of the laser beam, so that the weighting according to Eq. 8.3 has to be done spot-by-spot. Notably, the

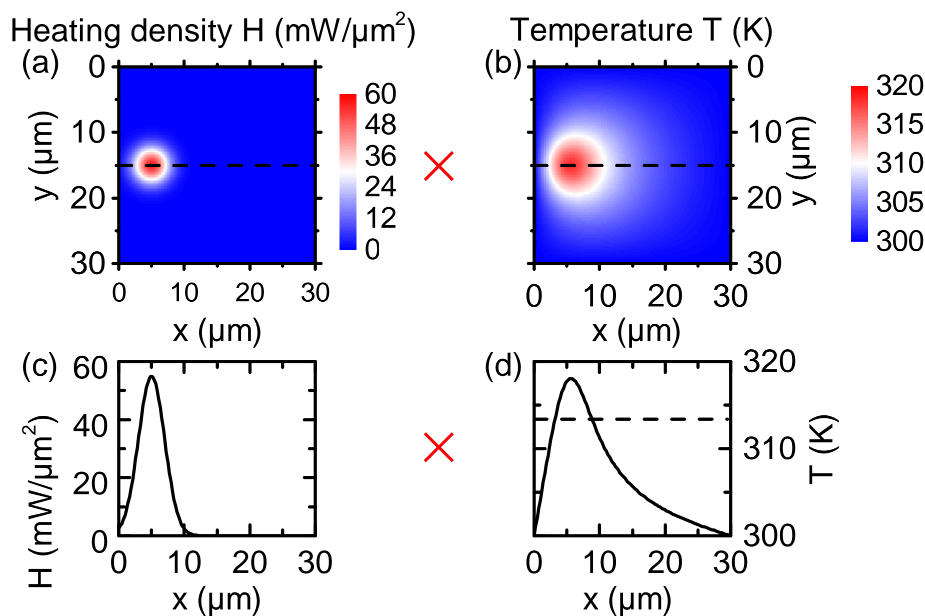

Figure 8.2. Interpretation of the Raman temperature: Panel (a) shows a colour-coded plot of the heating density H on a hypothetical 2-dimensional grid of 30 μm × 30 μm. The total absorbed power is 100 mW and the standard deviation of the Gaussian beam is 2 μm. The film has a thermal conductivity of $\kappa = 400\,\mathrm{W/m\,K}$ and is hit by the laser beam at $(x|y) = (5\,\mu\mathrm{m}|15\,\mu\mathrm{m})$. Panel (b) shows a colour-coded plot of the resulting temperature distribution. At the border of the film, the heat sink forces the temperature to 300 K. Panel (c) and (d) show cross sections of the colour plots at $y = 15\,\mu\mathrm{m}$. Notably, the sample temperature is not constant in the area of excitation. The effective Raman temperature, obtained by weighting the temperature distribution with the excitation power density, is indicated in panel (d) by the dashed line.

temperature distribution in Fig. 8.2 (b) cannot be obtained analytically, so that in this work a numerical approach is used. Details on the multigrid iterative Gauss-Seidel solver can be found in App. B. Panel (c) and (d) show cuts of the color-coded maps along the dashed lines in panel (a) and (b), respectively. In the case shown here, the Raman temperature T_{Raman} according to Eq. 8.3 at $(x|y) = (5\,\mu\mathrm{m}|15\,\mu\mathrm{m})$ is $T_{\mathrm{Raman}} = 313\,\mathrm{K}$, which is significantly less than the maximum temperature of 318 K at the excitation center.

It is important to note at this point that this weighting approach used in the following to determine T_{Raman} does neither include the line-shape of the Raman signal nor its temperature dependence,[Liu11] but nevertheless improves the understanding of the Raman shift method in comparison to most analyses in the literature and corrects the effects of different temperatures beneath the laser beam to first order.

Mapping Raman Temperatures for Improved Reliability

The discussion so far concentrated on how to obtain a single effective Raman temperature on a single spot on a sample. Later, this single temperature can be used with sufficient

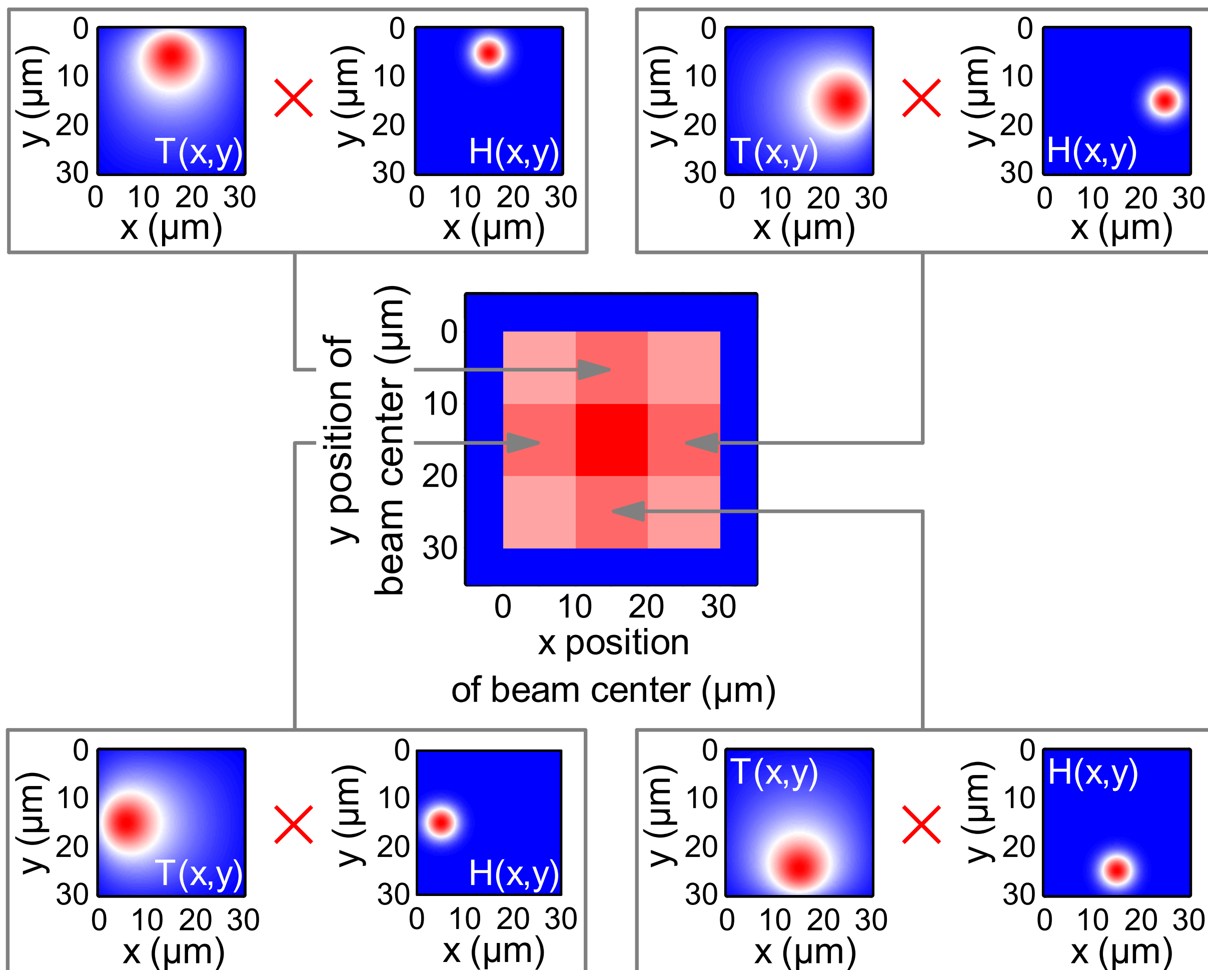

Figure 8.3. Simulation of a Raman temperature map. The laser beam is scanned across a sample and on every position, the effective Raman temperature is obtained by weighting the equilibrium temperature distribution $T(\vec{r})$ (left) with the local heating power density $H(\vec{r})$ of the excitation laser (right).

knowledge about the paths of heat transport to obtain κ. However, the reliability with which the thermal conductivity can be deduced by the Raman shift method can be drastically increased by measuring T_{Raman} not only at one spot, but on many spots on the sample. Such a mapping procedure is schematically shown in Fig. 8.3, and the result will be called a Raman temperature map. In Fig. 8.3 a numerical simulation is the basis of this Raman temperature map. For each laser position on the sample surface the local temperature distribution $T(\vec{r})$ is calculated and weighted with $H(\vec{r})$ to obtain T_{Raman} at this location. Experimentally, at each position a Raman spectrum is collected, and, using a relation such as the ones shown in Fig. 8.1, the corresponding effective temperature, identified with T_{Raman}, is deduced.

Because the thermal excitation as well as the temperature measurement are performed with a single laser beam, it is important to note, that such a Raman temperature map is

not a temperature distribution, which via Raman scattering could be obtained only by using two lasers.[Rep14] There, the temperature distribution excited by a strong laser would be probed using a rather weak second laser, keeping the additional heating by the second laser to a minimum.

A One-Dimensional Example

In this paragraph the simplest possible sample geometry, a quasi one-dimensional bar, attached to a perfect heat sink at one end, shall be used to shortly demonstrate how to obtain κ from measurements of T_{Raman}. Figure 8.4 schematically shows the focused Raman laser hitting the bar at its end and acting as the heat source. The heat generated at the right end will propagate through the bar to the heat sink on the left. For simplicity, it is assumed that κ in the bar is neither dependent on temperature nor position. Then, outside the laser beam where $H(x) = 0$, Eq. 8.1 can be written as

$$0 = \kappa \frac{\partial^2 T}{\partial x^2}. \tag{8.4}$$

Thus, the temperature decreases linearly from the excitation spot to the heat sink, as shown by the solid line in Fig. 8.4.

To quantitatively obtain the thermal conductivity from Eq. 8.4 and from the experimental value of T_{Raman}, appropriate boundary conditions have to be set. The continuity equation requires that the total heat generated at the bar's right end has to propagate to the heat sink. Neglecting the spatial extension of the laser beam and a thermal contact resistance between the bar and the heat sink, the temperature of the bar at its left end is equal to the temperature of the heat sink T_{sink}, so that

$$P = \frac{A}{l} \kappa \left(T_{\mathrm{Raman}} - T_{\mathrm{sink}} \right), \tag{8.5}$$

where A is the cross section and l the length of the bar. This directly leads to

$$\kappa = \frac{l}{A} \frac{P}{\left(T_{\mathrm{Raman}} - T_{\mathrm{sink}} \right)}. \tag{8.6}$$

Figure. 8.4 additionally sketches the effect of a finite contact resistance between the bar and the heat sink. The temperature profile in such a case is drawn as grey dashed line. If κ is lower than without contact resistance, this could lead to a misinterpretation of T_{Raman}. That scenario highlights the importance to map effective Raman temperatures, because with this, contact resistances can also be determined.

8.2.1. Model System I: 2-Dimensional Conduction of Heat

Before applying the Raman shift method to more complex structures, two model systems shall be investigated to validate the method. The first system is a freely suspended

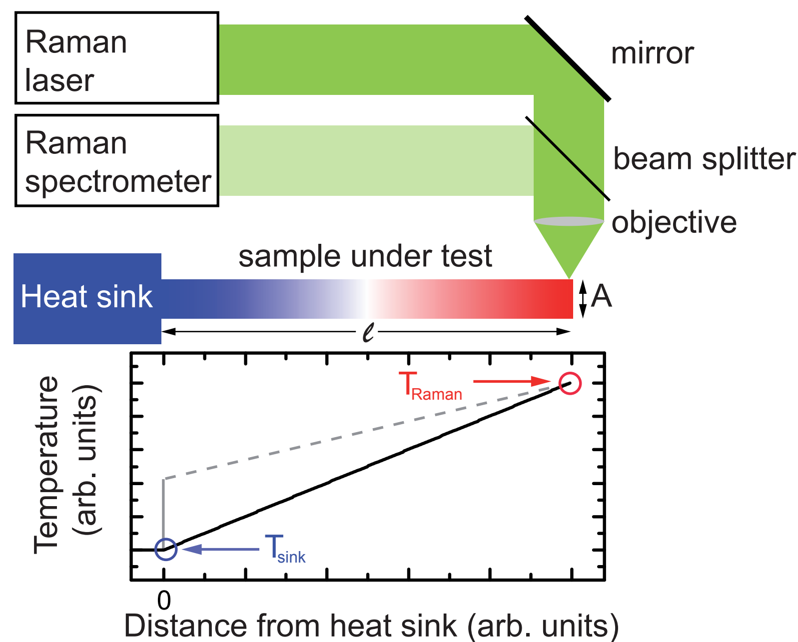

Figure 8.4. Measuring the thermal conductivity of a bar-shaped material by the Raman shift method: The Raman laser acts both as the heating source and, together with the Raman spectrometer, as the thermometer. The beam of the laser is focused on the sample of length l and cross section A. Raman scattered light is directed via a beam splitter to the Raman spectrometer where T_{Raman} is deduced. For vanishing contact resistance to the heat sink, the temperature distribution drawn as the black solid line is established in equilibrium. The grey dashed line considers a finite contact resistance to the heat sink and a lower thermal conductivity, so that the same Raman temperature would be measured at the end of the bar.

membrane of undoped single-crystalline Si with a thickness of 1.9 µm. For that thickness no significant reduction of the thermal conductivity can be expected from Fig. 2.8, compared to bulk Si. However, with lateral dimensions of $10 \times 10\,\mathrm{mm}^2$ width it is justified to approximate thermal transport as purely two-dimensional, i. e., in the plane of the film. Further, using an excitation wavelength of 514.5 nm, the absorption length for $\alpha_{\mathrm{Si}} = 2 \times 10^4\,\mathrm{cm}^{-1}$ is on the order of the wavelength, so a rather homogeneous heating independent of the depth in the membrane can be assumed, although the light absorption follows an exponential dependence according the the Lambert-Beer law.[Hum89, Sǐk98, Asp83] This leads to the neglect of heat transport perpendicular to the membrane in the simulation. An optical micrograph of the sample in transmission is shown in the inset in Fig. 8.5. The membrane with lateral dimensions of $10 \times 10\,\mathrm{mm}^2$ is freely suspended on an area of $4.9 \times 4.9\,\mathrm{mm}^2$. The film is carried by a 0.5 mm thick Si support at the border. For the experiment a $10\times$ objective is used, resulting in a laser spot with a standard deviation of $w = 2.4\,\mu\mathrm{m}$. The laser power is 60 mW.

The solid symbols in Fig. 8.5 show an experimental Raman temperature scan across the sample. Although the thermal conductivity κ can be expected to be homogeneous in the single-crystalline material, the conductance of the membrane is not, so that T_{Raman}

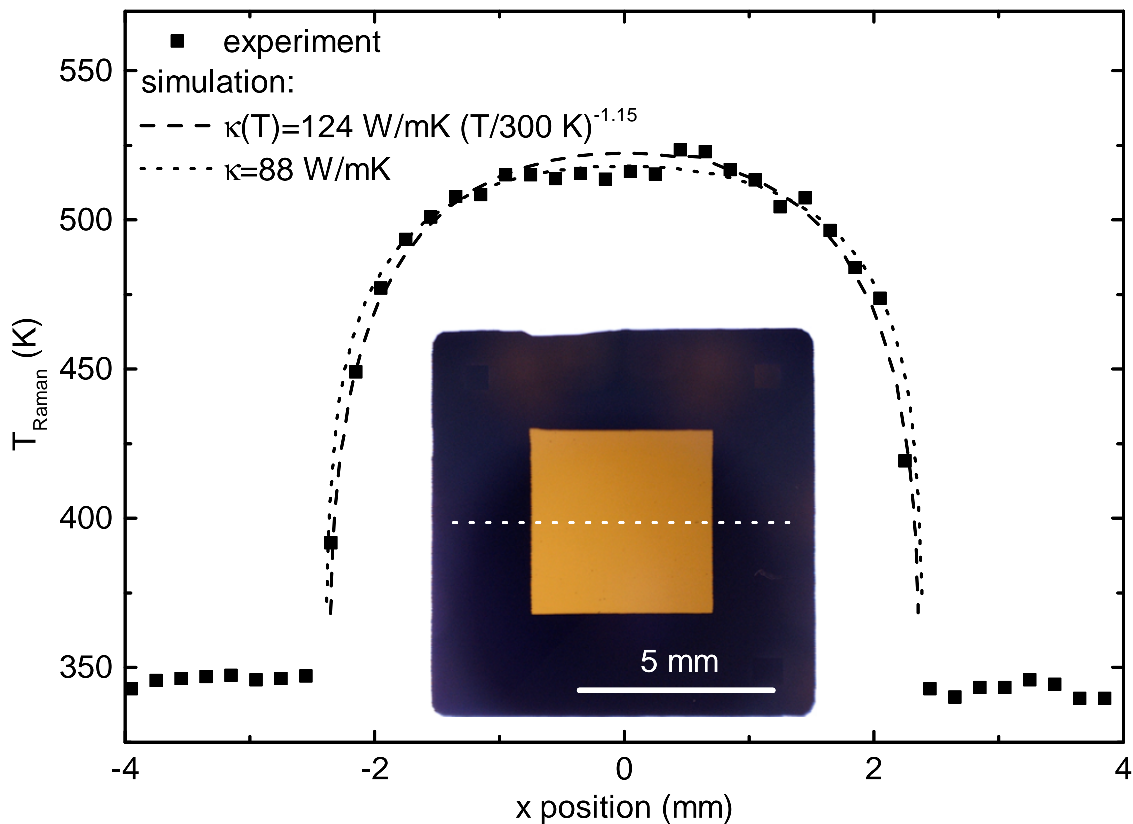

Figure 8.5. Raman temperature scan across a thin single-crystalline Si membrane: The 10 mm × 10 mm large membrane of 1.9 µm thickness is freely suspended on 4.9 mm × 4.9 mm. On the outer part it is supported by a 0.5 mm thick Si wafer. The inset is a transmission optical microscopy image of the sample. The full symbols show experimentally determined Raman temperatures as the excitation laser beam is scanned along the path indicated in the inset. T_{Raman} is increased on the suspended part and only weekly depends on the exact position in the center region. The dotted line is the result of a simulation of the scan assuming a temperature-independent thermal conductivity of $\kappa = 88\,\text{W/m K}$, whereas the dashed line is the result of a simulation with $\kappa_{300\,\text{K}} = 124\,\text{W/m K}$, decreasing with temperature according to a power law with an exponent of -1.15.[Ash97]

depends on the position where it is measured. As soon as the excitation spot is on the freely suspended part of the membrane T_{Raman} increases. The heat absorbed in the membrane has to flow in-plane, which increases T_{Raman} when the excitation spot is moved away from the underlying support acting as the heat sink. In the center region of the membrane T_{Raman} is rather independent of the exact position. The variation of the experimental data in Fig. 8.5 corresponds to an uncertainty of the determination of the thermal conductivity of the order of 10%.

The small ratio of beam diameter and lateral size of the suspended membrane necessitates a large number of grid points in the simulation of the Raman temperature scan to correctly cover the temperature distribution at the excitation spot. Assuming a reflectivity of 38%,[Hum89, Sǐk98, Asp83] neglecting the temperature dependence of κ would

yield $\kappa = 88\,\mathrm{W/m\,K}$. The corresponding Raman temperature scan is shown in Fig. 8.5 as dotted line. However, the highest Raman temperature measured is approximately 520 K, so that the thermal conductivity should be modelled by a power-law dependence on temperature.[Ash97] The dashed line in Fig. 8.5 is the result of such a simulation of the Raman temperature across the suspended membrane, with a room temperature thermal conductivity of $\kappa_{300\,\mathrm{K}} = 124\,\mathrm{W/m\,K}$ and an exponent of approximately -1.15.[Ash97] A thermal conductivity decreasing according to this exponent is also shown in Fig. 2.8 (a) as red line. The latter curve fits the experimental data slightly better, especially near the heat sink. For a membrane of 1.9 µm thickness the obtained thermal conductivity is in good agreement with values reported in the literature.[Son04, Ash98, Chá14] This can also be seen in Fig. 2.8 (b), which contains the thermal conductivity obtained here as red open square.

8.2.2. Model System II: 3-Dimensional Conduction of Heat

One of the most obvious experiments for the application of the Raman shift method is the determination of κ for an undoped single-crystalline piece of wafer. In this section first an analytical expression for the effective Raman temperature in analogy to Eq. 8.3 shall be given. Mathematical details of the derivation can be found in App. C.

Usually the thickness as well as the lateral dimensions of any piece of wafer are much larger than the dimensions of the focused laser beam. Thus, the derivation assumes a semi-infinite piece of sample, filling the half-space. The assumption of strongly absorbed light is justified if the penetration depth is smaller or at least comparable to the beam width.

The beam profile and the density of absorbed power in the depth of a wafer are shown in the simulation in Fig. 8.6 (a). The temperature distribution resulting from such a thermal excitation density is shown in panel (b). With the temperature of the heat sink T_{sink} in regions of the wafer very far from the excitation, the effective Raman temperature T_{Raman} can be written as

$$\kappa = \frac{P}{4\sqrt{\pi}\,(T_{\mathrm{Raman}} - T_{\mathrm{sink}})\,w}. \tag{8.7}$$

To test the validity of Eq. 8.7 single-crystalline Si and Ge wafers are investigated, using a 10× objective with a spot standard deviation of $w = 0.73\,\mu\mathrm{m}$. To enhance the accuracy not only a single Raman spectrum for one excitation power is measured, but instead series of measurements with different excitation powers are performed. Then, Eq. 8.7 changes to

$$\kappa = \frac{\frac{\partial \Delta k}{\partial T}}{4\sqrt{\pi} w \frac{\partial \Delta k}{\partial P}}. \tag{8.8}$$

Due to the high thermal conductivity of the single-crystalline wafers, only a small temperature increase of less than 60 K is observed during the experiments. Thus, the relation

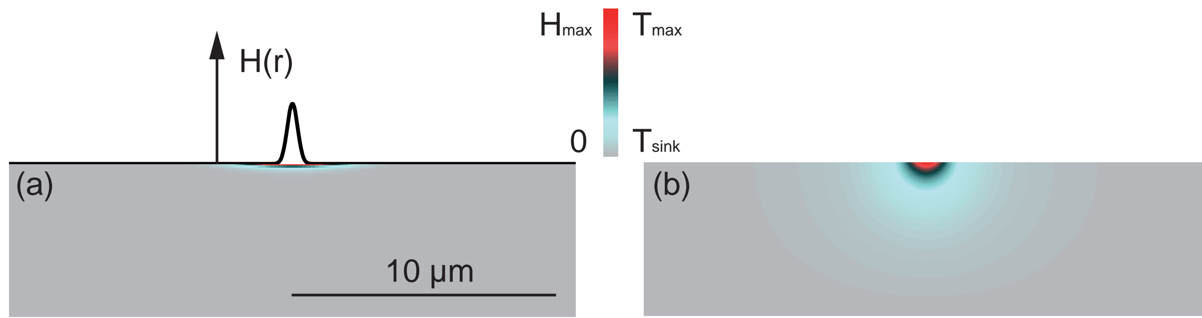

Figure 8.6. Excitation and heat spreading in a Raman shift experiment on a thick wafer: The panels illustrate cuts through a wafer at the position of the Raman excitation. Panel (a) shows the color-coded heating power density $H(r, z)$ as well as the corresponding Gaussian beam profile. For the deduction of Eq. 8.7 surface near excitation is assumed. The simulated temperature distribution in panel (b) assumes that the backside of the wafer (bottom) is perfectly bound to the heat sink.

in Fig. 8.1 can be linearized near room temperature, yielding $\frac{\partial \Delta k}{\partial T} = -0.0214\,\text{cm}^{-1}/\text{K}$ for Si. From the recorded power series on the single-crystalline Si wafer one obtains $\frac{\partial \Delta k}{\partial P} = -0.0245\,\text{cm}^{-1}/\text{mW}$. The thermal conductivity obtained via Eq. 8.8 then amounts to $\kappa_{\text{Si}} = 168\,\text{W/m K}$. Literature values of $\kappa_{\text{Si}} = 156\,\text{W/m K}$ to $\kappa_{\text{Si}} = 145\,\text{W/m K}$ are reported for Si around room temperature, which is slightly overestimated by the discussed Raman shift experiment.[Gla64, May67]

A similar experiment on a single-crystalline Ge wafer using $\frac{\partial \Delta k}{\partial P} = -0.0186\,\text{cm}^{-1}/\text{mW}$ from Fig. 8.1 and Ref. Men84 yields $\kappa_{\text{Ge}} = 49\,\text{W/m K}$, which is in similarly good agreement with the value of 60 W/m K reported in reference [Gla64].

The assumption of surface-near absorption of the excitation light, made during the derivation of Eq. 8.7, is better fulfilled for Ge, where the absorption coefficient for light at 514.5 nm is around $\alpha_{\text{Ge}} = 63 \times 10^4\,\text{cm}^{-1}$,[Hum89] compared to Si with around $\alpha_{\text{Si}} = 2 \times 10^4\,\text{cm}^{-1}$.[Hum89, Šik98, Asp83] For a penetration depth in the range of or larger than the excitation laser beam, the effective area through which the heat is introduced into the material is enhanced, so that the thermal conductivity is overestimated when Eq. 8.7 is applied. This may explain the tendency for the experiments on Si and Ge wafers. Nevertheless, the results show that by using the Raman shift method applying Eq. 8.8 the thermal conductivity of a homogeneous and 3-dimensional material can be measured with an accuracy of at least 20%.

8.2.3. The Raman Shift Method Applied to Thin Films of Laser-Sintered Nanoparticles

Preparation of Freely Suspended Laser-Sintered Films

To apply the Raman shift method to measure the in-plane thermal conductivity of laser-sintered NP thin films the conduction of heat perpendicular to the plane of the

film should be avoided. This can be done by, first, adapting the penetration depth via the used excitation wavelength to the film thickness, and second, by eliminating the heat sink beneath the excitation spot. Thus, the membrane needs to be prepared freely suspended, so that the heat is forced to flow in-plane for at least the distance of several laser beam diameters. It is also mandatory to prepare the films freely suspended, because even for in-plane heat flux, the substrate, which is much thicker than the film under investigation, would contribute significantly to the spreading of the heat.

To achieve a suitable measurement geometry for the thin films discussed in this thesis, the NPs, which usually carry a surface oxide, are oxide-etched by hydrofluoric acid (HF) first. In contrast to the usual procedure where dispersions are made from as-grown NPs, in this case the oxide-free NPs are dispersed. To optimize the dispersability, degassed isopropanol is used instead of ethanol. From such a dispersion a thin film is spin-coated on quartz substrates, which replace the usual polyimid substrates in view of the further processing steps. Laser-sintering is then again done as described in Chap. 5. With a slightly reduced sinter fluence compared to films on polyimid, the typical meander-like morphology can also be obtained for films on quartz substrates.

As a substrate for the Raman shift experiment on freely suspended thin films of laser-sintered NPs a Ge wafer is used. Ge was chosen initially because typical thermoelectric materials are rich of Si, so that the Si-Si Raman mode can serve to measure the temperature. To suppress the spectral overlap from the film and the substrate, Ge is well suited. Furthermore, the thermal conductivity of Ge is high enough for it to act as a heat sink. However, the films have to be suspended over an elongated trench, which is deep enough to prohibit optical interference between the film and the bottom of the trench. By Reactive Ion Etching (RIE) with fluoric gases trenches of 20 µm to 25 µm width are etched into the Ge wafer with a final depth of roughly 15 µm.

To transfer the laser-sintered film from the quartz substrate onto the trench structure the following procedure is followed: Using optical as well as electron microscopy, suitable regions are identified on the film on quartz. Then, the quartz substrate is laid face down onto the Ge wafer, so that the regions to be investigated come to lie on the region with trenches. A tiny amount of approximately 10 µl of a 5 % aqueous solution of hydrofluoric acid is pipetted into the contact edge of both substrates. The etchant immediately fills the gap between them. Within some seconds, the laser-sintered film is released from the quartz substrate, which can be followed easily by optical microscopy. To reduce the surface tension, which can break the flakes of the laser-sintered film during drying, the surface of the etchant is touched by a detergent. As the film sinks onto the trench structure, the quartz substrate can slowly be pulled from the Ge wafer in horizontal direction. Ideally, this does not disrupt too much the film. In contrast to completely closed structures such as quadratic holes, the elongated trenches ensure a smooth flow of the etchant beneath the film during drying of the etchant. After drying, the flakes are already firmly attached to the Ge wafer. Occasionally, during pull off of the quartz substrate flakes are turned from face-down to face-up. Actually, if such flakes are of proper morphology and isolated from other flakes, this is the ideal end

Figure 8.7. Transfer of a laser-sintered film: (a) Following the procedure described in the text, flakes of a laser-sintered NP film are transferred onto a Ge wafer with two trench structures in the upper and lower part of the wafer. In this optical micrograph face-down flakes appear brownish due to unsintered NPs at the backside of the film, whereas face-up flakes appear metallic. (b) Magnification of a flake in panel (a) which is suitable for investigation by the Raman shift method. (c) SEM micrograph of the same region as in panel (b), which shows that the flakes partly overlap. Regions i and ii are suited for Raman mapping.

situation because the bottom side of the laser-sintered films is much less rough, so that the thermal contact to the wafer is greatly enhanced. However, the low yield in terms of transferred film area of just approximately 20 % even for face-down flakes does not allow to intentionally flip the orientation of the flakes. Ruptures into small flakes, damage during drying and multi-flake attachment are some of the yield limiting problems, which can be seen in Fig. 8.7. An example for the typical mesoporous morphology of the laser-sintered NP thin films is shown in Fig. 8.8 (a). The lower part of Fig. 8.8 (b) shows a tilted angle view of a trench etched into the Ge substrate. The upper part of Fig. 8.8 (b) shows the result of a successful transfer of a flake onto the trench structure of a Ge wafer. A thin film is freely suspended across the trench, with nearly no sag. In panel (c) an SEM top view is shown. The borders of the trench beneath the film appear brighter due to the field enhancement in secondary electron SEM. Where the film lies on the Ge surface, four and five darker lines can be identified to the left and right of the trench, respectively. Those darker lines are welding lines to improve the thermal contact and also the mechanical stability of film attachment to the substrate. By scanning the focussed laser beam along the lines and using powers much higher than those used during the Raman experiment, the laser-sintered film compacts and melts to the wafer. A cross-cut image of such a weld is shown in Fig. 8.8 (d).

Investigated Samples, Experimental Details and Simulation Procedure

In the following two face-up laser-sintered NP samples are investigated by the Raman shift method. The first is a film of laser-sintered undoped Ge NPs (27 nm diameter) and the second is made from $Si_{78}Ge_{22}$ NPs (23 nm diameter), synthesized with approximately 2 % phosphine added to the gas phase as n-type dopant. The composition of the latter

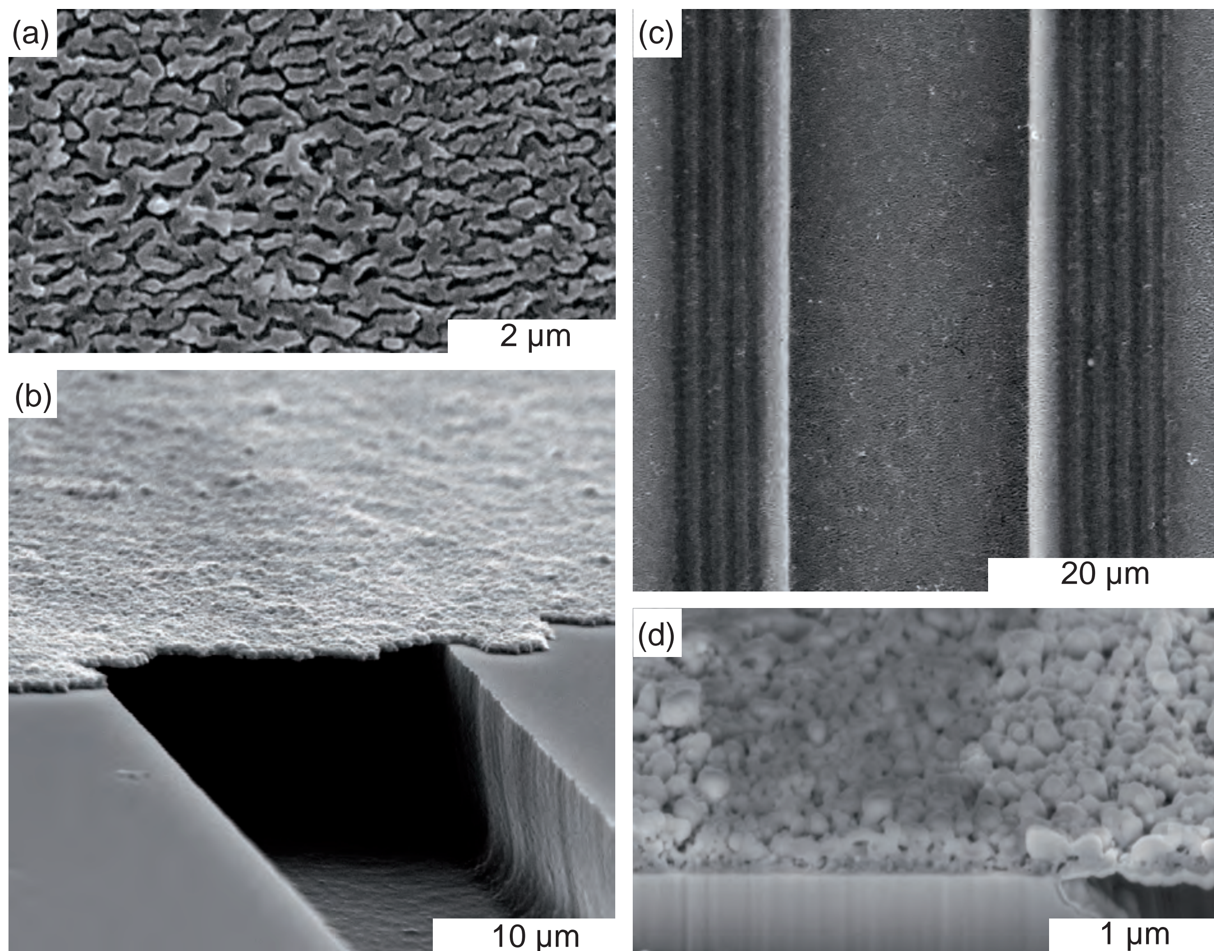

Figure 8.8. Preparation of laser-sintered NP films for the Raman shift method: (a) Typical SEM top-view of the microstructure of laser-sintered NP films. (b) SEM side-view of a suspended film as used in the Raman experiment. (c) Large-scale top-view of the film in panel (b). The dark vertical lines on the sides are welding lines to improve the thermal contact. (d) A high magnification cross view of a weld, obtained by a FIB cut perpendicular to the trench, suggests a densification of the film at the welding line.

material is typical for thermoelectric applications. Its heavy doping is common for Si-based thermoelectric materials to optimize the power factor.[Sla91, Dis64, Sny08, Ste11, Sch14] The trench widths for the Ge and the $Si_{78}Ge_{22}$ sample are 19.5 µm and 25 µm, respectively.

For the Raman experiment the sample was placed in a chamber which had an anti-reflection coated window and which was evacuated to 10^{-1} mbar. Above that pressure, the apparent thermal conductivity is approximately twice its value in vacuum. This is caused by the additional heat sink which is constituted by the high contact area of the mesoporous film to the surrounding gas. For the thin film experiments the laser beam was focussed onto the sample surface via a 20× objective with a spot standard deviation of 0.64 µm and a numerical aperture of 0.45. The objective corrected the disturbing

Table 8.1. Parameters used to extract the in-plane thermal conductivity by the combination of experiment and simulation. Numbers in brackets are estimated extreme values (minimum/maximum).

Parameter	Ge	$Si_{78}Ge_{22}$
trench width (µm)[a)]	19.5 (19.0/20.0)	25 (24.5/25.5)
spot FWHM (µm)[a)]	1.51 (1.41/1.61)	3.72 (3.52/3.92)
film thickness (µm)	0.20 (0.15/0.25)	0.20 (0.15/0.25)
absorption coefficient (μm^{-1})[b]	63.1 (49/76)	2.17 (1.7/2.6)
reflectivity (%)[b)]	51.4 (5/55)	40.6 (5/45)
laser power (µW)[a)]	148 (140/155)	57.1 (54/60)
porosity (%)	0 (0/50)	0 (0/50)
absorbed optical power (µW)[c)]	71.9 (30.7/147)	11.9 (1.78/27.2)
$\frac{\partial \Delta k}{\partial T}$ (cm^{-1}/K)	−0.0186	−0.0229
$\Rightarrow \kappa^{eff}$(W/m K)[d)]	0.51 (0.18/1.4)	0.047 (0.0058/0.15)

a) Value is measured. The uncertainty is estimated.

b) [Hum89]

c) Lambert-Beer's law without multiple internal reflection

d) The extreme values are obtained using all other extreme values.

effect of the entry window. For the Ge sample the spot was focused to minimum size, whereas for the SiGe sample, the spot was intentionally defocussed to further reduce the power density and thereby still maintaining a reasonably high signal-to-noise ratio of the recorded spectra. The power on the Ge sample was $P_{\text{absorbed}} = 72\,\mu\text{W}$, deduced from the incoming power of 148 µW and an assumed reflectivity of Ge of 51 % at the laser wavelength of 514.5 nm. For the $Si_{78}Ge_{22}$ sample the incoming power was 57.1 µW. With an assumed reflectivity of 40.6 % the absorbed power amounts to 12 µW. These numbers are based on the assumptions that the thin film behaves like the bulk material of the respective composition.[Hum89] Of course, the reflectivity values are greatly influenced by the microstructure and the roughness of the film. However, these effects will then be treated in the discussion of the results.

From both samples a Raman temperature map is recorded by measuring a Raman spectrum on each spot and calculating the temperature from the LO peak position using the relations in Fig. 8.1. Because of the high Si content in the $Si_{78}Ge_{22}$ alloy the phonon mode that was used to extract T_{Raman} was the Si-Si vibration. Its temperature dependence in such SiGe alloys is very similar to that in pure Si and can be linearized in the region from room temperature to 700 K by $\frac{\partial \Delta k}{\partial T} = -0.0229\,\text{cm}^{-1}/\text{K}$.[Bur93] Further parameters used for simulation are listed in Tab. 8.1.

As already discussed, in the case where the heat flux density cannot be calculated analytically, the geometry of the sample needs to be accounted for numerically. The simulation of the experimentally obtained Raman temperature maps uses an iterative multi-grid Gauss-Seidel algorithm. Details on the principle can be found in App. B. In

the simulation a spatially constant thermal conductivity is assumed and appropriate boundary conditions at the trench edges are set. In contrast to the measurement shown in Fig. 8.5, where the suspended part was 4.9 mm wide in x and y direction, the suspended part of the laser-sintered thin films have a width of only approximately 20 µm but a length of more than 100 µm. Thus, the simulation grid used had an aspect ratio of 3:1, which was found to be of sufficient accuracy, neglecting the small fraction of heat transport even further in y direction. The simulation treats the film as an effective medium, setting the porosity to $p = 0$. The corresponding effective thermal conductivity will be called κ^{eff}.

Results on the Thermal Conductivity of Laser-Sintered Films

Figure 8.9 (a) shows a color-coded map of the Raman temperatures obtained from scans across the Ge film sample. In the suspended part of the film the temperature increases up to approximately 700 K. The increased temperature of the part of the film which is in direct contact to the supporting Ge wafer results from the cross-plane thermal resistance and from the thermal contact resistance between the film and the underlying wafer. In panel (b) some selected horizontal lines (called x-scans) of the Raman temperature map are shown. For different x-scans the maximum variation of the temperatures at the same x-positions is $\pm 15\,\%$, which directly implies a corresponding variation of κ, evoked by local differences in the film morphology. The mean values of all measured data points, shown as full squares, are fairly symmetric with respect to the center of the trench, as it would be expected. Using the parameters listed in Tab. 8.1, the simulated temperature profile of the film across the trench is shown as solid line in Fig. 8.9 and describes the mean value of the experimental data within their typical variation.

The simulation assumes a temperature-independent thermal conductivity. In small grained and doped SiGe alloy thin films, it is justified to neglect the temperature dependence of the thermal conductivity, as has been discussed in the context of Fig. 2.8.[Ste11, Ste64, McC01] Thus, despite the large temperature differences in the experiment, useful values for κ_{eff} are obtained. For the experiment on the Ge film the simulation yields $\kappa^{\mathrm{eff}}_{\mathrm{Ge}} = 0.51\,\mathrm{W/m\,K}$.

A similar experiment was performed on a suspended laser-sintered film of $Si_{78}Ge_{22}$ NPs. The results are shown in Fig. 8.10 as a color-coded Raman temperature map in panel (a) and in a more quantitative way in panel (b). Again, the maximum temperature was kept below 700 K. Due to the increased spot size used in this case, the flanks of the curves representing the temperature increase are less steep compared to the Ge experiment. Also, the temperature of the film on the heat sink is only slightly above room temperature, which can be explained by an approximately 40-fold decrease of the power density compared to the experiment on the Ge film. This decrease of the power density is caused both by the increased spot size in the SiGe experiment as well as by the reduced absorbance of the SiGe film compared to the Ge film. The exact numbers can be found in Tab. 8.1. A comparable temperature increase with reduced impinging optical power, together with the increased spot size, already point toward a lower thermal

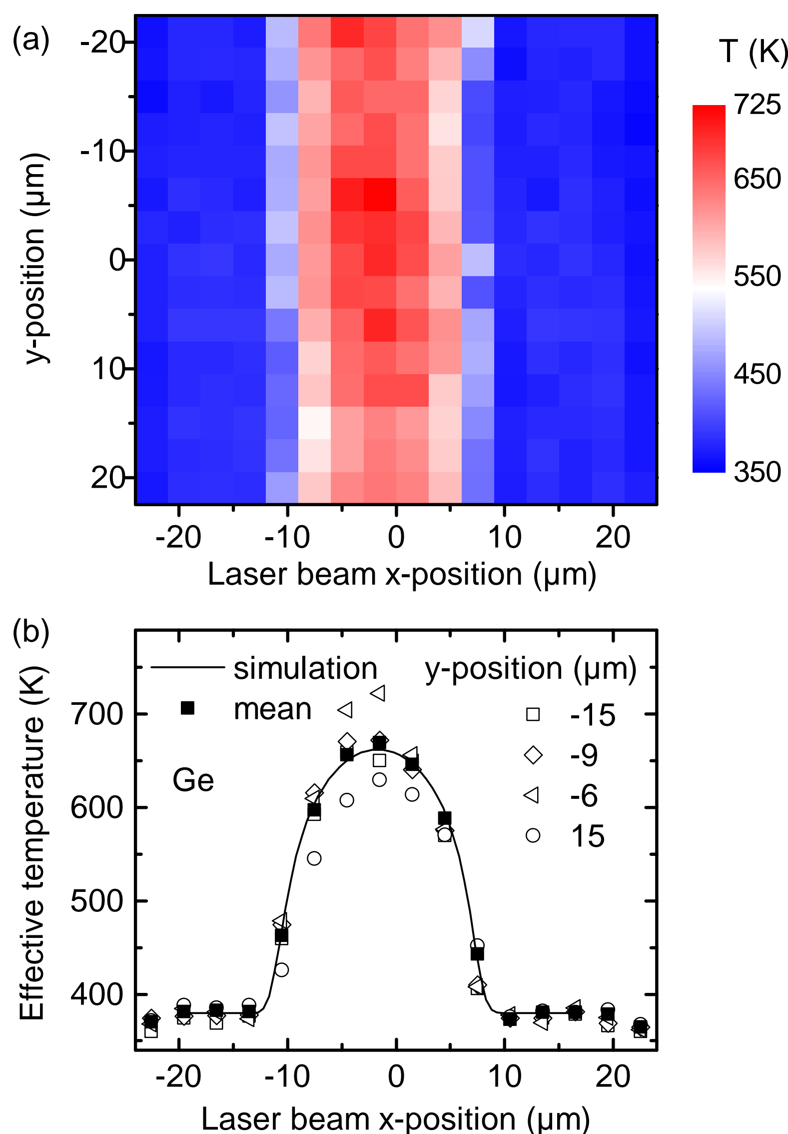

Figure 8.9. Raman temperatures on a freely suspended laser-sintered Ge NP film: (a) Color-coded map of Raman temperatures for a laser power of 148 μW. On the suspended part of the film across the trench the experiment yields an increased temperature. (b) Some extreme (-6 μm and 15 μm) and representative (-15 μm and -9 μm) x-scans are shown together with the mean of all data from (a). The simulated curve yields $\kappa_{\mathrm{Ge}}^{\mathrm{eff}} = 0.51\,\mathrm{W\,K/m}$.

conductivity, compared to the Ge film. This is confirmed by the simulation. The thermal conductivity obtained is $\kappa_{\mathrm{Si_{78}Ge_{22}}}^{\mathrm{eff}} = 0.047\,\mathrm{W/m\,K}$.

Since in thermoelectric materials a low κ is desired, it is advisable to assess the maximum thermal conductivity which is still consistent with the experimental results. Therefore, extreme input parameters as listed in Tab. 8.1 are used, rather than Gaussian error propagation, because the large uncertainties for the experimental input parameters are not distributed according to Gaussian statistics. The thermal conductivity is determined here by adjusting the simulated x-scan to the experimental x-scan, such as shown

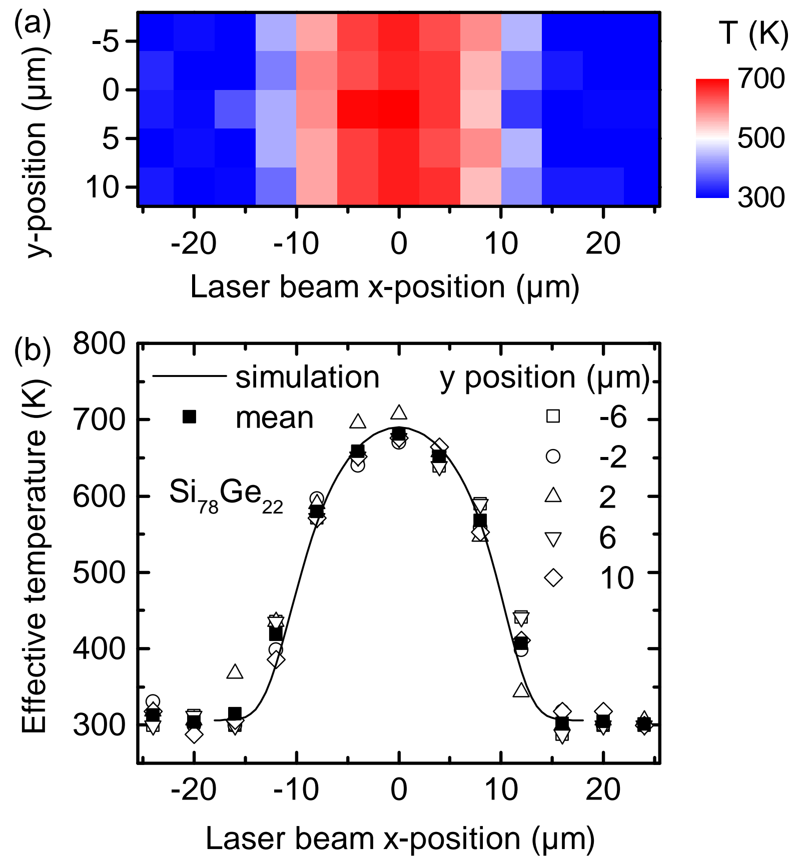

Figure 8.10. Raman temperatures on a freely suspended laser-sintered SiGe NP film: (a) Color-coded map of Raman temperatures across the suspended $Si_{78}Ge_{22}$ film for a laser power of 57.1 µW. (b) The same data shown more quantitatively, together with their mean value. The simulated curve describes a film with $\kappa^{\text{eff}}_{Si_{78}Ge_{22}} = 0.047\,\text{W K/m}$.

in Fig. 8.10 (b). There are parameters entering the simulation that change the shape of the x-scan as well as parameters that simply scale the temperature by a constant factor for all x-values. In the simulation only the trench width and the spot size slightly change the curve's shape. However, their uncertainty is small enough to only vary the resulting thermal conductivity by less than 5 %, so that their influence will be neglected.

Among those parameters that scale the simulated temperature of the x-scan, which is then accounted for by adjusting the thermal conductivity in the simulation, the porosity of the film is the most important. As a reminder, porosity is defined as the fraction of void space within the total volume. Here, a short discussion of different types of porosity shall be given first. The projected area of the meander network seen by the laser beam can be described by a porosity p_{proj}, which typically amounts to 30 %, as can be seen in Fig. 8.8 (a). The cross section of the meanders is round and further, the depth structure of the film contains some holes, too. This porosity can be called p_{depth}, amounts to approximately 20 % and can be seen for example in Fig. 8.8 (d). The discussed porosities

would enter the absorbed power according to

$$P_{\text{abs}} = P_{\text{in}} \left(1 - R\right) e^{-\alpha d \left(1 - p_{\text{depth}}\right)} \left(1 - p_{\text{proj}}\right) . \tag{8.9}$$

As known from "black" silicon, structures with sizes smaller than the wavelength of the light can decrease the reflectivity R drastically.[Alg13] This is why a reflectivity of 5 % as the lowest plausible value enters the maximum estimation. As a result, the maximum effective thermal conductivities for both samples are enhanced by approximately a factor of 3, with $\kappa_{\text{Ge}}^{\text{eff,max}} = 1.4\,\text{W/m K}$ and $\kappa_{\text{Si}_{78}\text{Ge}_{22}}^{\text{eff,max}} = 0.15\,\text{W/m K}$. These numbers also take into account the variation of other parameters, such as the absorption coefficient α or the film thickness d.

There is a third porosity which is very difficult to quantify, as it describes the transport of heat (or also charge carriers) in the plane of the film. This porosity can be called p_{transp} and is affected not only by the fraction of the covered projected area, but also by the shape and the orientation of the holes. For example, elongated holes along the transport direction are much less detrimental to the transport than elongated holes perpendicular to the transport direction. This porosity may amount to up to 90 %, as it is also discussed in the context of electrical transport in laser-sintered NP films in Fig. 5.12.

It is, however, probably more appropriate to merge the different porosities to a single porosity p, which represents an average value of roughly $p = 50\,\%$. This is also in accordance to the literature, where mostly only a single porosity is taken into account when treating a material as an effective medium.

The non-effective thermal conductivity, as it is usually found in literature,[Boo11, Tan10] would then be written as

$$\kappa = \frac{\kappa^{\text{eff}}}{1 - p}, \tag{8.10}$$

which doubles the values obtained by simulation of an effective medium. Roughly this yields $\kappa_{\text{Ge}} \approx 1\,\text{W/m K}$ and $\kappa_{\text{Si}_{78}\text{Ge}_{22}} \approx 0.1\,\text{W/m K}$.

The latter values are now suited tocompare them to bulk and other porous materials. In the temperature range between 300 K and 700 K, values for κ in undoped bulk Ge were reported to be 20 W/m K and higher.[Gla64] For micrograined n-type SiGe of approximately the composition used in this work, the minimum κ was found to be 3.5 W/m K in this temperature range.[Dis64, Vin91] In nanograined SiGe, a reduction to 2.2 W/m K or even 1.8 W/m K was achieved.[Wan08, Ste11] The values found here for κ in mesoporous Ge and n-type doped SiGe are approximately a factor of 20 lower in both cases.

It seems likely that the mesoporous structure of the laser-sintered thin films is the main reason for their reduced thermal conductivity. Studied almost exclusively in pure Si materials, a significant reduction of κ due to the nano- or micro-sized porosity was reported in literature, where mainly the smallness of the neck size, i. e., the width of remaining material between pores, is held responsible for the reduction. Compared to $\kappa = 140\,\text{W/m K}$ for bulk Si, de Boor et al. investigated etched porous-Si and reported $\kappa =$

20 W/m K for a structure size of ≈ 100 nm, which is also near the typical structure size in laser-sintered material (see Fig. 8.8 (a)).[Boo11] An even more pronounced reduction of κ was found in Si membranes with a periodic pore lattice, where the restriction of the film thickness adds to the necking effect. There, $\kappa \approx 10$ W/m K for a structure size of ≈ 159 nm was reported.[Tan10] In the systems mentioned, going from bulk to porous material leads to a reduction of κ by approximately one order of magnitude. The factor of 20 found here is slightly higher and may be explained the meander-like morphology, i. e., the fact that the films are not porous with cylindrical holes but with elongated holes having an aspect ratio of up to 5:1 in some cases. Depending on their orientation with respect to the heat flux, this can increase the effect of porosity on the reduction of the thermal conductivity.

Structuring a thermoelectric material often does not only affect κ, but also σ. This is also true for the laser-sintered films, where σ is reduced by percolation effects as studied already earlier.[Sto12] A typical electrical conductivity of samples prepared similarly to the ones used for the Raman shift method in this chapter and comprising a composition of $Si_{80}Ge_{20}$ with 1 % P-doping is $\sigma \approx 15$ S/cm at $\bar{T} \approx 500$ K.[Sto12] This value has not been normalized by porosity, so that it should be related to κ^{eff} again. Compared to bulk-nanostructured samples made from the same NP batches using CAPAD,[Ste11] the ratio σ/κ is approximately twice as high for the laser-sintered films. For both sintering methods similar Seebeck coefficients were measured. However, it is important to note here, that for laser-sintered films the ratio σ/κ was not determined on the same sample.

8.2.4. The Raman Shift Method Applied to Bulk-Nano-Crystalline Si

In this section a second application of the Raman shift method will be discussed. In contrast to the porous thin film investigated in the previous section, now almost perfectly dense bulk-nano-crystalline Si prepared by CAPAD is investigated. The fabrication and the most important morphological features are discussed in Sec. 5.2. Thermoelectric parameters of similar samples already were discussed previously in Chap. 6. The absence of Ge in the sample studied makes the materials much more interesting from an economical point of view.

The Raman shift method applied to freely suspended thin films attributed locally differing Raman temperatures and, thus, locally differing thermal conductances, to the varying distance of the excitation laser beam to the heat sink. For the large dimensions of the bulk-nano-crystalline samples here, in contrast, the geometry is assumed to be constant, namely that of a semi-infinite half space similar to the model system in Sec. 8.2.2. The local variation of Raman temperatures is now ascribed to local variations of κ. Equation 8.7 is thus taken as a basis for the evaluation of Raman temperature maps.

The sample studied is synthesized from a powder of microwave plasma grown Si NPs, which are doped with 1% P in the gas phase and have a diameter of $22 - 25$ nm. The Si NP powder used for this sample was exposed on purpose to ambient oxygen for three weeks to obtain a significant oxygen content known to impact the microstructure.

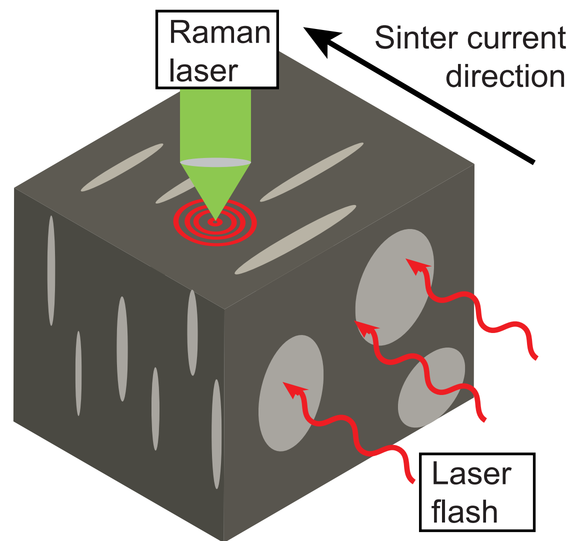

Figure 8.11. Illustration of the different measurement geometries used to study the CAPAD sample in Fig. 8.12: The oxygen-rich areas of precipitates (grey) are disc shaped and lie perpendicularly to the laser flash measurement direction. For the microscopic Raman shift method, these precipitates play a less important role as barriers for thermal transport. The direction of the sinter current was the same as the heat flux in the laser flash measurement.

The powder was then pre-compacted and solidified by CAPAD, resulting in a slight increase in crystallite size to approximately 50 nm.[Pet11, Ste11, Sch11a]

The direction of current in this sintering method leads to an anisotropy of the resulting material.[Mes12] During densification, oxygen relocates within the NP network and forms mainly two types of oxygen-rich precipitates: small and rather spherical precipitates of approximately 100 nm in size and larger agglomerates of such small precipitates forming larger structures of SiO_x.[Sch11a, Mes12] The latter are shaped like a disc, with their axis pointing in the direction of the sinter current, and have diameters of several tens of microns and a thickness of approximately 5 µm. The enriched oxygen content in the larger precipitates is accompanied by an enhanced porosity in this region.[Sch11a] Both, the different elemental composition and the different microstructure of the precipitates compared to the surrounding matrix, suggest a non-uniform thermal conductivity of the material. After densification, the sample investigated here was cut and polished by ion milling, so that the surface was flat on a tens of nanometer scale. Figure 8.11 illustrates the orientation of the precipitates within the sample investigated. The Raman experiments were carried out on the polished top surface. Additional laser flash measurements of κ were conducted from the orthogonal direction, due to geometrical restrictions of the sample. The direction of the sinter current was parallel to the direction of laser flash measurements.

The investigation of local variations of the thermal conductivity of this sample is based on the following procedure: Applying the Raman shift method, first a Raman temperature map is extracted. Using an incident laser power of 600 mW the sample is partly

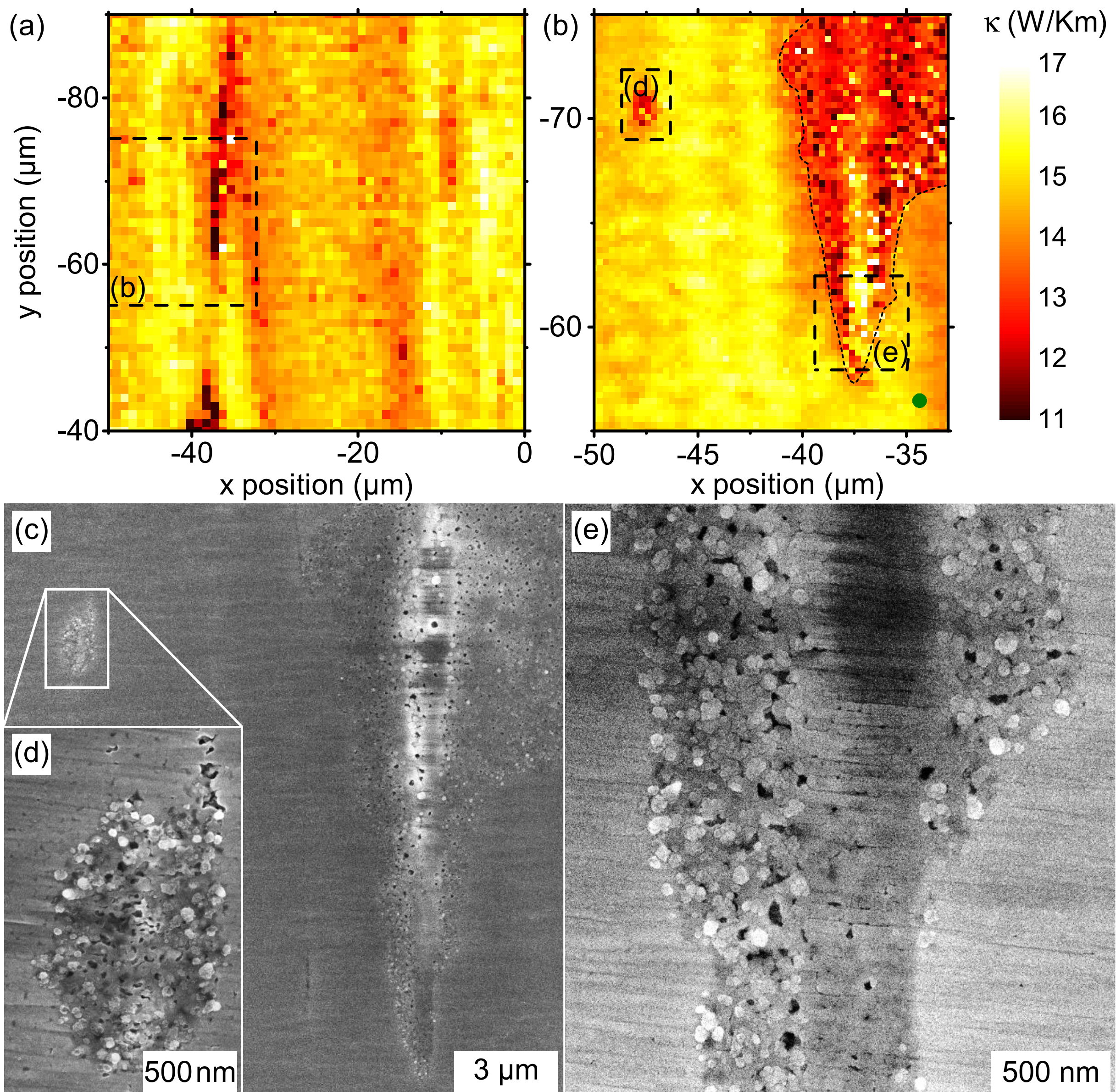

Figure 8.12. Investigation of a CAPAD sample by the Raman shift method: The locally varying thermal conductivity of heavily P-doped bulk-nano-crystalline Si is obtained from a Raman temperature map using Eq. 8.7. In panel (a) an overview of the thermal conductivity map is shown. A zoom-in of in the dashed region in panel (a) is shown in panel (b), demonstrating a nearly micron resolution of the thermal conductivity mapping. The green dot in the lower right corner shows the Gaussian full width of the laser beam used. The darker regions with a lower thermal conductivity coincide with oxygen-rich precipitates. Panel (c) shows an SEM image of the area investigated in panel (b). Panel (d) and (e) show SEM details of precipitates, which are also marked by dashed lines in panel (b). Outside the border of the precipitate in panel (e), marked with a dotted line in panel (b), the sample surface is flat.

heated up to 800 °C, so that $\frac{\partial \Delta k}{\partial T} = -0.0255\,\mathrm{cm}^{-1}/\mathrm{K}$ is used as a linear interpolation in Fig. 8.1. The high signal-to-noise ratio in the Raman experiments allows to include the contribution of free charge carriers, introduced by the high amount of P and the strong illumination, in the evaluation of the Raman spectrum. Therefore, in contrast to the other experiments of this work, the Raman temperature is not determined experimentally from the maximum of the Raman line, but rather from a fit of a Fano lineshape to the spectra (see also Fig.7.18).[Cer72, Cha78] Although the material is not homogeneous on a large scale, it is assumed to be homogeneous in the near field of the excitation laser beam. In this study a 100× objective is used, resulting in a Gaussian beam of 0.29 µm standard deviation, which is much smaller than average distances of the oxygen-rich precipitates. A reflectivity of 38% is assumed for this pure Si material.[Hum89, Šik98, Asp83] By applying Eq. 8.7 a map of local thermal conductivities is then calculated from the map of Raman temperatures.

Figure 8.12 shows such a map of the thermal conductivity, using a different color scale than in the maps of T_{Raman} discussed earlier, and the corresponding microstructure of the bulk-nano-crystalline Si sample as observed by SEM. In panel (a) an overview map of κ is shown. The map exhibits anisotropic structures which are elongated in y direction and have a lower thermal conductivity compared to the surrounding Si matrix. The dashed rectangle in (a) is shown in panel (b) with a higher resolution compared to panel (a). Structures on the length scale of a micrometer can be discerned, which demonstrates that the measurement is capable of detecting local variations in κ close to the resolution limit given by the spot size. As a guide to the eye, the green dot in the lower right corner illustrates the full Gaussian width of the laser excitation spot.

The thermal conductivities obtained by the Raman shift experiment range from 11 to 17 W/m K. This is an order of magnitude lower compared to the values reported for undoped single-crystalline Si.[Gla64, May67] The extremely high content of P and the small grained nanostructure on a scale of 50 nm resulting from sintering the small NPs can be made responsible for this reduced thermal conductivity.[Pet11, Sch14, Ste11, Sch11b] The thermal conductivity of the very sample investigated here has also been characterized as a function of temperature using the laser flash method. At room temperature the laser flash method yields a thermal conductivity of $\kappa = 9.5\,\mathrm{W/m\,K}$, which decreases to $\kappa = 6.5\,\mathrm{W/m\,K}$ at 1240 K. Thus, the temperature dependence is not pronounced, justifying the neglect of a temperature dependence of κ when deducing Eq. 8.7 also for this type of sample. However, the values obtained for κ obtained by the laser flash method are roughly a factor of 2 lower, compared to the results obtained by the Raman shift method. The most likely reason for this difference is the measurement geometry. As sketched in Fig. 8.11, for the laser flash measurements the heat flow was perpendicular to the disc shaped precipitates, making them a maximum barrier for heat transport. In the Raman shift method, the heat is spread radially into the material, with heat transport suffering only little from the alignment of the precipitates. Other reasons of minor importance for the discrepancy of a factor of 2 are spurious thermal conduction by air during the Raman measurements and the finite absorption coefficient of Si at the

wavelength used, which leads to a slight over-estimation of κ using Eq. 8.7 as discussed before.

To attribute the local variations in κ observed in this material to structural features, SEM micrographs of the areas investigated by the Raman shift method are shown in panel (c) to (e) of Fig. 8.12. Panel (c) shows the region investigated in panel (b). The large structure in the right half of the panel can clearly be recovered in the SEM image. Also the smaller feature in the upper left corner of panel (b) can be found in panel (c), and is magnified in panel (d). In contrast to the surrounding area, the surface of this feature is less flat and shows a porous interior. The same conclusion can be drawn from panel (e), which shows the second rectangular area marked with dashed lines in panel (b). A similar porosity as in the small feature can be found here. EDX scans across the structure in panel (e) confirm that the oxygen content in the porous region is enhanced by at least a factor of 4.[Sto14b, Mes12] Correlating the SEM image in panel (e) to the thermal conductivity map in panel (b) suggests that the porous regions clearly visible in SEM exhibit a lower thermal conductivity compared to the surrounding area. At least in principle, this apparently lower thermal conductivity could arise from the local increase of the absorbed laser power, which in turn could be caused by the roughness of the surface visible in the SEM micrographs.[Alg13] However, since strong variations in κ are also found for flat parts of the bulk nano-crystalline sample studied, it can be concluded that the contrast in the maps of thermal conductivity originates to a significant part from the locally varying thermal conductivity.

8.2.5. The Raman Shift Method Summarized

The Raman shift method is a versatile tool to investigate thermal properties of different materials. As a kind of summary here at the end of the chapter on the Raman shift method some essential requirements and the challenges are shortly reviewed.

The method is applicable to materials with a well defined phonon mode having a temperature-dependent Stokes shift Δk, which is used as a non-contact thermometer. The larger $\frac{\partial \Delta k}{\partial T}$, the more the method is suited. This virtually prohibits measurements at low temperatures. For heat to flow in the sample, a temperature gradient is required, which is excited by the very laser that also excites the Raman scattering. For known absorbed power and temperature at the excitation spot, the thermal conductance between the excitation spot and a heat sink can be deduced. Knowledge about the vector field of heat flux enables to calculate the material specific thermal conductivity, assuming that this quantity is spatially constant in the near field of the excitation spot.

Especially for structurally complex materials, the most challenging task is to measure the absorbed fraction of the impinging optical power. Both, the reflectivity and the absorption greatly depend on roughness, phase segregation and material density. The second challenge is to correctly account for the geometry of the sample. In only very few cases an analytical expression can be found to relate the thermal conductance to the thermal conductivity. Most realistic scenarios require a numerical analysis. Furthermore,

it is important to reduce spurious thermal conductances, as e. g. caused by substrates or ambient atmosphere. Vacuum and well defined sample structures are, thus, required in most cases. And finally: when using the Stokes shift as a local thermometer the temperature distribution beneath the excitation laser beam should be taken into account.

8.3. Lock-In Infrared Thermography to Determine the Thermal Conductivity

As an alternative thermal conductivity measurement technique to the Raman shift method, lock-in infrared thermography is proposed in this section. It offers similar robustness with respect to the roughness of the sample and, in addition, is able to measure the temperature distribution on the whole sample simultaneously, instead of spot-by-spot as it is the case for the Raman shift method.

After introducing the fundamentals of infrared thermography, this section provides a short literature survey and presents a proof-of-principle measurement on laser-sintered NP films. Challenges and advantages of lock-in infrared thermography for the measurement of the thermal conductivity are discussed.

8.3.1. Fundamentals of Lock-In Infrared Thermography

The Spectral Emission Density

The electromagnetic radiation emitted by a body is directly correlated to its temperature by Planck's law. Depending on the sample temperature T the spectral emission density P_λ for a black body is

$$P_\lambda\left(T\right) = \frac{2\pi hc^2}{\lambda^5}\frac{1}{e^{\frac{hc}{\lambda k_\mathrm{B} T}} - 1}, \tag{8.11}$$

with the Planck constant h, the wavelength λ and the Boltzmann constant k_B. This dependence is shown for some temperatures in Fig. 8.13. The absorption bands of infrared radiation by H_2O and CO_2 naturally defines mid infrared radiation or short wavelength infrared (SWIR) as the wavelength range between 3 µm and 5 µm and long wavelength infrared radiation between 8 µm and 14 µm. The InSb detector used in the following experiment is sensitive to SWIR, which offers a higher spatial resolution according to the Abbe limit. However, as obvious from Fig. 8.13, the emission density of a body at room temperature is low in the SWIR range, so that additional effort is needed to obtain a sufficient signal-to-noise ratio.

A Body's Emissivity

The radiation emitted from a body not only depends on its temperature but also on other physical properties, such as surface roughness, its band structure or its electrical

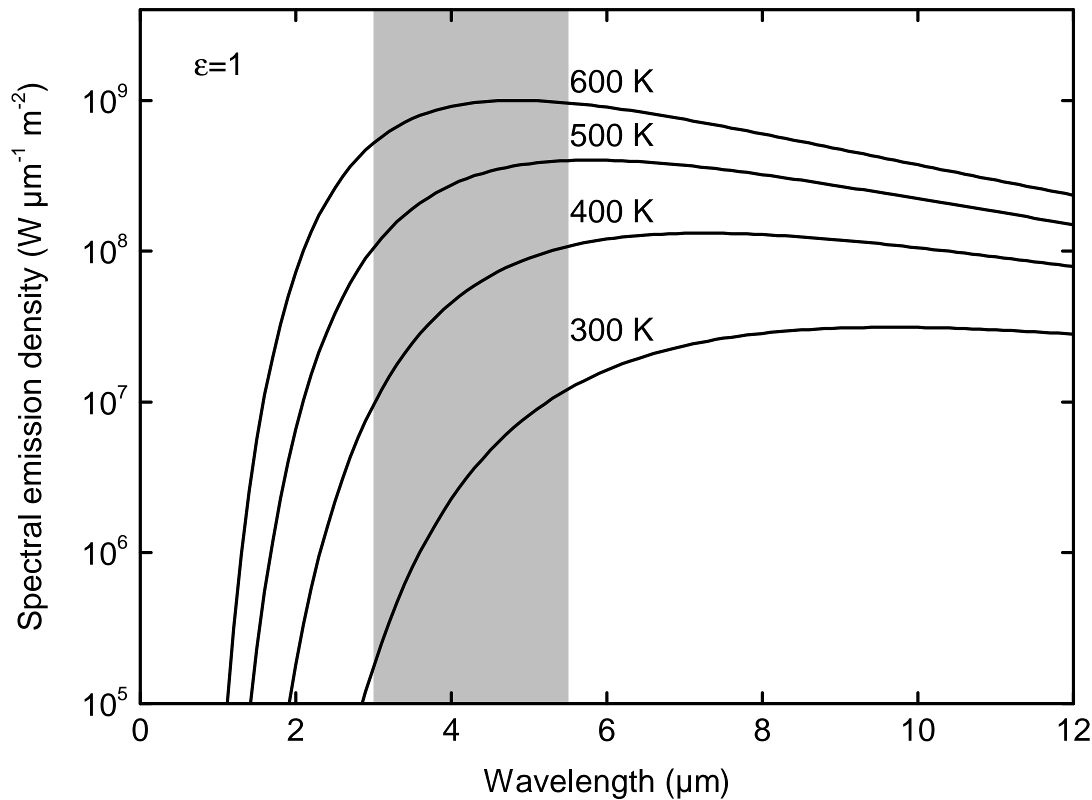

Figure 8.13. Spectral emission density $P_{\lambda}(T)$ according to Planck's law: For different temperatures the spectral emission density according to Eq. 8.11 is shown as a function of the emitted wavelength. In the shaded region the infrared detector used here is most sensitive.

conductivity. These effects are included in the emissivity ϵ, which ranges between 1 for a black body and 0. In thermal radiation equilibrium a body absorbs as much as it emits, otherwise its temperature would change. Since the absorption below the bandgap of Si as well as of Ge is rather low, ϵ is significantly lower than 1 in the SWIR regime. For example, a double side polished undoped single-crystalline Si wafer has a room temperature emissivity of approximately 5 %.[Sat67]

The highly doped laser-sintered materials discussed here, however, exhibit a variety of properties that can enhance the emissivity drastically. First, the order of magnitude of the films' roughness is in a range slightly smaller than the wavelength in the mid infrared range used to detect the temperature. This is just as in black Si, where the reflectivity is reduced and, hence, the absorption is enhanced. As a result also the emission is increased.[All57, Van92] Rough silicon at 380 °C exhibits an emissivity of 50 % between 3 and 5 µm, in contrast to $\epsilon = 10\,\%$ for smooth silicon.[Abe98] Optimized black Si can reach values of $\epsilon = 90\,\%$ or even 99 %.[Mal10, Fen11] Second, especially with regard to thermoelectric applications, the alloying of Si with Ge reduces the band

gap and, thus, also increases the absorption in the mid infrared.[Mad97] Third, the infrared absorption caused by free carriers enhances the material's emissivity.[Sat67, Lie67, Tim96, Sop99, Fu06] The relevant doping density is approximately $10^{19}\,\mathrm{cm}^{-3}$, which is easily reached by thermoelectric Si-based materials. Fourth, since SiGe is usually used as a high temperature thermoelectric material, the effect of enhanced emissivity at high temperatures should be kept in mind for thermographic measurements of these materials.[Sat67, Tim93, Rav98, Rav01]

The term emissivity is misleading since it should be called emittance, at least in the majority of measurements in the literature, which use very thick samples. So it has to be kept in mind that the emissivity stated in literature is, just as is the absorbance, an extensive quantity, which in principle depends on the sample thickness. Samples thinner than the penetration length valid at the infrared wavelength will emit less than suggested by the values obtained on bulk wafers.

Lock-In Thermography

The low spectral emission density for room temperature experiments, even for $\epsilon = 1$, discussed earlier for the SWIR regime, necessitates the use of lock-in techniques to increase the sensitivity. Most simply, a suitable camera system records frames without thermal excitation (off), which are subtracted from frames with thermal excitation (on), so that an amplitude image can be obtained. This then only shows the signal induced by the thermal excitation and background effects are largely suppressed. The more frames are taken within one excitation cycle, the more information can be gained on the diffusion of heat in the sample. This time evolution of heat spreading allows to create a phase image in addition to the amplitude image. Together, both constitute the complete information of thermal diffusion and conduction. An introduction of lock-in techniques for infrared thermography is, e. g., given in Ref. Bre00.

Optical as well as SWIR illumination (e. g., by a Light Emitting Diode (LED)), a current through the sample or thermal waves induced by heaters can be used to heat the sample periodically and supplying the reference frequency for lock-in detection. The frequency has to be chosen according to the thermal time constant of the sample structure. Since for micron-sized thin films of laser-sintered NPs this time constant is typically shorter than the shortest acquisition time of an infrared image by the system used, which is in the ms range, the sample reacts very quick to the excitation. This allows to use a square function as the correlation function for optical on/off illumination.[Bre00]

8.3.2. Previous Works on Thermographic Thermal Conductivity Measurements

There are only very few examples in the literature for measurements of the thermal conductivity or the thermal diffusivity by infrared thermography. Most works measure macroscopic samples where the thermal time constant discussed above is large

enough to follow the diffusion of heat through the sample. For a known heat capacity, which can be determined by other means, this is then directly correlated to the thermal conductivity.[Bou09, Did08] This situation is very similar to the laser-flash method.

Because the samples studied in that particular publication are at least similarly complex as laser-sintered thin films of NPs, the work of Wolf et al. is worth to note. They measured the in-plane thermal conductivity of free standing films of 20 µm thick porous Si by lock-in thermography using a line laser to excite a cylindircal heat wave in the material, which was followed by an infrared camera.[Wol04, Wol06] Another measurement, which is interesting with respect to thermoelectricity, is the work by Straube et al..[Str09] They measured the Peltier coefficient of multi-crystalline Si samples by lock-in thermography. Alternating current in forward and reverse direction leads to identical Joule heating according to $P_{\mathrm{Joule}} \propto I^2$, but the Peltier coefficient is sensitive to the direction of I. By subtracting the sample infrared images of both current directions, the net cooling and heating at the contacts reveals the Peltier coefficient.

8.3.3. A Proof-of-Principle Measurement

Measurement Geometry and Expected Temperature Profile

When samples similar to those in Sec. 8.2 are excited by, e. g., a homogenous optical illumination, they rapidly reach an equilibrium state due to the very small thermal capacitance of such thin samples. Thus, the thermal time constants are short, so that even fast infrared cameras with frame rates of up to several thousand Hz cannot follow the real-time diffusion of heat to the heat sink. These short time constants enable to investigate the difference of excitation and without excitation by lock-in thermography.

A possible sample structure for the thermographic determination of the in-plane thermal conductivity of laser-sintered NP thin films is shown in Fig. 8.14. Using an optically transparent substrate, homogeneous green illumination is absorbed in the laser-sintered NP film, which is freely suspended across a trench to avoid spurious thermal conductance by the substrate. Assuming a spatially homogeneous thermal conductivity and a perfect heat sink at the border of the trench the temperature gradient is maximal at the border of the trench and decreases linearly in magnitude towards the center of the trench. The temperature profile $T(x)$ can be written as

$$T(x) = T_{\mathrm{sink}} + p_{\mathrm{abs}} \left(\frac{\left(\frac{w}{2}\right)^2 - x^2}{2\kappa D} \right), \tag{8.12}$$

where T_{sink} is the temperature of the film in contact to the heat sink, p is the absorbed (spatially constant) illumination density, w is the width of the trench, κ is the film's in-plane thermal conductivity and D is the film thickness.

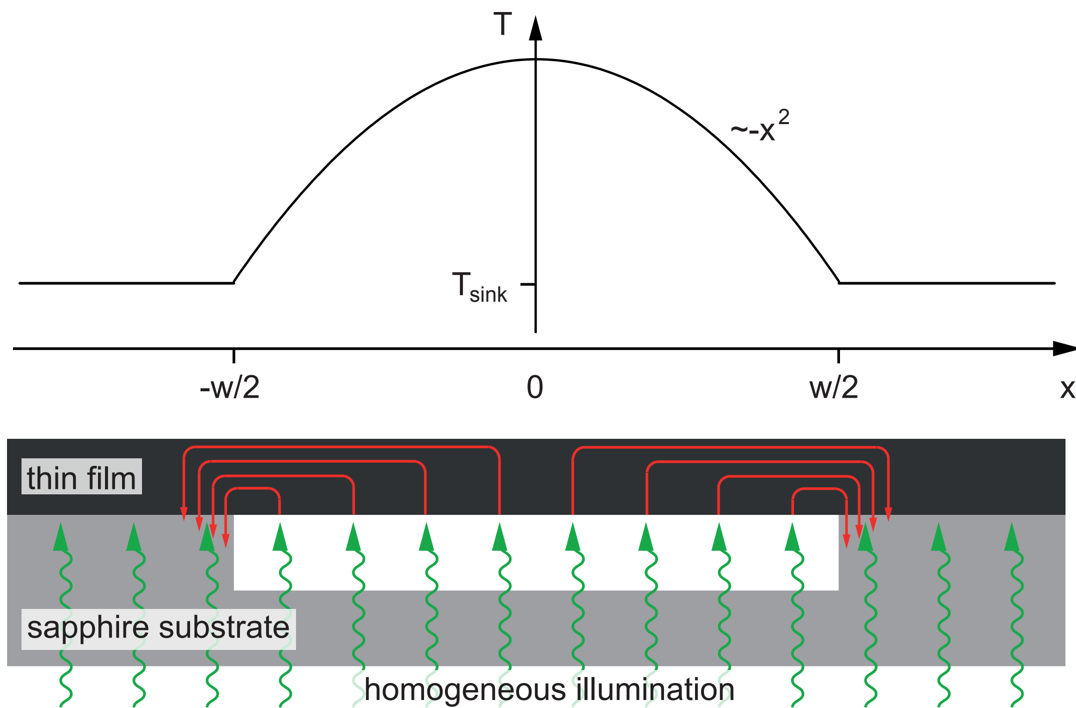

Figure 8.14. Heat flow and temperature profile for a thin film suspended over a trench: Homogenous illumination of a thin suspended film leads to a parabolic temperature profile.

Experimental Details

As a substrate for such an experiment sapphire is suitable. Its chemical inertness and hardness allows the transfer of the laser-sintered film similar to the Raman shift experiment. Illumination of the film with visible as well as with infrared radiation is possible through the substrate.[Har98] A typical room temperature thermal conductivity of sapphire of 30 W/m K makes the material an appropriate heat sink.[Dob09] Well defined trench structures can be etched into sapphire by RIE, however, chloric gases have to be used. The depth of only several µm that can typically be reached is enough to freely suspend a laser-sintered NP film.

The sample is illuminated by a green high power LED through the substrate, operated in pulsed mode. Green light is sufficiently absorbed in the thin film as was already discussed in Sec. 8.2.

In Fig. 8.15 SEM micrographs of a transferred laser-sintered $Si_{20}Ge_{80}$ NP film are shown. The region indicated by the dashed rectangle is almost free of cracks and is, thus, investigated in the following lock-in infrared thermography experiment. The composition of 20 % Ge is chosen to obtain a low thermal conductivity as well as to increase the emissivity of the film by admixture of Ge to Si.

The thermal image is detected by a Stirling-cooled SWIR camera with an InSb detector. The pixel resolution is 1.5 µm, given by a detector pitch of 15 µm and a 10× objective. The lock-in frequency is 20 Hz, which is a compromise between detector integration

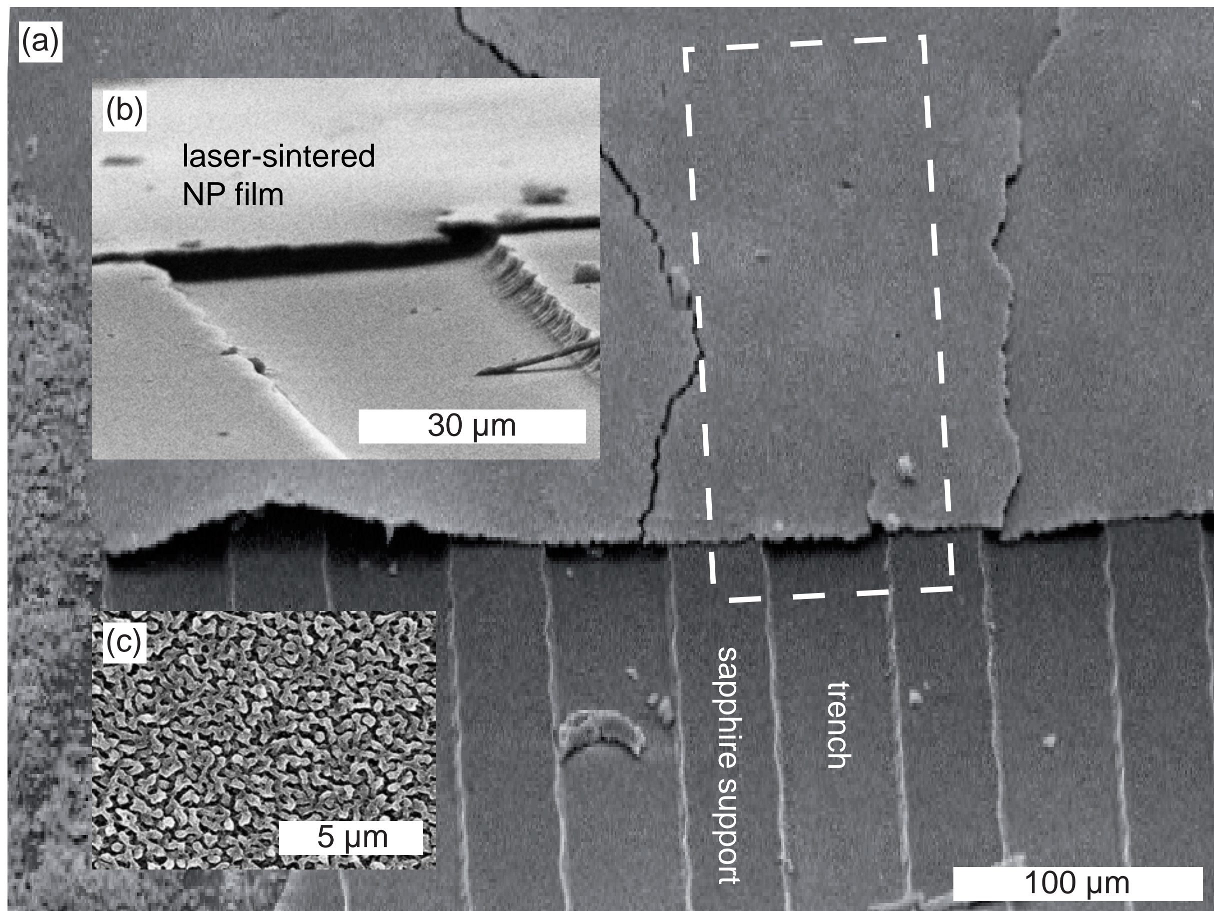

Figure 8.15. SEM views of the sample for the determination of the thermal conductivity by lock-in thermography: (a) Top view of the laser-sintered $Si_{20}Ge_{80}$ NP film on the sapphire substrate. 48 µm wide and 3 µm deep trenches were etched into the substrate by RIE. The film was transferred similarly to the experiments described in conjunction with Fig. 8.8 and lies face-down on the substrate in this case. The dashed field marks the region which is shown in the experiments in Fig. 8.16. (b) Tilted side view of the film on the trenches. (c) SEM image of the morphology of the film prior to the film transfer.

time and measurement speed.

Qualitative Results

Figure 8.16 (a) shows a so-called topography infrared image (i. e., no excitation, no lock-in action) of the region marked by dashed lines in Fig. 8.15. It shows one trench of the sample structure with the film lying on the sapphire support on the left and on the right. The thin film ends at the bottom of panel (a), where the sapphire substrate appears bright due to ou-of-focus thermal radiation from the illuminating LED. Some point defects are visible as sprinkles on the film, which can also be correlated to the SEM image in Fig. 8.15. Differences in the signal strength originate from local differences of the sample emissivity, spurious infrared radiation emitted by the underlying high

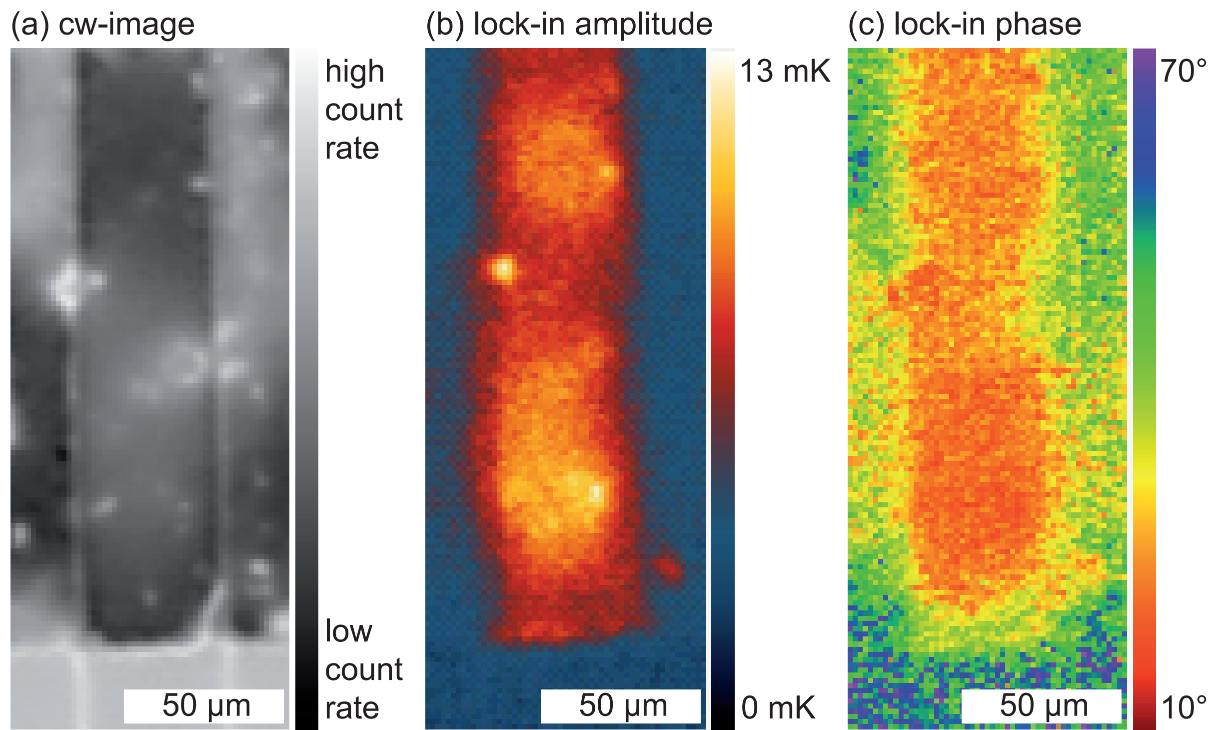

Figure 8.16. Lock-in infrared thermography of a suspended laser-sintered SiGe NP film: (a) CW topography view of the region marked by dashed lines in Fig. 8.15. At the bottom, the film ends. (b) Amplitude image of the lock-in measurement, excited by a high intensity green LED from the bottom. (c) Phase image of the lock-in measurement.

power LED and constructive or destructive infrared interference between the film and the sapphire substrate.

All those aspects cancel to first order in the amplitude image obtained by lock-in thermography in panel (b). The trench is visible by the enhanced temperature difference of the suspended part of the thin film, in comparison to the film on the sapphire support, which appears to be only slightly heated by the optical illumination. The temperature increase detected is not homogeneous along the trench, but varies by approximately a factor of two. Apart from these general features the infrared image shows some point-like hot spots, which again correlate to the defects in the SEM micrograph. The absolute temperature increase given in panel (b) must be taken with a grain of salt, since the sample's emissivity and the temperature calibration of the infrared camera setup is still ongoing at the time of the completion of this thesis. The obtained results are, thus, only qualitatively and should be understood as a proof-of-principle experiment.

The phase of the lock-in measurement in Fig. 8.16 (c) is well defined only in the region of the thin film. The freely suspended part shows a lower phase compared to the film on the sapphire support. This is an indication for heat flow from the trench center to the borders of the trench, as it can be expected. However, the absolute value of the phase holds no conclusive information, since the camera software and the synchronization

between camera, excitation and acquisition software had not been optimized yet.

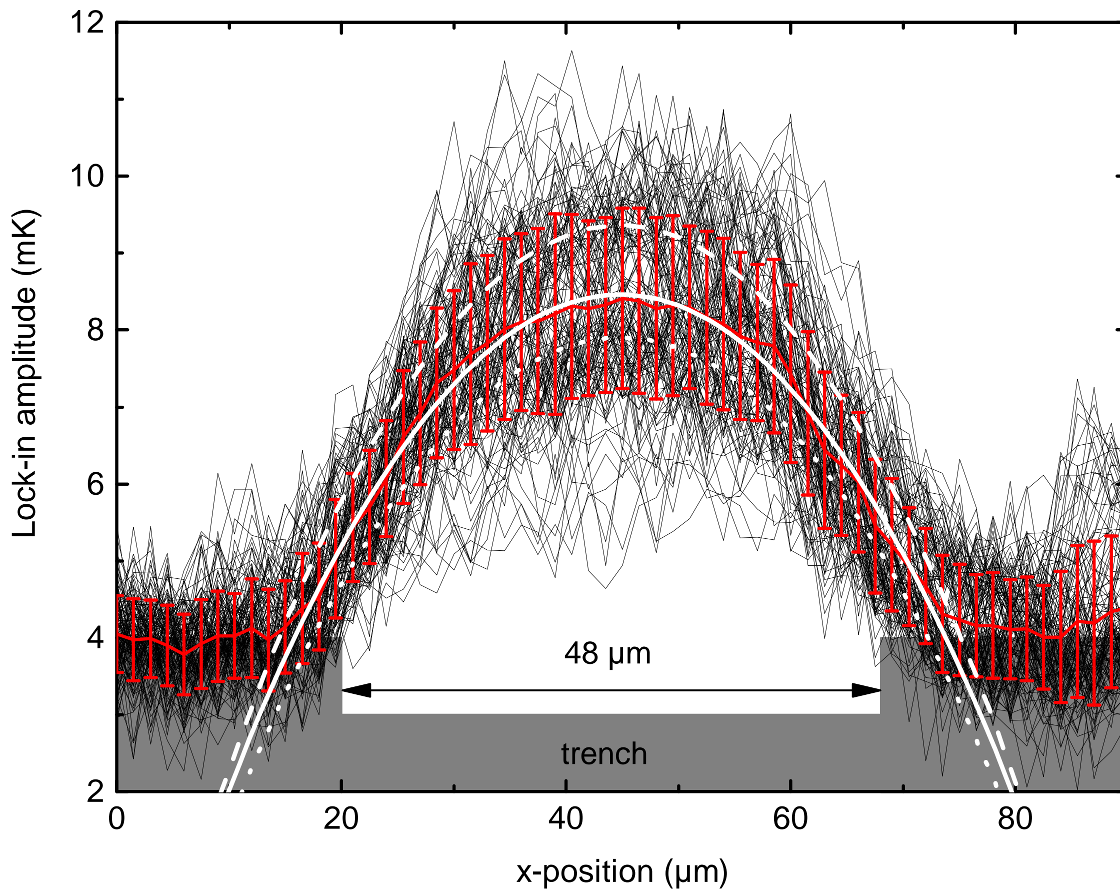

Figure 8.17. Horizontal scans of the lock-in thermography measurement on the suspended laser-sintered NP film: Horizontal lines in Fig. 8.16 are plotted as black lines. The mean value and the standard deviation are shown in red. According to Eq. 8.12, a parabola is adapted to the average value in solid white. As can also be seen in Fig. 8.16 (b), the film exhibits regions of different temperature increase. Here, this is reflected by two bunches of data, the hotter one approximately above, the colder one below the average values. The dotted and dashed lines are adapted parabolas for the corresponding data sets.

The amplitude information contained in Fig. 8.16 (b) is again shown quantitatively in Fig. 8.17. Black lines depict the experimental data, which vary by a factor of 2, as already found in Fig. 8.16 (b). Their mean value and the corresponding standard deviation are shown in red. As predicted by Eq. 8.12 the mean value can well be approximated by a parabola, which is shown as solid white line. The support structure is schematically contained in the figure and shows that the parabola reaches the temperature amplitude at the heat sink of 4 mK not exactly at the trench of the border but approximately 3 μm beyond that line. A possible reason for that is that the thin film lies face-down on the sapphire, so that a larger area is needed to transport the heat into the heat sink.

A closer look reveals that the experimental data in Fig. 8.17 consists of at least two

sub-ensembles. Each of those two can separately be described by a parabola, which are shown as white dashed lines in the figure. The signal-to-noise ratio of the infrared micrograph does not allow to reasonably adapt a parabola to a single x-scan, which would give a more useful information on the variation of the in plane thermal conductivity along the trench.

Some Remarks on Lock-In Infrared Thermography for the Determination of the Thermal Conductivity

To finally deduce the thermal conductivity quantitatively some important requirements must be met, which shall be listed here.

The most important deficiency of the measurement presented so far temperature determination, which still requires calibration. This is mainly a result of the unknown emittance of the sample and can best be overcome by calibration using an external heater leading th a well defined and known temperature of the film. It has, however, to be ensured that the infrared signal mostly originates from the film itself and not from the substrate, so that for each temperature relative measurements are necessary. To understand the thermal transport phenomena in the thin film more thoroughly the phase image must also be well understood.

A very important physical improvement to be implemented the suppression of spurious thermal conductances, mainly by ambient atmosphere. A suitable vacuum chamber needs to be designed. Pressure levels of less than 10^{-1} mbar should be already sufficient.[Fil13] The window could be made from sapphire again.[Har98] However, its thickness should be kept to a minimum to reduce the disturbing effect of this additional, optically thicker material on the infrared measurements.

However, the proof-of-principle experiment discussed above demonstrated that the temperature profile of a homogeneously excited thin film which is freely suspended across a trench indeed can be described by a parabola, as predicted by thermal transport theory. This confirms that the method is suited in general as a thin film metrology for thermal conductivity.

9 Conclusion

This final chapter summarizes the main results obtained in the framework of this thesis and attempts some conclusions with respect to thermoelectric applications.

The overall scope of this work were investigations on the processability of Si, Ge and SiGe nanoparticles (NPs) to form solid thin films and the characterization of their thermoelectric properties. A high intensity pulsed laser was used to sinter the NPs to improve the films' electrical performance. During the melting of the NPs with the nanosecond-long laser pulses, the driving force for structure formation are the different surface energies of solid and molten Si(Ge) and of the substrate. The fast crystallization forms structures of very different sizes, the largest of them being a meander-like mesoporous network, which is the most characteristic feature of laser-sintered NP films. The size of the meander network can be tuned by the fluence of the sinter laser.

An increase of the films' electrical in-plane conductivity by several orders of magnitude was observed as the meander structure evolves. Laser-sintered undopded Ge NP films, e. g., have a conductivity of 0.5 S/cm, which is up to six orders of magnitude higher than that of the initial unsintered NP film. Laser-sintering of heavily doped Ge or Si NPs can lead to conductivities of almost 100 S/cm. The effectively 2-dimensional mesoporosity of the laser-sintered films decreases the electrical conductivity by percolation effects. Typically, a reduction by a factor of 10 compared to a non-porous film was observed for the laser-sintered NP films in this thesis. After a correction for this effect, the electrical performance of laser-sintered NP films is competitive to bulk-nano-crystalline samples made from the same initial NPs by Current-Activated Pressure-Assisted Densification (CAPAD). Such samples exhibit conductivities of up to 400 S/cm for heavily n-doped SiGe NPs. By direct comparison with CAPAD samples the Seebeck coefficient of laser-sintered NP films was found to be independent of the

samples' microstructure, solely depending on the doping concentration according to basic transport theory.

Two methods to dope laser-sintered NP films were employed in this thesis: addition of dopant gases during the synthesis of the NPs and application of dopants from a liquid source prior to the laser-sintering step. The latter method was developed in this thesis and thoroughly investigated. Compared to gas-phase doping, laser-assisted wet-chemical doping is able to dope Si as well as Ge films with almost all group-III and -V elements. Both doping methods can generate charge carrier densities of up to $10^{20}\,\mathrm{cm}^{-3}$ in the materials.

For the characterization of laser-sintered NP films the determination of the thermal conductivity is the most difficult task due to the samples' very complex microstructure. Two non-contact measurement techniques were applied in this thesis: the Raman shift method and lock-in infrared thermography. While the latter was demonstrated to have the potential as a metrology tool, the first was further developed and provided quantitative results. In combination with numeric simulation the Raman shift method yields an effective thermal conductivity of 0.5 W/m K for a laser-sintered undoped Ge NP film and of 0.05 W/m K for a heavily n-doped $Si_{78}Ge_{22}$ film. These are minimum values, maximum values should not be higher by more than a factor of 3.

At the end of this thesis it has now to be assessed whether laser-sintered NP films are competitive to other thermoelectric materials and whether the unique meander structure is of benefit for thermoelectric applications. To answer this question the most useful comparison with benchmark materials is that of heavily doped SiGe with high Si content. For this, the thermal conductivity of 0.05 W/m K obtained from the data in Fig. 8.10 on $Si_{78}Ge_{22}$ is assumed to be valid also for other laser-sintered samples of similar composition. Then, e. g., from the electrical data on the gas-phase P-doped $Si_{95}Ge_{05}$ sample in Fig. 6.8 and Fig. 6.9, a ZT value of roughly 0.05 at 300 K and of 0.8 at 600 K can be estimated. As another example, the laser-assisted wet-chemically As-doped $Si_{76}Ge_{24}$ sample with the highest electrical conductivity from Fig. 7.14 is evaluated to have a ZT value of 0.4 at 300 K.

As stated above, the effective thermal conductivity values used for this ZT calculation are minimum values. Thus, these data should be understood as best-case ZT values. In Fig. 9.1 these values are shown together with benchmark SiGe material from Ref. Dis64 and CAPAD material from Ref. Ste11. The shaded region below the data representing the ZT numbers calculated above marks the influence of the uncertainty factor of 3 for the thermal conductivity. Compared to the benchmark materials SiGe thermoelectric materials, the ZT values for the laser-sintered SiGe NP films look promising since they suggest that the material is very competitive to the benchmark materials, even if a higher thermal conductivity is assumed to calculate ZT.

Although the data shown in Fig. 9.1 looks promising, there are two important facts that put these data in a different perspective. First, the electrical conductivity and the Seebeck coefficient of the samples are measured right after their fabrication, so that the

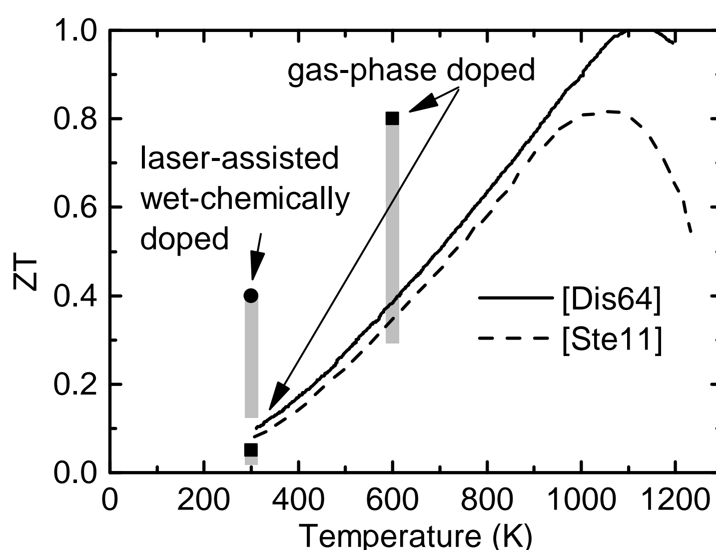

Figure 9.1. Best case evaluation of ZT for laser-sintered SiGe NP films: Assuming an effective thermal conductivity of 0.05 W/m K the calculated ZT values for two different laser-sintered SiGe NP samples are shown together with benchmark materials from Ref. Dis64 and Ref. Ste11. Since the thermal conductivity is a minimum value, the shaded region depicts the range of ZT for a more conservative estimation. It has to be noted here, that electrical and thermal data have been determined on different samples.

thin films are manipulated as little as possible. In contrast, the thermal conductivity determination requires a substantial amount of manipulation of the films, since they have to be prepared in a form suspended across a trench. The mechanical forces acting during this manipulation are known to lead to a low yield of transferable sample area. Therefore, one must assume that even in those parts of the film that could be transferred onto the trenches, micro-cracks deteriorate the integrity of the materials. Second, electrical conductivity and thermal conductivity have not been measured on identical samples. This is one of the most widespread reasons to mistrust calculated ZT values. As it is known from SEM investigations of the samples used for the calculation of the ZT values in Fig. 9.1, their morphology in detail is different: The interconnection of the samples evaluated for their electrical performance is superior to the one of the samples used for determination of the thermal conductivity. To be precise, the well connected samples tend to have a higher degree of substrate coverage, where the meander structure already disappeares and only circular holes are left within a dense matrix. The samples used for the determination of the thermal conductivity are known to contain a significant amount of unsintered NPs beneath the meander structure, which were necessary to increase the mechanical stability for laser-sintering on glass substrates and the film transfer. In such a case, films with meanders that are not completely connected still can look fine in SEM investigations. In summary, taking samples with exceptionally high electrical conductivities adds a selection bias to the ZT evaluation, as the statistical basis for electrical measurements is much larger than the one for thermal measurements.

This deficiency could only be remedied if both thermal and electrical measurements are performed on identical samples, ideally at identical positions after identical mechanical treatment. In such a case it would also be possible to more deeply investigate the impact of the tunable meander structure size on the ratio σ/κ. Also, cross-correlation with other metrology methods could help to remove the uncertainty of the ZT evaluation given here.

To summarize, the mentioned aspects of uncertainty of the thermal conductivity and the selection bias evaluating ZT allow a rather large range of conclusions concerning the possible benefit of the meander structure for thermoelectric applications. The best-case evaluation shown in Fig. 9.1 allows the conclusion that, indeed, laser-sintered NP films show a superior performance to benchmark material. However, following the discussions above and according to his basic careful attitude, the author prefers to phrase the conclusion that the meander structure is non-detrimental to thermoelectric performance.

As a final aspect, a very general remark shall be made concerning the applicability of thin films for thermoelectric energy harvesting. For a material to serve as an energy supply using thermoelectrics, the optimization with respect to efficiency should be substituted by an optimization for maximum power output. However, according to $P = U\,I$ and the underlying relations of U and I with the TEG's vertical and lateral dimensions, "power needs volume". Even assuming highest ZT values for the thin film materials studied, no significant power output beyond the range of mW appears possible. Not withstanding the fact that the discussed structurally complex materials are of highest relevance for academia and the advancement of materials science, this fundamental aspect basically limits the application of these thin films to low power applications such as sensing. There, by the way, the prospect of ink-jet printing such structures provides an essential degree of freedom.

Acronyms

BET Brunauer-Emmett-Teller

CAPAD Current-Activated Pressure-Assisted Densification

DOS Density Of States

EDX Energy-Dispersive X-ray spectroscopy

FIB Focussed Ion Beam

FTIR Fourier Transform Infrared Spectroscopy

ICP Inductively-Coupled Plasma

LAICP-MS Laser-Ablation Inductively-Coupled Plasma Mass Spectrometry

LED Light Emitting Diode

Nd:YAG Neodymium-doped Yttrium Aluminum Garnet

NP NanoParticle

PDS Photothermal Deflection Spectroscopy

RIE Reactive Ion Etching

SEM Scanning Electron Microscopy

SIMS Secondary Ion Mass Spectroscopy

SPS Spark Plasma Sintering

STEM Scanning Transmission Electron Microscopy

TEG Thermoelectric Generator

TEM Transmission Electron Microscopy

XPS X-ray Photo-electron Spectroscopy

XRD X-Ray Diffraction

Simulation of Thermoelectric Properties for Laser-Sintered Ge Films

In Fig. 6.2, the temperature dependence of the Seebeck coefficient for laser-sintered Ge NP films is simulated and adapted to experimental data. The simulation is based on assumptions for the DOS and the group velocity in this poly-crystalline Ge material, shown in Fig. 6.3. The effective density of states masses are calculated according to

$$N_{\mathrm{VB/CB}}^{\mathrm{eff}} = 2 \cdot \left(\frac{2\pi m_{\mathrm{h/e}}^{\mathrm{eff}} kT}{h^2} \right)^{3/2}, \tag{A.1}$$

where the effective densities of states at 300 K are taken from Ref. Sze1981. This yields $m_{\mathrm{h}}^{\mathrm{eff}} = 0.370\ m_0$ and $m_{\mathrm{e}}^{\mathrm{eff}} = 0.549\ m_0$.

The main intention of the simulation is to back up the hypothesis that the pronounced p-type behavior of laser-sintered Ge films is the result of a density of dangling bonds with a charge transfer level positioned within the band gap near the valence band. The main result presented in Sec. 6.2 is that the experimental data can well be described when introducing a dangling bond density of $2 \times 10^{17}\ \mathrm{cm}^{-3}$. In the DOS used in Fig. 6.3 this dangling bond density is modeled by a Gaussian distribution 30 meV above the valence band and having a FWHM of 60 meV. In this appendix the influence of a variation of size, position and width of this dangling bond density on the resulting Seebeck coefficient will be shown. Since the value of the group velocity in the band gap in Fig. 6.3 has been chosen rather arbitrarily, an influence of a variation also of this quantity will be discussed.

In Fig. A.1 the density of dangling bonds is varied by a factor of roughly 3. The

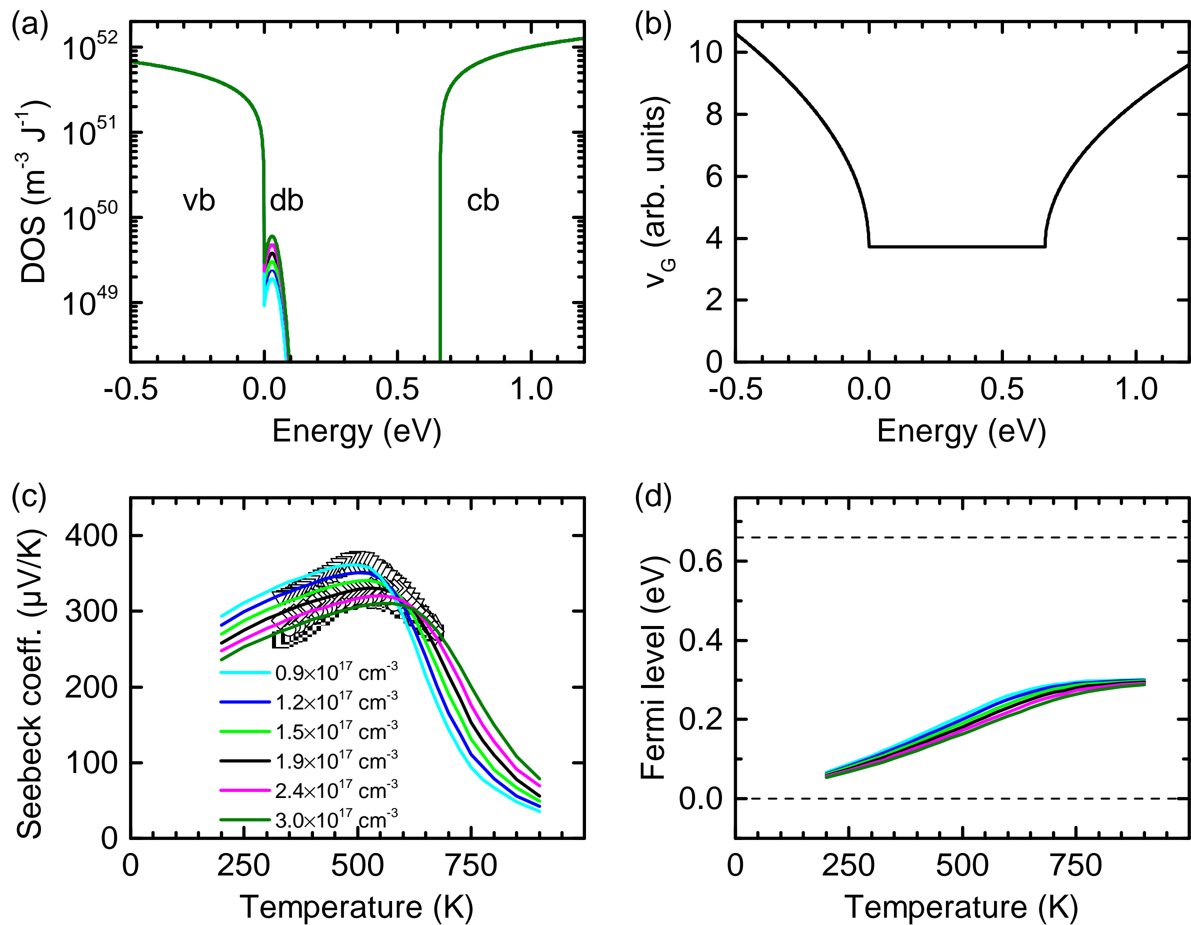

Figure A.1. Influence of a variation of the Ge dangling bond density on the temperature dependence of the Seebeck coefficient: (a) The DOS and (b) the group velocity as assumed for the simulation. (c) The Seebeck coefficient, shown together with experimental data and (d) the resulting Fermi level as calculated by the simulation. The density of dangling bonds is varied here.

main effect of this variation is a more persistent pinning of the Fermi level at the dangling bond position for a higher dangling bond density. For all data sets the Seebeck coefficient is qualitatively similar, but the temperature, where the Seebeck coefficient is maximal, is shifted. By comparison to the experimental data the variation of the dangling bond density by a factor of 3 seems to be in agreement with experiment for moderate temperatures, whereas for higher temperatures the experimental data merge more clearly compared to the simulated data sets. Since in this work the temperature of the maximum Seebeck coefficient is taken as a measure to adapt the dangling bond density in the simulation, a value of roughly $2 \times 10^{17}\ \mathrm{cm}^{-3}$ is the best compromise.

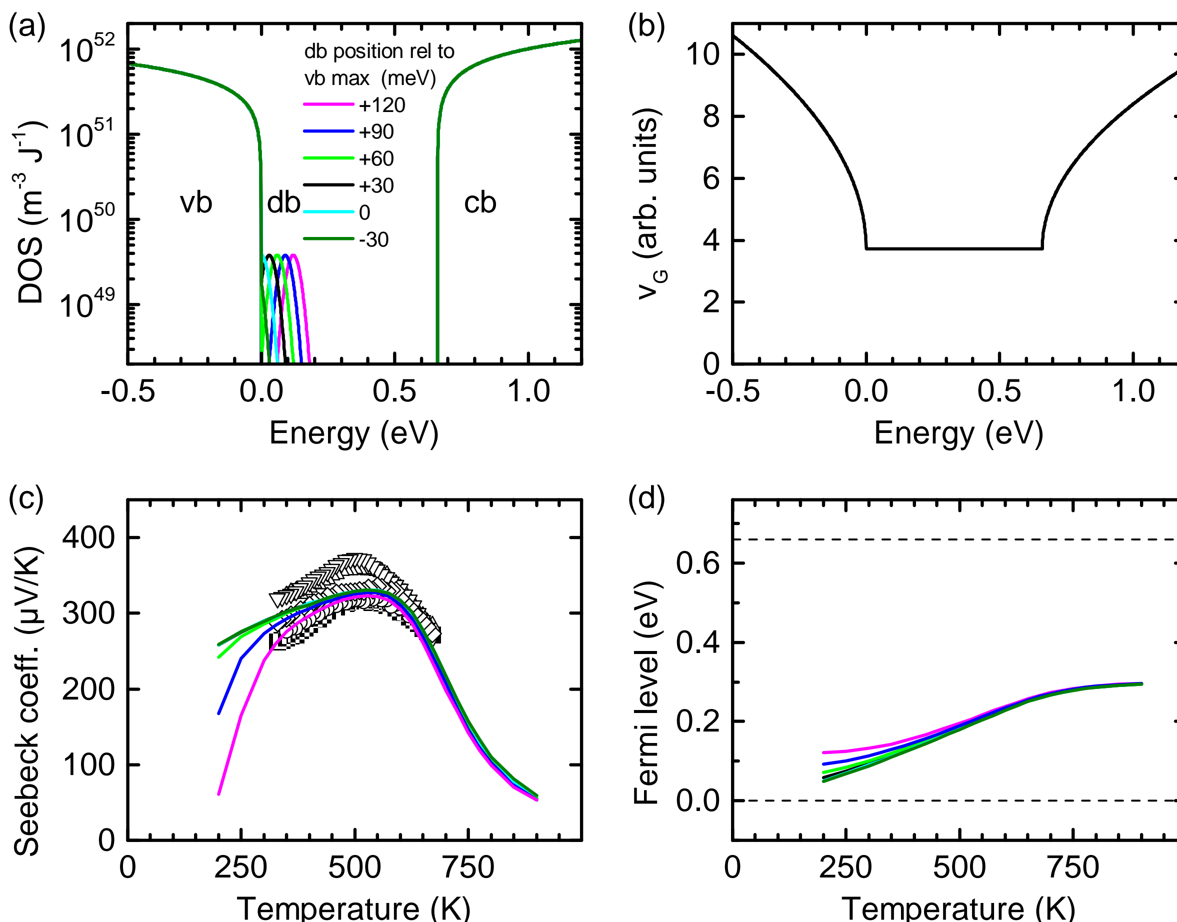

Figure A.2. Influence of a variation of the Ge dangling bond position on the temperature dependence of the Seebeck coefficient: (a) The DOS and (b) the group velocity as assumed for the simulation. (c) The Seebeck coefficient, shown together with experimental data and (d) the resulting Fermi level as calculated by the simulation. The energy of the dangling bond charge transfer level is varied here.

As a second investigation, in Fig. A.2 the position of the dangling bond level is varied. This quantity is discussed controversly in the literature. Theoretical values above the band edge as well as theoretical predictions below the band edge have been reported.[Bro10, Bro12, Web13] Therefore, it is interesting to see that in the temperature range of interest for this work, above room temperature, a shift of the dangling bond level by the values indicated in panel (a) has nearly no influence on the resulting Seebeck coefficient. As a result, a value of 30 meV above the band edge is taken for the simulation discussed in Sec. 6.2.

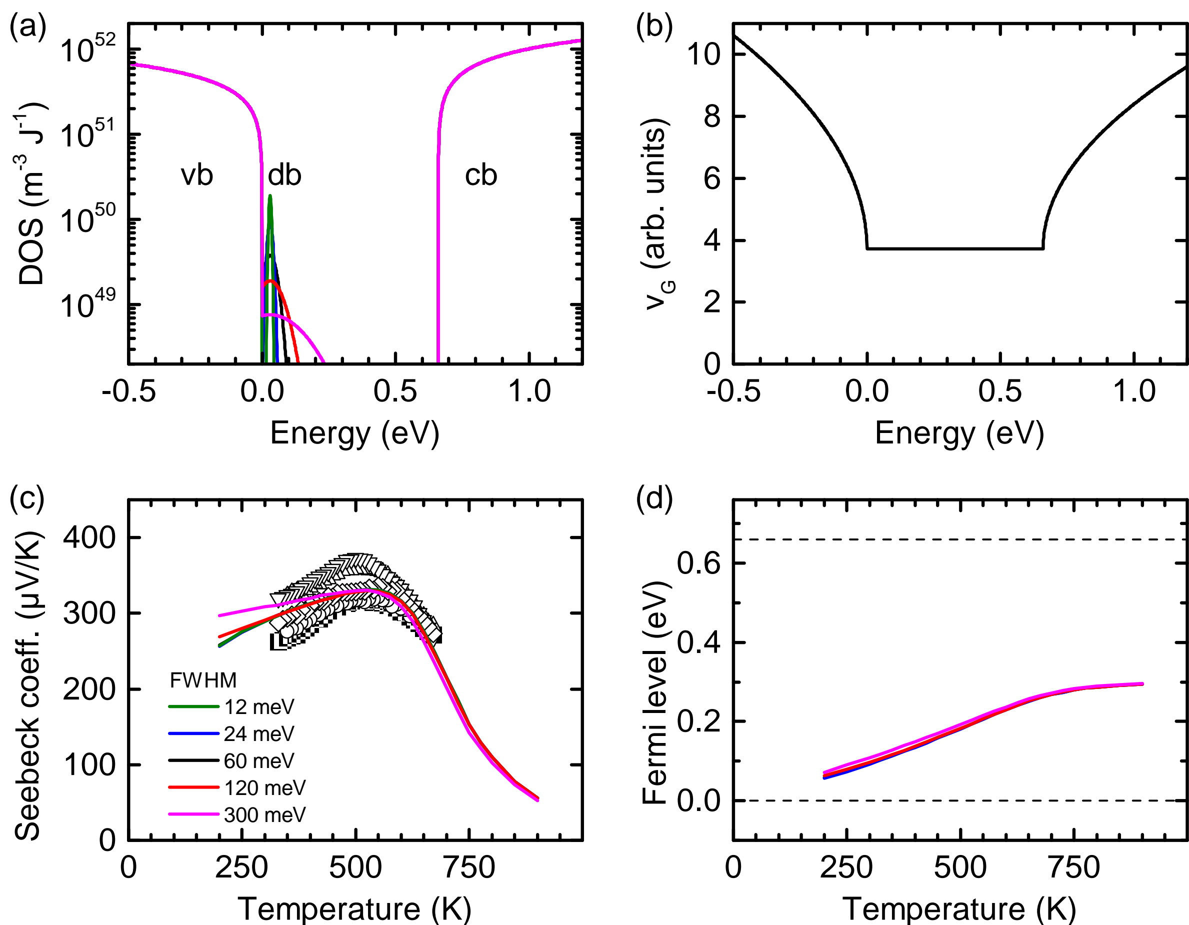

Figure A.3. Influence of a variation of the Ge dangling bond width on the temperature dependence of the Seebeck coefficient: (a) The DOS and (b) the group velocity as assumed for the simulation. (c) The Seebeck coefficient, shown together with experimental data and (d) the resulting Fermi level as calculated by the simulation. The width of the dangling bond DOS is varied here.

In the literature there is hardly any information on the distribution of the dangling bond charge transfer levels. But as can be seen in Fig. A.3 also this quantity has no significant influence above room temperature. This is why a FWHM value of 60 meV is taken here.

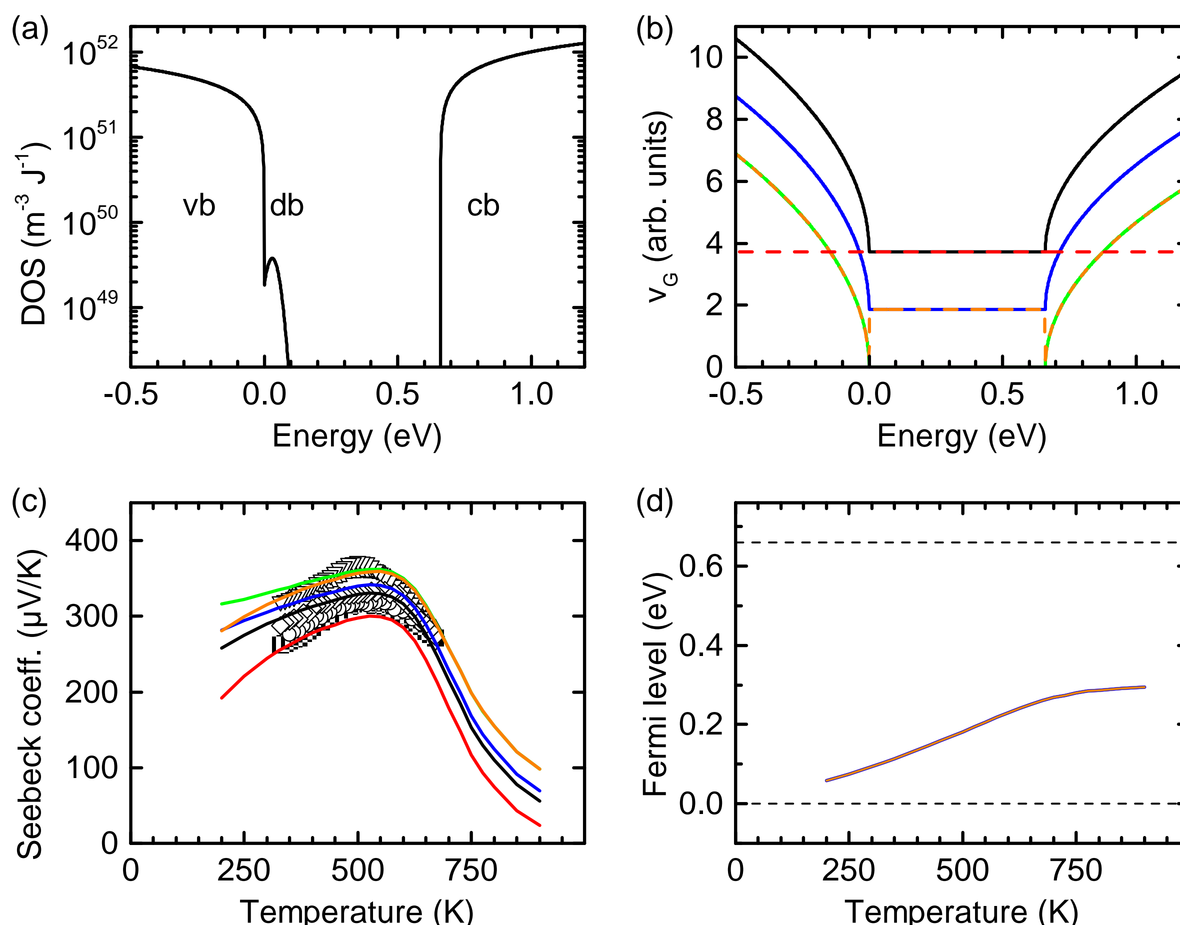

Figure A.4. Influence of a variation of the group velocity on the temperature dependence of the Seebeck coefficient : (a) The DOS and (b) the group velocity as assumed for the simulation. (c) The Seebeck coefficient, shown together with experimental data and (d) the resulting Fermi level as calculated by the simulation. The different assumptions for the energy-dependent group velocity are shown in panel (b).

Finally, Fig. A.4 summarizes the effect of a variation of the group velocity. In panel (b) a couple of different functions are shown. However, especially the temperature where the maximum Seebeck coefficient occurs is hardly influenced by the specific type of function, so that it appears appropriate to choose the group velocity distribution shown also in Fig. 6.3.

It has to be noted that the somewhat strong variation of the Seebeck coefficient at temperatures below room temperature in all figures shown in this appendix can also be a result of the quantization in the simulation. The Fermi distribution function for these temperatures varies within an energy range which is already in the range of the energy quantization steps. This can result in wrongly calculated Fermi levels since the charge neutrality condition cannot be evaluated correctly in this very simple simulation.

B

Iterative Multigrid Gauss-Seidel Algorithm

For most sample geometries the temperature distribution for a given excitation cannot be calculated analytically. Whenever this is not possible, a numerical approach is used, where the field of interest is discretized in a rectangular grid and the discretized stationary heat diffusion equation is solved on every grid point. As an example a two-dimensional quadratic grid of dimension a, divided into n grid points in each direction is discussed, so that one pixel has a width of $h = \frac{a}{n}$. The spatial coordinates x and y can be expressed by two indices i and j

$$(x, y) \rightarrow (i \times h, j \times h). \tag{B.1}$$

Derivatives in Eq. 8.1 are expressed in terms of discrete differences, e.g.

$$\frac{\partial^2 T}{\partial x^2} \rightarrow \frac{T_{i+1,j} + T_{i-1,j} - 2T_{i,j}}{h^2}. \tag{B.2}$$

The boundary conditions of a constant temperature T_{sink} outside of the simulation area and the continuity of heat flow, so that the heat introduced by $H(\vec{r})$ and the heat flowing into the heat sink are identical, are included. A thermal resistance R_{th} to the heat sink can also be considered. The problem to be solved can then be written as

$$\underline{A} \cdot T_{i,j} = H_{i,j}, \tag{B.3}$$

which is a linear set of equations with the matrix $\underline{A}$ containing all thermal conductivities and contact resistances.

Instead of directly solving Eq. B.3, computation speed is enhanced by implementing a solver, based on an iterative Gauss-Seidel algorithm, where the computation effort only scales almost proportionally to the number of grid points.[Bri00] In this algorithm the differential equation is not solved for all grid points simultaneously, but for each grid point in successive cycles, so that the discretized heat equation on each point is solved for $T_{i,j}$ with the values of neighboring points inserted from the previous cycle. This is repeated until a desired accuracy is achieved. Since spatially slowly varying temperature distributions converge only weakly, a multigrid algorithm is employed on several grid sizes, first approximating the global temperature distribution on a coarse grid, and then refining this grid by factors of 2 and interpolating the temperature distribution stepwise.[Bri00] Between all steps, Gauss-Seidel iterations are performed. The use of different grid sizes drastically speeds up the convergence of the method.

The Raman Temperature for Heat Spreading into a Semi-Infinite Sample

In Sec. 8.2 a rather simple equation was used to relate the Raman temperature T_{Raman} deduced from a single Raman measurement to the (spatially constant) thermal conductivity κ of a bulk sample. Here, the analytical derivation of Eq. 8.7 shall be reproduced from Ref. Fil13, which in turn essentially follows the work in Refs. Car86 and Wat95.

A homogeneous and semi-infinite bulk material is assumed, which fills a half-space. Cylindrical coordinates ϕ, r and z are used. The azimuthal angle is denoted by ϕ. $z = 0$ marks the surface of the semi-infinite sample with the z-axis pointing into the sample. r is the radius from the center of the excitation Raman laser beam, which is assumed to exhibit a radially Gaussian-shaped excitation power density

$$H(r, z = 0) = \frac{P}{2\pi w^2} e^{-\frac{r^2}{2w^2}}, \tag{C.1}$$

with absorbed power P and standard deviation w. This derivation assumes that the heat supplied by the Raman laser beam is only introduced into the sample in the plane $z = 0$, which corresponds to a model where the excitation power is strongly absorbed at the surface.

Within the material (i. e. for $z > 0$) the sample temperature $T(\vec{r})$ must obey the stationary heat equation in cylindrical coordinates without heat sources

$$\frac{\partial^2 T}{\partial r^2} + \frac{1}{r}\frac{\partial T}{\partial r} + \frac{\partial^2 T}{\partial z^2} = 0, \tag{C.2}$$

which is satisfied by

$$T \propto e^{-|\lambda|z} J_0(\lambda r) \tag{C.3}$$

for any λ with $J_0(\lambda r)$ being the Bessel function of first kind and zeroth order. Circular heat flow in direction of the azimuthal angle ϕ can be neglected due to the symmetry of the problem. Equation C.2 is then also satisfied by

$$T = \int_0^\infty e^{-|\lambda|z} J_0(\lambda r) f(\lambda) \mathrm{d}\lambda, \tag{C.4}$$

where $f(\lambda)$ can be chosen to fulfil the boundary conditions. In this problem the Neumann boundary condition is given by the energy flow from the surface into the sample, introduced by the laser power density $H(r, z = 0)$,

$$-\kappa \left. \frac{\partial T}{\partial z} \right|_{z=0+} = \frac{P}{2\pi w^2} e^{-\frac{r^2}{2w^2}}. \tag{C.5}$$

Inserting Eq. C.4 into Eq. C.5 leads to the condition

$$\kappa \int_0^\infty \lambda J_0(\lambda r) f(\lambda) \mathrm{d}\lambda = \frac{P}{2\pi w^2} e^{-\frac{r^2}{2w^2}} \tag{C.6}$$

for $f(\lambda)$. For the solution, the identity

$$\int_0^\infty x J_0(xr) e^{-\frac{w^2 x^2}{2}} \mathrm{d}x = \frac{1}{w^2} e^{-\frac{r^2}{2w^2}} \tag{C.7}$$

is needed.[Wat95] Therefore, one can insert the function

$$f(\lambda) = \frac{P}{2\pi\kappa} e^{-\frac{w^2\lambda^2}{2}} \tag{C.8}$$

into Eq. C.4, resulting in

$$T(r) = \frac{P}{2\pi\kappa} \int_0^\infty J_0(\lambda r) e^{-\frac{w^2\lambda^2}{2}} \mathrm{d}\lambda. \tag{C.9}$$

The effective Raman temperature T_{Raman} can then be obtained from Eq. 8.3 and Eq. C.7

as

$$
\begin{aligned}
T_{\mathrm{Raman}} &= T_{\mathrm{sink}} + \tfrac{1}{P} \int\limits_{\phi=0}^{2\pi} \int\limits_{r=0}^{\infty} T(r) H(r)\, r \,\mathrm{d}\phi \,\mathrm{d}r \\
&= T_{\mathrm{sink}} + \tfrac{P}{4\sqrt{\pi}\kappa w}.
\end{aligned}
\tag{C.10}
$$

For a homogeneous semi-infinite sample, excited by a Gaussian-shaped laser beam with strong absorption, the spatially constant thermal conductivity κ is then in turn given by

$$
\kappa = \frac{P}{4\sqrt{\pi}\,(T_{\mathrm{Raman}} - T_{\mathrm{sink}})\,w}. \tag{C.11}
$$

Bibliography

[Abe98] S. Abedrabbo, J. C. Hensel, O. H. Gokce, F. M. Tong, B. Sopori, A. T. Fiory, and N. M. Ravindra: *Issues in emissivity of silicon*, Mat. Res. Soc. Symp. Proc. **525**, 95 (1998).

[Ada96] S. Adachi, T. Arai, and K. Kobayashi: *Chemical treatment effect of Si(111) surfaces in F-based aqueous solutions*, J. Appl. Phys. **80**, 5422 (1996).

[Ada97] A. W. Adamson and A. P. Gast: *Physical chemistry of surfaces* (Wiley, New York, 1997), 6th edn..

[Alg13] M. Algasinger, J. Paye, F. Werner, J. Schmidt, M. S. Brandt, M. Stutzmann, and S. Koynov: *Improved black silicon for photovoltaic applications*, Adv. Energy Mater. **3**, 1068 (2013).

[All18] E. Allen and E. Zies.: *The condition of arsenic in glass and its role in glass-making*, J. Am. Ceram. Soc. **1**, 787 (1918).

[All57] F. G. Allen: *Emissivity at 0.65 micron of silicon and germanium at high temperatures*, J. Appl. Phys. **28**, 1510 (1957).

[Alt09] E. Altenkirch: *Über den Nutzeffekt der Thermosäule*, Physikalische Zeitschrift **16**, 560 (1909).

[An13] T. An, V. I. Vasyuchka, K. Uchida, A. V. Chumak, K. Yamaguchi, K. Harii, J. Ohe, M. B. Jungfleisch, Y. Kajiwara, H. Adachi, B. Hillebrands, S. Maekawa, and E. Saitoh: *Unidirectional spin-wave heat conveyer*, Nature Mater. **12**, 549 (2013).

[Ant07] T. Antesberger, C. Jäger, M. Scholz, and M. Stutzmann: *Structural and electronic properties of ultrathin polycrystalline Si layers on glass prepared by aluminum-induced layer exchange*, Appl. Phys. Lett. **91**, 201909 (2007).

[App79] B. R. Appleton, B. C. Larson, C. W. White, J. Narayan, S. R. Wilson, and P. P. Pronko: *New materials properties achievable by ion implantation doping and laser processing*, AIP Conf. Proc. **50**, 291 (1979).

[Ash97] M. Asheghi, Y. K. Leung, S. S. Wong, and K. E. Goodson: *Phonon-boundary scattering in thin silicon layers*, Appl. Phys. Lett. **71**, 1798 (1997).

[Ash98] M. Asheghi, M. N. Touzelbaev, K. E. Goodson, Y. K. Leung, and S. S. Wong: *Temperature-dependent thermal conductivity of single-crystal silicon layers in SOI substrates*, J. Heat Transfer **120**, 30 (1998).

[Asp83] D. E. Aspnes and A. A. Studna: *Dielectric functions and optical parameters of Si, Ge, GaP, GaAs, GaSb, InP, InAs, and InSb from 1.5 to 6.0 eV*, Phys. Rev. B **27**, 985 (1983).

[Aw91] S. E. Aw, H. S. Tan, and C. K. Ong: *Optical absorption measurements of band-gap shrinkage in moderately and heavily doped silicon*, J. Phys.: Condens. Matter **3**, 8213 (1991).

[Bac57] G. Backenstoss: *Conductivity mobilities of electrons and holes in heavily doped silicon*, Phys. Rev. **108**, 1416 (1957).

[Bai99] R. Baierle, M. Caldas, J. Dabrowski, H.-J. Müssig, and V. Zavodinsky: *A unified microscopic mechanism for donor deactivation in Si*, Physica B **273-274**, 260 (1999).

[Bal75] M. Balkanski, K. P. Jain, R. Beserman, and M. Jouanne: *Theory of interference distortion of Raman scattering line shapes in semiconductors*, Phys. Rev. B **12**, 4328 (1975).

[Bal83] M. Balkanski, R. F. Wallis, and E. Haro: *Anharmonic effects in light scattering due to optical phonons in silicon*, Phys. Rev. B **28**, 1928 (1983).

[Bal08] A. A. Balandin, S. Ghosh, W. Bao, I. Calizo, D. Teweldebrhan, F. Miao, and C. N. Lau: *Superior thermal conductivity of single-layer graphene*, Nano Lett. **8**, 902 (2008).

[Bal10] J. Bal, S. Kundu, and S. Hazra: *Hydrophobic to hydrophilic transition of HF-treated Si surface during Langmuir-Blodgett film deposition*, Chem. Phys. Lett. **500**, 90 (2010).

[Bal11] A. A. Balandin: *Thermal properties of graphene and nanostructured carbon materials*, Nature Mater. **10**, 569 (2011).

[Bar76] S. K. Barthwal and K. L. Chopra: *Thermoelectric power of amorphous germanium films*, Phys. Status Solidi A **36**, 533 (1976).

[Bat00] J. E. Bateman, R. D. Eagling, B. R. Horrocks, and A. Houlton: *A deuterium labeling, FTIR, and ab initio investigation of the solution-phase thermal reactions of alcohols and alkenes with hydrogen-terminated silicon surfaces*, J. Phys. Chem. B **104**, 5557 (2000).

[Bec09] M. Becker, U. Gösele, A. Hofmann, and S. Christiansen: *Highly p-doped regions in silicon solar cells quantitatively analyzed by small angle beveling and micro-Raman spectroscopy*, J. Appl. Phys. **106**, 074515 (2009).

[Bec12] A. Becker, S. Angst, A. Schmitz, M. Engenhorst, J. Stötzel, D. Gautam, H. Wiggers, D. E. Wolf, G. Schierning, and R. Schmechel: *The effect of Peltier heat during current activated densification*, Appl. Phys. Lett. **101**, 013113 (2012).

[Beh12] D. Behrenberg, S. Franzka, N. Petermann, H. Wiggers, and N. Hartmann: *Photothermal laser processing of thin silicon nanoparticle films: on the impact of oxide formation on film morphology*, Appl. Phys. A **106**, 853 (2012).

[Ben06] G. L. Bennett, K. J. Lombardo, R. J. Hemler, G. Silverman, C. W. Whitmore, W. R. Amos, E. W. Johnson, A. Schock, R. W. Zochter, T. K. Keenan, J. C. Hagan, and R. W. Englehart: *Mission of daring: The general-purpose heat source radioisotope thermoelectric generator*, 4th International Energy Conversion Engineering Conference and Exhibit (IECEC) **AIAA 2006-4096**, 1 (2006).

[Ben98] R. B. Bentley: *Handbook of Temperature Measurement Vol. 3: The Theory and Practice of Thermoelectric Thermometry* (Springer, Singapore, 1998).

[Ber75] R. Berman, P. R. W. Hudson, and M. Martinez: *Nitrogen in diamond: evidence from thermal conductivity*, J. Phys. C: Solid State Phys. **8**, L430 (1975).

[Ber03] F. Bernhard: *Technische Temperaturmessung. Physikalische und meßtechnische Grundlagen, Sensoren und Meßverfahren, Meßfehler und Kalibrierung* (Springer, Berlin, Heidelberg, 2003).

[Ber10] C. Bera, N. Mingo, and S. Volz: *Marked effects of alloying on the thermal conductivity of nanoporous materials*, Phys. Rev. Lett. **104**, 115502 (2010).

[Bey91] W. Beyer: *Hydrogen effusion: a probe for surface desorption and diffusion*, Physica B **170**, 105 (1991).

[Bis12] K. Biswas, J. He, I. Blum, C.-I. Wu, T. Hogan, D. Seidman, V. Dravid, and M. Kanatzidis: *High-performance bulk thermoelectrics with all-scale hierarchical architectures*, Nature **489**, 414 (2012).

[Bjö09] M. Björk, H. Schmid, J. Knoch, H. Riel, and W. Riess: *Donor deactivation in silicon nanostructures*, Nature Nanotech. **4**, 103 (2009).

[Bod03] D. Bodlaki, H. Yamamoto, D. H. Waldeck, and E. Borguet: *Ambient stability of chemically passivated germanium interfaces*, Surf. Sci. **543**, 63 (2003).

[Boo11] J. de Boor, D. S. Kim, X. Ao, D. Hagen, A. Cojocaru, H. Föll, and V. Schmidt: *Temperature and structure size dependence of the thermal conductivity of porous silicon*, Europhys. Lett. **96**, 16001 (2011).

[Bor01] T. Borca-Tasciuc, A. R. Kumar, and G. Chen: *Data reduction in 3-ω method for thin-film thermal conductivity determination*, Rev. Sci. Instr. **72**, 2139 (2001).

[Bor94] A. Borghesi, G. Guizzetti, A. Sassella, O. Bisi, and L. Pavesi: *Induction-model analysis of Si-H stretching mode in porous silicon*, Solid State Commun. **89**, 615 (1994).

[Bou08] A. I. Boukai, Y. Bunimovich, J. Tahir-Kheli, J.-K. Yu, W. A. Goddard, and J. R. Heath: *Silicon nanowires as efficient thermoelectric materials*, Nature **451**, 168 (2008).

[Bou09] C. Boué and D. Fournier: *Infrared thermography measurement of the thermal parameters (effusivity, diffusivity and conductivity) of materials*, Quant. Infrared Thermogr. J. **6**, 175 (2009).

[Bra89] J. Brandrup and E. Immergut (eds.): *Polymer Handbook* (Wiley-Interscience, New York, 1989), 3rd edn..

[Bra98] M. S. Brandt, P. Herbst, H. Angerer, O. Ambacher, and M. Stutzmann: *Thermopower investigations of n- and p-type GaN*, Phys. Rev. B **58**, 7786 (1998).

[Bra00] V. V. Brazhkin, S. G. Lyapin, I. A. Trojan, R. N. Voloshin, A. G. Lyapin, and N. N. Mel'nik: *Anharmonicity of short-wavelength acoustic phonons in silicon at high temperatures*, J. Exp. Theor. Phys. Lett. **72**, 195 (2000).

[Bre00] O. Breitenstein, M. Langenkamp, F. Altmann, D. Katzer, A. Lindner, and H. Eggers: *Microscopic lock-in thermography investigation of leakage sites in integrated circuits*, Rev. Sci. Instr. **71**, 4155 (2000).

[Bri00] W. L. Briggs, V. E. Henson, and S. F. McCormick: *A multigrid tutorial* (Society for Industrial and Applied Mathematics, Philadelphia, 2000), 2nd edn..

[Bro77] M. H. Brodsky, M. Cardona, and J. J. Cuomo: *Infrared and Raman spectra of the silicon-hydrogen bonds in amorphous silicon prepared by glow discharge and sputtering*, Phys. Rev. B **16**, 3556 (1977).

[Bro81] A. Broniatowski: *Charged grain boundaries in germanium*, J. Physique **42**, 741 (1981).

[Bro08] P. Broqvist, A. Alkauskas, and A. Pasquarello: *Defect levels of dangling bonds in silicon and germanium through hybrid functionals*, Phys. Rev. B **78**, 075203 (2008).

[Bro10] P. Broqvist, A. Alkauskas, and A. Pasquarello: *Defect levels of the Ge dangling bond defect*, AIP Conf. Proc. **1199**, 81 (2010).

[Bro12] P. Broqvist, J. F. Binder, and A. Pasquarello: *First principles study of electronic and structural properties of the Ge/GeO_2 interface*, Physica B **407**, 2926 (2012).

[Bru38] S. Brunauer, P. H. Emmett, and E. Teller: *Adsorption of gases in multimolecular layers*, J. Am. Chem. Soc. **60**, 309 (1938).

[Bud96] M. Budde, B. Bech Nielsen, R. Jones, J. Goss, and S. Öberg: *Local modes of the H_2^* dimer in germanium*, Phys. Rev. B **54**, 5485 (1996).

[Bur93] H. H. Burke and I. P. Herman: *Temperature dependence of Raman scattering in $Ge_{1-x}Si_x$ alloys*, Phys. Rev. B **48**, 15016 (1993).

[Bur97] T. A. Burr, A. A. Seraphin, E. Werwa, and K. D. Kolenbrander: *Carrier transport in thin films of silicon nanoparticles*, Phys. Rev. B **56**, 4818 (1997).

[Bur10] B. G. Burke, J. Chan, K. A. Williams, Z. Wu, A. A. Puretzky, and D. B. Geohegan: *Raman study of Fano interference in p-type doped silicon*, J. Raman Spectrosc. **41**, 1759 (2010).

[Cah89] D. G. Cahill, H. E. Fischer, T. Klitsner, E. T. Swartz, and R. O. Pohl: *Thermal conductivity of thin films: Measurements and understanding*, J. Vac. Sci. Tech. A **7**, 1259 (1989).

[Cah92] D. G. Cahill, S. K. Watson, and R. O. Pohl: *Lower limit to the thermal conductivity of disordered crystals*, Phys. Rev. B **46**, 6131 (1992).

[Cah04] D. G. Cahill: *Analysis of heat flow in layered structures for time-domain thermoreflectance*, Rev. Sci. Instr. **75**, 5119 (2004).

[Cai10] W. Cai, A. L. Moore, Y. Zhu, X. Li, S. Chen, L. Shi, and R. S. Ruoff: *Thermal transport in suspended and supported monolayer graphene grown by chemical vapor deposition*, Nano Lett. **10**, 1645 (2010).

[Cal] Caltech: *http://thermoelectrics.caltech.edu/thermoelectrics/history.html*, accessed: 09.12.2014.

[Cam86] I. Campbell and P. Fauchet: *The effects of microcrystal size and shape on the one phonon Raman spectra of crystalline semiconductors*, Solid State Commun. **58**, 739 (1986).

[Cap63] J. A. Cape and G. W. Lehman: *Temperature and finite pulse-time effects in the flash method for measuring thermal diffusivity*, J. Appl. Phys. **34**, 1909 (1963).

[Car] Carl Roth GmbH + Co. KG: *Certificate of analysis: Single-element standard solution for ICP*, Art. No. 2491.1, LOT 20900, 29.03.2009.

[Car83a] M. Cardona: *Vibrational spectra of hydrogen in silicon and germanium*, Phys. Status Solidi B **118**, 463 (1983).

[Car83b] M. Cardona (ed.): *Light scattering in solids I* (Springer, Berlin, Heidelberg, 1983).

[Car86] H. S. Carslaw and J. C. Jaeger: *Conduction of heat in solids* (Oxford University Press, Oxford, 1986).

[Cas06] W. H. Casey: *Large aqueous aluminum hydroxide molecules*, Chem. Rev. **106**, 1 (2006).

[Cer72] F. Cerdeira and M. Cardona: *Effect of carrier concentration on the Raman frequencies of Si and Ge*, Phys. Rev. B **5**, 1440 (1972).

[Cer73a] F. Cerdeira, T. A. Fjeldly, and M. Cardona: *Effect of free carriers on zone-center vibrational modes in heavily doped p-type Si. II. Optical modes*, Phys. Rev. B **8**, 4734 (1973).

[Cer73b] F. Cerdeira, T. A. Fjeldly, and M. Cardona: *Interaction between electronic and vibronic Raman scattering in heavily doped silicon*, Solid State Commun. **13**, 325 (1973).

[Cha77] M. Chandrasekhar, M. Cardona, and E. O. Kane: *Intraband Raman scattering by free carriers in heavily doped n-Si*, Phys. Rev. B **16**, 3579 (1977).

[Cha78] M. Chandrasekhar, J. B. Renucci, and M. Cardona: *Effects of interband excitations on Raman phonons in heavily doped n-Si*, Phys. Rev. B **17**, 1623 (1978).

[Cha80] M. Chandrasekhar, H. R. Chandrasekhar, M. Grimsditch, and M. Cardona: *Study of the localized vibrations of boron in heavily doped Si*, Phys. Rev. B **22**, 4825 (1980).

[Cha85] Y. J. Chabal and K. Raghavachari: *New ordered structure for the H-saturated Si(100) surface: The (3×1) phase*, Phys. Rev. Lett. **54**, 1055 (1985).

[Cha86] Y. Chabal: *High-resolution infrared spectroscopy of adsorbates on semiconductor surfaces: Hydrogen on Si(100) and Ge(100)*, Surf. Sci. **168**, 594 (1986).

[Cha89] Y. J. Chabal, G. S. Higashi, K. Raghavachari, and V. A. Burrows: *Infrared spectroscopy of Si(111) and Si(100) surfaces after HF treatment: Hydrogen termination and surface morphology*, J. Vac. Sci. Tech. A **7**, 2104 (1989).

[Cha96] M. H. Chan, S. K. So, and K. W. Cheah: *Optical absorption of free-standing porous silicon films*, J. Appl. Phys. **79**, 3273 (1996).

[Chá14] E. Chávez-Ángel, J. S. Reparaz, J. Gomis-Bresco, M. R. Wagner, J. Cuffe, B. Graczykowski, A. Shchepetov, H. Jiang, M. Prunnila, J. Ahopelto, F. Alzina, and C. M. Sotomayor Torres: *Reduction of the thermal conductivity in free-standing silicon nano-membranes investigated by non-invasive Raman thermometry*, Appl. Phys. Lett. Mater. **2**, 012113 (2014).

[Che05] G. Chen: *Nanoscale Energy Transport and Conversion: A Parallel Treatment of Electrons, Molecules, Phonons, and Photons* (Oxford University Press, Oxford, 2005).

[Che12] S. Chen, Q. Wu, C. Mishra, J. Kang, H. Zhang, K. Cho, W. Cai, A. A. Balandin, and R. S. Ruoff: *Thermal conductivity of isotopically modified graphene*, Nature Mater. **11**, 203 (2012).

[Chr00] D. Chrisey, A. Pique, J. Fitz-Gerald, R. Auyeung, R. McGill, H. Wu, and M. Duignan: *New approach to laser direct writing active and passive mesoscopic circuit elements*, Appl. Surf. Sci. **154**, 593 (2000).

[Chr07] A. Chroneos, R. W. Grimes, B. P. Uberuaga, S. Brotzmann, and H. Bracht: *Vacancy-arsenic clusters in germanium*, Appl. Phys. Lett. **91**, 192106 (2007).

[Chr14] A. Chroneos and H. Bracht: *Diffusion of n-type dopants in germanium*, Appl. Phys. Rev. **1**, 011301 (2014).

[Cla13] T. Claudio, G. Schierning, R. Theissmann, H. Wiggers, H. Schober, M. Koza, and R. P. Hermann: *Effects of impurities on the lattice dynamics of nanocrystalline silicon for thermoelectric application*, J. Mater. Sci. **48**, 2836 (2013).

[Com83] A. Compaan, G. Contreras, M. Cardona, and A. Axmann: *Phonon softening in ultra heavily doped Si and Ge*, J. Phys. Colloques **44**, 197 (1983).

[Com84a] A. Compaan, G. Contreras, M. Cardona, and A. Axmann: *Raman scattering in ultra heavily doped Si and Ge: The dependence on free carrier and substitutional dopant densities*, Mat. Res. Soc. Symp. Proc. **23**, 117 (1984).

[Com84b] A. Compaan and H. J. Trodahl: *Resonance Raman scattering in Si at elevated temperatures*, Phys. Rev. B **29**, 793 (1984).

[Con52] E. M. Conwell: *Properties of silicon and germanium*, Proc. IRE **40**, 1327 (1952).

[Con58] E. M. Conwell: *Properties of silicon and germanium: II*, Proc. IRE **46**, 1281 (1958).

[Con84] G. Contreras, A. Sood, M. Cardona, and A. Compaan: *Effect of free carriers on the Raman frequency of ultraheavily doped n-Si*, Solid State Commun. **49**, 303 (1984).

[Con85] G. Contreras, M. Cardona, and A. Axmann: *Raman scattering studies in phosphorus implanted and laser annealed boron doped Si*, Solid State Commun. **53**, 861 (1985).

[Cor64] J. Corbett, R. McDonald, and G. Watkins: *The configuration and diffusion of isolated oxygen in silicon and germanium*, J. Phys. Chem. Solids **25**, 873 (1964).

[Cow65] R. Cowley: *Raman scattering from crystals of the diamond structure*, J. Phys. **26**, 659 (1965).

[Cra79] N. C. Craig and I. W. Levin: *Calibrating Raman spectrometers with plasma lines from the argon ion laser*, Appl. Spectrosc. **33**, 475 (1979).

[Cui98] J. B. Cui, K. Amtmann, J. Ristein, and L. Ley: *Noncontact temperature measurements of diamond by Raman scattering spectroscopy*, J. Appl. Phys. **83**, 7929 (1998).

[Cus58] N. Cusack and P. Kendall: *The absolute scale of thermoelectric power at high temperature*, Proc. Phys. Soc. **72**, 898 (1958).

[Deb54] P. P. Debye and E. M. Conwell: *Electrical properties of n-type germanium*, Phys. Rev. **93**, 693 (1954).

[Dec12] E. Dechaumphai and R. Chen: *Thermal transport in phononic crystals: The role of zone folding effect*, J. Appl. Phys. **111**, 073508 (2012).

[Did08] J. Didierjean, E. Herault, F. Balembois, and P. Georges: *Thermal conductivity measurements of laser crystals by infrared thermography. Application to Nd:doped crystals*, Opt. Express **16**, 8995 (2008).

[Dim07] A. Dimoulas, E. Gusev, P. McIntyre, and M. Heyns (eds.): *Advanced Gate Stacks for High-Mobility Semiconductors* (Springer, Berlin, Heidelberg, 2007).

[Dis64] J. P. Dismukes, I. Ekstrom, E. F. Steigmeier, I. Kudman, and D. S. Beers: *Thermal and electrical properties of heavily doped Ge-Si alloys up to 1300 K*, J. Appl. Phys. **35**, 2899 (1964).

[Dob09] E. R. Dobrovinskaya, L. A. Lytvynov, and V. Pishchik: *Sapphire - Material, Manufacturing, Applications* (Springer, New York, 2009).

[Doe09] G. S. Doerk, C. C. Carraro, and R. Maboudian: *Temperature dependence of Raman spectra for individual silicon nanowires*, Phys. Rev. B **80**, 073306 (2009).

[Doe10] G. S. Doerk, C. C. Carraro, and R. Maboudian: *Single nanowire thermal conductivity measurement by Raman thermography*, ACS Nano **4**, 4908 (2010).

[Dra14] E. Drahi, A. Gupta, S. Blayac, S. Saunier, and P. Benaben: *Characterization of sintered inkjet-printed silicon nanoparticle thin films for thermoelectric devices*, Phys. Status Solidi A **211**, 1301 (2014).

[Dre07] M. S. Dresselhaus, G. Chen, M. Y. Tang, R. Yang, H. Lee, D. Wang, Z. Ren, J.-P. Fleurial, and P. Gogna: *New directions for low-dimensional thermoelectric materials*, Adv. Mater. **19**, 1043 (2007).

[Dre09] V. Drebushchak: *Universality of the emf of thermocouples*, Thermochim. Acta **496**, 50 (2009).

[Ein06] A. Einstein: *Zur Theorie der Brownschen Bewegung*, Ann. Phys. **324**, 371 (1906).

[Ell53] W. Ellis and E. Greiner: *Production of acceptor centers in germanium and silicon by plastic deformation*, Phys. Rev. **92**, 1061 (1953).

[Eus13] N. Eustathopoulos and B. Drevet: *Surface tension of liquid silicon: High or low value?*, J. Cryst. Growth **371**, 77 (2013).

[Eve93] M. P. D'Evelyn, S. M. Cohen, E. Rouchouze, and Y. L. Yang: *Surface π bonding and the near-first-order desorption kinetics of hydrogen from Ge(100)2$\times$1*, J. Chem. Phys. **98**, 3560 (1993).

[Fal08] S. Faleev and F. Léonard: *Theory of enhancement of thermoelectric properties of materials with nanoinclusions*, Phys. Rev. B **77**, 214304 (2008).

[Fan61] U. Fano: *Effects of configuration interaction on intensities and phase shifts*, Phys. Rev. **124**, 1866 (1961).

[Far09] R. S. Farr and R. D. Groot: *Close packing density of polydisperse hard spheres*, J. Chem. Phys. **131**, 244104 (2009).

[Fen11] G. Feng, Y. Li, Y. Wang, P. Li, and T. Guo: *Enhanced infrared normal spectral emissivity of microstructured silicon at 200 to 400°C*, Proc. SPIE **8202**, 82020M (2011).

[Fie99] G. B. M. Fiege, A. Altes, R. Heiderhoff, and L. J. Balk: *Quantitative thermal conductivity measurements with nanometre resolution*, J. Phys. D: Appl. Phys. **32**, L13 (1999).

[Fil13] S. Filser: *Thermal conductivity measurements on laser-sintered films of group-IV nanoparticles using the Raman shift method*, Master Thesis, Technische Universität München (2013).

[Fri71] H. Fritzsche: *A general expression for the thermoelectric power*, Solid State Commun. **9**, 1813 (1971).

[Fu06] C. Fu and Z. Zhang: *Nanoscale radiation heat transfer for silicon at different doping levels*, Int. J. Heat Mass Transf. **49**, 1703 (2006).

[Fuk10] N. Fukata, K. Sato, M. Mitome, Y. Bando, T. Sekiguchi, M. Kirkham, J. Hong, Z. L. Wang, and R. L. Snyder: *Doping and Raman characterization of boron and phosphorus atoms in germanium nanowires*, ACS Nano **4**, 3807 (2010).

[Gar11] J. Garg, N. Bonini, B. Kozinsky, and N. Marzari: *Role of disorder and anharmonicity in the thermal conductivity of silicon-germanium alloys: A first-principles study*, Phys. Rev. Lett. **106**, 045901 (2011).

[Geb54] T. H. Geballe and F. J. Morin: *Ionization energies of group III and V elements in germanium*, Phys. Rev. **95**, 1085 (1954).

[Geb55] T. Geballe and G. Hull: *Seebeck effect in silicon*, Phys. Rev. **98**, 940 (1955).

[Gho09] S. Ghosh, D. L. Nika, E. P. Pokatilov, and A. A. Balandin: *Heat conduction in graphene: experimental study and theoretical interpretation*, New J. Phys. **11**, 095012 (2009).

[Gho10] S. Ghosh, W. Bao, D. L. Nika, S. Subrina, E. P. Pokatilov, C. N. Lau, and A. A. Balandin: *Dimensional crossover of thermal transport in few-layer graphene*, Nature Mater. **9**, 555 (2010).

[Gla64] C. Glassbrenner and G. Slack: *Thermal conductivity of silicon and germanium from 3 K to the melting point*, Phys. Rev. **134**, 1058 (1964).

[Gla96] J. A. Glass Jr., E. A. Wovchko, and J. T. Yates Jr.: *Reaction of atomic hydrogen with hydrogenated porous silicon - detection of precursor to silane formation*, Surf. Sci. **348**, 325 (1996).

[God94] D. J. Godbey, J. V. Lill, J. Deppe, and K. D. Hobart: *Ge surface segregation at low temperature during SiGe growth by molecular beam epitaxy*, Appl. Phys. Lett. **65**, 711 (1994).

[Gol54] H. J. Goldsmid and R. W. Douglas: *The use of semiconductors in thermoelectric refrigeration*, Brit. J. Appl. Phys. **5**, 386 (1954).

[Gol99] H. Goldsmid and J. Sharp: *Estimation of the thermal band gap of a semiconductor from Seebeck measurements*, J. Electron. Mater. **28**, 869 (1999).

[Gom07] S. Gomès, L. David, V. Lysenko, A. Descamps, T. Nychyporuk, and M. Raynaud: *Application of scanning thermal microscopy for thermal conductivity measurements on meso-porous silicon thin films*, J. Phys. D: Appl. Phys. **40**, 6677 (2007).

[Gra09] S. Grasso, Y. Sakka, and G. Maizza: *Electrical current activated/assisted sintering (ECAS): a review of patents 1906-2008*, Sci. Technol. Adv. Mater. **10**, 1 (2009).

[Gre90] M. A. Green: *Intrinsic concentration, effective densities of states, and effective mass in silicon*, J. Appl. Phys. **67**, 2944 (1990).

[Gre13] A. Greppmair: *Laser-Assisted Wet-Chemical Doping of Silicon and Germanium Nanoparticle Films*, Diplomarbeit, Technische Universität München (2013).

[Gro12] R. Gross and A. Marx: *Festkörperphysik* (Oldenbourg Verlag, München, 2012).

[Gun10] P. Gundel, M. C. Schubert, F. D. Heinz, J. Benick, I. Zizak, and W. Warta: *Submicron resolution carrier lifetime analysis in silicon with Fano resonances*, Phys. Status Solidi RRL **4**, 160 (2010).

[Gün02] H. Günzler and H.-U. Gremlich: *IR-Spektroscopy - An introduction* (Viley-VCH, Weinheim, 2002).

[Hal10] T. C. Hales, J. Harrison, S. McLaughlin, T. Nipkow, S. Obua, and R. Zumkeller: *A revision of the proof of the Kepler conjecture*, Discrete Comput. Geom. **44**, 1 (2010).

[Ham62] Y. Hamakawa and J. Yamaguchi: *Electrical conduction in germanium grain boundary plane*, Jap. J. Appl. Phys. **1**, 334 (1962).

[Har67] T. C. Harman and J. M. Honig: *Thermoelectric and Thermomagnetic Effects and Applications* (McGraw-Hill, New York, 1967).

[Har70] T. Hart, R. Aggarwal, and B. Lax: *Temperature dependence of Raman scattering in silicon*, Phys. Rev. B **1**, 638 (1970).

[Har98] D. C. Harris: *Durable 3-5 μm transmitting infrared window materials*, Infrared Phys. Technol. **39**, 185 (1998).

[Hau92] D. Hauschildt: *Elektronischer Tansport in a-Si:H und a-Ge:H Filmen*, Dissertation, Philipps Universität Marburg (1892).

[Her05] J. P. Heremans, C. M. Thrush, and D. T. Morelli: *Thermopower enhancement in PbTe with Pb precipitates*, J. Appl. Phys. **98**, 063703 (2005).

[Her07] E. M. Herzig, K. A. White, A. B. Schofield, W. C. Poon, and P. S. Clegg: *Bicontinuous emulsions stabilized solely by colloidal particles*, Nature Mater. **6**, 966 (2007).

[Her08] J. P. Heremans, V. Jovovic, E. S. Toberer, A. Saramat, K. Kurosaki, A. Charoenphakdee, S. Yamanaka, and G. J. Snyder: *Enhancement of thermoelectric efficiency in PbTe by distortion of the electronic density of states*, Science **321**, 554 (2008).

[Her11] I. P. Herman: *Peak temperatures from Raman Stokes/anti-Stokes ratios during laser heating by a Gaussian beam*, J. Appl. Phys. **109**, 016103 (2011).

[Hic93a] L. D. Hicks and M. S. Dresselhaus: *Effect of quantum-well structures on the thermoelectric figure of merit*, Phys. Rev. B **47**, 12727 (1993).

[Hic93b] L. D. Hicks, T. C. Harman, and M. S. Dresselhaus: *Use of quantum-well superlattices to obtain a high figure of merit from nonconventional thermoelectric materials*, Appl. Phys. Lett. **63**, 3230 (1993).

[Hic96] L. D. Hicks, T. C. Harman, X. Sun, and M. S. Dresselhaus: *Experimental study of the effect of quantum-well structures on the thermoelectric figure of merit*, Phys. Rev. B **53**, R10493 (1996).

[Hil13] H. Hilbig, A. Gmell, M. Nakonz, and D. Heinz: *Laser ablation ICP-MS for spatially resolved element analysis*, 3rd Colloquium of the Munich School of Engineering (MSE) (2013).

[Hob57] J. N. Hobstetter and P. Breidt: *Detection of both vacancies and interstitials in deformed germanium*, J. Appl. Phys. **28**, 1214 (1957).

[Hoc08] A. I. Hochbaum, R. Chen, R. D. Delgado, W. Liang, E. C. Garnett, M. Najarian, A. Majumdar, and P. Yang: *Enhanced thermoelectric performance of rough silicon nanowires*, Nature **451**, 163 (2008).

[Hoe10] M. A. Hoeb: *Funktionalisierung von Gruppe IV-Halbleitern*, Dissertation, Technische Universität München (2010).

[Hoh14] G. T. Hohensee, R. B. Wilson, J. P. Feser, and D. G. Cahill: *Magnon-phonon coupling in the spin-ladder compound $Ca_9La_5Cu_{24}O_{41}$ measured by time-domain thermoreflectance*, Phys. Rev. B **89**, 024422 (2014).

[Hop11] P. E. Hopkins, C. M. Reinke, M. F. Su, R. H. Olsson, E. A. Shaner, Z. C. Leseman, J. R. Serrano, L. M. Phinney, and I. El-Kady: *Reduction in the thermal conductivity of single crystalline silicon by phononic crystal patterning*, Nano Lett. **11**, 107 (2011).

[Hop12] P. E. Hopkins, B. Kaehr, E. S. Piekos, D. Dunphy, and C. J. Brinker: *Minimum thermal conductivity considerations in aerogel thin films*, J. Appl. Phys. **111**, 113532 (2012).

[Hou80] R. S. Houk, V. A. Fassel, G. D. Flesch, H. J. Svec, A. L. Gray, and C. E. Taylor: *Inductively coupled argon plasma as an ion source for mass spectrometric determination of trace elements*, Anal. Chem. **52**, 2283 (1980).

[Hua09] S. Huang, X. Ruan, J. Zou, X. Fu, and H. Yang: *Thermal conductivity measurement of submicrometer-scale silicon dioxide films by an extended micro-Raman method*, Microsyst. Technol. **15**, 837 (2009).

[Hui67] W. L. C. Hui and J. P. Corra: *Seebeck coefficient of thin-film germanium*, J. Appl. Phys. **38**, 3477 (1967).

[Hum89] J. Humliček, M. Garriga, M. I. Alonso, and M. Cardona: *Optical spectra of Si_xGe_{1-x} alloys*, J. Appl. Phys. **65**, 2827 (1989).

[Hum05] T. Humphrey and H. Linke: *Reversible thermoelectric nanomaterials*, Phys. Rev. Lett. **94**, 096601 (2005).

[Hux04] S. Huxtable, D. G. Cahill, V. Fauconnier, J. O. White, and J.-C. Zhao: *Thermal conductivity imaging at micrometre-scale resolution for combinatorial studies of materials*, Nature Mater. **3**, 298 (2004).

[Inn03] P. Innocenzi: *Infrared spectroscopy of sol-gel derived silica-based films: a spectra-microstructure overview*, J. Non-Cryst. Solids **316**, 309 (2003).

[Iny04] A. V. Inyushkin, A. N. Taldenkov, A. M. Gibin, A. V. Gusev, and H.-J. Pohl: *On the isotope effect in thermal conductivity of silicon*, Phys. Status Solidi C **11**, 2995 (2004).

[Iof57] A. F. Ioffe: *Semiconductor Thermoelements and Thermoelectric Cooling* (Infosearch Ldt., London, 1957).

[Iqb82] Z. Iqbal and S. Veprek: *Raman scattering from hydrogenated microcrystalline and amorphous silicon*, J. Phys. C: Sol. State Phys. **15**, 377 (1982).

[Jai13] A. Jain, Y.-J. Yu, and A. J. H. McGaughey: *Phonon transport in periodic silicon nanoporous films with feature sizes greater than 100 nm*, Phys. Rev. B **87**, 195301 (2013).

[Jai14] A. Jain and A. J. H. McGaughey: *Thermal conductivity of compound semiconductors: Interplay of mass density and acoustic-optical phonon frequency gap*, J. Appl. Phys. **116**, 073503 (2014).

[Joh54] E. R. Johnson and S. M. Christian: *Some properties of germanium-silicon alloys*, Phys. Rev. **95**, 560 (1954).

[Joh11] S. Johnsen, J. He, J. Androulakis, V. P. Dravid, I. Todorov, D. Y. Chung, and M. G. Kanatzidis: *Nanostructures boost the thermoelectric performance of PbS*, J. Am. Chem. Soc. **133**, 3460 (2011).

[Jou75] M. Jouanne, R. Beserman, I. Ipatova, and A. Subashiev: *Electron-phonon coupling in highly doped n-type silicon*, Solid State Commun. **16**, 1047 (1975).

[Ju99] Y. S. Ju and K. E. Goodson: *Phonon scattering in silicon films with thickness of order 100 nm*, Appl. Phys. Lett. **74**, 3005 (1999).

[Ju05] Y. S. Ju: *Phonon heat transport in silicon nanostructures*, Appl. Phys. Lett. **87**, 153106 (2005).

[Jul73] C. L. Julian and F. O. Lane Jr.: *Change of the density-of-states effective mass of holes in germanium induced by [111] and [100] one-dimensional strain and by [111] and [100] uniaxial stress*, Phys. Rev. B **7**, 723 (1973).

[Kam10] S. Kameoka, T. Tanabe, and A. P. Tsai: *Self-assembled porous nano-composite with high catalytic performance by reduction of tetragonal spinel $CuFe_2O_4$*, Appl. Catal. A **375**, 163 (2010).

[Kan10] M. G. Kanatzidis: *Nanostructured thermoelectrics: The new paradigm?*, Chem. Mater. **22**, 648 (2010).

[Kec53] P. H. Keck and W. van Horn: *The surface tension of liquid silicon and germanium*, Phys. Rev. **91**, 512 (1953).

[Kim87] D. Kim, F. Qian, C. Bickford, and H. K. Park: *Electrical characterization of heavily doped polycrystalline silicon for high-frequency bipolar transistor application*, IEEE Trans. Electron. Dev. **34**, 1774 (1987).

[Kim06] W. Kim, J. Zide, A. Gossard, D. Klenov, S. Stemmer, A. Shakouri, and A. Majumdar: *Thermal conductivity reduction and thermoelectric figure of merit increase by embedding nanoparticles in crystalline semiconductors*, Phys. Rev. Lett. **96**, 045901 (2006).

[Kim08] J. Kim, J. McVittie, K. Saraswat, and Y. Nishi: *Passivation studies of germanium surfaces*, Solid State Phenom. **134**, 33 (2008).

[Kim13] G.-H. Kim, L. Shao, K. Zhang, and K. P. Pipe: *Engineered doping of organic semiconductors for enhanced thermoelectric efficiency*, Nature Mater. **12**, 719 (2013).

[Kir73] S. Kirkpatrick: *Percolation and conduction*, Rev. Mod. Phys. **45**, 574 (1973).

[Kir88] C. T. Kirk: *Quantitative analysis of the effect of disorder-induced mode coupling on infrared absorption in silica*, Phys. Rev. B **38**, 1255 (1988).

[Kis99] M. M. Kish and R. E. Viola: *Oxyanion specificity of aspartate-semialdehyde dehydrogenase*, Inorg. Chem. **38**, 818 (1999).

[Kle71] D. D. Kleppinger and F. A. Lindholm: *Impurity concentration dependent density of states and resulting Fermi level for silicon*, Solid State Electron. **14**, 407 (1971).

[Kni04] J. Knipping, H. Wiggers, B. Rellinghaus, P. Roth, D. Konjhodzic, and C. Meier: *Synthesis of high purity silicon nanoparticles in a low pressure microwave reactor*, J. Nanosci. Nanotech. **4**, 1039 (2004).

[Knu06] H. A. Knudsen and S. Fazekas: *Robust algorithm for random resistor networks using hierarchical domain structure*, J. Comput. Phys. **211**, 700 (2006).

[Kod92] S. Kodato, Y. Naitoh, and K. Kuroda: *The Seebeck effect in highly conductive μc-Ge:H films and its application to sensors*, Sens. Actuator. A **34**, 161 (1992).

[Kun13] T. Kunz, M. T. Hessmann, S. Seren, B. Meidel, B. Terheiden, and C. J. Brabec: *Dopant mapping in highly p-doped silicon by micro-Raman spectroscopy at various injection levels*, J. Appl. Phys. **113**, 023514 (2013).

[Kuz86] W. Kuzmicz: *Ionization of impurities in silicon*, Solid State Electron. **29**, 1223 (1986).

[Kuz09] D. Kuzum, K. Martens, T. Krishnamohan, and K. C. Saraswat: *Characteristics of surface states and charge neutrality level in Ge*, Appl. Phys. Lett. **95**, 252101 (2009).

[Lab91] R. Labusch and J. Luedecke: *Grain boundary states in germanium*, Phil. Mag. B **64**, 463 (1991).

[Lan10] Y. Lan, A. J. Minnich, G. Chen, and Z. Ren: *Enhancement of thermoelectric figure-of-merit by a bulk nanostructuring approach*, Adv. Func. Mater. **20**, 357 (2010).

[Lan12] T. Langmann: *Herstellung und thermoelektrische Charakterisierung lasergesinterter Nanopartikelfilme*, Diplomarbeit, Technische Universität München (2013).

[Las71] B. J. Last and D. J. Thouless: *Percolation theory and electrical conductivity*, Phys. Rev. Lett. **27**, 1719 (1971).

[Lau32] A. W. Laubengayer and D. S. Morton: *Germanium XXXIX. The polymorphism of germanium dioxide*, J. Am. Chem. Soc. **54**, 2303 (1932).

[Lau87] P. Lautenschlager, M. Garriga, L. Vina, and M. Cardona: *Temperature dependence of the dielectric function and interband critical points in silicon*, Phys. Rev. B **36**, 4821 (1987).

[Lec08] R. Lechner, A. R. Stegner, R. N. Pereira, R. Dietmueller, M. S. Brandt, A. Ebbers, M. Trocha, H. Wiggers, and M. Stutzmann: *Electronic properties of doped silicon nanocrystal films*, J. Appl. Phys. **104**, 053701 (2008).

[Lec09] R. W. Lechner: *Silicon nanocrystal films for electronic applications*, Dissertation, Technische Universität München (2009).

[Lee08] Y. Lee, K. Park, and S. Lim: *Oxidation of hydrogen terminated Ge(100) surface in the presence of iodine in methanol*, Appl. Surf. Sci. **255**, 3318 (2008).

[Lee09] J.-H. Lee and J. C. Grossman: *Thermoelectric properties of nanoporous Ge*, Appl. Phys. Lett. **95**, 013106 (2009).

[Lee10] H. Lee, D. Vashaee, D. Z. Wang, M. S. Dresselhaus, Z. F. Ren, and G. Chen: *Effects of nanoscale porosity on thermoelectric properties of SiGe*, J. Appl. Phys. **107**, 094308 (2010).

[Lee11a] J.-U. Lee, D. Yoon, H. Kim, S. W. Lee, and H. Cheong: *Thermal conductivity of suspended pristine graphene measured by Raman spectroscopy*, Phys. Rev. B **83**, 081419 (2011).

[Lee11b] M. N. Lee and A. Mohraz: *Hierarchically porous silver monoliths from colloidal bicontinuous interfacially jammed emulsion gels*, J. Am. Chem. Soc. **133**, 6945 (2011).

[Len01] P. Lengsfeld: *Successive laser crystallization of doped and undoped a-Si:H*, Dissertation, Technische Universität Berlin (2001).

[Len03] P. Lengsfeld, S. Brehme, K. Brendel, C. Genzel, and N. H. Nickel: *Raman spectroscopy of heavily doped polycrystalline and microcrystalline silicon*, Phys. Status Solidi B **235**, 170 (2003).

[Lev55] A. Levitas: *Electrical properties of germanium-silicon alloys*, Phys. Rev. **99**, 1810 (1955).

[Lev83] I. N. Levine: *Physical Chemistry* (McGraw-Hill, New York, 1983), 2nd edn..

[Lew76] A. J. Lewis: *Conductivity and thermoelectric power of amorphous germanium and amorphous silicon*, Phys. Rev. B **13**, 2565 (1976).

[Li03] D. Li, Y. Wu, P. Kim, L. Shi, P. Yang, and A. Majumdar: *Thermal conductivity of individual silicon nanowires*, Appl. Phys. Lett. **83**, 2934 (2003).

[Li09a] C. W. Li, M. M. McKerns, and B. Fultz: *Raman spectrometry study of phonon anharmonicity of hafnia at elevated temperatures*, Phys. Rev. B **80**, 054304 (2009).

[Li09b] Q. Li, C. Liu, X. Wang, and S. Fan: *Measuring the thermal conductivity of individual carbon nanotubes by the Raman shift method*, Nanotechnology **20**, 145702 (2009).

[Lie67] C. H. Liebert: *Spectral emissivity of highly doped Si*, Proc. AIAA Thermophys. Spec. Conf. (1967).

[Lim12] J. Lim, K. Hippalgaonkar, S. C. Andrews, A. Majumdar, and P. Yang: *Quantifying surface roughness effects on phonon transport in silicon nanowires*, Nano Lett. **12**, 2475 (2012).

[Lip58] E. R. Lippincott, A. V. Valkenburg, C. E. Weir, and E. N. Bunting: *Infrared studies on polymorphs of silicon dioxide and germanium dioxide*, J. Res. Nat. Bur. Stand. **61**, 61 (1958).

[Liu99] M. S. Liu, L. A. Bursill, S. Prawer, K. W. Nugent, Y. Z. Tong, and G. Y. Zhang: *Temperature dependence of Raman scattering in single crystal GaN films*, Appl. Phys. Lett. **74**, 3125 (1999).

[Liu04] W. Liu and M. Asheghi: *Phonon-boundary scattering in ultrathin single-crystal silicon layers*, Appl. Phys. Lett. **84**, 3819 (2004).

[Liu05] W. Liu and M. Asheghi: *Thermal conduction in ultrathin pure and doped single-crystal silicon layers at high temperatures*, J. Appl. Phys. **98**, 123523 (2005).

[Liu06a] W. Liu and M. Asheghi: *Thermal conductivity measurement of ultra-thin single crystal silicon layers*, J. Heat Transfer **128**, 75 (2006).

[Liu06b] W. Liu, K. Etessam-Yazdani, R. Hussin, and M. Asheghi: *Modeling and data for thermal conductivity of ultrathin single-crystal SOI layers at high temperature*, IEEE Trans. Electron. Dev. **53**, 1868 (2006).

[Liu11] X. Liu, X. Wu, and T. Ren: *In situ and noncontact measurement of silicon membrane thermal conductivity*, Appl. Phys. Lett. **98**, 174104 (2011).

[Liu13] J. Liu, H. Wang, W. Ma, X. Zhang, and Y. Song: *Simultaneous measurement of thermal conductivity and thermal contact resistance of individual carbon fibers using Raman spectroscopy*, Rev. Sci. Instr. **84**, 044901 (2013).

[Log59] R. A. Logan, G. L. Pearson, and D. A. Kleinman: *Anisotropic mobilities in plastically deformed germanium*, J. Appl. Phys. **30**, 885 (1959).

[Los06] P. W. Loscutoff and S. F. Bent: *Reactivity of the germanium surface: Chemical passivation and functionalization*, Ann. Rev. Phys. Chem. **57**, 467 (2006).

[Luc87] G. Lucovsky, M. J. Mantini, J. K. Srivastava, and E. A. Irene: *Low-temperature growth of silicon dioxide films: A study of chemical bonding by ellipsometry and infrared spectroscopy*, J. Vac. Sci. Tech. B **5**, 530 (1987).

[Lyk83] J. Lyklema: *Adsorption from solution at the solid/liquid interface* (Academic Press, London, 1983).

[Ma10] X. Ma, W. Liu, X. Du, X. Liu, Z. Song, C. Lin, and P. K. Chu: *Germanium surface hydrophilicity and low-temperature Ge layer transfer by Ge-SiO_2 bonding*, J. Vac. Sci. Tech. B **28**, 769 (2010).

[Mad97] H. Madura, H. Polakowski, and B. Wicek: *Spectral emissivity evaluation for materials used in microelectronics*, Proc. QIRT **96**, 52 (1997).

[Mai97] A. Maiti, G. Mahan, and S. Pantelides: *Dynamical simulations of nonequilibrium processes - Heat flow and the Kapitza resistance across grain boundaries*, Solid State Commun. **102**, 517 (1997).

[Maj99] A. Majumdar: *Scanning thermal microscopy*, Annu. Rev. Mater. Sci. **29**, 505 (1999).

[Maj04] A. Majumdar: *Thermoelectricity in semiconductor nanostructures*, Science **303**, 777 (2004).

[Mal10] P. G. Maloney, P. Smith, V. King, C. Billman, M. Winkler, and E. Mazur: *Emissivity of microstructured silicon*, Appl. Opt. **49**, 1065 (2010).

[Mal12] M. Maldovan: *Thermal conductivity of semiconductor nanowires from micro to nano length scales*, J. Appl. Phys. **111**, 024311 (2012).

[Maw97] D. B. Mawhinney, J. A. Glass, and J. T. Yates: *FTIR study of the oxidation of porous silicon*, J. Phys. Chem. B **101**, 1202 (1997).

[May67] P. Maycock: *Thermal conductivity of silicon, germanium, III-V compounds and III-V alloys*, Solid State Electron. **10**, 161 (1967).

[McC01] A. McConnell, S. Uma, and K. E. Goodson: *Thermal conductivity of doped polysilicon layers*, J. Microelectromech. Syst. **10**, 360 (2001).

[Mec08] R. Meckenstock: *Microwave spectroscopy based on scanning thermal microscopy: Resolution in the nanometer range*, Rev. Sci. Instr. **79**, 041101 (2008).

[Med09] D. Medlin and G. Snyder: *Interfaces in bulk thermoelectric materials: A review for current opinion in colloid and interface science*, Curr. Opinion in Colloid & Interface Sci. **14**, 226 (2009).

[Mei06] C. Meier, S. Lüttjohann, V. G. Kravets, H. Nienhaus, A. Lorke, and H. Wiggers: *Raman properties of silicon nanoparticles*, Physica E **32**, 155 (2006).

[Men84] J. Menéndez and M. Cardona: *Temperature dependence of the first-order Raman scattering by phonons in Si, Ge, and α-Sn: Anharmonic effects*, Phys. Rev. B **29**, 2051 (1984).

[Mer07] P. Mertens, M. Meuris, and M. Heyns: *Passivation studies of germanium surfaces*, Solid State Phenom. **134**, 33 (2007).

[Mes12] M. Meseth, P. Ziolkowski, G. Schierning, R. Theissmann, N. Petermann, H. Wiggers, N. Benson, and R. Schmechel: *The realization of a pn-diode using only silicon nanoparticles*, Scripta Mater. **67**, 265 (2012).

[Mes13] M. Meseth, B. C. Kunert, L. Bitzer, F. Kunze, S. Meyer, F. Kiefer, M. Dehnen, H. Orthner, N. Petermann, M. Kummer, H. Wiggers, N.-P. Harder, N. Benson, and R. Schmechel: *Excimer laser doping using highly doped silicon nanoparticles*, Phys. Status Solidi A **210**, 2456 (2013).

[Mid53] A. E. Middleton and W. W. Scanlon: *Measurement of the thermoelectric power of germanium at temperatures above 78 K*, Phys. Rev. **92**, 219 (1953).

[Mil08] F. Millot, V. Sarou-Kanian, J.-C. Rifflet, and B. Vinet: *The surface tension of liquid silicon at high temperature*, Mat. Sci. Eng. A **495**, 8 (2008).

[Min07] A. Minnich and G. Chen: *Modified effective medium formulation for the thermal conductivity of nanocomposites*, Appl. Phys. Lett. **91**, 073105 (2007).

[Min09a] N. Mingo, D. Hauser, N. P. Kobayashi, M. Plissonnier, and A. Shakouri: *Nanoparticle-in-alloy approach to efficient thermoelectrics: Silicides in SiGe*, Nano Letters **9**, 711 (2009).

[Min09b] A. J. Minnich, M. S. Dresselhaus, Z. F. Ren, and G. Chen: *Bulk nanostructured thermoelectric materials: current research and future prospects*, Energy Environ. Sci. **2**, 466 (2009).

[Min09c] A. J. Minnich, H. Lee, X. W. Wang, G. Joshi, M. S. Dresselhaus, Z. F. Ren, G. Chen, and D. Vashaee: *Modeling study of thermoelectric SiGe nanocomposites*, Phys. Rev. B **80**, 155327 (2009).

[Mit11] J. I. Mitchell, S. J. Park, C. A. Watson, P. Srisungsitthisunti, C. Tansarawiput, M. Qi, E. A. Stach, C. Yang, and X. Xu: *Laser direct write of silicon nanowires*, Opt. Eng. **50**, 104301 (2011).

[Mue04] D. C. Mueller and W. Fichtner: *Highly n-doped silicon: Deactivating defects of donors*, Phys. Rev. B **70**, 245207 (2004).

[New55] R. Newman: *Optical properties of indium-doped silicon*, Phys. Rev. **99**, 465 (1955).

[Nic00] N. H. Nickel, P. Lengsfeld, and I. Sieber: *Raman spectroscopy of heavily doped polycrystalline silicon thin films*, Phys. Rev. B **61**, 15558 (2000).

[Nie11] K. Nielsch, J. Bachmann, J. Kimling, and H. Böttner: *Thermoelectric nanostructures: From physical model systems towards nanograined composites*, Adv. Energy Mater. **1**, 713 (2011).

[Nie12] S. Niesar: *Hybrid polymer/silicon nanocrystal solar cells*, Dissertation, Technische Universität München (2012).

[Nik12] D. L. Nika and A. A. Balandin: *Two-dimensional phonon transport in graphene*, J. Phys.: Condens. Matter **24**, 233203 (2012).

[Niw94] M. Niwano, J.-I. Kageyama, K. Kurita, K. Kinashi, I. Takahashi, and N. Miyamoto: *Infrared spectroscopy study of initial stages of oxidation of hydrogen-terminated Si surfaces stored in air*, J. Appl. Phys. **76**, 2157 (1994).

[Nob82] D. Nobili, A. Armigliato, M. Finnetti, and S. Solmi: *Precipitation as the phenomenon responsible for the electrically inactive phosphorus in silicon*, J. Appl. Phys. **53**, 1484 (1982).

[Nol99] G. S. Nolas, D. T. Morelli, and T. M. Tritt: *Skutterudites: A phonon-glass-electron crystal approach to advanced thermoelectric energy conversion applications*, Ann. Rev. Mater. Sci. **29**, 89 (1999).

[Non92] M. Nonnenmacher and H. K. Wickramasinghe: *Scanning probe microscopy of thermal conductivity and subsurface properties*, Appl. Phys. Lett. **61**, 168 (1992).

[Oga95a] Y. Ogata, H. Niki, T. Sakka, and M. Iwasaki: *Hydrogen in porous silicon: Vibrational analysis of SiH_x species*, J. Electrochem. Soc. **142**, 195 (1995).

[Oga95b] Y. Ogata, H. Niki, T. Sakka, and M. Iwasaki: *Oxidation of porous silicon under water vapor environment*, J. Electrochem. Soc. **142**, 1595 (1995).

[Ole81] D. Olego and M. Cardona: *Self-energy effects of the optical phonons of heavily dopedp-GaAs and p-Ge*, Phys. Rev. B **23**, 6592 (1981).

[Ols93] J. R. Olson, R. O. Pohl, J. W. Vandersande, A. Zoltan, T. R. Anthony, and W. F. Banholzer: *Thermal conductivity of diamond between 170 and 1200 K and the isotope effect*, Phys. Rev. B **47**, 14850 (1993).

[Ont67] A. Onton, P. Fisher, and A. K. Ramdas: *Spectroscopic investigation of group-III acceptor states in silicon*, Phys. Rev. **163**, 686 (1967).

[Ort80] J. W. Orton and M. J. Powell: *The Hall effect in polycrystalline and powdered semiconductors*, Rep. Prog. Phys. **43**, 1263 (1980).

[Pae14] D. Paeng, D. Lee, and C. P. Grigoropoulos: *Characteristic time scales of coalescence of silver nanocomposite and nanoparticle films induced by continuous wave laser irradiation*, Appl. Phys. Lett. **105**, 073110 (2014).

[Pan08] H. Pan, S. H. Ko, and C. P. Grigoropoulos: *The solid-state neck growth mechanisms in low energy laser sintering of gold nanoparticles: A molecular dynamics simulation study*, J. Heat Transfer **130**, 092404 (2008).

[Par08a] K. Park, Y. Lee, J. Lee, and S. Lim: *Oxidation mechanism of hydrogen-terminated Ge(100) surface*, Appl. Surf. Sci. **254**, 4828 (2008).

[Par08b] K. Park, Y. Lee, and S. Lim: *Modification of H-terminated Ge surface in hydrochloric acid*, Appl. Surf. Sci. **254**, 1842 (2008).

[Pay05] K. B. Payne and T. M. Abdel-Fattah: *Adsorption of arsenate and arsenite by iron-treated activated carbon and zeolites: Effects of pH, temperature, and ionic strength*, J. Environ. Sci. Health **40**, 723 (2005).

[Pei12] Y. Pei, H. Wang, and G. J. Snyder: *Thermoelectric materials: Band engineering of thermoelectric materials*, Adv. Mater. **24**, 6124 (2012).

[Pen04] Y. C. Peng, G. S. Fu, W. Yu, S. Q. Li, and Y. L. Wang: *Crystallization of amorphous Si films by pulsed laser annealing and their structural characteristics*, Semicond. Sci. Tech. **19**, 759 (2004).

[Pen12] P. Peng, A. Hu, and Y. Zhou: *Laser sintering of silver nanoparticle thin films: microstructure and optical properties*, Appl. Phys. A **108**, 685 (2012).

[Pér99] S. Périchon, V. Lysenko, B. Remaki, D. Barbier, and B. Champagnon: *Measurement of porous silicon thermal conductivity by micro-Raman scattering*, J. Appl. Phys. **86**, 4700 (1999).

[Pér00] S. Périchon, V. Lysenko, P. Roussel, B. Remaki, B. Champagnon, D. Barbier, and P. Pinard: *Technology and micro-Raman characterization of thick meso-porous silicon layers for thermal effect microsystems*, Sens. Actuator. A **85**, 335 (2000).

[Pet11] N. Petermann, N. Stein, G. Schierning, R. Theissmann, B. Stoib, M. S. Brandt, C. Hecht, C. Schulz, and H. Wiggers: *Plasma synthesis of nanostructures for improved thermoelectric properties*, J. Phys. D: Appl. Phys. **44**, 174034 (2011).

[Phi05] S. Phillpot, P. Schelling, and P. Keblinski: *Interfacial thermal conductivity: Insights from atomic level simulation*, J. Mater. Sci. **40**, 3143 (2005).

[Pi07] X. D. Pi, L. Mangolini, S. A. Campbell, and U. Kortshagen: *Room-temperature atmospheric oxidation of Si nanocrystals after HF etching*, Phys. Rev. B **75**, 085423 (2007).

[Pic11] P. Pichanusakorn, Y. J. Kuang, C. J. Patel, C. W. Tu, and P. R. Bandaru: *The influence of dopant type and carrier concentration on the effective mass and Seebeck coefficient of* GaN_xAs_{1-x} *thin films*, Appl. Phys. Lett. **99**, 072114 (2011).

[Pis03] S. Piscanec, M. Cantoro, A. C. Ferrari, J. A. Zapien, Y. Lifshitz, S. T. Lee, S. Hofmann, and J. Robertson: *Raman spectroscopy of silicon nanowires*, Phys. Rev. B **68**, 241312 (2003).

[Pőd71] B. Pődör, B. Bodó, and K. Somogyi: *Thermoelectric power of plastically deformed germanium*, Phys. Status Solidi A **7**, K105 (1971).

[Pér96] A. Pérez-Rodríguez, A. Romano-Rodríguez, R. Cabezas, J. R. Morante, T. Jawhari, and C. E. Hunt: *Effect of stress and composition on the Raman spectra of etch-stop SiGeB layers*, J. Appl. Phys. **80**, 5736 (1996).

[Qiu15] B. Qiu, Z. Tian, A. Vallabhaneni, B. Liao, J. M. Mendoza, O. D. Restrepo, X. Ruan, and G. Chen: *First-principles simulation of electron mean-free-path spectra and thermoelectric properties in silicon*, Europhys. Lett. **109**, 57006 (2015).

[Qué08] D. Quéré: *Wetting and roughness*, Ann. Rev. Mat. Res. **38**, 71 (2008).

[Que01] K. T. Queeney, H. Fukidome, E. E. Chaban, and Y. J. Chabal: *In-situ FTIR studies of reactions at the silicon/liquid interface: Wet chemical etching of ultrathin SiO_2 on Si(100)*, J. Phys. Chem. B **105**, 3903 (2001).

[Raf06] M. A. Rafiq, Y. Tsuchiya, H. Mizuta, S. Oda, S. Uno, Z. A. K. Durrani, and W. I. Milne: *Hopping conduction in size-controlled Si nanocrystals*, J. Appl. Phys. **100**, 014303 (2006).

[Rav98] N. Ravindra, S. Abedrabbo, W. Chen, F. Tong, A. Nanda, and A. Speranza: *Temperature-dependent emissivity of silicon-related materials and structures*, IEEE Trans. Semicond. Man. **11**, 30 (1998).

[Rav01] N. Ravindra, B. Sopori, O. Gokce, S. Cheng, A. Shenoy, L. Jin, S. Abedrabbo, W. Chen, and Y. Zhang: *Emissivity measurements and modeling of silicon-related materials: An overview*, Int. J. Thermophys. **22**, 1593 (2001).

[Ree59] B. Reed, O. Weinreich, and H. Mataré: *Conductivity of grain boundaries in grown germanium bicrystals*, Phys. Rev. **113**, 454 (1959).

[Reg07] P. Regenfuss, A. Streek, L. Hartwig, S. Klötzer, T. Brabant, M. Horn, R. Ebert, and H. Exner: *Principles of laser micro sintering*, Rapid Prototyping J. **13**, 204 (2007).

[Rep14] J. S. Reparaz, E. Chávez-Ángel, M. R. Wagner, B. Graczykowski, J. Gomis-Bresco, F. Alzina, and C. M. Sotomayor Torres: *A novel contactless technique for thermal field mapping and thermal conductivity determination: Two-laser Raman thermometry*, Rev. Sci. Instr. **85**, 034901 (2014).

[Rif03] S. Riffat and X. Ma: *Thermoelectrics: a review of present and potential applications*, Appl. Therm. Eng. **23**, 913 (2003).

[Rif11] D. M. Riffe: *Classical Fano oscillator*, Phys. Rev. B **84**, 064308 (2011).

[Riv05] S. Rivillon, Y. J. Chabal, F. Amy, and A. Kahn: *Hydrogen passivation of germanium (100) surface using wet chemical preparation*, Appl. Phys. Lett. **87**, 253101 (2005).

[Ros55] A. Rose: *Space-charge-limited currents in solids*, Phys. Rev. **97**, 1538 (1955).

[Sah13] S. Sahoo, A. P. S. Gaur, M. Ahmadi, M. J.-F. Guinel, and R. S. Katiyar: *Temperature-dependent Raman studies and thermal conductivity of few-layer MoS_2*, J. Phys. Chem. C **117**, 9042 (2013).

[Sak99] Y. Sakai, T. Yamada, T. Suzuki, and T. Ichinokawa: *Contrast mechanisms of secondary electron images in scanning electron and ion microscopy*, Appl. Surf. Sci. **144**, 96 (1999).

[San13a] A. Sanson, M. Giarola, E. Napolitani, G. Impellizzeri, V. Privitera, A. Carnera, and G. Mariotto: *Study of carrier concentration profiles in Al-implanted Ge by micro-Raman spectroscopy under different excitation wavelengths*, J. Raman Spectrosc. **44**, 665 (2013).

[San13b] A. Sanson, E. Napolitani, M. Giarola, G. Impellizzeri, V. Privitera, G. Mariotto, and A. Carnera: *Non-conventional characterization of electrically active dopant profiles in Al-implanted Ge by depth-resolved micro-Raman spectroscopy*, Appl. Phys. Expr. **6**, 042404 (2013).

[Sat67] T. Satõ: *Spectral emissivity of silicon*, Jap. J. Appl. Phys. **6**, 339 (1967).

[Sch81] P. E. Schmid: *Optical absorption in heavily doped silicon*, Phys. Rev. B **23**, 5531 (1981).

[Sch91] P. Scheuerpflug, H. J. Morper, and G. Neubert: *Low-temperature thermal transport in silica aerogels*, J. Phys. D: Appl. Phys. **24**, 1395 (1991).

[Sch96] S. Schöninger: *Laser-Strukturierung von μc-Si/a-Si-Heterosystemen*, Diplomarbeit, Technische Universität München (1996).

[Sch08a] G. Schierning, R. Theissmann, H. Wiggers, D. Sudfeld, A. Ebbers, D. Franke, V. T. Witusiewicz, and M. Apel: *Microcrystalline silicon formation by silicon nanoparticles*, J. Appl. Phys. **103**, 084305 (2008).

[Sch08b] S. Schlecht and H. Böttner: *Energiewandler mit großem Zukunftspotenzial*, Nachrichten aus der Chemie **56**, 136 (2008).

[Sch11a] G. Schierning, R. Theissmann, N. Stein, N. Petermann, A. Becker, M. Engenhorst, V. Kessler, M. Geller, A. Beckel, H. Wiggers, and R. Schmechel: *Role of oxygen on microstructure and thermoelectric properties of silicon nanocomposites*, J. Appl. Phys. **110**, 113515 (2011).

[Sch11b] D. Schwesig, G. Schierning, R. Theissmann, N. Stein, N. Petermann, H. Wiggers, R. Schmechel, and D. E. Wolf: *From nanoparticles to nanocrystalline bulk: percolation effects in field assisted sintering of silicon nanoparticles*, Nanotechnology **22**, 135601 (2011).

[Sch14] G. Schierning: *Silicon nanostructures for thermoelectric devices: A review of the current state of the art*, Phys. Status Solidi A **211**, 1235 (2014).

[Sco69] G. D. Scott and D. M. Kilgour: *The density of random close packing of spheres*, J. Phys. D.: Appl. Phys. **2**, 863 (1969).

[See26a] T. J. Seebeck: *Ueber die magnetische Polarisation der Metalle und Erze durch Temperatur-Differenz*, Annalen der Physik **82**, 133 (1826).

[See26b] T. J. Seebeck: *Ueber die magnetische Polarisation der Metalle und Erze durch Temperaturdifferenz*, Annalen der Physik **82**, 253 (1826).

[Sei83] H. Seiler: *Secondary electron emission in the scanning electron microscope*, J. Appl. Phys. **54**, R1 (1983).

[Set75] J. Y. W. Seto: *The electrical properties of polycrystalline silicon films*, J. Appl. Phys. **46**, 5247 (1975).

[Sha11] A. Shakouri: *Recent developments in semiconductor thermoelectric physics and materials*, Ann. Rev. Mater. Res. **41**, 399 (2011).

[Shi09] H. J. Shipley, S. Yean, A. T. Kan, and M. B. Tomson: *Adsorption of arsenic to magnetite nanoparticles: Effect of particle concentration, pH, ionic strength, and temperature*, Environ. Toxicol. Chem. **28**, 509 (2009).

[Sǐk98] J. Sǐk, J. Hora, and J. Humlíček: *Optical functions of silicon at high temperatures*, J. Appl. Phys. **84**, 6291 (1998).

[Sim09] E. Simoen and J. Vanhellemont: *On the diffusion and activation of ion-implanted n-type dopants in germanium*, J. Appl. Phys. **106**, 103516 (2009).

[Sla91] G. A. Slack and M. A. Hussain: *The maximum possible conversion efficiency of silicon-germanium thermoelectric generators*, J. Appl. Phys. **70**, 2694 (1991).

[Sny08] G. J. Snyder and E. S. Toberer: *Complex thermoelectric materials*, Nature Mater. **7**, 105 (2008).

[Soi10] M. Soini, I. Zardo, E. Uccelli, S. Funk, G. Koblmüller, A. Fontcuberta i Morral, and G. Abstreiter: *Thermal conductivity of GaAs nanowires studied by micro-Raman spectroscopy combined with laser heating*, Appl. Phys. Lett. **97**, 263107 (2010).

[Sol96] S. Solmi, A. Parisini, R. Angelucci, A. Armigliato, D. Nobili, and L. Moro: *Dopant and carrier concentration in Si in equilibrium with monoclinic SiP precipitates*, Phys. Rev. B **53**, 7836 (1996).

[Son04] D. Song and G. Chen: *Thermal conductivity of periodically microporous silicon films*, Appl. Phys. Lett. **84**, 687 (2004).

[Soo09] J. Sootsman, D. Chung, and M. Kanatzidis: *New and old concepts in thermoelectric materials*, Angewandte Chemie Int. Edn. **48**, 8616 (2009).

[Sop99] B. Sopori, W. Chen, J. Madjdpour, and N. Ravindra: *Calculation of emissivity of Si wafers*, J. Electron. Mater. **28**, 1385 (1999).

[Spi61] W. G. Spitzer, F. A. Trumbore, and R. A. Logan: *Properties of heavily doped n-type germanium*, J. Appl. Phys. **32**, 1822 (1961).

[Ste64] E. F. Steigmeier and B. Abeles: *Scattering of phonons by electrons in germanium-silicon alloys*, Phys. Rev. **136**, A1149 (1964).

[Ste09] A. R. Stegner, R. N. Pereira, R. Lechner, K. Klein, H. Wiggers, M. Stutzmann, and M. S. Brandt: *Doping efficiency in freestanding silicon nanocrystals from the gas phase: Phosphorus incorporation and defect-induced compensation*, Phys. Rev. B **80**, 165326 (2009).

[Ste10] A. R. Stegner: *Shallow dopants in nanostructured and in isotopically engineered silicon*, Dissertation, Technische Universität München (2010).

[Ste11] N. Stein, N. Petermann, R. Theissmann, G. Schierning, R. Schmechel, and H. Wiggers: *Artificially nanostructured n-type SiGe bulk thermoelectrics through plasma enhanced growth of alloy nanoparticles from the gas phase*, J. Mater. Res. **26**, 1872 (2011).

[Stö40] H. Stöhr and W. Klemm: *Über Zweistoffsysteme mit Germanium. II. Germanium/Arsen, Germanium/Antimon, Germanium/Wismut*, Z. Anorg. Allg. Chem. **244**, 205 (1940).

[Sto12] B. Stoib, T. Langmann, S. Matich, T. Antesberger, N. Stein, S. Angst, N. Petermann, R. Schmechel, G. Schierning, D. E. Wolf, H. Wiggers, M. Stutzmann, and M. S. Brandt: *Laser-sintered thin films of doped SiGe nanoparticles*, Appl. Phys. Lett. **100**, 231907 (2012).

[Sto13] B. Stoib, T. Langmann, N. Petermann, S. Matich, M. Sachsenhauser, H. Wiggers, M. Stutzmann, and M. S. Brandt: *Morphology, thermoelectric properties and wet-chemical doping of laser-sintered germanium nanoparticles*, Phys. Status Solidi A **210**, 153 (2013).

[Sto14a] B. Stoib, S. Filser, N. Petermann, H. Wiggers, M. Stutzmann, and M. S. Brandt: *Thermal conductivity of mesoporous films measured by Raman spectroscopy*, Appl. Phys. Lett. **104**, 161907 (2014).

[Sto14b] B. Stoib, S. Filser, J. Stötzel, A. Greppmair, N. Petermann, H. Wiggers, G. Schierning, M. Stutzmann, and M. S. Brandt: *Spatially resolved determination of thermal conductivity by Raman spectroscopy*, Semicond. Sci. Techn. **29**, 124005 (2014).

[Sto15] B. Stoib, A. Greppmair, N. Petermann, H. Wiggers, M. Stutzmann, and M. S. Brandt: *Laser-assisted wet-chemical doping of sintered nanoparticle films*, Adv. Electron. Mater. **1**, doi:10.1002/aelm.201400029 (2015).

[Str09] H. Straube, J.-M. Wagner, and O. Breitenstein: *Measurement of the Peltier coefficient of semiconductors by lock-in thermography*, Appl. Phys. Lett. **95**, 052107 (2009).

[Sun08] Y. Sun, Z. Liu, S. Sun, and P. Pianetta: *The effectiveness of HCl and HF cleaning of* $Si_{0.85}Ge_{0.15}$ *surface*, J. Vac. Sci. Technol. A **26**, 1248 (2008).

[Sze81] S. M. Sze: *Physics of semiconductor devices* (Wiley & Sons, New York, 1981).

[Tad12] T. F. Tadros: *Dispersion of powder in liquids and stabilization of suspensions* (Wiley-VCH, Weinheim, 2012).

[Tak02] Y. Takamura, A. Vailionis, A. F. Marshall, P. B. Griffin, and J. D. Plummer: *Dopant deactivation in heavily Sb doped Si (001): A high-resolution x-ray diffraction and transmission electron microscopy study*, J. Appl. Phys. **92**, 5503 (2002).

[Tak11] Y. Takahashi, M. Sakamitsu, and M. Tanaka: *Diffusion coefficients of arsenate and arsenite in water at various pH*, Chem. Lett. **40**, 1187 (2011).

[Tan10] J. Tang, H.-T. Wang, D. H. Lee, M. Fardy, Z. Huo, T. P. Russell, and P. Yang: *Holey silicon as an efficient thermoelectric material*, Nano Lett. **10**, 4279 (2010).

[Tan11] G. H. Tang, Y. Zhao, G. X. Zhai, and C. Bi: *Phonon boundary scattering effect on thermal conductivity of thin films*, J. Appl. Phys. **110**, 046102 (2011).

[Tan80] M. Taniguchi, M. Hirose, Y. Osaka, S. Hasegawa, and T. Shimizu: *Current transport in doped polycrystalline silicon*, Jap. J. Appl. Phys. **19**, 665 (1980).

[Tew10] D. Teweldebrhan, V. Goyal, and A. A. Balandin: *Exfoliation and characterization of bismuth telluride atomic quintuples and quasi-two-dimensional crystals*, Nano Lett. **10**, 1209 (2010).

[The97] W. Theiß: *Optical properties of porous silicon*, Surf. Sci. Rep. **29**, 91 (1997).

[Thu53] C. D. Thurmond: *Equilibrium thermochemistry of solid and liquid alloys of germanium and of silicon I: The solubility of Ge and Si in elements of groups III, IV and V*, J. Phys. Chem. **57**, 827 (1953).

[Tim93] P. J. Timans: *Emissivity of silicon at elevated temperatures*, J. Appl. Phys. **74**, 6353 (1993).

[Tim96] P. J. Timans: *The role of thermal radiative properties of semiconductor wafers in rapid thermal processing*, Mat. Res. Soc. Symp. Proc. **429**, 3 (1996).

[Tok04] E. S. Tok, S. W. Ong, and H. C. Kang: *Hydrogen desorption kinetics from the $Si_{1-x}Ge_x$(100)-(2×1) surface*, J. Chem. Phys. **120**, 5424 (2004).

[Tri04] T. M. Tritt: *Thermal conductivity: theory, properties, and applications* (Springer, New York, 2004).

[Tru60] F. A. Trumbore: *Solid solubilities of impurity elements in germanium and silicon*, Bell Labs Techn. J. **39**, 205 (1960).

[Tru90] G. W. Trucks, K. Raghavachari, G. S. Higashi, and Y. J. Chabal: *Mechanism of HF etching of silicon surfaces: A theoretical understanding of hydrogen passivation*, Phys. Rev. Lett. **65**, 504 (1990).

[Twe55] A. G. Tweet: *Electrical properties of plastically deformed germanium*, Phys. Rev. **99**, 1245 (1955).

[Uma01] S. Uma, A. McConnell, M. Asheghi, K. Kurabayashi, and K. E. Goodson: *Temperature-dependent thermal conductivity of undoped polycrystalline silicon layers*, Int. J. Thermophys. **22**, 605 (2001).

[Und08] G. Underwood, L. K. Ballast, and A. Campion: *On the existence of a stable, room temperature dihydride-terminated Ge(100) surface in ultrahigh vacuum*, Surf. Sci. **602**, 2055 (2008).

[Upr91] N. Upreti and S. Singh: *Grain boundary effect on the electrical properties of boron-doped polysilicon films*, Bull. Mater. Sci. **14**, 1331 (1991).

[Van92] P. Vandenabeele and K. Maex: *Influence of temperature and backside roughness on the emissivity of Si wafers during rapid thermal processing*, J. Appl. Phys. **72**, 5867 (1992).

[Ved98] M. Vedernikov and E. Iordanishvili: *A.F. Ioffe and origin of modern semiconductor thermoelectric energy conversion*, Proc. ICT, 37 (1998).

[Vin91] C. B. Vining: *A model for the high temperature transport properties of heavily doped n-type silicon-germanium alloys*, J. Appl. Phys. **69**, 331 (1991).

[Vin10] C. J. Vineis, A. Shakouri, A. Majumdar, and M. G. Kanatzidis: *Nanostructured thermoelectrics: Big efficiency gains from small features*, Adv. Mater. **22**, 3970 (2010).

[Völ10] F. Völklein, H. Reith, M. C. Schmitt, M. Huth, M. Rauber, and R. Neumann: *Microchips for the investigation of thermal and electrical properties of individual nanowires*, J. Electron. Mater. **39**, 1950 (2010).

[Wag85] J. Wagner and M. Cardona: *Electronic Raman scattering in heavily doped p-type germanium*, Phys. Rev. B **32**, 8071 (1985).

[Wan08] X. W. Wang, H. Lee, Y. C. Lan, G. H. Zhu, G. Joshi, D. Z. Wang, J. Yang, A. J. Muto, M. Y. Tang, J. Klatsky, S. Song, M. S. Dresselhaus, G. Chen, and Z. F. Ren: *Enhanced thermoelectric figure of merit in nanostructured n-type silicon germanium bulk alloy*, Appl. Phys. Lett. **93**, 193121 (2008).

[Wan11] Z. Wang, J. E. Alaniz, W. Jang, J. E. Garay, and C. Dames: *Thermal conductivity of nanocrystalline silicon: Importance of grain size and frequency-dependent mean free paths*, Nano Lett. **11**, 2206 (2011).

[Wat95] G. N. Watson: *A treatise on the theory of Bessel functions* (Cambridge University Press, Cambridge, 1995).

[Web77] W. Weber: *Adiabatic bond charge model for the phonons in diamond, Si, Ge, and $\alpha-Sn$*, Phys. Rev. B **15**, 4789 (1977).

[Web91] L. Weber, and E. Gmelin: *Transport properties of silicon*, Appl. Phys. A **53**, 136 (1991).

[Web13] J. R. Weber, A. Janotti, and C. G. Van de Walle: *Dangling bonds and vacancies in germanium*, Phys. Rev. B **87**, 035203 (2013).

[Wei13] C. Wei, X. Zheng, D. G. Cahill, and J.-C. Zhao: *Micron resolution spatially resolved measurement of heat capacity using dual-frequency time-domain thermoreflectance*, Rev. Sci. Instr. **84**, 071301 (2013).

[Wei79] Ch. Weißmantel and C. Hamann: *Grundlagen der Festkörperphysik* (Springer Verlag, Berlin, Heidelberg, New York, 1979).

[Wib95] N. Wiberg (ed.): *Lehrbuch der anorganischen Chemie* (de Gruyter, Berlin, New York, 1995), 101st edn..

[Win81] P. H. Winterfeld, L. E. Scriven, and H. T. Davis: *Percolation and conductivity of random two-dimensional composites*, J. Phys. C **14**, 2361 (1981).

[Woh09] C. J. Wohl, M. A. Belcher, S. Ghose, and J. W. Connell: *Modification of the surface properties of polyimide films using polyhedral oligomeric silsesquioxane deposition and oxygen plasma exposure*, Appl. Surf. Sci. **255**, 8135 (2009).

[Wol04] A. Wolf, P. Pohl, and R. Brendel: *Thermophysical analysis of thin films by lock-in thermography*, J. Appl. Phys. **96**, 6306 (2004).

[Wol06] A. Wolf and R. Brendel: *Thermal conductivity of sintered porous silicon films*, Thin Solid Films **513**, 385 (2006).

[Yam61] T. Yamashita and T. Ohta: *Measurement of Seebeck effect in plastically bent germanium*, J. Phys. Soc. Jap. **16**, 1565 (1961).

[Yam00] O. Yamashita and N. Sadatomi: *Thermoelectric properties of $Si_{1-x}Ge_x$ ($x \leq 0.10$) with alloy and dopant segregations*, J. Appl. Phys. **88**, 245 (2000).

[Yan80] J. J. J. Yang, P. D. Dapkus, R. D. Dupuis, and R. D. Yingling: *Electrical properties of polycrystalline GaAs films*, J. Appl. Phys. **51**, 3794 (1980).

[Yan97] B.-K. Yang, M. Krishnamurthy, and W. H. Weber: *Incorporation and stability of carbon during low-temperature epitaxial growth of $Ge_{1-x}C_x$ alloys on Si(100): Microstructural and Raman studies*, J. Appl. Phys. **82**, 3287 (1997).

[Yan13] Z. Yan, C. Jiang, T. R. Pope, C. F. Tsang, J. L. Stickney, P. Goli, J. Renteria, T. T. Salguero, and A. A. Balandin: *Phonon and thermal properties of exfoliated $TaSe_2$ thin films*, J. Appl. Phys. **114**, 204301 (2013).

[Yu10] J.-K. Yu, S. Mitrovic, D. Tham, J. Varghese, and J. Heath: *Reduction of thermal conductivity in phononic nanomesh structures*, Nature Nanotech. **5**, 718 (2010).

[Yu12] B. Yu, M. Zebarjadi, H. Wang, K. Lukas, H. Wang, D. Wang, C. Opeil, M. Dresselhaus, G. Chen, and Z. Ren: *Enhancement of thermoelectric properties by modulation-doping in silicon germanium alloy nanocomposites*, Nano Lett. **12**, 2077 (2012).

[Zah07] J. M. Zahler, A. Fontcuberta i Morral, M. J. Griggs, H. A. Atwater, and Y. J. Chabal: *Role of hydrogen in hydrogen-induced layer exfoliation of germanium*, Phys. Rev. B **75**, 035309 (2007).

[Zar10] I. Zardo: *Growth and Raman spectroscopy studies of gold-free catalyzed semiconductor nanowires*, Dissertation, Technische Universität München (2010).

[Zeb11] M. Zebarjadi, G. Joshi, G. Zhu, B. Yu, A. Minnich, Y. Lan, X. Wang, M. Dresselhaus, Z. Ren, and G. Chen: *Power factor enhancement by modulation doping in bulk nanocomposites*, Nano Lett. **11**, 2225 (2011).

[Zeb12] M. Zebarjadi, K. Esfarjani, M. S. Dresselhaus, Z. F. Ren, and G. Chen: *Perspectives on thermoelectrics: from fundamentals to device applications*, Energy Environ. Sci. **5**, 5147 (2012).

[Zen04] L. Zeng: *Arsenic adsorption from aqueous solutions on an Fe(III)-Si binary oxide adsorbent*, Water Qual. Res. J. Can. **39**, 267 (2004).

[Zha93] X.-J. Zhang, G. Xue, A. Agarwal, R. Tsu, M.-A. Hasan, J. E. Greene, and A. Rockett: *Thermal desorption of ultraviolet-ozone oxidized Ge(001) for substrate cleaning*, J. Vac. Sci. Techn. A **11**, 2553 (1993).

[Zha01] X. Zhang, Y. J. Chabal, S. B. Christman, E. E. Chaban, and E. Garfunkel: *Oxidation of H-covered flat and vicinal Si(111)-1$\times$1 surfaces*, J. Vac. Sci. Technol. A **19**, 1725 (2001).

[Zha10] Y. Zhang, C. L. Hapenciuc, E. E. Castillo, T. Borca-Tasciuc, R. J. Mehta, C. Karthik, and G. Ramanath: *A microprobe technique for simultaneously measuring thermal conductivity and Seebeck coefficient of thin films*, Appl. Phys. Lett. **96**, 062107 (2010).

[Zha12] J.-C. Zhao, X. Zheng, and D. G. Cahill: *Thermal conductivity mapping of the Ni-Al system and the beta-NiAl phase in the Ni-Al-Cr system*, Scripta Mater. **66**, 935 (2012).

[Zhe07] X. Zheng, D. Cahill, P. Krasnochtchekov, R. Averback, and J.-C. Zhao: *High-throughput thermal conductivity measurements of nickel solid solutions and the applicability of the Wiedemann-Franz law*, Acta Mater. **55**, 5177 (2007).

List of Publications

Articles Published in the Framework of this Thesis

1. *Plasma synthesis of nanostructures for improved thermoelectric properties*
   N. Petermann, N. Stein, G. Schierning, R. Theissmann, B. Stoib, M. S. Brandt, C. Hecht, C. Schulz, and H. Wiggers – J. Phys D: Appl. Phys. **44**, 174034 (2011).
   Harman measurement in Fig. 6 (a) and minor contributions to the text.

2. *Laser-sintered thin films of doped SiGe nanoparticles*
   B. Stoib, T. Langmann, S. Matich, T. Antesberger, N. Stein, S. Angst, N. Petermann, R. Schmechel, G. Schierning, D. E. Wolf, H. Wiggers, M. Stutzmann, and M. S. Brandt – Appl. Phys. Lett. **100**, 231907 (2012).
   Experiment design, sample preparation, evaluation and interpretation of the results, writing of the manuscript

3. *Morphology, thermoelectric properties and wet-chemical doping of laser-sintered germanium nanoparticles*
   B. Stoib, T. Langmann, N. Petermann, S. Matich, M. Sachsenhauser, H. Wiggers, M. Stutzmann, and M. S. Brandt – Phys. Stat. Solidi A **210**, 153 (2013).
   Experiment design, sample preparation, evaluation and interpretation of the results, writing of the manuscript

4. *Thermal conductivity of mesoporous films measured by Raman spectroscopy*
   B. Stoib, S. Filser, N. Petermann, H. Wiggers, M. Stutzmann, and M. S. Brandt – Appl. Phys. Lett. **104**, 161907 (2014).
   Experiment design, sample preparation, evaluation and interpretation of the results, writing of the manuscript

5. *Spatially resolved determination of thermal conductivity by Raman spectroscopy*
   B. Stoib, S. Filser, J. Stötzel, A. Greppmair, N. Petermann, H. Wiggers, G. Schierning, M. Stutzmann, and M. S. Brandt – Semicond. Sci. Technol. **29**, 124005 (2014).
   Experiment design, sample preparation, evaluation and interpretation of the results, writing of the manuscript

6. *Laser-assisted wet-chemical doping of sintered nanoparticle films*
   B. Stoib, A. Greppmair, N. Petermann, H. Wiggers, M. Stutzmann, and M. S. Brandt – Adv. Electron. Mat., **1**, 1400029 (2015).
   Experiment design, sample preparation, evaluation and interpretation of the results, writing of the manuscript

Other Articles

1. *The electrically detected magnetic resonance microscope: Combining conductive atomic force microscopy with electrically detected magnetic resonance*
   K. Klein, B. Hauer, B. Stoib, M. Trautwein, S. Matich, H. Huebl, O. Astakhov, F. Finger, R. Bittl, M. Stutzmann, and M. S. Brandt – Rev. Sci. Instr. **84**, 103911 (2013)
   Parts of this publication (esp. in part IV and V) resulted from the content of the author's diploma thesis.

2. *Sample temperature profile during the excimer laser annealing of silicon nanoparticles*
   M. Caninenberg, E. Verheyen, D. Kiesler, B. Stoib, M. S. Brandt, N. Benson, R. Schmechel – Opt. Laser Technol. **74**, 132 (2015)
   Reflectivity measurement and Raman measurements

Talks, Poster and other Presentations

1. *Nanotechnologie und Solarzellen*
   S. Niesar, B. Stoib, and N. Erhard – Live-videoconference from Walter Schottky Institut to Deutsches Museum München, June 15th 2010

2. *Harman measurements on laser-annealed thin films of Si and Ge nanoparticles*
   B. Stoib*, M. S. Brandt, N. Petermann, H. Wiggers, and M. Stutzmann – Talk at the Spring Meeting of the German Physical Society, Dresden, Germany, March 18th 2011

3. *Short-pulse laser annealing of SiGe nanocomposites*
   B. Stoib*, M. S. Brandt, N. Petermann, H. Wiggers, and M. Stutzmann – Poster at the Spring School of the German Thermoelectric Society, Cologne, Germany, March 28th to April 1st 2011

4. *Laser sintering of nanoparticles - morphologic and thermoelectric aspects*
   B. Stoib*, T. Langmann, M. S. Brandt, N. Petermann, H. Wiggers, and M. Stutzmann – Talk at the Spring Meeting of the German Physical Society, Berlin, Germany, March 30th 2012

5. *Von Silizium-Nanopartikeln zu Solarzellen - ein Blick ins Forschungslabor*
   B. Stoib, S. Niesar, and W. Aigner – Live-videoconference from Walter Schottky Institut to Deutsches Museum München, January 17th 2012

6. *Thermoelectric properties of laser-assisted wet-chemically doped group-IV nanoparticles*
   B. Stoib*, A. Greppmair, T. Langmann, N. Petermann, H. Wiggers, M. Stutzmann, and M. S. Brandt – Talk at the Spring Meeting of the German Physical Society, Regensburg, Germany, March 13th 2013

7. *Nanostrukturierte thermoelektrische Materialien*
   B. Stoib*, A. Greppmair, and M. S. Brandt – Talk at the kick-off meeting of the joint project *UMWELTnanoTECH*, Deutsches Museum München, Germany, November 22nd 2013

8. *Laser-assisted wet-chemical doping applied to films of Si and Ge nanoparticles*
   B. Stoib*, A. Greppmair, N. Petermann, H. Wiggers, M. Stutzmann, and M. S. Brandt – Talk at the Material Research Society Spring Meeting, San Francisco, USA, April 23rd 2014

9. *Microscopic infrared thermography of meso-porous thin films from laser-sintered group-IV nano-particles*
   A. Greppmair*, B. Stoib, N. Petermann, H. Wiggers, M. Stutzmann, and M. S. Brandt – Poster at the Material Research Society Spring Meeting, San Francisco, USA, April 9th 2015

Acknowledgments

Ich danke

Prof. Dr. Martin S. Brandt für die außergewöhnlich freundschaftliche Aufnahme in Deine Gruppe und das Interesse an meinem Thema, obwohl oder gerade weil es etwas exotisch war. Noch mehr danke ich Dir für das intensive und lehrreiche Betreuen beim Verfassen von Veröffentlichungen - von Deiner Liebe zum Detail hoffe ich jetzt etwas geerbt zu haben. Vielen Dank auch für die enge, konstruktive und promte Verständigung beim Abfassen der Arbeit jetzt am Ende. Ganz allgemein hast Du bei der Erziehung zum eigenständigen wissenschaftlichen Arbeiten genau die richtige Länge der Leine gewählt. Danke dafür!

Prof. Dr. Martin Stutzmann für das Zusammenhalten des E25-Haufens. Es war schön, hilf- und lehrreich mit Kollegen zusammenzuarbeiten, die so unterschiedliche Dinge machen. Viele Deiner Kommentare will man zuerst nicht hören, stellt aber dann fest, dass man sollte. Danke für Dein Querdenken und In-Frage-stellen!

meinen Diplomanden und Bachelorstudenten **Tim Langmann**, **Anton Greppmair**, **Simon Filser** und **Michael Obermaier**. Ihr habt wertvolle Arbeit geleistet, ohne die die vorliegende Arbeit so nicht zu Stande gekommen wäre. Und was mindestens so wichtig war, ihr habt mir täglich einen neuen Grund gegeben, die Arbeit weiter zu machen, die ich ohne diese Verantwortung manches Mal geschmissen hätte. Ein Dank gebührt auch meinen Werk- und Projektstudenten **Markus Felgenhauer**, **Clemens Borys**, **Verena Hintermayr**, **Andreas Wörfel** und **Florian Wiesinger**.

Sonja Matich für ungezählte Stunden, die Du für uns am FIB zugebracht hast. Dein Einsatz ist ohne Beispiel! Danke!

Dr. Hartmut Wiggers und **Nils Petermann** für die Herstellung der Nanopartikel und deren Überlassung. Unseren Wünschen nachzukommen war sicher nicht immer einfach. Zudem danke ich für die wirklich außer der Norm hilfreichen Kommentare zu Papern!

Dr. Gabi Schierning für die super Repräsentation des SiGe-Konsortiums im DFG-Projekt und Deine ewig gute Laune. Gleicher Dank gilt auch **Prof. Dr. Roland Schmechel**.

Julia Stötzel für die REM-Aufnahmen der ungesinterten Filme und die gute und prompte Zusammenarbeit für das SST-Paper.

Dr. Nils Benson und **Matthias Caninenberg** für die herzliche Aufnahme in Duisburg und die Möglichkeit, ihren Sinterlaser zu benutzen.

Prof. Dr. Dietrich Wolf und **Sebastian Angst** für die Simulation der Stromdichteverteilung in unseren Proben.

Prof. Dr. med. Christoph Alexiou und **Dr. Christina Janko** von der Sektion für Experimentelle Onkologie und Nanomedizin des Universitätsklinikums Erlangen für die unkomplizierte, interessante und hoffentlich aufschlussreiche Zusammenarbeit bezüglich der Toxizität der Si und Ge Nanopartikel.

Prof. Dr. Marcus Reichenberger, **Prof. Dr. Günther Benstetter** von der Technischen Hochschule Nürnberg bzw. der Technischen Hochschule Deggendorf für die tolle Zusammenarbeit im Rahmen des gemeinsamen Projektes. Ebenso sei den Mitarbeitern **Kristina Grundewald** bzw. **Alexander Hofer** gedankt .

Veronika Enter und **Joana Figueiredo** für so viel Kümmern und Organisieren.

Claudia Paulus, **Michi Fischer** und **Fritz Sedlmeir** für viele ad-hoc und hau-ruck Aktionen. Ich hoffe, ich habe meinen Arbeitsplatz anständig aufgeräumt.

Hubert Riedl und **Julian Treu** für Ihre Hilfe und Assistenz bei der Benutzung der RIE.

Priv.-Doz. Dr. Hans Hübl für Deine Hilfsbereitschaft und die Motivation, die Du mir hast zukommen lassen.

Und nun die lieben Doktorandenkollegen: Zuvorderst steht hier ein Dank an Dich, **Konrad Klein**, für Dein offenes Ohr, das Lesen der Arbeit, Deine Freundschaft und Deine verrückten Radtourvorschläge. Danke auch an **Felix Buth**. Mit Bozen verbinde ich noch immer die 348 km an einem Tag und vor allem die schmerzenden Gesäßknochen.

Ich danke natürlich auch meinen Kollegen **Tobias Antesberger**, **Sabrina Niesar**, **Andre Stegner**, **Alexander Kupijai**, **Willi Aigner**, **Lukas Dreher**, **Felix Höhne**, **Florian Furtmaier**, **Marco Höb**, **Bernhard Laumer**, **Christian Jäger**, **Max Seifert**, **Flo Hrubesch**, **Max Suckert**, **David Franke**, sowie allen anderen, hier nicht explizit genannten **E25**ern.

Ein wichtiger Dank gebührt den finanzierenden Organen, namentlich der **Deutschen Forschungsgemeinschaft** und dem **Bayerischen Staatsministerium für Umwelt und Verbraucherschutz**, für die Förderung der Projekte *SPP 1386 Nanostrukturierte Thermoelektrika* bzw. *UMWELTnanoTECH*. Ohne diese Finanzierungen wäre die vorliegende Arbeit nicht möglich gewesen. Danke!

Kaum in Worten auszudrücken ist der Dank, den ich meiner Familie aussprechen möchte. Ihr wart es, die mir oft denjenigen Druck nahmt, den ich mir selbst gemacht habe. Insbesondere meinen Eltern **Sabine** und **Max Stoib** danke ich dafür, dass Ihr mich von klein an habt „machen lassen“. Heute, gerade als junger Vater, schätze ich es enorm, dass ich (fast) alles durfte, und nichts musste. Nur so konnte ich kreativ werden und diejenige intrinsische Motivation wachsen lassen, die ich für diesen Bildungsmarathon von der Grundschule bis zum Doktortitel brauchte. Ich bin geehrt, dass ich, auch ohne einer Familientradition folgen zu müssen, diesen Weg habe einschlagen dürfen. Danke Mama und Papa! Ich danke auch meinen lieben Großeltern **Eleonore** und **Josef Danninger** dafür, dass sie mich immer auf meinem Weg geleitet und begleitet haben. Ja, Oma, das Daumen drücken hat geholfen. Und Recht hast Du auch noch gehabt mit Deiner Feststellung: „Nano!? Das ist doch das wo alles abperlt!“

Nur im Text am Ende, nicht aber im Ranking danke ich Dir, **Sandra**! Ich muss teilweise echt schwer auszuhalten gewesen sein. Fürs Bremsen und Ablenken, fürs Motivieren und Scheuchen, für alles, was ich hier aus Platzgründen gar nicht hinschreiben kann. Kurz: Danke! Halt! Dafür muss Platz sein: Für **Amalia**! Du kleines Wunder hast mir zwar bei der Fertigstellung dieser Arbeit ordentlich zwischen die Beine respektive den Kalender gegrätscht, dafür hast Du auch alles relativiert, was vorher den Anspruch hatte, Maßstäbe zu setzen. Das ist eine sehr schöne Erfahrung. Danke!